2010

Experimental And Cfd Investigations Of Lifted Tribrachial Flames

Zhiliang Li
University of Central Florida

University of
Central Florida

STARS
Showcase of Text, Archives, Research & Scholarship

EXPERIMENTAL AND CFD INVESTIGATIONS OF LIFTED TRIBRACHIAL FLAMES

by

Zhiliang Li
B.S. University of Science and Technology of China, 2004

A dissertation submitted in partial fulfillment of the requirement
for the degree of Doctor of Philosophy
in the Department of Mechanical, Material and Aerospace Engineering
in the College of Engineering and Computer Science
at the University of Central Florida
Orlando, Florida

Spring Term

2010

Major Professor: Ruey-Hung Chen

ABSTRACT

Experimental measurements of the lift-off velocity and lift-off height, and numerical simulations were conducted on the liftoff and stabilization phenomena of laminar jet diffusion flames of inert-diluted C_3H_8 and CH_4 fuels. Both non-reacting and reacting jets were investigated, including effects of multi-component diffusivities and heat release (buoyancy and gas expansion). The role of Schmidt number for non-reacting jets was investigated, with no conclusive Schmidt number criterion for liftoff previously known in similarity solutions. The cold-flow simulation for He-diluted CH_4 fuel does not predict flame liftoff; however, adding heat release reaction leads to the prediction of liftoff, which is consistent with experimental observations. Including reaction was also found to improve liftoff height prediction for C_3H_8 flames, with the flame base location differing from that in the similarity solution - the intersection of the stoichiometric and iso-velocity contours is not necessary for flame stabilization (and thus lift-off). Possible mechanisms other than that proposed for similarity solution may better help to explain the stabilization and liftoff phenomena. The stretch rate at a wide range of isotherms near the base of the lifted tribrachial flame were also quantitatively plotted and analyzed.

TABLE OF CONTENTS

LIST OF FIGURES

LIST OF TABLES

LIST OF ACRONYMS/ABBREVIATIONS

d jet exit inner diameter

D mass diffusivity

D_{ij} binary mass diffusion coefficient

D_{F-A} diffusivity of fuel into air

D_{ij}^{M} Maxwell diffusion coefficient

D_T thermal diffusion

H_L lift-off height

H_I maximum ignition height

$\vec{J}_i$ diffusive mass flux vector of species i

k stretch rate

Le Lewis number

L_F flame height (distance from the jet exit to the flame top)

Q the volume flow rate

r radius coordinate

RR   volumetric Arrhenius reaction rate

Sc Schmidt numbers

S_L^0 stoichiometric one-dimensional laminar flame speed

S_{tri} propagation speed of the tribriachial flame

T_{ad} adiabatic flame temperature

T_0 initial gas temperature

$V_{lift-off}$ lift-off velocity

$V_{blow-out/off}$ blow-out/off velocity

$Re_{blow-out/off}$ blow-out/off Reynolds number

$V_{Peak\ maximum\ ignition\ height}$ peak maximum ignition height velocity

V_0 jet exit average velocity

V_P perpendicular velocity

V_X axial velocity

W_F flame width

x axial coordinate

Y_i local mass fraction of species i

α thermal diffusivity

$\alpha \equiv (T_{ad} - T_0)/T_{ad}$ heat release factor

ν_{air} viscosity of the air

χ_S dissipation rate

CHAPTER 1: INTRODUCTION

This chapter summarizes the relevant published lift-off flame studies that experimentally and analytically investigate the critical Schmidt number, lift-off and reattachment hysteresis, tribrachial flame propagation speed and the flame stretch rate. The present work is an experimental study and CFD study of the lift-off theory and tribrachial flame structure.

1.1 Critical Schmidt Number concern of the Lift-off flame phenomena

The characterization of lifted flames in laminar non-premixed fuel round jet has been extensively studied for the mechanisms of flame stabilization. Various gas fuel jets have been tested experimentally and analyzed theoretically. Lee and Chung [1] arrived at a simple theoretical formula for the lift-off height of non-premixed jet flames based on laminar cold jet theory [2-3] in the region between the flame and the jet exit. In their theory, the flame base is located on the intersection of the stoichiometric fuel-air contour and the corresponding stoichiometric flame speed contour where the axial flow speed u is equal to the one-dimensional laminar flame speed S_L^0 (refer to Fig. 1.1). The lift-off height $H_L= CQ^{(2Sc-1)/(Sc-1)} d^{-2Sc/((Sc-1)} \times 10^{-11}$, where C is a constant depending on fuel type, and Q and d are the volume flow rate and jet exit diameter, respectively. Lee and Chung predicted that the lift-off height increases with increasing flow rate for Schmidt numbers ($Sc \equiv \nu_{air} / D_{F-A}$, where ν_{air} is the viscosity of the room air and D_{F-A} is the diffusivity of fuel into air) in the range $Sc > 1$ or $Sc < 0.5$; but lift-off height decreases for $0.5 < Sc < 1$, which is physically impossible. This theory was verified by experiments that propane and n-butane jets ($Sc > 1$) have stable lifted flames [1, 4] while methane and ethane ($0.5 < Sc < 1$) blow out directly from the attached jet without any stationary lift-off [1, 4].

The detailed analysis [1, 4, 5, 6] of the lifted non-premixed flame was based on the observation of tribrachial structure (illustrated in Figure 1.2): a lean premixed flame, a rich premixed flame, and a diffusion flame, all extending from a single location which is the flame base and is located in the stoichiometric contour, where the propagation speed of tribrachial flame and local axial flow velocity component are equal.

Lee and Chung's theory was not supported by experiment for $Sc < 0.5$. For hydrogen ($Sc < 0.5$), the flames persistently attach to the jet at extremely high jet velocity up to sonic speed. This behavior of hydrogen is explained by the upstream diffusion which extended the isoconcentration contours upstream from the jet exit and anchor the flame free from the high shear region of the near field of the jet mixing layer [4]. When the heat release and curvature effects were considered, Vervisch and coworkers predicted stable lifted flame for all $Sc \geq 0.8$ [7, 8].

Chen et al. [9] tested the Schmidt number theory [1, 4]. They systematically used He and Ar to dilute three fuels H_2, CH_4 and C_3H_8, so that their Schmidt numbers varied over a wide range. These binary diffusivities previously used to calculate Sc [1, 4] were replaced by the multi-component mass diffusivities while calculating the Sc for fuel diluent mixtures. This method will be introduced in Chapter 2. Chen et al. determined the critical Schmidt number for a flame to have stable lift-off prior to blowout is 0.715, resulting from CH_4 flame with 20% (by volume) dilution with He. Stable lift-off was not observed for pure CH_4 and CH_4 with any level of Ar dilution [9]. Therefore, the conclusion from pure CH_4 flames (that they do not lift off) cannot be extended to diluted CH_4 flames. Furthermore, the effect of multi-component transport properties plays an important role as, for the given CH_4 fuel, one diluent (He) leads to liftoff while the other (Ar) does not. The C_3H_8 fuel with both He and Ar dilution, if ignitable, achieved liftoff configurations for jet velocity (V_0) values prior to reaching blow-off jet velocity (V_{BO}) [9]. N_2-diluted H_2 flames (with N_2 dilution up to 70% [10]) might

achieve stable liftoff depending on the combination of jet velocity and the flame ignition location, even though $Sc < 0.3$. However, if N_2-H_2 flame was first established at the burner lip followed by increasing jet velocity, it would directly blow out without liftoff. These results are consistent with the observation in pure C_3H_8 flames that whether the flame is lifted or attached for a given V_0 may depend on the location where the ignition source is applied [11]. In summary, the Schmidt number criterion based on pure fuel results may not be extended to diluted fuels. It is suspected that the mass diffusivity of fuel in the multi-component fuel-inert gas-air environment might not have been properly treated in the literature.

Takahashi and coworkers [12 - 14] explained the stabilization mechanism of the flame base (i.e. the "edge" flame) without resorting to the Schmidt number reasoning. They found that the edge of the flame formed a rigorously burning zone, i.e., reaction kernel, propagating through the flammable mixture layer. If the local Damkohler number is critically reduced, then the flame kernel ceased to exist leading to flame extinction. The flame structure at the base depends on the fuel properties, and may thus vary with the type of diluents and the level of dilution.
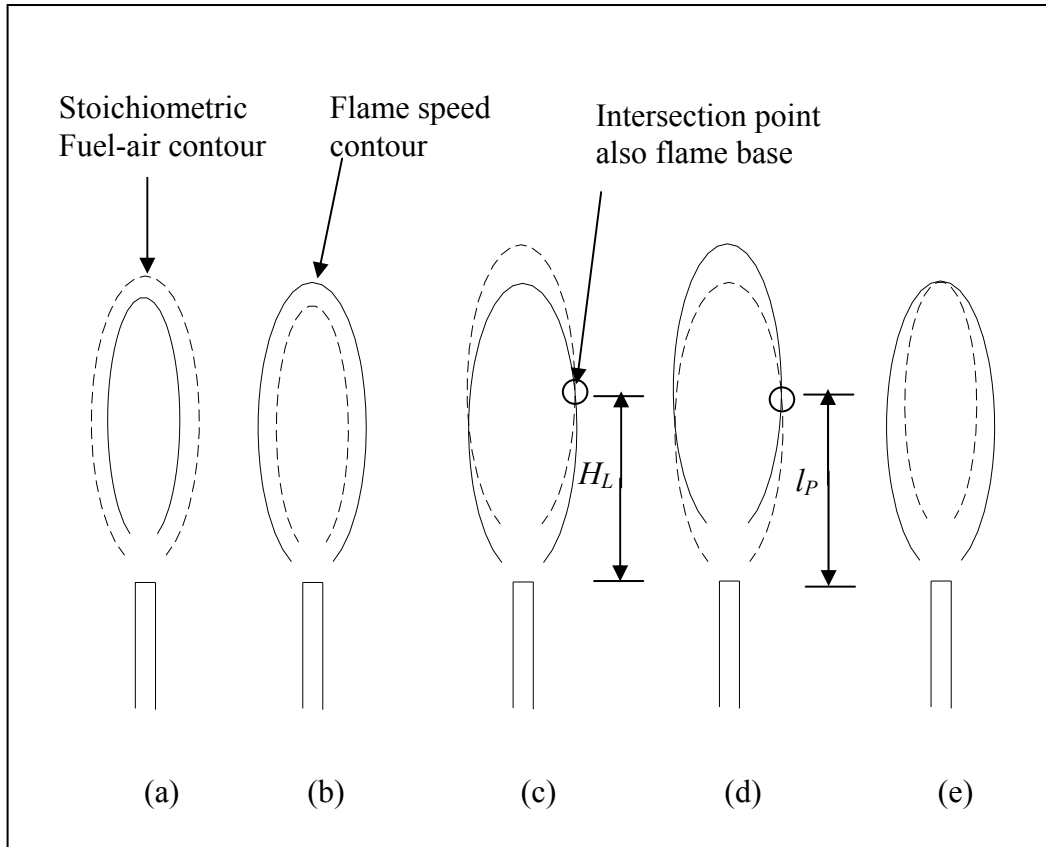
Figure 1.1 - Schematic diagram of flame speed and stoichiometric contours for a) Sc = 1, stable flame b) Sc = 1, blow-off c) Sc > 1, stable lifted flame, with lift-off height HL. d) Sc < 1, stable attached flame, with partial flame length lp. e) Sc > 1, blow-off.
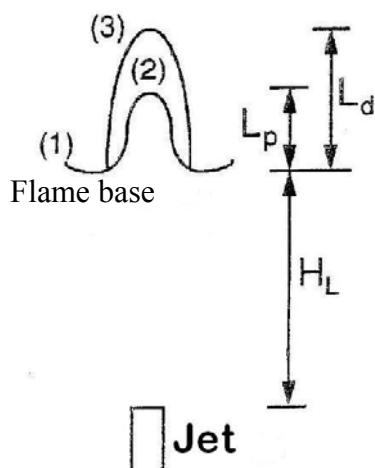
Figure 1.2 - Lift-off tribrachial flame structure for 1) lean premixed flame, 2) rich premixed flame, 3) diffusion flame, where HL is lift-off height, Lp is the length of rich premixed flame measured from the lifted flame base, and Ld is the length of diffusion flame measured from the lifted flame base.

4

Chung et al. [15] designed an experiment to verify the assumption that the tribrachial flame base propagates along the stoichiometric fuel-oxygen concentration profile. They measured the methane and nitrogen concentration profile using a spontaneous Raman scattering technique. They then calculated the equivalence ratio Φ of each point and compared it with the ICCD image observation of the loci of tribrachial points when the leading edge of the tribrachial flame was ignited downstream and propagated upstream in laminar methane jets. Figure 1.3 clearly demonstrated that the base of a tribrachial flame base (solid symbols) propagates close to the stoichiometric countours (open symbols and real line) in laminar methane jets for three different jet velocities, thus three different Reynolds numbers.
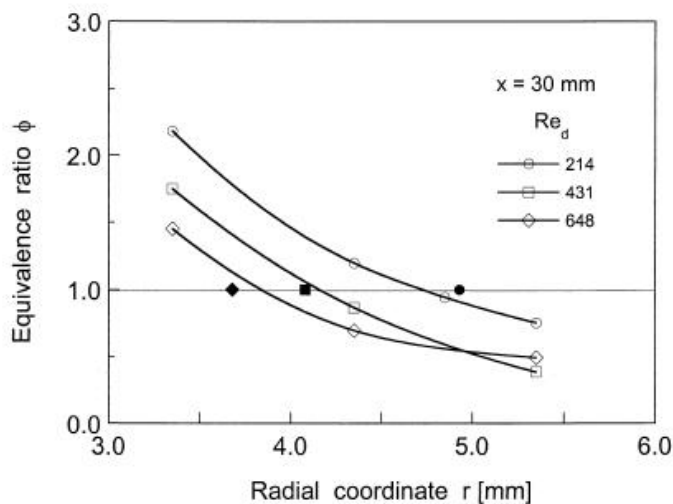
Figure 1.3 - Comparison of Raman scattering date (open symbols) and tribrachial points from ICCD images (solid symbols indicating locations of tribrachial points during flame propagation, with a fuel jet of 2.08mm i.d. [15]

1.2 Lift-off and reattachment hysteresis phenomena

In a series of experiments [1, 4, 5, 11, 16], successively increasing jet velocity of propane and n-butane flames leads to lift-off from an attached flame beyond a critical jet velocity. While decreasing jet velocity from a lifted flame, the lifted flame can abruptly

reattach to the jet; however, the critical lift-off jet velocity (U_{LO}) is usually larger than the reattachment jet velocity (U_{RA}). This phenomenon is called hysteresis [11], which can not be predicted by the far field jet Landau-Squire similarity solution [1, 4]. Similarity solution with virtual origin [11] can elucidate the hysteresis between the reattachment and liftoff for propane-air jet diffusion flame, and can also explain the abrupt lift-off height change between liftoff and reattachment as explained in the following.

Figure 1.4 shows the non-dimensional axial velocity along stoichiometric contour for $Y_{F,0} = 1.0$ (*Sc* =1.366 for C_3H_8 and *Sc* = 0.704 for CH_4). The similarity solution without virtual origin [1] predicts monotonic decrease for propane and increase for methane in axial velocity with distance. When virtual origin [11] was taken into account for both velocity and concentration contour, the monotonic tendency for propane was changed, the ridged real line in Figure 1.4 shows that the axial velocity increases close to the nozzle, has a maximum at *x* = *0.2Red*, and then decreases further away.
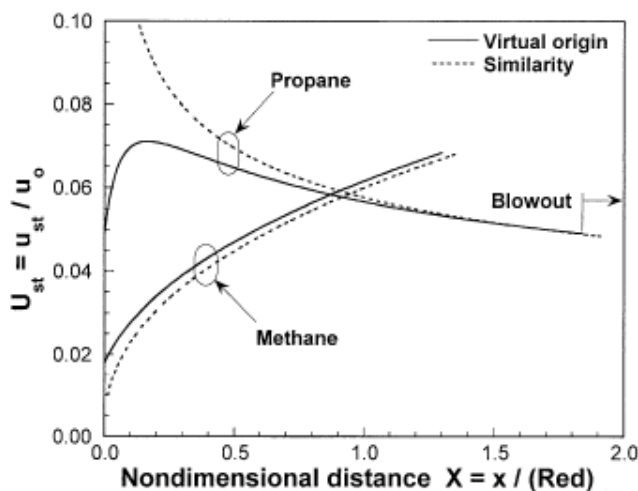
Figure 1.4 - Non-dimensional axial velocity along stoichiometric contour for the similarity solution and the similarity solution with virtual origin. [11]

In Figure 1.5, axial velocity profile with virtual origins along stoichiometric contour demonstrates blowout and reattachment for C_3H_8 jet flame. The jet exit velocities for four different cases (A, B, C and D) decreases successively; the stable lift-off phenomenon is able

to exist for the jet velocity between V_C and V_A, the propagation speed of a tribriachial flame S_{tri} balances with flow velocity u_{st} at their crossing points (C', B' and A'), the tribriachial flame base either perturbed to upstream or downstream, the difference between S_{tri} and u_{st} will push the tribriachial flame base back to the crossing point. V_C is the critical reattachment velocity. However, the lift off velocity is higher than V_C, because the flow velocity near the jet is lower than the maximum velocity at C'; the jet velocity must increase further in order to lift off from the jet in the attached flame initial conditions, thus $U_{LO} > U_{RA}$, which is called hysteresis. [11]
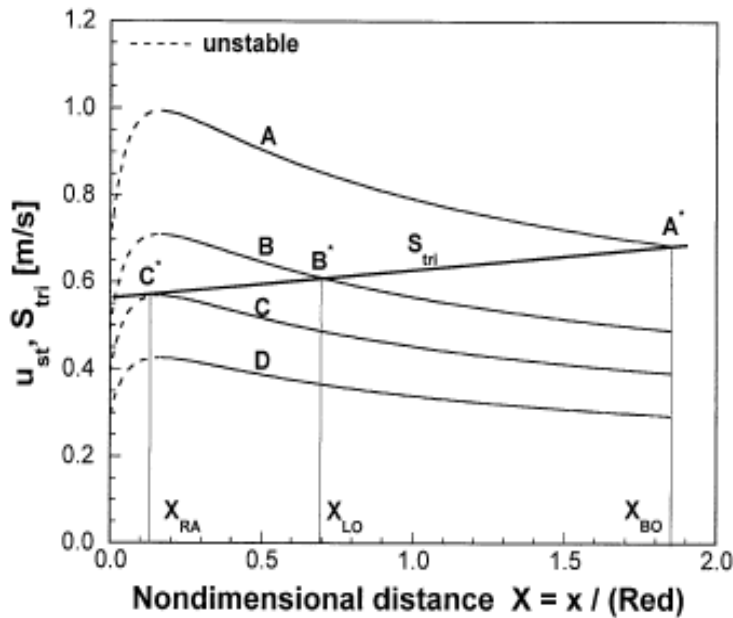
Figure 1.5 - Axial velocity profile with virtual origins along stoichiometric contour. [11]

1.3 Theoretic analysis and measurement for the tribrachial flame propagation speed Stri of the stable lift-off flame base

In the theoretical analysis of Chung and Lee [1] based on the constant density assumption, the tribrachial flame propagation speed (S_{tri}) was assumed to be equal to the planar laminar flame speed. Later Chung and Lee [4] designed a coflow lifted propane-air flame experiment to test the cold jet theory of lift-off height by measuring the velocity profiles. Their results showed that the axial and radial velocities for the cold flow field and the

reacting field agreed well from the jet exit to the lift-off height and the lifted tribrachial flame only affected the upstream flow within 1mm. The velocity ahead of the lifted propane-air flame base was found to be 0.53cm/s [4], which is larger than the stoichiometric laminar burning velocity of 0.44m/s [17]. Chung and Lee [4] explained that the streamlines near the tribrachial flame region were highly deflected due to gas expansion, and the upstream gas velocity was decreased near the preheat zone of the tribrachial point. (See the velocity distribution Figure 1.6) However, for different flow rates and also with different lift-off heights, the propagation speed remains nearly constant. They concluded that the flame front slantedness and the flame curvature have mitigating effects to the increase in the propagation speed by the flow redirection; therefore, the propagation speed remains constant irrespective of the jet flow rate. Thus, the assumption of a constant laminar burning velocity balanced against a constant axial velocity component in theoretical prediction is validated. However, their coflow velocity $U_{air} = 0.3$m/s was in the order of laminar stoichiometric propane-air flame speed, which minimized the buoyancy effect and other upstream effects that existed without coflows.
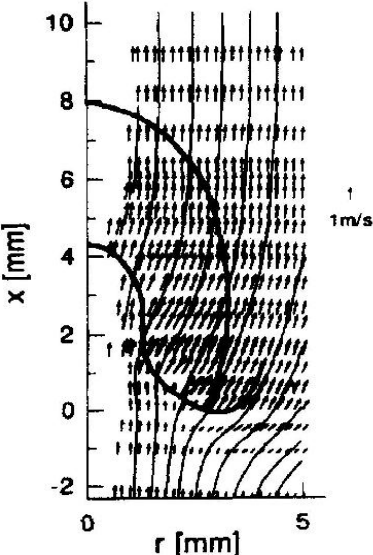
Figure 1.6 - Velocity distribution near lifted flame for $U_{air} = 0.3$m/s and $u_o = 7.9$m/s coflow lift-off flame. Fuel nozzle with 0.65mm o.d. and 0.37 mm i.d., coflow air nozzle with 21mm diameter. [4]

Ruetsch and Vervisch [5, 7] showed that the tribrachial flame speed was affected by the thermal expansion and the mixture fraction gradient. Ghosal and Vervisch [7] presented a new correlation between the tribrachial flame speed S_{tri} and the laminar flame speed S_L^0 by considering these factors,

$$S_{tri} = S_L^0 (1+\alpha) - f(\chi_S), \qquad (1.1)$$

where $\alpha \equiv (T_{ad} - T_0)/T_{ad}$ is the heat release factor, where T_{ad} is the adiabatic flame temperature, and T_0 is the fresh gas temperature, and

$$f(\chi_S) = \frac{\beta(\lambda/\rho C_P)^{1/2}}{(1+\alpha)Y_{F,st}\sqrt{4\nu_F - 2}} \chi^{1/2}, \qquad (1.2)$$

where χ_S is the dissipation rate of mixture fraction,

$$\chi_S \approx \left(\frac{\lambda}{\rho C_P}\right)\left(\frac{1}{r}\frac{\partial Y_F}{\partial \theta}\right)^2 \Big|_{r=r_{st}}, \qquad (1.3)$$

and ν_F is the molar stoichiometric coefficient of the fuel. They found that stable lifted flames could exist for any values of Schmidt number, but the region of jet exit velocity space that supports a lifted laminar flame is very narrow for Schmidt number less than 1. However, this model did not consider the stretch effect. That effect is significant when the fuel Lewis number ($Le = \alpha/D$, where α is the thermal diffusivity and D is the mass diffusivity) is far from unity.
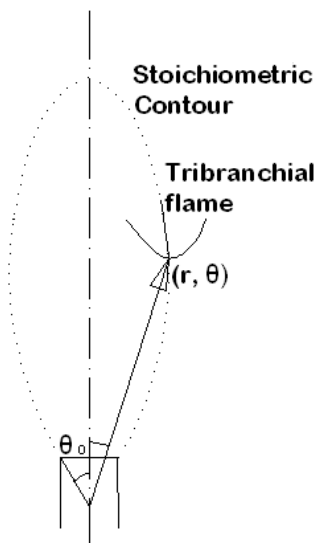
Figure 1.7 - Coordinate system for the tribrachial flame.

Daou and Liñán [18] considered the flame stretch (Lewis number effect and the flow velocity gradient) effect to the tribrachial flame propagation speed function, using the counter flow diffusion flame and constant density model. They described the tribrachial flame propagation speed (S_{tri}) as

$$S_{tri} = S_L^0 \left(1 - \frac{\sqrt{2}}{\sqrt{\pi}} \varepsilon \left[1 + \frac{l_F + l_O}{4} \right] \right),$$ (1.4)

where ε is defined as the ratio of the expected characteristic value of the flame front curvature radius, and the laminar flame thickness is $l_{Fl}^0 \equiv \lambda/(\rho c_P S_L^0)$, the thermal conductivity (λ), the density (ρ), and the heat capacity (c_P) are assumed to be constant. l_F and l_O are the reduced Lewis numbers, $\beta(Le_F - 1)$ and $\beta(Le_O - 1)$, where $\beta \equiv E(T_{ad} - T_0)/RT_{ad}^2$ is Zeldovich number, $Le_F \equiv D_T/D_F$ and $Le_O \equiv D_T/D_O$ are the Lewis numbers of the fuel and of the oxidizer, respectively. Here D_T, D_F and D_O respectively denote the diffusion coefficients for the heat, the fuel and the oxidizer. The second term in Equation (1.4) represents the combined effects of flame stretch and mixture fraction gradient on the tribrachial flame speed. With Lewis number equal to unity, it represents pure mixture fraction gradient effect.

Xue and Ju [19] experimentally and theoretically analyzed the lifted flame for dimethyl ether (DME), methane, and propane flame. They improved the tribrachial flame speed calculation by coupling the heat release effect with the flame stretch and mixture fraction gradient. They arrived at the following relation between the tribrachial flame speed and the laminar flame speed:

$$S_{tri} = S_L^0 \left(1 + \alpha - Ax(1 + x^2)^{2Sc-1} \right)$$ (1.5)

where $A = \frac{\sqrt{2}}{\sqrt{\pi}} \left[1 + \frac{l_F + l_O}{4} \right] \frac{8\sqrt{3} l_{Fl}^0 Y_{F,st}}{(2Sc + 1)d}$, and $x = \theta/\theta_0$.

Xue and Ju [18] imposed the three models (explained in the caption of Fig1.8) of theoretical predictions for tribrachial flame speed into the Landau-Squire similarity solution for 0.2mm diameter propane jet, and compared that with the experimental results of the lifted propane flames in Figure 1.8, which shows that the Model III (Eq. 1.5) predicted a more accurate lift off height compared with the experimental results.
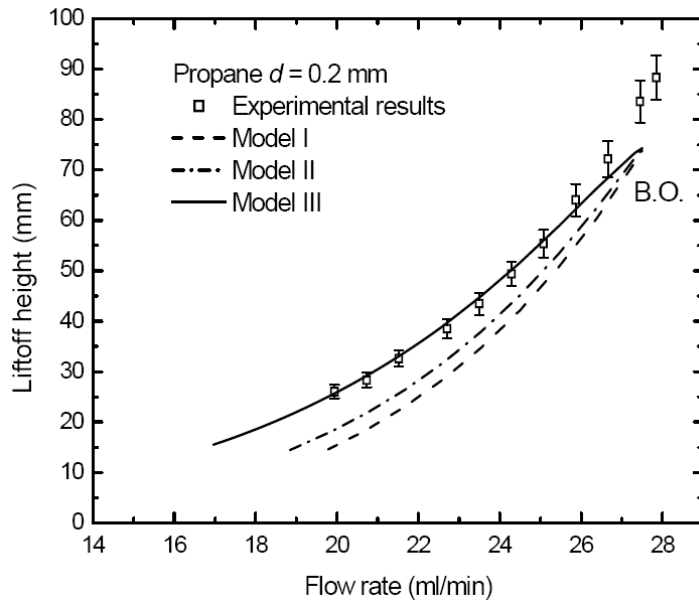
Figure 1.8 - Comparison between the predicted liftoff heights and experimental results of propane. Model I) the heat release effect is only considered. Model II) proposed by Ghosal and Vervisch, Eq. (1.1). Model III) proposed by Ju and Xu, Eq. (1.5). [19]

Vervisch and Ghosal [7] also used the Landau-Squire theory predicted for very weakly curved hydrocarbon flame, so the second term in Equation (1.1) is negligible, then $\alpha \approx 0.8$, $u_P = 1.8 S_L^0$, consistent with the experimental observation by Chung and Ko [6]. In Chung and Ko's experiment, the fuel nozzle is a stainless steel tube (2.08 mm i.d. and 600 mm length) with a length to diameter ratio large enough for the fuel flow to be fully developed. The fuel is pure methane, and the oxidizer is the ambient air, but the lifted tribrachial flame for pure methane cannot exist in stable status. Thus they designed a transient approach described in the following. Jet velocities were measured by a two component laser Doppler velocimetry (LDV), consisting of a 4-W Ar-ion laser, an optical fiber probe, photomultiplier tubes, and

counter-type signal processors. Seeded particles were 0.3 μm aluminum oxiders. The probing volume was a 0.26mm long and 0.05mm diameter ellipsoid. They measured the cold flow velocity fields in the absence of flame by LDV. After that, they used a pulsed Nd: YAG laser to ignite the fuel flow from 100 or 200mm downstream of the nozzle. Then the images of flame propagation fronts were recorded with either schlieren (500-1000 fps) or direct photography and measured with a file analyzer. The Intensified DDS camera, synchronized with the laser to capture flame images at proper location, determines the flame curvature of the tribrachial flames. The flame displacement speed at a certain position is equal to the derivative of flame edge height with respect to time. The tribrachial flame propagation speed, S_{tri}, is the sum of flame displacement speed and axis flow velocity (without flame), as shown in Figure 1.9. It ranges from 0.68m/s to 0.87m/s with various flame curvatures, which is approximately 1.7 to 2.2 times of the adiabatic flame speed (0.39m/s) for the corresponding stoichiometric mixture. Their axial flow velocity is measured without flame. However, when the tribrachial flame base approaches the position, the buoyancy effect has accelerated the axis flow velocity, so the actual tribrachial flame propagation speed would be even larger.
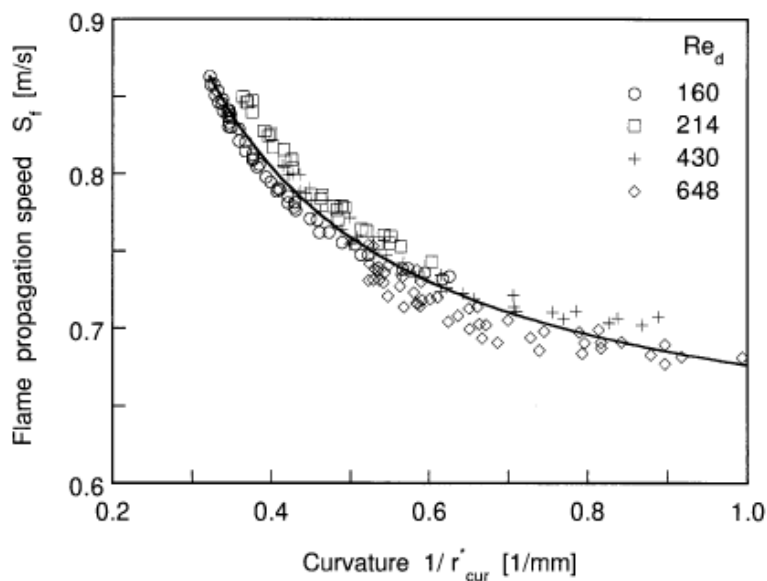
Figure 1.9 - Methane-air Tribrachial flame propagation speed with flame curvature for various Reynolds number. [6]

12

In Lee and Chung's earlier work [4], for stable lifted flame in propane-air coflow, the flame propagation speed was measured by the same LDV apparatus above. The velocity at the tribrachial flame base was approximately 0.53 m/s, which was only 1.2 times of the stoichiometric laminar burning velocity of 0.44 m/s [17] for propane-air, while the ratio for methane-air was 1.7 to 2.2 as mentioned in the previous paragraph. Several factors could contribute to such a difference. However, both of their heat release factors are approximately 0.8; the curvature for propane-air coflow flame is in the curvature range for methane-air flames (show in Figure 1.9).

We can preliminarily study the structure of the 1-Dimensional planar flame; a stoichiometric premixed methane-air planar flame is calculated by Chemkin3.7, using Gri-Mech3.0 mechanism, without radioactive heat loss and gravity. Figure 1.10 is a profile for the temperature, velocity and heat release rate distribution. We can see most of the heat is released within the 0.5mm thickness reaction zone. At the entrance of the 1-D tube($x = 0$), with the initial temperature at T=298K, and the initial inlet flow speed at V=39cm/s, the temperature and velocity increase proportionally in the pre-heat zone($1.3\text{mm} < x < 1.6\text{mm}$). Their gradients ahead of the maximum heat release rate zone are estimated to be 4285K/mm and 562cm/s/mm respectively. For the 2-D lifted jet flame measurements, accurate assessment of these large gradients and air entrainment, buoyancy, flow redirection, flame stretch, and flame slantedness are difficult to quantify at the tribrachial flame base. Moreover, the flow and flame fluctuation and the measurement resolution also contribute to the deficiencies of the experimental study for the detail structure of the tribrachial flame.
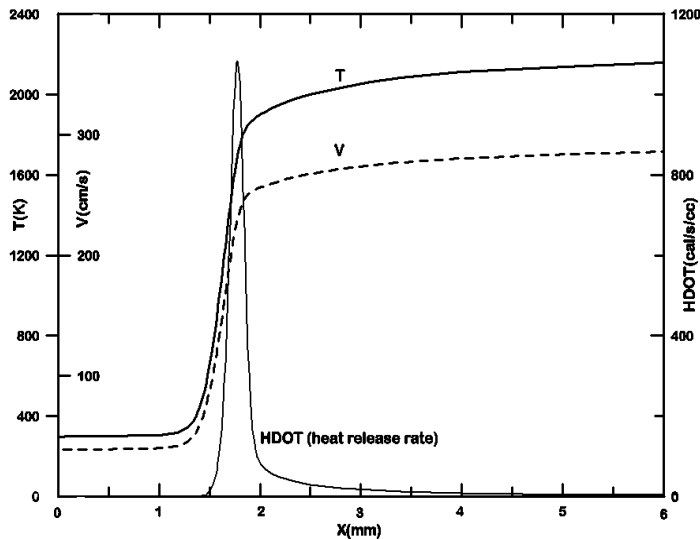
Figure 1.10 - Temperature, Velocity, and Heat release rate profile for Stoichiometric premixed Methane-Air 1-D Planar flame

1.4 The applicability of CFD method

Similarity solutions [1, 4, 6, 7, 11, and 18] have to assume constant density and diffusivity, which intrinsically affected the accuracy of the flow field prediction. Experimental methods, such as thermocouple, LDV method, and Raman scattering technique could be costly and not easily available. Experimental limitations also exist due to spatial resolution. CFD calculations make it possible to investigate the microstructure of the tribrachial: the detailed mass fraction, velocity field, reaction rate, and temperature distribution prior to the tribrachial flame base.

1.5 Current work

In the present study, we will use the FLUENT code to verify the Schmidt number theory for a series of different jet diameters, and validate all the factors that contribute to the tribrachial flame propagation speed.

In the experimental portion, we measured the flame height, lift-off height, maximum ignition height, and blow-out velocity. By the numerical calculation of the cold fuel jet flow field, we can analyze the intersection of the isoconcentration and iso-velocity contours, which

14

should help us to understand the mechanism of the stable flame lift-off. Different fuel mixtures (i.e. fuels diluted with He and Ar) and jet velocities are studied, and the lift-off heights are compared with our experimental results. Reacting flows are also investigated for lift-off height, flame propagation speed, concentration, temperature and velocity contours. Argon and helium are added systematically as dilution to the fuel because they have the same heat capacity; thus their mass diffusivity difference is the key effect to their flame lift-off height difference. The flame stretch rate for all the lift-off tribrachial flame at a variety of isotherm in the flame base are systematically plotted and analyzed.

CHAPTER 2: EXPERIMENT SETUPS
AND NUMERICAL APPROACH

The experiment was conducted to ensure that the CFD simulation adequately predicts global flame results such as lift-off heights, flame heights and the blow-out velocities. The experimental apparatus is shown in Figure 2.1. A diffusion flame was formed by issuing a jet of fuel-diluent mixture through a burner tube with an inner diameter (D_i) 0.04064cm. To make sure the pipe flow was fully developed, the following relation was used to select the length of the tube, $l_e = (0.05 \cdot D_i \cdot Re_D)$, where l_e is the entrance length required for the fully developed pipe flow, and Re_D is the Reynolds number of a fuel-diluent mixture. The Reynolds number is defined as $Re_D = U \cdot D_i / v$, in which U is the average flow velocity, and v is the kinematic viscosity of the fuel-diluent mixture, and $U = Q/A_i$, with Q being the flowrate of a mixture and A_i is the inner area of the burner ($A_r = 0.001297 \text{cm}^2$). Re_D of various mixtures at their laminar blow-off or blow-out velocity were typically less than 1700 [20]. Therefore, using the above-mentioned relation for l_e and for the Re_D of 1700, the required entrance length of the burner was found to be 3.45cm. The length of the burner was kept to 7.62cm; thus, the flows of various fuel-diluent mixtures in this study were laminar and fully developed. Values of Re_D of various fuel-diluent mixtures at their blow-off or blow-out velocity are tabulated (see Section 1 of Chapter 4) for Ar or He diluted CH_4 and C_3H_8 flames, respectively. Values of kinematic viscosities (v) of mixtures were calculated using the software tool available on the Colorado State University website (http://navier.engr.colostate.edu/tools/diffus.html).
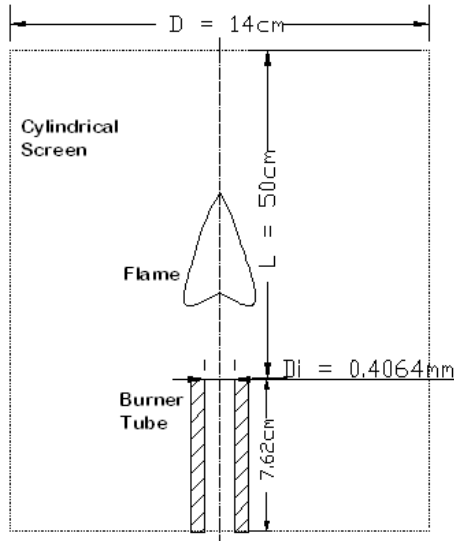
Figure 2.1 - Burner (Inner diameter = 0.4064mm, Outer diameter = 0.7112mm)

Two inlets for the fuel and the inert gases are connected from the high pressure gas tank with pressure regulator. The gas flow rates are controlled by the Omega mass flow meters. The gases were mixed to form fuel-inert mixtures downstream of the mass flow meters and upstream of the fuel tube. To accurately control the flow rates of fuels and diluents, 2 flowmeters (Omege FMA 1700/1800 series mass flowmeter) of different ranges were used. These flowmeters are calibrated with reference gas N_2, so there is a relative K factor for each specified gas to the reference gas N_2, $K = Q_a/Q_r$, where Q_r = volumetric flow rate of the reference gas N_2 (unit: sccm), and Q_a = volumetric flow rate of the actual gas. To gradually increase the jet velocity of a given composition mixture a chart is prepared, which gives the volumetric flow rates of fuel and diluent. The velocity increment is set to be 0.25m/s due to the resolution of the flowmeters. The average velocity U is calculated using the relation, $Q_{total} = A \times U$, where A is the inner area of the burner tube, and Q_{total} is the mixture flow rate. For example (see Table 2.1), for the 40%C_3H_8 - 60%He mixture with a jet exit velocity of $U = 500$cm/s, a total flow rate would be $Q_{total} = 0.001297$ cm^2 × 500 cm/s = 0.6485 cm^3/s = 0.03891 L/min, $Q_{C3H8} = Q_{total} \times 40\% = 0.015564$ L/min, and $Q_{C3H8\text{-}ref} = Q_{C3H8}/ (K_{C3H8} = 0.35) = 0.04447$ L/min, while $Q_{He\text{-}ref} = Q_{total} \times 60\% / (K_{He} = 1.454) = 0.01606$ L/min. $Q_{C3H8\text{-}ref}$ and

17

Q_{He-ref} are the numbers that should be read in the flowmeters. The maximum ignition height is defined as the maximum height above the fuel jet exit level, where the fuel-air mixture can be ignited by an electrical spark and the flame can propagate upstream to an equilibrium lift-off height or attach to the fuel jet exit

Table 2.1 - Values of experimental parameters and observations of 40% C_3H_8 – 60% He diluted fuel mixture flame. HL: lift-off height, LF: flame height (distance from the jet exit to the flame top), HI: maximum ignition height

40% C_3H_8 – 60%He fuel mixture						
U(cm/s)	$Q_{C3H8-ref}$	Q_{He-ref}	Re	H_L(cm)	L_F(cm)	H_I (cm)
100	0.009	0.003	30	0	0.2	1
200	0.018	0.006	60	0	0.3	1.5
300	0.027	0.01	90	0.1	0.5	2.5
400	0.036	0.013	120	0.4	1.0	4.0
500	0.044	0.016	150	0.7	1.5	5.0
600	0.053	0.019	180	1.5	2.4	6.5
700	0.062	0.022	210	2.4	3.2	8.0
800	0.071	0.026	240	4.0	4.5	9.5
900	0.08	0.029	270	5.5	6.0	10.5
1000	0.089	0.032	300	7.5	7.8	12.0
1050	0.093	0.034	315	Blow-off		

To mitigate the disturbance from the room airflow, the burner is surrounded with a wire cylindrical screen (mesh size 2 mm X 2 mm), with a diameter of 14cm and length of 50cm. During the lift off height measurement process, if the screen is removed, the lift-off height will decrease about 20% when the lift-off height is around 20cm because screen removal would improve the air entrainment. There is also an exhaust fan in the ceiling, which is about 1.5 meters higher than the fuel jet. When the exhaust fan is turned on to keep the air fresh, the lift-off height and flame height would be extended by 20% when the lift-off height is more than 20cm. On the other hand, it also reduces the minimum blow off velocity. To eliminate these affect, we turn off the exhaust fan temporarily when the jet velocity is close to the minimum blow off velocity or the lift-off height is more than 20cm. Figure 2.2 shows a typical laminar lift-off flame phenomenon for C_3H_8-He flames.
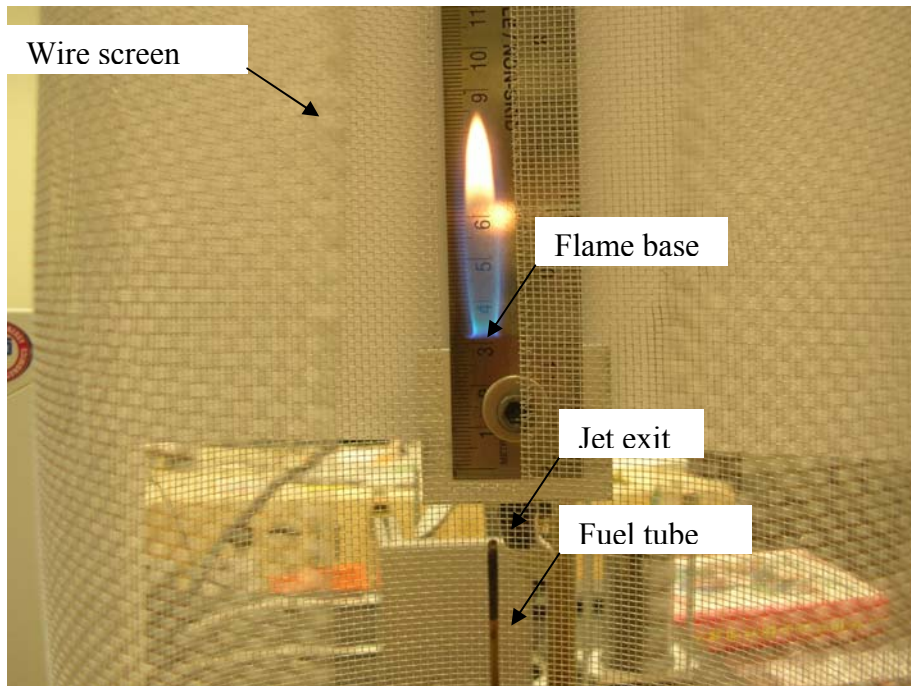
Figure 2.2 - A typical laminar lifted flame, $40\%C_3H_8 + 60\%He$, $V_0 = 8$ m/s

Different fuel mixtures (i.e. fuels diluted with He and Ar) listed in Table 2.2 were used in this experiment. The three different definitions of Schmidt numbers for each fuel mixture are also listed in Table 2.2, which will be compared with the experimental results and discussed in Chapter 4.

Table 2.2 - Test conditions

Fuel	% He dilution	$Sc_{(1)}$	$Sc_{(2)}$	% Ar dilution	$Sc(1)$	$Sc(2)$
CH$_4$						
	0%	0.714	0.714		0.714	0.714
	20%	0.712	0.717	20%	0.724	0.705
	40%	0.692	0.722	40%	0.724	0.698
	60%	0.656	0.732	60%	0.724	0.680
	80%	0.577	0.760	80%	0.724	0.644
C$_3$H$_8$						
	0%	1.449	1.403		1.449	1.403
	20%	1.437	1.404	20%	1.450	1.398
	40%	1.419	1.407	40%	1.453	1.392
	60%	1.384	1.412	60%	1.457	1.379
	80%	1.291	1.427	80%	1.470	1.345

(1) and (2) indicate the 2 different definitions of Schmidt number.

The first definitions for Schmidt number is as following:

$$D_i = (1 - X_i) / \sum_{j=1, j \neq i}^{N} \frac{X_j}{D_{ij}}, \ Sc = v_{air} / D_i \qquad (2.1)$$

where X_i is the stoichiometric mole fraction of fuel, X_j is the stoichiometric mole fraction of no-fuel species, D_{ij} is the binary mass diffusion coefficient, v_{air} is the kinetic viscosity of air. This definition was used by Turns' text book [21]. The second definition of *Sc* is:

$$Sc = v_{air} / D_i \qquad (2.2)$$

where D_i equals to the $D_{fuel \rightarrow N_2}$ component for the 3 x 3 stoichiometric multi-component diffusion coefficients matrix, which can be calculated using the Colorado State University website software tool mentioned in the beginning of this chapter. This definition is cited from Chen's early work [9] and also Lee and Chung's [1, 4]. When the tool software is used to calculate $D_{fuel \rightarrow N_2}$, because the diffusivity properties for O_2 and N_2 are very close, for simplicity the air is considered to be N_2, the 3x3 matrix being the results of three components: fuel, inert gas and N_2.

CHAPTER 3: CFD SIMULATION

To numerically model the laminar round jet diffusion flames, the governing equations of mass, momentum, energy and chemical species for a reacting flow are solved using the FLUENT code. The details are described in the following.

3.1 Governing Equations

3.1.1 The Mass Conservation Equation

The equation for conservation of mass is written as follows:

$$\frac{\partial}{\partial t}\rho + \nabla \cdot (\rho \vec{\upsilon}) = S_m \tag{3.1}$$

Equation (3.1) is the general form of the mass conservation equation and is valid for incompressible as well as compressible flows. The source S_m is the mass added to the continuous phase from the dispersed second phase (e.g., due to vaporization of liquid droplets) and any user-defined sources, and it is set to zero for this study.

3.1.2 Momentum Conservation Equations

Conservation of momentum is described by [20]

$$\frac{\partial}{\partial t}(\rho \vec{\upsilon}) + \nabla \cdot (\rho \vec{\upsilon} \vec{\upsilon}) = -\nabla p + \nabla \cdot \left(\overline{\overline{\tau}} \right) + \rho \vec{g} + \vec{F} \tag{3.2}$$

where p is the static pressure, $\overline{\overline{\tau}}$ is the stress tensor (described below), and $\rho \vec{g}$ and $\vec{F}$ are the gravitational body force and external body forces (e.g., that arise from interaction with the dispersed phase), respectively.

The stress tensor $\overline{\overline{\tau}}$ is given by

$$\overline{\overline{\tau}} = \mu \left[\left(\nabla \vec{\upsilon} + \nabla \vec{\upsilon}^T \right) - \frac{2}{3} \nabla \cdot \vec{\upsilon} I \right] \tag{3.3}$$

where μ is the molecular viscosity, I is the unit tensor, and the second term on the right hand side represents the effect of volume dilation.

3.1.3 Energy Equation

The energy equation for laminar flow is in the following form:

$$\frac{\partial}{\partial t}(\rho E) + \nabla \cdot (\vec{\upsilon}(\rho E + p)) = \nabla \cdot \left(k\nabla T - \sum_{j} h_j \vec{J}_j + \left(\overline{\overline{\tau}} \cdot \vec{\upsilon} \right) \right) + S_h \qquad (3.4)$$

where k is the conductivity, and $\vec{J}_j$ is the diffusion flux of species j. The first three terms on the right-hand side of Equation (3.4) represent energy transfer due to conduction, species diffusion, and viscous dissipation, respectively. S_h includes the heat of chemical reaction and any other volumetric heat sources, which are not of concern in this study.

In Equation (3.4),

$$E = h - \frac{p}{\rho} + \frac{\upsilon^2}{2} \qquad (3.5)$$

where sensible enthalpy h is defined for ideal gases as

$$h = \sum_{j} Y_j h_j \qquad (3.6)$$

where Y_j is local mass fraction of each species, and h_j is the enthalpy for species j.

3.1.4 Species Transport Equations

For the local mass fraction of each species, Y_i, the convection and diffusion terms are considered for the ith species, and the conservation equation has the following general form:

$$\frac{\partial}{\partial t}(\rho Y_i) + \nabla \cdot (\rho \vec{\upsilon} Y_i) = -\nabla \cdot \vec{J}_i + R_i + S_i \qquad (3.7)$$

where R_i is the net rate of production of species i by chemical reaction (described later in this section) and S_i is the rate of creation by addition from the dispersed phase plus any user-defined sources, which is not the concern in this study. An equation of this form will be solved for ($N-1$) species where N is the total number of fluid phase chemical species present in the system. Since the mass fraction of the species must sum to unity, the Nth mass fraction is determined as one minus the sum of the ($N-1$) solved mass fractions. To minimize the numerical error, the Nth species should be selected as that species with the overall largest mass fraction. In this study, N_2 is selected when the oxidizer is air.

3.1.5 Mass Diffusion in Laminar Flows

In Equation (3.7), $\vec{J}_i$ is the diffusion flux of species i, which arises due to concentration gradients. For our laminar flow (diffusion-dominated laminar flow), the details of the molecular transport processes are significant, and full multi-component diffusion is required. Here, the Maxwell-Stefan equations will be used to obtain the diffusive mass flux. This will lead to the definition of generalized Fick's law diffusion coefficients. This method is preferred over computing the multi-component diffusion coefficients since their evaluation requires the computation of N^2 co-factor determinants of size $(N-1)\times(N-1)$, and one determinant of size $N \times N$, where N is the number of chemical species.

3.1.6 Maxwell-Stefan Equations

From Merk [22], the Maxwell-Stefan equation can be written as

$$\sum_{j=1,j\neq i}^{N} \frac{X_i X_j}{D_{ij}^M}\left(\vec{V}_j - \vec{V}_i\right) = \vec{d}_i - \frac{\nabla T}{T}\sum_{j=1,j\neq i}^{N}\frac{X_i X_j}{D_{ij}^M}\left(\frac{D_{T,j}}{\rho_j} - \frac{D_{T,i}}{\rho_i}\right) \qquad (3.8)$$

Where X is the mole fraction, $\vec{V}$ is the diffusion velocity, D_{ij}^M is the Maxwell diffusion coefficient, D_T is the thermal diffusion (or Soret effect) coefficient, $\vec{d}$ is the general driving force term, and the subscriptions i and j donate species i and j in the mixture, respectively.

For an ideal gas the Maxwell diffusion coefficient D_{ij}^M is equal to the binary diffusion coefficient D_{ij}. If the external force (such as magnetic or gravitational force) is assumed to be the same on all species and that pressure diffusion is negligible, then $\vec{d}_i = \nabla X_i$. Since the diffusive mass flux vector, which was mentioned in Equation (3.7), is $\vec{J}_i = \rho_i \vec{V}_i$, the above equation can be written as

$$\sum_{j=1, j \neq i}^{N} \frac{X_i X_j}{D_{ij}} \left(\frac{\vec{J}_j}{\rho_j} - \frac{\vec{J}_i}{\rho_i} \right) = \nabla X_i - \frac{\nabla T}{T} \sum_{j=1, j \neq i}^{N} \frac{X_i X_j}{D_{ij}} \left(\frac{D_{T,j}}{\rho_j} - \frac{D_{T,i}}{\rho_i} \right) \qquad (3.9)$$

After some mathematical manipulations, the diffusive mass flux vector, $\vec{J}_i$, can be obtained from

$$\vec{J}_i = -\sum_{j=1}^{N-1} \rho D_{ij}^a \nabla Y_j - D_{T,i} \frac{\nabla T}{T} \qquad (3.10)$$

where Y_j is the mass fraction of species j. Other terms are defined as follows:

$$D_{ij}^a = [D] = [A]^{-1} [B] \qquad (3.10b)$$

$$A_{ii} = -\left(\frac{X_i}{D_{iN}} \frac{M_w}{M_{w,N}} + \sum_{j=1, j \neq i}^{N} \frac{X_j}{D_{ij}} \frac{M_w}{M_{w,i}} \right)$$

$$A_{ij} = X_i \left(\frac{1}{D_{ij}} \frac{M_w}{M_{w,j}} - \frac{1}{D_{iN}} \frac{M_w}{M_{w,N}} \right)$$

$$B_{ii} = -\left(X_i \frac{M_w}{M_{w,N}} + (1 - X_i) \frac{M_w}{M_{w,i}} \right)$$

$$B_{ij} = X_i \left(\frac{M_w}{M_{w,j}} - \frac{M_w}{M_{w,N}} \right)$$

where $[A]$ and $[B]$ are $(N-1) \times (N-1)$ matrices and $[D]$ is an $(N-1) \times (N-1)$ matrix of the generalized Fick's law diffusion coefficients D_{ij}^a (multi-component diffusion coefficients), M_w denotes the average molar mass of the mixture, and $M_{w,i}$, $M_{w,i}$, $M_{w,N}$ donate the molar mass of species i, j and N.

3.1.7 Treatment of Species Transport in the Energy Equation

For the multi-component mixing flow with volumetric reaction in the energy equation, the transport of enthalpy due to species diffusion $\nabla \cdot \left[\sum_{i=1}^{n} h_i \vec{J}_i \right]$ can have a significant effect on the enthalpy field and should not be neglected. In particular, when the Lewis number $Le_i = \dfrac{\alpha}{D_{i,m}}$ for any species is far from unity, neglecting this term can lead to significant errors.

In this equation, α is the thermal diffusivity, and $D_{i,m}$ is the mass diffusivity for species i in the mixture, $D_{i,m} = (1 - X_i) / \sum_{j=1, j \neq i}^{N} \dfrac{X_j}{D_{ij}}$ (see the first definition of Schmidt number in Chapter 2).

3.1.8 Laminar Finite-Rate Chemistry reaction Model

The laminar finite-rate model computes the chemical source terms using Arrhenius expressions, and ignores the effects of turbulent fluctuations. The model is exact for laminar flames, but is generally inaccurate for turbulent flames due to highly non-linear Arrhenius chemical kinetics. Our calculation is limited to the laminar flame case.

The net source of chemical species i due to reaction R_i is computed as the sum of the Arrhenius reaction sources over the N_R reactions that the species participate in:

$$R_i = M_{w,i} \sum_{r=1}^{N_R} \hat{R}_{i,r} \qquad\qquad (3.11)$$

where $M_{w,i}$ is the molecular weight of species i and $\hat{R}_{i,r}$ is the Arrhenius molar rate of creation/destruction of species i in the r-th reaction.

Consider the r-th reaction written in general form as follows:

$$\sum_{i=1}^{N} v'_{i,r} M_i \xrightleftharpoons[k_{b,r}]{k_{f,r}} \sum_{i=1}^{N} v''_{i,r} M_i \qquad\qquad (3.12)$$

where,

N = number of chemical species in the system

$v'_{i,r}$ = stoichiometric coefficient for reactant i in reaction r

$v''_{i,r}$ = stoichiometric coefficient for product i in reaction r

M_i = symbol denoting species i

$k_{f,r}$ = forward rate constant for reaction r

$k_{b,r}$ = backward rate constant for reaction r

Equation (3.12) is valid for both reversible and non-reversible reactions. For non-reversible reactions, the backward rate constant $k_{b,r}$ is simply omitted.

The summations in Equation (3.12) are for all chemical species in the system, but only species that appear as reactants or products will have non-zero stoichiometric coefficients. Hence, species that are not involved will drop out of the equation.

The molar rate of creation/destruction of species i in reaction r ($\hat{R}_{i,r}$ in Equation (3.11)) is given by

$$\hat{R}_{i,r} = \Gamma \left(v''_{i,r} - v'_{i,r} \right) \left(k_{f,r} \prod_{j=1}^{N_r} \left[C_{j,r} \right]^{\eta'_{j,r}} - k_{b,r} \prod_{j=1}^{N_r} \left[C_{j,r} \right]^{\eta''_{j,r}} \right) \qquad\qquad (3.13)$$

where

N_r = number of chemical species in reaction r

$C_{j,r}$ = molar concentration of each reactant and product species j in reaction r (kgmole/m^3)

$\eta'_{j,r}$ = forward rate exponent for each reactant and product species j in reaction r

$\eta''_{j,r}$ = backward rate exponent for each reactant and product species j in reaction r

Γ represents the net effect of third bodies on the reaction rate. This term is given by

$$\Gamma = \sum_{j}^{N_r} \gamma_{j,r} C_j \qquad (3.14)$$

where $\gamma_{j,r}$ is the third-body efficiency of the j th species in the r th reaction.

The forward rate constant for reaction r, $k_{f,r}$, is computed using the Arrhenius expression

$$k_{f,r} = A_r T^{\beta_r} e^{-E_r/RT} \qquad (3.15)$$

where

A_r = pre-exponential factor (consistent units)

β_r = temperature exponent (dimensionless)

E_r = activation energy for the reaction (J/kgmol)

R = universal gas constant (J/kgmol-K)

You (or the database) will provide values for $v'_{i,r}$, $v''_{i,r}$, $\eta'_{j,r}$, $\eta''_{j,r}$, β_r, A_r, E_r, and, optionally,

$\gamma_{j,r}$ during the problem definition in FLUENT.

If the reaction is reversible, the backward rate constant for reaction r, $k_{b,r}$, is computed from the forward rate constant using the following relation:

$$k_{b,r} = \frac{k_{f,r}}{K_r} \qquad (3.16)$$

where K_r is the equilibrium constant for the r th reaction, computed from

$$K_r = \exp\left(\frac{\Delta S_r^0}{R} - \frac{\Delta H_r^0}{RT}\right)\left(\frac{Patm}{RT}\right)^{\sum\limits_{r=1}^{N_R}\left(v_{j,r}'' - v_{j,r}'\right)} \qquad (3.17)$$

where *Patm* denotes atmospheric pressure (101325 Pa). The term within the exponential function represents the change in Gibbs free energy, and its components are computed as follows:

$$\frac{\Delta S_r^0}{R} = \sum_{i=1}^{N}\left(v_{i,r}'' - v_{i,r}'\right)\frac{S_i^0}{R} \qquad (3.18)$$

$$\frac{\Delta H_r^0}{RT} = \sum_{i=1}^{N}\left(v_{i,r}'' - v_{i,r}'\right)\frac{h_i^0}{RT} \qquad (3.19)$$

where S_i^0 and h_i^0 are the standard-state entropy and standard-state enthalpy (heat of formation). These values are specified in FLUENT as properties of the mixture.

In our FLUENT volumetric reaction simulation, we apply the methane-air one-step reaction model for methane-helium/argon flame, and we applied the propane –air one-step reaction model for the propane-helium/argon flame, the parameters for each model are stated in following paragraphs of this section. These reaction models are provided by the FLUENT database; in each model, the backward reaction, third-body efficiencies, and pressure dependence are not considered. For the 1atm open air reaction problem, the backward reaction, pressure dependence is negligible, and third-body efficiencies are not available for non-elementary reactions. The full Gri-Mech 3.0 and C3 mechanism (from Curran [23]) are beyond the species and reaction loading capacities for FLUENT6.2. Multi-step kinetics was not adopted, as the goal of including the reaction is to investigate the effects of heat release – buoyancy and gas expansion – without examining detailed radical structure and diffusion.

(a) Methane-air one-step reaction

The methane reaction is

$CH_4 + 2O_2 + $ (inert gases) $\rightarrow CO_2 + 2H_2O + $ (inert gases)
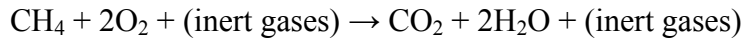
where forward rate exponents used are: $\eta'_{CH_4,1} = 0.2$, $\eta'_{O_2,1} = 1.3$, $\eta'_{CO_2,1} = 0$, $\eta'_{H_2O,1} = 0$. The Arrhenius pre-exponential factor is $A_1 = 2.119 \times 10^{11}$, the temperature exponent $\beta_1 = 0$, and the activation energy $E_1 = 2.027 \times 10^8$ j/kgmol. It is noted that backward reaction, third-body efficiencies, and pressure dependence are not considered.

(b) Propane-air one-step reaction

The propane reaction is

$C_3H_8 + 5O_2 + $ (inert gases) $\rightarrow 3CO_2 + 4H_2O + $ (inert gases)
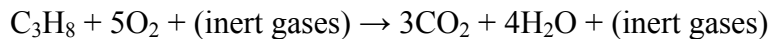
where forward rate exponents are $\eta'_{C_3H_8,1} = 0.1$, $\eta'_{O_2,1} = 1.65$, $\eta'_{CO_2,1} = 0$, $\eta'_{H_2O,1} = 0$. The Arrhenius pre-exponential factor $A_1 = 4.836 \times 10^9$, the temperature exponent $\beta_1 = 0$, and the activation energy $E_1 = 1.256 \times 10^8$ j/kgmol. Again as for the methane reaction, the backward reaction, third-body efficiencies, and pressure dependence are not considered.

3.2 Cold flow calculations

The base of the tribrachial flame propagates along the stoichiometric fuel concentration contour, stabilized at a location where the axial flow velocity is equal to the tribrachial flame speed. And the axial velocity should monotonically decrease in the flow direction at that point for flame stabilization [1, 4].

Lee and Chung [1, 4] analyzed the similarity solution of velocity and concentration contour for pure fuels such as methane, propane, n-butane, and hydrogen. By eliminating the

29

volume flow rate Q using this relation, $Q = U·\pi\ d^2/4$, they formulized the height of the intersection of the stoichiometric fuel concentration line and the stoichiometric flame speed line, $H_L = CU^{(2Sc-1)/(Sc-1)}\ d^2$, where C is a constant depending on fuel type, and U and d are the average jet flow velocity and jet diameter, respectively. When $Sc > 1$, the constant velocity line with stoichiometric flame speed is located outside of the stoichiometric fuel line to the upstream and inside in the downstream of that intersection point, so the lifted flame can be stabilized at that height.

The FLUENT software can be set up to simulate the velocity and species concentration field for the cold fuel jet flow. In the species model, the Full Multi-component Diffusion option was activated with the input of the binary mass diffusion coefficients for both fuel and the inert species. The multi-component diffusion coefficients matrix (Equ.-3.10b) was calculated based on the mass fraction composition on that grid. Values of binary mass diffusion coefficients were calculated using a software tool based on the kinetic theory available on the Colorado State University website (http://navier.engr.colostate.edu/tools/diffus.html). Gravity and buoyancy effects are taken into account in the momentum equation. For cold flow calculations, the volumetric reaction option was deactivated.

Our calculation domain and boundary conditions are shown in Figure 3.1, the domain size equals 7cm in the radial direction by 57.62cm, 87.62cm or 117.62cm in the axial direction. The domain length depends on the jet velocity. With higher jet velocity, the domain length needs to be extended longer in order to keep accuracy. However, the domain length cannot be extended indefinitely, because in the experiment there is an exhaust 1.5m above the burner tube and a minimum space should be kept to avoid the vacuum effect which might conflict with the constant pressure boundary assumption; this will be discussed in Chapter 5. The fuel burner tube is set with a length of 7.62cm, an inner radius of 0.4064mm, and an outer

radius of 0.7112mm. We divided this domain into several zones, and added a tight grid and mesh to the area close to the fuel jet and axis, where the velocity and concentration gradients are larger than elsewhere.

The ambient air consists of 0.7671 N_2 and 0.2329 O_2 (Y_{O2} = 0.2329) at room temperature 298.15K and 1atm pressure. The fuel inlet is set to be the velocity inlet with an average velocity; the fuel mixture will develop into a Poiseuille flow after it passes through the 7.62cm long burner tube.

The residual convergence criterion for velocity (m/s) and species mass fraction are set to 10^{-6} and 10^{-7}, respectively. The calculation for each case usually turns convergence after ten thousands of iterations within about ten hours of computer time. Then we can export the velocity and species mass fraction field, and plot their contours by using TECPLOT software.
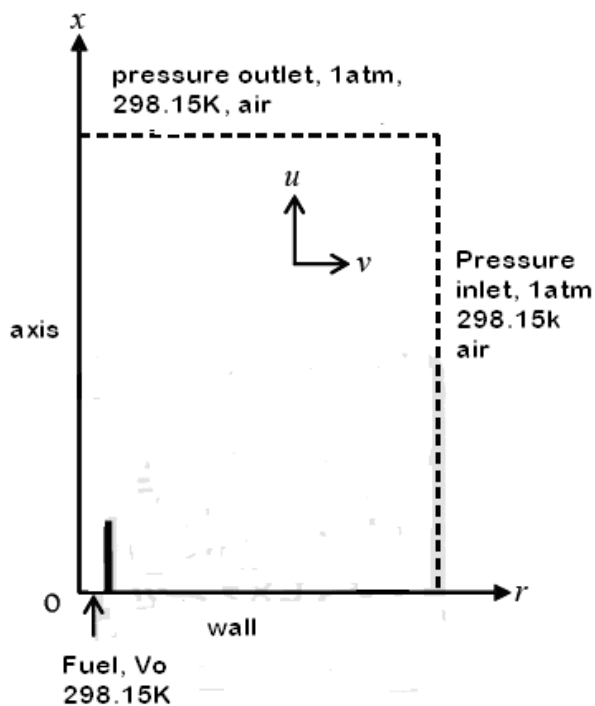

Figure 3.1 - the boundary conditions for the calculation domain

3.3 Combusting simulation

The volumetric reaction (as mentioned in Chapter3.1) and energy equations can be turned on in the FLUENT model panel. Then we can load the reactions to the solver. For simplicity, only one-step reaction is loaded; all the parameters such as Arrhenius pre-exponential factor, temperature exponent, and activation energy are from the FLUENT data file. The binary diffusion coefficients and thus multi-component diffusion coefficients are calculated by the kinetic theory. They are dependent on the temperature, which is no longer a constant compared to the cold flow calculation. The boundary conditions for the combusting simulation are the same as that for the cold flow.

After several thousands of iterations of the cold flow field, we can patch a high temperature to a small zone about 5cm downstream of the jet to ignite the fuel-air mixture. The flame base could propagate upstream or downstream depending on the fuel mixture fraction and jet velocity. As the iteration increases, it could converge to a certain height or attach to the jet or blow off. We will analyze the species concentration, temperature, reaction rate, and velocity contours for these lift-off flames in the following chapter.

The stoichiometric 1-D laminar flame speed was calculated by CHEMKIN3.7 with the PREMIX application, using the Gri-Mech3.0 mechanism for CH_4 flame and C3 mechanism (from Curran [23]) for C_3H_8 flame, with He or Ar diluents. In this model, the 1-Dimensional flame was stabilized in the horizontal tube against the cold flow of a stoichiometric fuel-inert gas-air mixture, and S_L^o was equal to the inlet cold gas flow speed. The results for CH_4 and C_3H_8 fuels are shown in Table 3.1. As reported in the literature, the experimental value of S_L^o for the stoichiometric C_3H_8–air flame at 1 atm falls in the range of approximately 39 – 42 cm/s [24]. The present result demonstrates a good agreement on the flame speed (41.2 cm/s,

as shown in Table 3.1). The flame speed for CH_4-air stoichiometric is known to fall within the

range of approximately 37 – 40 cm/s, as reported in [25], while the predicted value is 39.0 m/s.

Table 3.1 - Calculated flame speeds and adiabatic flame temperatures using CHEMKIN with Gri-Mech3.0 mechanism for CH4 and C3 mechanism [23] for C3H8 at 1 atm and 298.15 K inlet condition.

	Dilution level											
	He							Ar				
	0%	10%	20%	40%	60%	80%	90%	10%	20%	40%	60%	80%
CH_4												
$S_L^0(cm/s)$	39.0	38.5	38.2	37.1	34.4	26.4		38.2	37.2	34.5	29.5	18.2
$T_{ad}(K)$	2229	2221	2214	2187	2135	1983		2222	2211	2185	2130	1969
C_3H_8												
$S_L^0(cm/s)$	41.2		41.1	40.7	40.0	36.6	31.2		40.4	39.2	36.9	30.7
$T_{ad}(K)$	2275		2270	2259	2239	2174	1926		2269	2258	2237	2171

The residual convergence criterion for velocity (in m/s) and species mass fraction were set to 10^{-4} and 10^{-3} for reacting flows. Typically, more than 10^5 iterations (approximately 20 days on a desktop PC with a 3.0 GHz processor) were needed for reacting flow convergence. The convergence is determined if the value of H_L fell within 1 mm in two consecutive sequences of 10^4 iterations. The fine grid and mesh need to be adapted in the reacting zone where the species mass gradient and temperature gradient are high.

CHAPTER 4: EXPERIMENT RESULTS
AND CRITICAL SCHMIDT NUMBER

This chapter reports and analyzes the experimental data and critical Schmidt number of the pure propane/methane and helium/argon diluted propane/methane jet flame.

4.1 Experiment results

From the experimental results of lift-off height (H_L) shown in Figure 4.1(a – e) and 4.2(a - c), helium/argon-diluted propane flames with dilution level from 0% to 80% volumetric percentage can become lifted as the jet velocity is increased. The minimum velocity at which the lift-off occurs is called lift-off velocity ($V_{lift-off}$). As the fuel jet velocity is further increased, the value of H_L also increases and finally a laminar blow-off velocity $V_{blow-off}$ is reached if no turbulent phenomenon appears. For the testing burner diameter of 0.4064 mm, flames usually blow off before the jet flow velocities (Reynolds number) reach turbulence transition limit (Re = 2300).

Table 4.1 summarizes the lift-off velocity, blow-off velocity and blow-off Reynolds number for each fuel composition. It shows that both the lift-off and blow-off velocity decrease while increasing the helium or argon dilution level. It could be interpreted that the existence of helium and argon affected the oxygen and fuel mass fraction concentration contour shown in Figure 1.1(c), which pushed the jet-attached flame into lifted flame. The higher the dilution level is, the lower the lift-off and blow-off velocities. The 80%Ar diluted C_3H_8 fuel mixture cannot be ignited, while the 80%He diluted C_3H_8 still has attached and lifted flames. Even though the atomic weight for Ar (39.94) is almost 10 times that of He (4.00), Ar has the same molar heat capacity (20.7862 J/mol·K) as He. One possible reason is that their atomic weight difference (thus buoyancy effect difference) and difference in

diffusivities affected the velocity and C_3H_8 stoichiometric contours. This effect will be analyzed in the cold flow CFD simulation section in the following chapter.

The maximum ignition height is defined as the maximum height above the fuel jet exit level, where the fuel-air mixture can be ignited by an electrical spark and the flame can propagate upstream to an equilibrium lift-off height or attach to the fuel jet exit. From Figure 4.1(a - e) and 4.2(a - c), the maximum ignition height for each He/Ar-diluted C_3H_8 flow for both attached and lift-off flame increase with the average jet exit velocity V_0.

For 100% C_3H_8 flame, as shown in Figure 4.1(a), there are two possible maximum ignition heights for $V_0 = 11.0$ m/s and 12.0 m/s. One maximum ignition height results in an attached flame, the other lifted. The flame would pull back and attach to the fuel jet if the electrical spark was discharged below the maximum ignition height for attached flames; while igniting between the maximum ignition height for attached flames and maximum ignition height for lift-off flames, the flame will propagate downstream or upstream until the tribrachial flame base reaches an equilibrium position. This phenomenon is called lift-off / re-attachment hysteresis, which was introduced in Section 2 of Chapter 1. Oscillations of the flame base in the lifted configuration were observed for the pure propane, and propane with 20%He and 40%He dilution, for which the tribrachial flame bases' height from the jet exit fluctuated within 20% of their H_L value.

From Figure 4.3(a – c), the pure CH_4 flame cannot lift off over the jet velocity range studied. With 20% and 40%He dilution, the CH_4 flames lifted off from the fuel jet when the jet velocities reach 8.0 m/s and 4.0 m/s, respectively. With 20% and 40% Ar dilution (Figure 4.4(a, b)), the flame did not lift off prior to reaching the blow-out limit. The mass diffusivity difference between helium and argon is believed to be the key reason for these results. For 60% or higher He/Ar dilution levels, the fuel mixture could not be ignited at all.

(a)

(b)

(c)

(d)

(e)
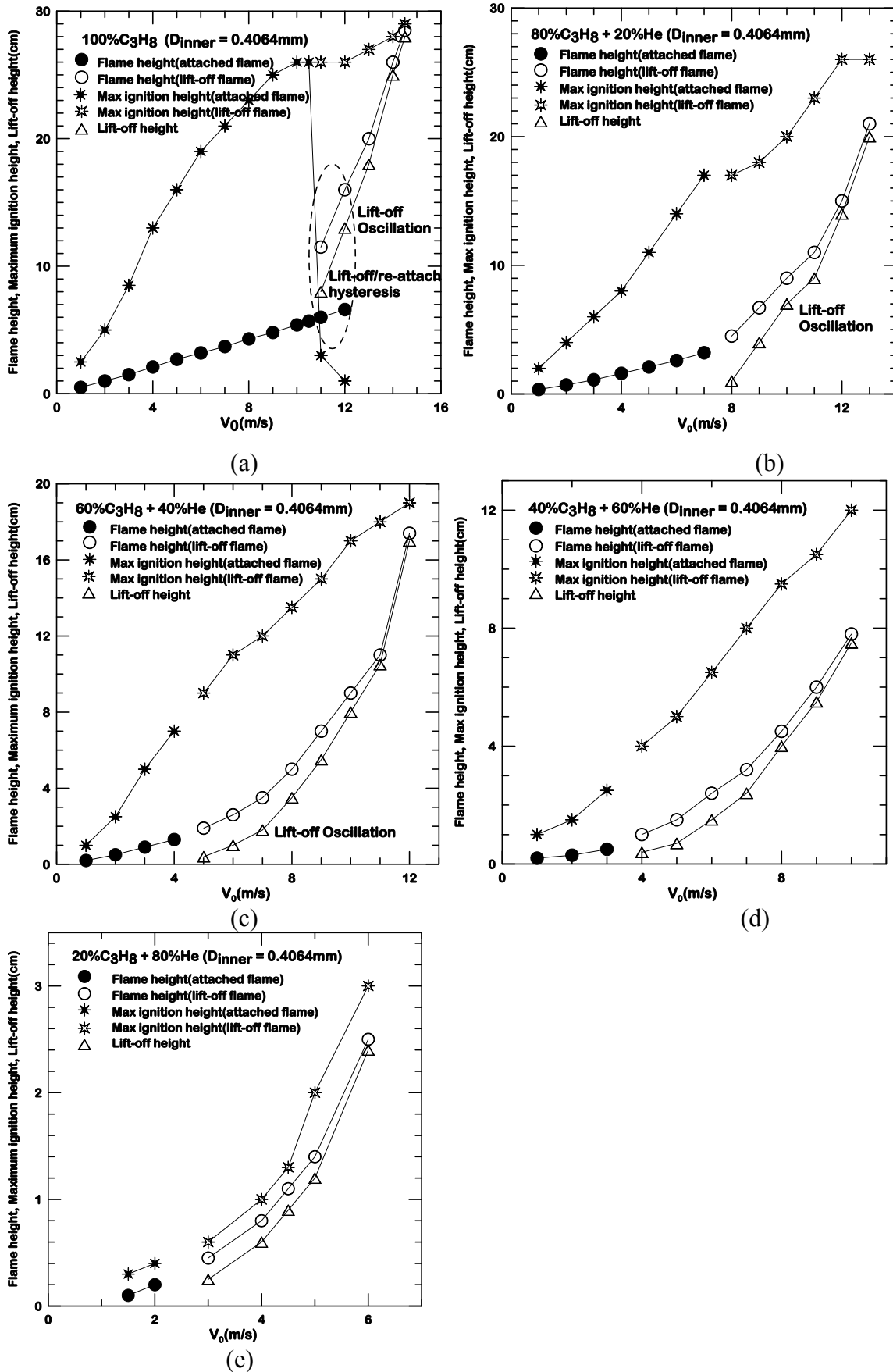
Figure 4.1(a - e) – experimental results of the flame height, maximum ignition height and lift-off height for the $D_{inner} = 0.4064$ mm jet, He-diluted C_3H_8 flame
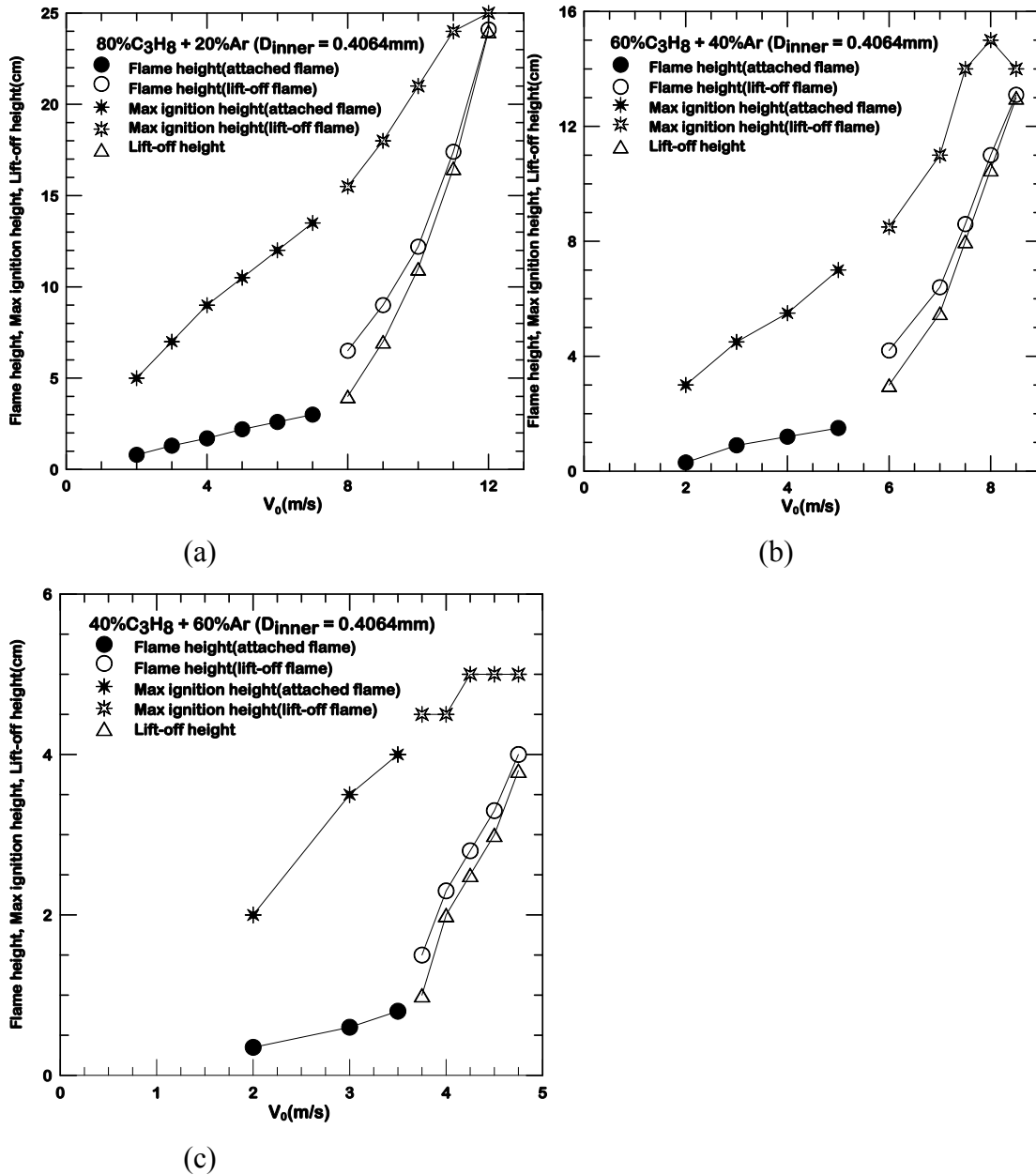
Figure 4.2(a, b, c) – experimental results of the flame height, maximum ignition height and lift-off height for the D_{inner} = 0.4064 mm jet, Ar-diluted C_3H_8 flame

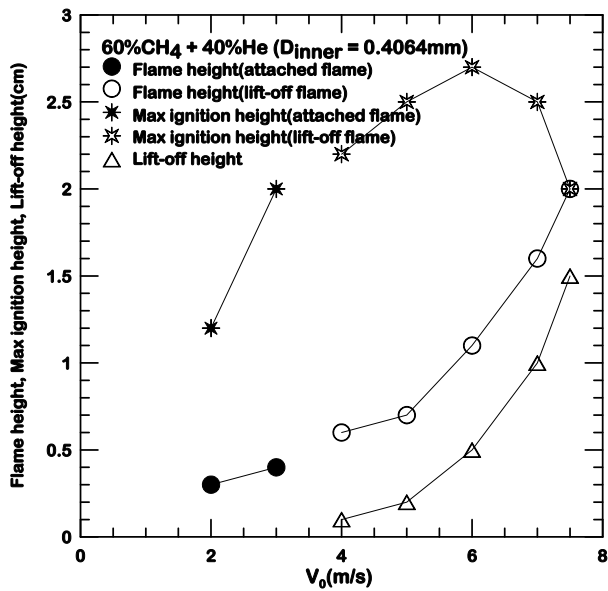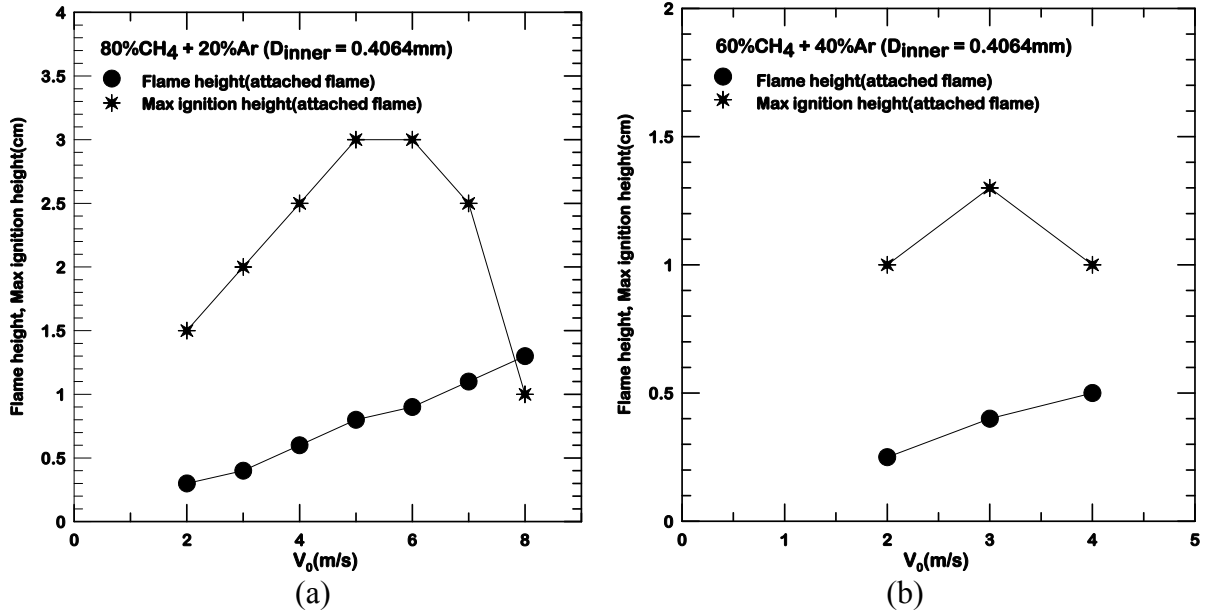Table 4.1 – Lift-off, blow-off velocity and Reynolds number for He/Ar-diluted C3H8 flame

He/Ar dilution	0%	20%He	40%He	60%He	80%He	20%Ar	40%Ar	60%Ar
$V_{lift-off}$ (m/s)	12.0	8.0	5.0	4.0	3.0	8.0	6.0	3.75
$V_{blow-off}$ (m/s)	15.0	14.0	12.5	10.5	6.5	12.5	9.0	5.0
$Re_{blow-off}$	1326	945	599	315	95	906	530	236
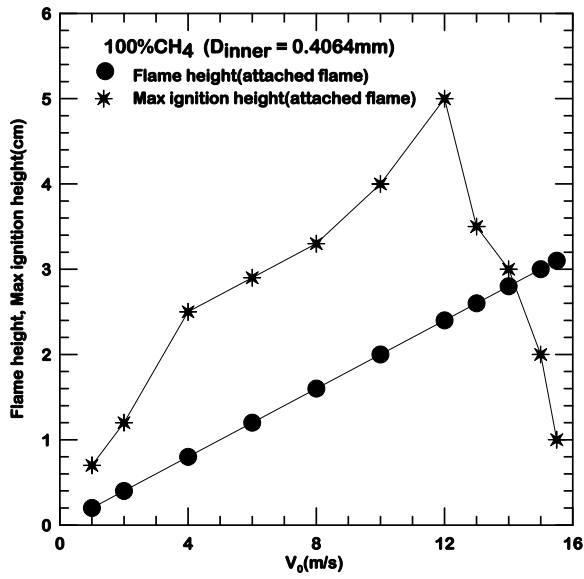
(a)
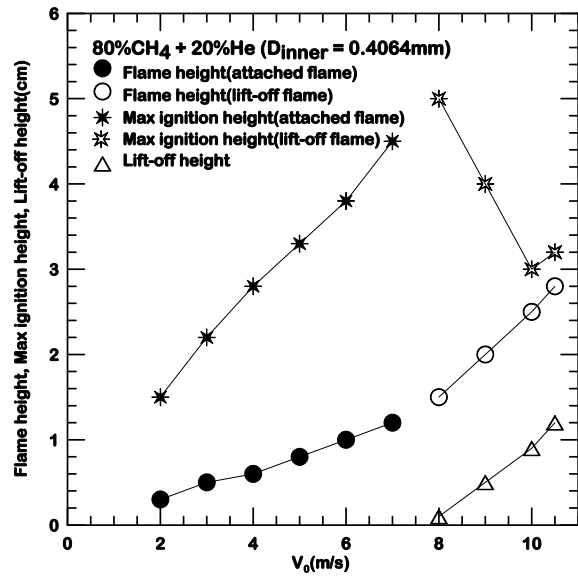
(b)

(c)

Figure 4.3(a, b, c) – experimental results of the flame height, maximum ignition height and lift-off height for the D_{inner} = 0.4064 mm jet, He-diluted CH_4 flame

Figure 4.4(a, b) – experimental results of the flame height and maximum ignition height for the D_{inner} = 0.4064 mm jet, Ar-diluted CH_4 flame

Table 4.2 – Lift-off, blow-out/off, peak maximum ignition height velocity and Reynolds number for He/Ar-diluted CH_4 flame

He/Ar dilution	0%	20%He	40%He	20%Ar	40%Ar
$V_{lift-off}$ (m/s)	N	8.0	4.0	N	N
$V_{blow-out/off}$ (m/s)	16.0	11.0	8.0	9.0	5.0
$Re_{blow-out/off}$	369	202	112	216	125
$V_{Peak\ maximum\ ignition\ height}$ (m/s)	12.0	8.0	6.0	6.0	3.0

For all the He/Ar diluted CH_4 flame cases, a peak maximum ignition height can be reached before the jet velocities further increase until the flame reaches the blow-out or blow-off limits; these peak maximum ignition height values ($V_{Peak\ maximum\ ignition\ height}$) are listed in Table 4.2, their peak maximum ignition height are reached at these velocities below their blow-out/off jet velocities ($V_{blow-out/off}$). While the maximum ignition height for He/Ar diluted C_3H_8 flames monotonously increase with the jet velocities, their peak maximum ignition height values are reached at the flame blow-off jet velocities.

4.2 Critical Schmidt Number

Two different methods of calculating species diffusivity (and therefore Schmidt number) are described in Chapter 2. The calculated values of Sc using the two methods are given in Table 4.3. First consider the cases of CH_4-He mixtures. With no dilution, both methods are expected to produce similar values of Sc, which are shown in Table 4.3. Equation (2.1) yields a decrease in Sc ($Sc^{(1)}$ in Table 4.3) from 0.714 to 0.577 as the dilution level increases from 0% to 80%. This is expected because in the stoichiometric fuel-He-air environment, diffusivity should increase with the He concentration, resulting in a lighter and faster diffusing mixture. These results are qualitatively contrary to those reported earlier using the second method ($Sc^{(2)}$ in Table 4.3), where the Sc value increases from 0.715 to 0.760 in the corresponding range of dilution level (0 to 80%) (also listed in Table 4.3). Secondly, for CH_4-Ar mixtures, the first method produces increasing values of Sc. This is consistent with the fact that Ar gas is heavier than other gases in the multi-component environment. The first method therefore appears to be a more reasonable approach than those previously used in Ref. [9]; it might therefore be appropriate for exploring the critical Schmidt number as in the similarity analysis of pure fuel [1, 4]. Similar observations can be made for the C_3H_8-inert gas mixture, also shown in Table 4.3.

To find out the feasibility of using Equation (2.1) for CH_4-inert mixtures, consider again $Sc^{(1)}$ in Table 4.3. Equation (2.1) appears to produce results qualitatively contradictory to the critical Schmidt number criteria given in Refs. [1, 4, 7, 9] (the criteria are: $Sc > 1$ in [1, 4], > 0.8 in [7], and $Sc > 0.715$ in [9]) in two aspects: (1) a decrease in Sc below 0.715 (CH_4-He mixtures) is accompanied by the experimentally observed liftoff of CH_4-He flames, and (2) an increase in Sc above 0.715 (CH_4-Ar mixtures) fails to yield the experimentally observed lifted flames.

Schmidt numbers calculated using both methods satisfy the liftoff criterion for C_3H_8-He and C_3H_8-Ar mixtures, for both of which Sc is greater than 1 (or > 0.8 in [7] and > 0.715 in [9]). For the second method, the large amounts of air needed for stoichiometry result in an essentially binary mixture of fuel and air by diminishing the role of the diluents in determining Sc.

Table 4.3 - Calculated Schmidt number values of various fuel-diluent mixtures

Fuel	% He dilution	Lifted (Y/N?)	$Sc^{(1)}$	$Sc^{(2)}$	% Ar dilution	Lifted (Y/N?)	$Sc^{(1)}$	$Sc^{(2)}$
CH_4								
	0%	no	0.714	0.714			0.714	0.714
	20%	yes	0.712	0.717	20%	no	0.724	0.705
	40%	yes	0.692	0.722	40%	no	0.724	0.698
	60%	-(3)	0.656	0.732	60%	-(3)	0.724	0.680
	80%	-(3)	0.577	0.760	80%	-(3)	0.724	0.644
C_3H_8								
	0%	yes	1.449	1.403			1.449	1.403
	20%	yes	1.437	1.404	20%	yes	1.450	1.398
	40%	yes	1.419	1.407	40%	yes	1.453	1.392
	60%	yes	1.384	1.412	60%	yes	1.457	1.379
	80%	yes	1.291	1.427	80%	-(3)	1.470	1.345

(1) Using methods described by Equation (2.1) and in Ref. [21].
(2) Following methods described in Refs. [1, 4] and cited from Ref. [9].
(3) No flame could be established experimentally.

The above results of diluted C_3H_8 and CH_4 suggest that there perhaps is no simple Sc criterion for predicting flame liftoff as in analysis of pure fuel jets with similarity assumptions. Numerical simulations with full multi-component diffusivities appear to be necessary for predicting whether any given fuel-inert mixture allows a stable lifted flame to be achieved.

CHAPTER 5: COLD FLOW CFD SIMULATION RESULTS

This chapter presents the cold flow CFD simulation results for the pure propane/methane and helium/argon diluted propane/methane jet flame. The cold flow CFD simulations predicted the lift off and blow-off/out phenomenon for the pure and diluted propane jet flow. However, this simulation failed to even quantitatively predict the lift off for helium diluted methane. Including reaction and heat release will help to resolve this difficulty, as will be shown in Chapter 6.

5.1 Pure propane

Cold flow simulation results for pure C_3H_8 are shown in Figure 5.1(a - n). In these figures, axial velocity and C_3H_8 mass fraction contours are plotted. One of the constant-velocity lines ($u = S_L^o$) represents the stoichiometric laminar flame velocity. The dashed lines with arrows (shown in some representative figures) denote the streamlines. The low speed cases ($V_0 \leq 8$ m/s) are simulated under domain (1) -0.0762 m $\leq x \leq$ 0.5 m, $0 \leq r \leq 0.07$ m; the medium speed cases (8 m/s $< V_0 \leq 12$ m/s) are simulated under domain (2) -0.0762 m $\leq x \leq$ 0.8 m, $0 \leq r \leq 0.07$ m; the high speed cases ($V_0 \geq 12$ m/s) are simulated under domain (3) -0.0762 m $\leq x \leq$ 1.1 m, $0 \leq r \leq 0.07$ m. The calculation domain selection is introduced in Chapter 3.2. The influence of domain length will be discussed later in the following.
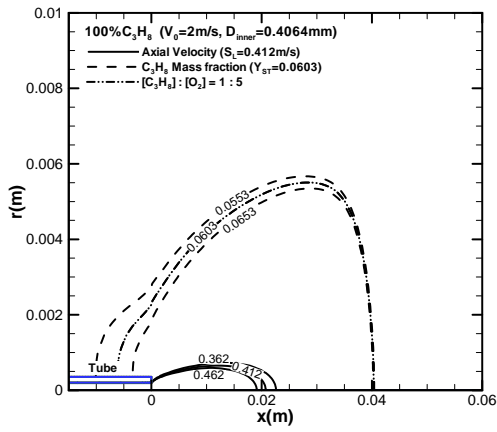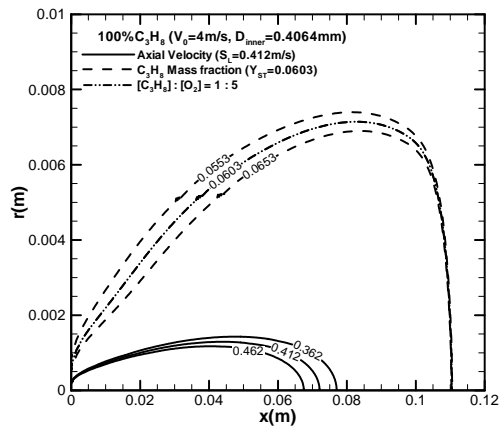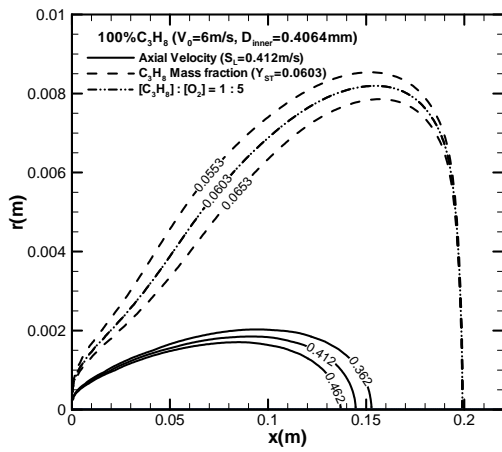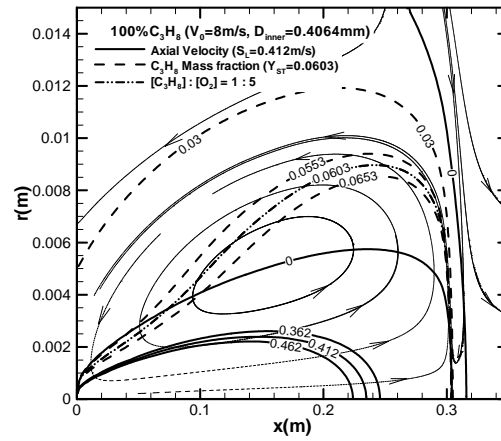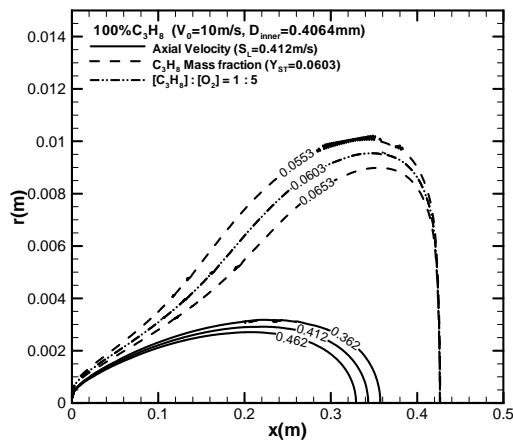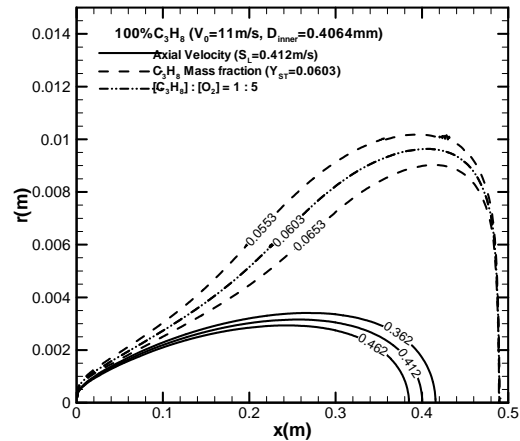
Figure 5.1(a-n) – Contours of constant velocity and concentration for 100% C_3H_8 cold flow CFD simulation
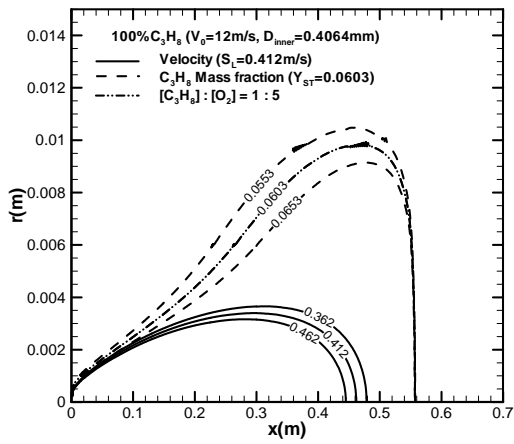
(g)
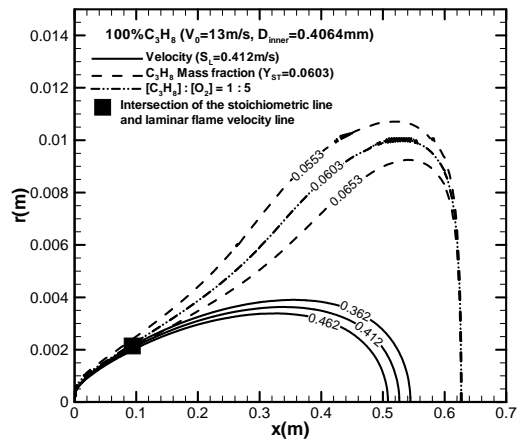
(h)
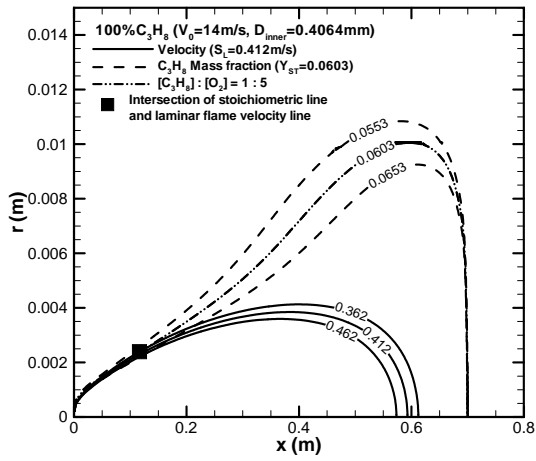
(i)
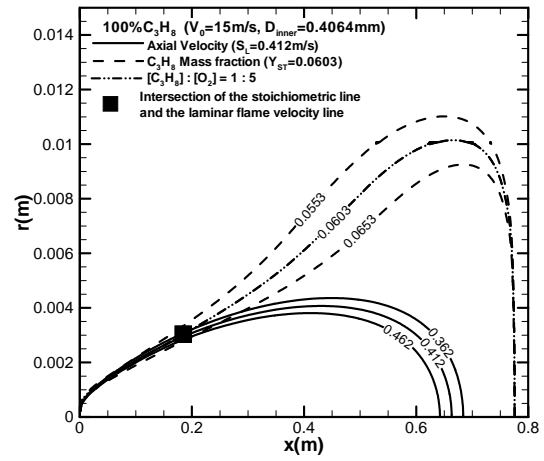
(j)
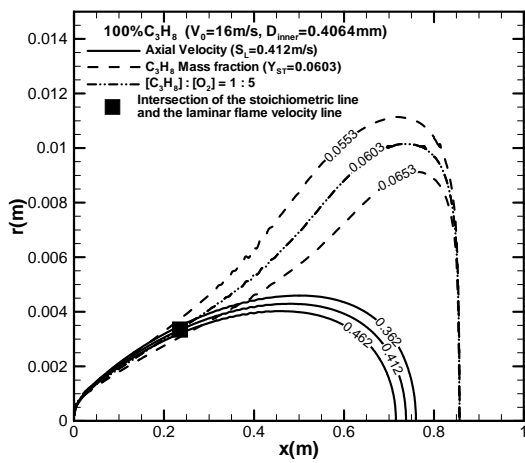
(k)
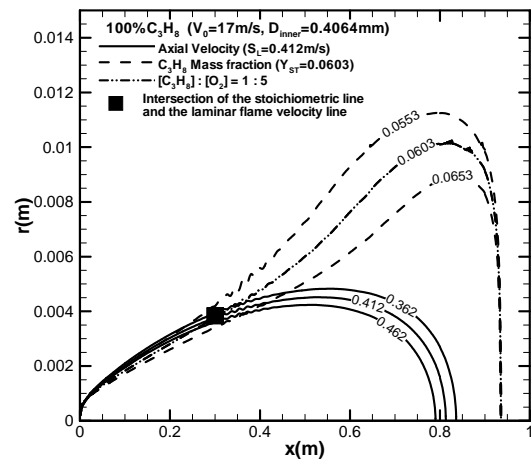
(l)

Figure 5.1(a-n) - (continued)

(m)   (n)
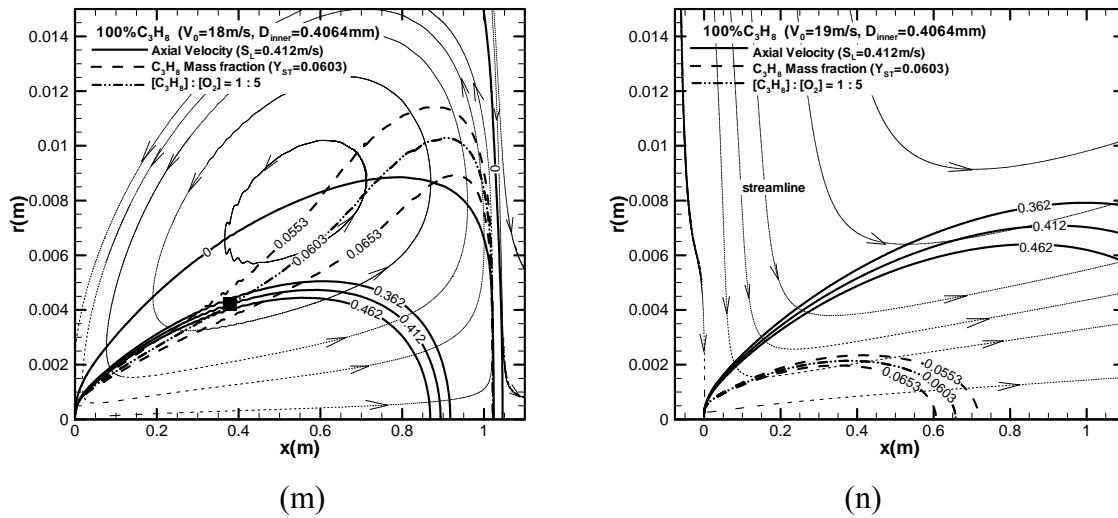
Figure 5.1(a-n) - (continued)

From Figure 5.1 (a – n), for all the jet velocities, the stoichiometric line ([C_3H_8] : [O_2] = 1 : 5) coincides with the stoichiometric C_3H_8 mass fraction Y_{ST} = 0.0603 line; this is because the binary diffusivity coefficients $D_{C_3H_8 \leftrightarrow O_2}$ and $D_{C_3H_8 \leftrightarrow N_2}$ are nearly equal. The zero axial velocity lines in Figure 5.1 (d) and Figure 5.1(m) represent the boundary that the cold C_3H_8 flow cannot penetrate due to its larger molecule weight and higher density than air. Outside the zero axial velocity boundary, the streamline shows the flow turns to the radially outward direction then to the downward direction, and then the C_3H_8 is convected radially inward. A back flow stream lies between the two zero axial velocity lines in Figure 5.1(a-m). For simplicity, the zero axial velocity lines and streamlines are only shown in Figure 5.1 (d) and Figure 5.1(m).

For the lower jet velocity cases, $V_0 \leq 12$ m/s (Figure 5.1 (a – g)), the stoichiometric line is located outside of the stoichiometric laminar flame velocity line. This suggests if the cold flow is ignited at a distance from the fuel jet exit, because the tribrachial flame base can propagate in the low-velocity region, it can propagate along the stoichiometric line upstream util attaching to as close to the fuel jet rim as the quenching distance would allow. The quenching distance for the stoichiometric propane / air flame was reported at 2 mm [26]. For

45

the higher jet velocity cases, $V_0 \geq 13$ m/s (Figure 5.1 (h – l)), the stoichiometric line intersects the stoichiometric laminar flame velocity line. Below that intersection, the velocity line lies outside the stoichiometric line. Above the intersection (denoted by a square), the velocity line lies inside the stoichiometric line. As discussed in Chapter 1, the tribrachial flame base will stabilize at the intersection whether the flame is ignited upstream or downstream. Thus it is predicted that the lift-off phenomenon will happen when the jet velocity is equal to or higher than 13 m/s.

Table 5.1 – Lift-off height (H_L), maximum ignition height (H_I) comparison between the experimental data and cold flow simulation for 100% C_3H_8

V_0 (m/s)	2.0	4.0	6.0	8.0	10.0	11.0	12.0	13.0	14.0	14.5	15.0	16.0	17.0	19.0
H_L (cm)-exp	N	N	N	N	N	8	13	18	25	28	blow off			
H_L (cm)-CFD	N	N	N	N	N	N	N	9	12	-	18	23	30	off
H_I (cm)-exp	5	13	19	23	26	26	26	27	28	29	N	N	N	N
H_I (cm)-CFD	4[a]	11[a]	20[a]	30[a]	42[a]	48[a]	55[a]	62[a]	70[a]	-	77[a]			

The maximum ignition height is defined as the maximum height above the fuel jet exit level, where the fuel-air mixture can be ignited by an electrical spark and the flame can propagate upstream to an equilibrium lift-off height or attach to the fuel jet exit
Refer: [a] – maximum height for the stoichiometric line

The experimental and cold flow simulated lift-off heights and maximum ignition heights (defined in Chapter 4) are listed in Table 5.1; the experimental result shows the flames lift off when $V_0 \geq 11$ m/s, and blow off when $V_0 = 15$ m/s. The cold flow simulation result shows the flames lift off at $V_0 \geq 13$ m/s, agreeing well with the experiment.

Two conditions for successful ignition are that (1) the point in the cold flow field is in the flammability limits (0.51 < equivalence ratio < 2.83, for propane-air mixture) [27], thus the ignitable area is close to the stoichiometric line; (2) the flow field allows the flame to propagate to a flame-stabilized position. The flame-stabilized position can be the intersection

of the stoichiometric line and laminar flame velocity line; it also can be the jet exit if the stoichiometric line is outside of the laminar flame velocity line.

For the low jet velocity cases, $V_0 \leq 8$ m/s, the maximum ignition heights for the stoichiometric line, which are marked by the superscript "a" in Table 5.1, agree well with the experimental maximum ignition heights. That means if the flow is ignited at the top of the stoichiometric line, the flame can propagate upstream to the jet exit. From Figure 5.1(d), four C_3H_8 mass fraction lines (0.03, 0.0553, 0.0603 and 0.0653) coincide ahead of the stagnation level, the $Y_{st} = 0.0603$ line is corresponding to the stoichiometric line (equivalence ratio = 1), and the 0.03 mass fraction line is approximately the lean flammability limit (equivalence ratio ≈ 0.5). This coincidence also exists for the other C_3H_8 flows (Figure 5.1(a-m).

However, for higher jet velocity cases (Table 5.1), $V_0 \geq 8$ m/s, the top of the stoichiometric line is much higher than the maximum ignition height. The explanation for the inconsistency is that, the higher the jet velocity is, the higher the top of the stoichiometric line, then more disturbances to this region from the ambient air and the exhaust during the experiment. For experimental safety purposes, an exhaust is set 1.5m above the fuel jet exit, which has some influence to the flow field, especially to the region higher above the jet exit.

During the study, the axial extent of the calculation domain was found to influence the cold flow simulation result. Figure 5.2 and Figure 5.3 show the examples of pure C_3H_8 of the difference for the flow field under different calculation domains. Pictures in Figure 5.3(a1, a2, b1, b2) are the amplificatory graphs of Figure 5.2(a1, a2, b1, b2), respectively. For all the calculations, the $r = 0.07$ m boundary condition was set to the 1 atm air pressure inlet boundary. In the axial direction, the $x = -0.0762$ m profile (the board of the jet stand) is set to the wall boundary. The $x = 0.8$m boundary condition is set to the 1 atm air pressure outlet boundary for domain (2), and the $x = 1.1$ m boundary condition is also set to the 1 atm air pressure outlet boundary for domain (3). For all the 100% C_3H_8 cold flow cases in Figure

5.1(a - n), the medium speed cases (8 m/s $< V_0 \leq$ 12 m/s) are calculated in domain (2), and the high speed cases ($V_0 \geq$ 13 m/s) are calculated in domain (3). Domain (2) requires less computation time than domain (3), but for the medium speed case (8 m/s $< V_0 \leq$ 12 m/s), it still has essentially the same result as that calculated in domain (3) in the flow region that we are interested in.
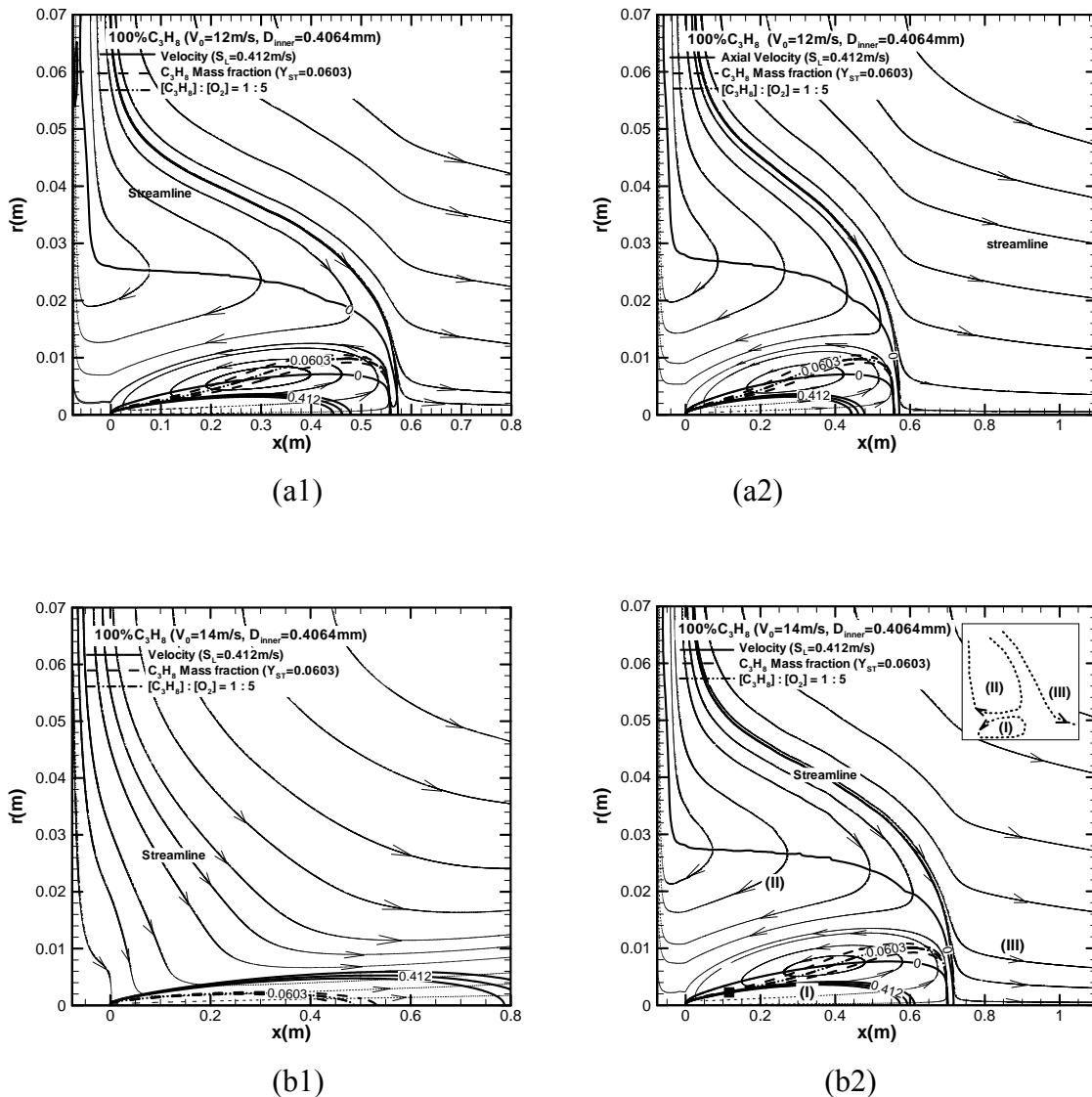
(a1)   (a2)

(b1)   (b2)

Figure 5.2(a1,a2,b1,b2) – Full zone comparison of the streamline, velocity and mass fraction contour for the 100%C_3H_8 cold flow CFD simulation for V_0 = 12 m/s and 14 m/s under different calculating domain: (2) -0.0762 m $\leq$ x $\leq$ 0.8 m, 0 $\leq$ r $\leq$ 0.07 m; (3) -0.0762 m $\leq$ x $\leq$ 1.1 m, 0 $\leq$ r $\leq$ 0.07m. For Figure 5.2(b2): (I) denotes the entrainment and backflow region, (II) denotes the backflow region, (III) denotes the down flow region

48

(a1)

(a2)

(b1)

(b2)
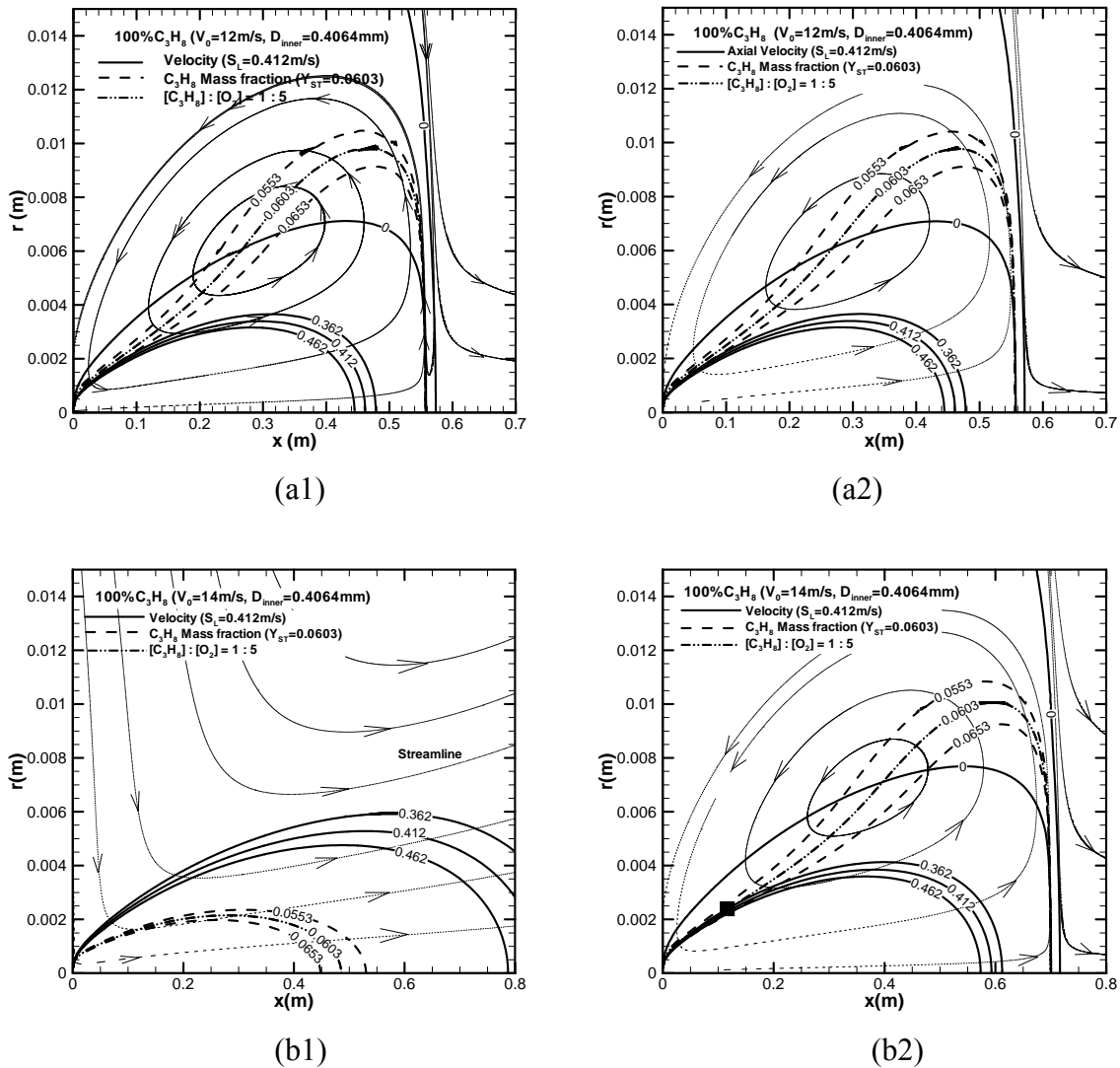
Figure 5.3(a1,a2,b1,b2) – Amplificatory comparison of the streamline, velocity and mass fraction contour for the $100\%C_3H_8$ cold flow CFD simulation for V_0 = 12 m/s and 14 m/s under different calculating domain: (2) -0.0762 m ≤ x ≤ 0.8 m, 0 ≤ r ≤ 0.07 m; (3) -0.0762 m ≤ x ≤ 1.1 m, 0 ≤ r ≤ 0.07 m

For Figure 5.3(b1) (V_0 = 14 m/s), the laminar flame velocity line is outside of the stoichiometric concentration line, which suggests the blow-off phenomenon and the jet fuel flow just penetrates the ambient 1atm air pressure outlet top boundary under calculation domain(2) (-0.0762 m ≤ x ≤ 0.8 m). But V_0 = 14 m/s is less than the experimental blow-off velocity ($V_{blow-off}$ = 15.0 m/s). For Figure 5.3(b2), under the calculating domain(3) (-0.0762 m ≤ x ≤ 1.1 m), the intersection shows a lift-off phenomenon, and there is a stagnation level at x

49

= 0.7 m profile where the jet fuel flow cannot penetrate. If V_0 is increased till 19 m/s (see Figure 5.1(n)), the stagnation point moves to the top boundary and eventually disappears from the domain, then the velocity and concentration lines are such that they indicate a blow-off phenomenon. This blow-off velocity is slightly higher than the experimental result (Table 5.1). So the blow-off velocity is determined by the calculation domain; for the top boundary position selection, we need to find the equilibrium between the fuel composition, jet velocity and the influence of the exhaust.

In the experiment, the exhaust blower affected the experimental lift-off and blow-off velocity. The exhaust is set 1.5 m higher than the jet exit, and the 1 atm air pressure outlet boundary condition cannot by applied if the top boundary is close to the exhaust, so the top boundary is not extended over $x = 1.1$ m.

For Figure 5.3(a1) and Figure 5.3(a2), the velocity, mass fraction, and streamline profiles for $V_0 = 12$ m/s under the simulation domain (2) and domain (3) essentially coincide, thus below that velocity, the smaller domain (2) has essentially the same results as domain (3). A similar comparison was made for the $V_0 \leq 8$ m/s cases under the simulation domain (1) (-0.0762 m $\leq x \leq$ 0.5 m) and domain (2) (-0.0762 m $\leq x \leq$ 0.8 m) during the computation process. When $V_0 \leq 8$ m/s, these velocity, mass fraction and streamline profiles from domain (1) and domain (2) essentially coincide, but when $V_0 > 10$ m/s, the contour under domain (1) shows a blow-out phenomenon and the streamlines are similar to that in Figure 5.2(b1).

Figure 5.2(b2) is the full view of $V_0 = 14$m/s under domain (3). There are three flow regions: (I) the entrainment and backflow region, (II) the backflow region, and (III) the down flow region. The streamlines of the velocities (below $V_{blow\text{-}off}$) at Figure 5.1(a - m) are similar to this three flow regions' structure. The entrainment and backflow region (flow region (I)) is crucial for this computation, because the stoichiometric line and stoichiometirc laminar flame velocity line lie inside of the region. Flow region (I) lies close to the jet exit, thus is relatively

less influenced by the ambient disturbances. From the comparison of different velocities under the domain sizes in the previous paragraph, we can see that, for the smaller calculation domain (2) as the jet velocity increases to 14 m/s (Figure 5.2(b1)), the three flow region structure disappears, leading to early blow-off. This domain independence concern also applies to the remaining results of the simulations.

5.2 Argon diluted propane

Cold flow simulation results for $60\%C_3H_8 + 40\%Ar$ are shown in Figure 5.4. In these figures, axial velocity (represented by solid lines) and C_3H_8 mass fraction (represented by broad dashed lines) are plotted. One of the constant-velocity lines represents the stoichiometric laminar flame velocity. The dashed lines with arrows in Figure 5.4(d) denote the streamlines.

(a)   (b)

(c)   (d)
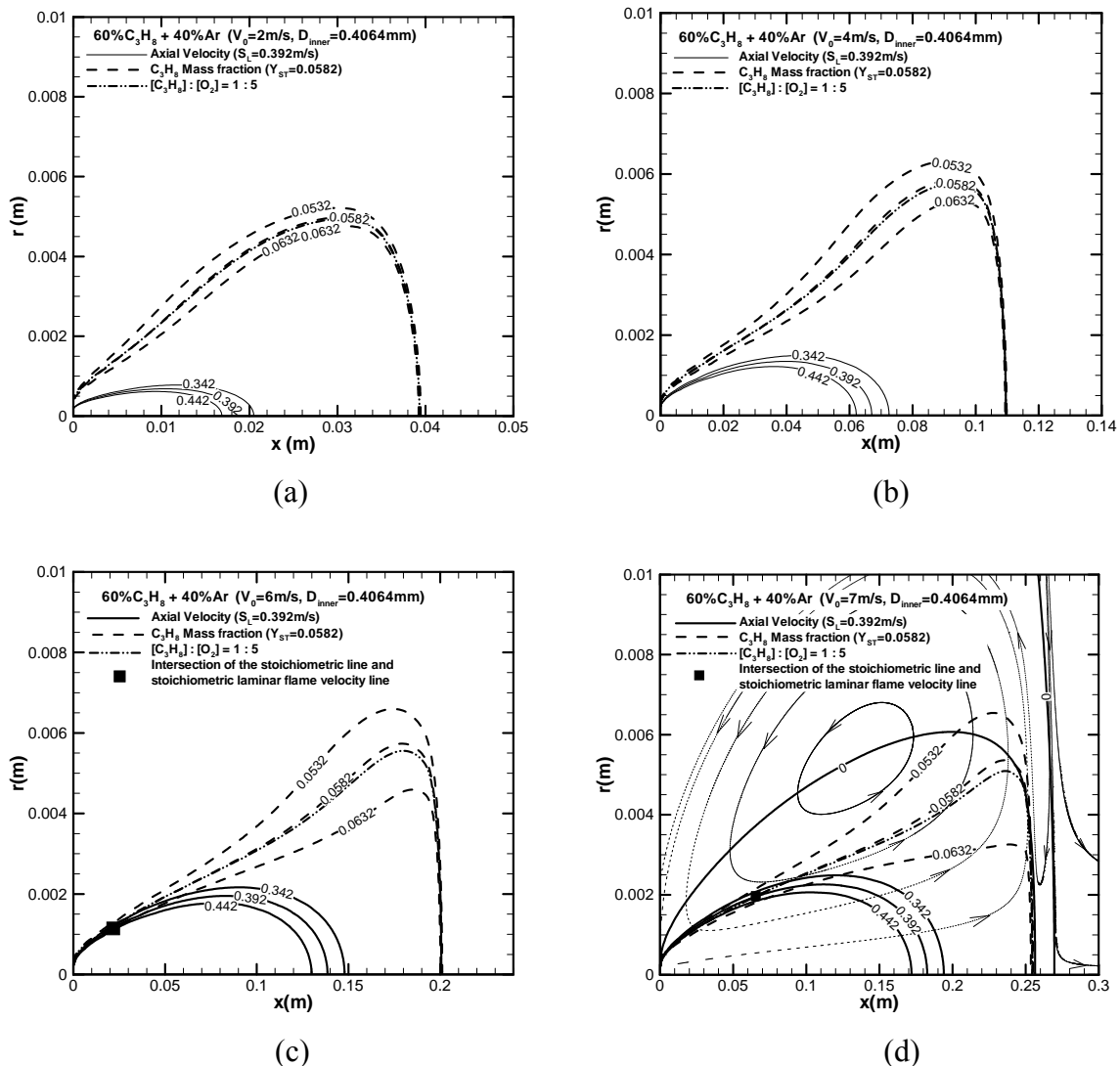
Figure 5.4(a - i) – Contours of constant velocity and concentration for $60\%C_3H_8 + 40\%Ar$ cold flow CFD simulation. For simplicity, the zero axial velocity lines and streamlines are only showed in Figure 5.4 (d), but they exist in Figure 5.4 (a-i).
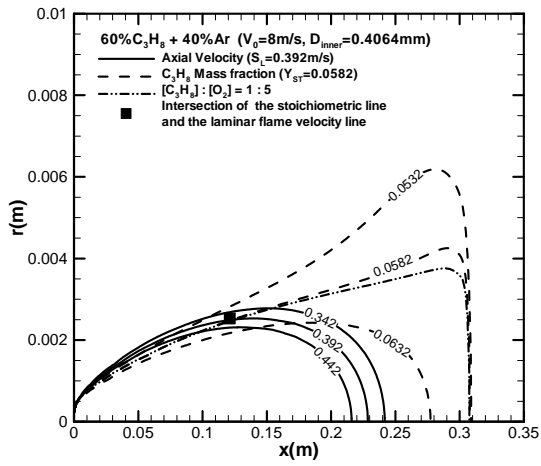
(e)
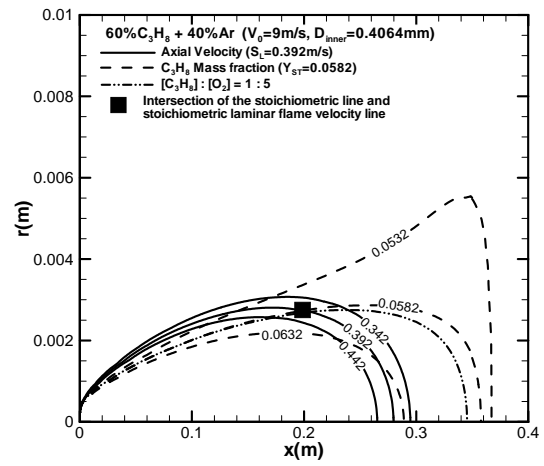
(f)
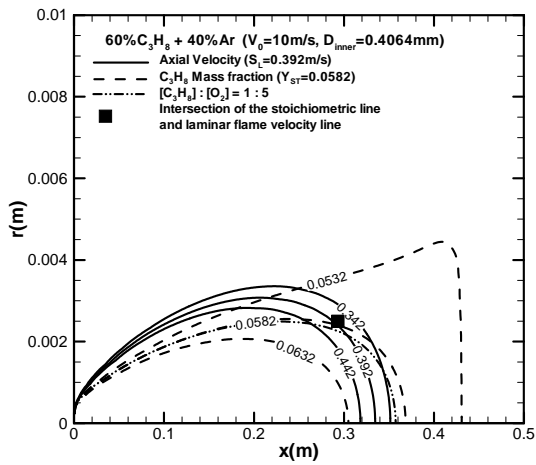
(g)
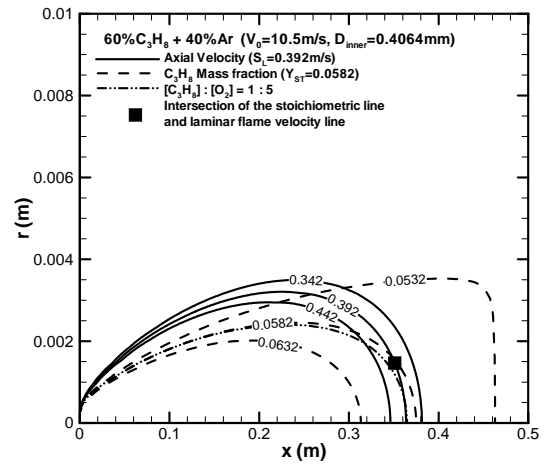
(h)
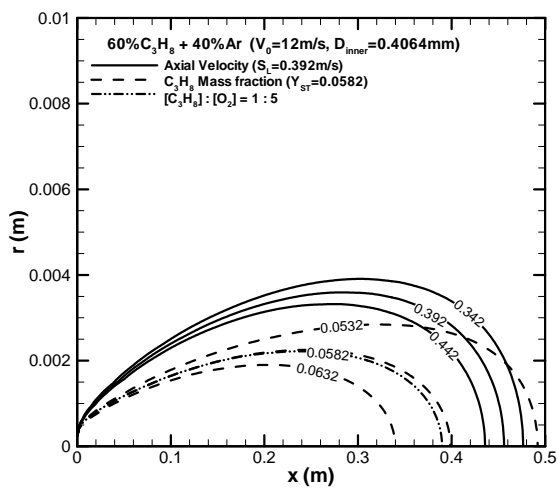
(i)

Figure 5.4(a - i) – (continued)

53

Table 5.2 – Lift-off height(H_L), maximum ignition height(H_I) comparison between the experimental data and cold flow simulation for 60%C_3H_8 + 40%Ar

V_0 (m/s)	2.0	4.0	5.0	6.0	7.0	7.5	8.0	8.5	9.0	10.0	10.5	12.0
H_L (cm)-exp	N	N	N	3.0	5.5	8.0	10.5	13.0	blow off			
H_L (cm)-CFD	N	N	-	2.0	6.4	-	12.0	-	20	29	35	blow
H_I (cm)-exp	3.0	5.5	7.0	8.5	11	14	15	14	N	N	N	N
H_I (cm)-CFD	3.9[a]	11[a]	-	20[a]	25[a]	-	31[a]	-	35[a]			

Refer: [a] – maximum height for the stoichiometric line

From Table 5.2, the lift-off velocity and height for the 60%C_3H_8 + 40%Ar cold flow CFD simulation agrees well with the experimental results. The lift-off velocity for both CFD and experiment results are V_0 = 6.0 m/s, though the calculated blow off velocity is V_0 = 11.0 m/s, which is higher than the experimental data V_0 = 9.0 m/s, the error is about 20%. And the lift-off heights for the lifted velocities (V_0 = 6.0 m/s, 7.0 m/s and 8.0 m/s) are 2.0 cm, 6.4 cm and 12.0 cm respectively, which generally match the experimental data of 3.0 cm, 5.5 cm and 10.5 cm. However, the ignition height prediction is only accurate for low jet velocities, V_0 < 4.0 m/s. The enlarged view of 60%C_3H_8 + 40%Ar cold flow with V_0 = 7.0 m/s and 10.5 m/s and reacting flow with V_0 = 7.0 m/s in Figure 5.5(a-d) indicate the substructure near the burner exit.
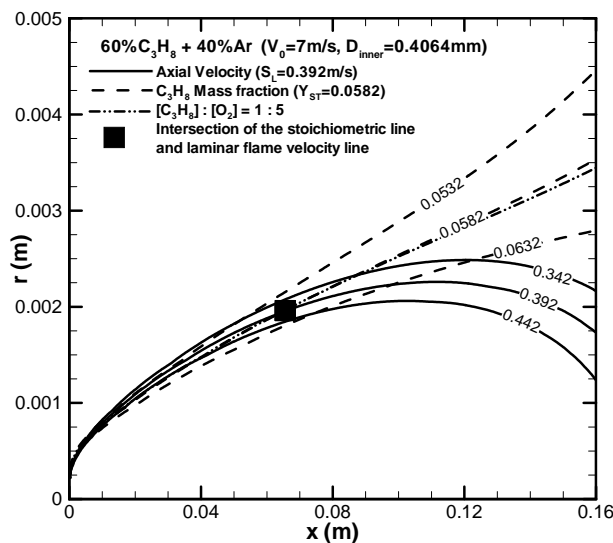
Figure 5.5(a) – Cold-flow prediction of 60%C_3H_8-40%Ar mixture with V_0 = 7.0 m/s; flame is lifted ($H_L \approx 0.065$ m indicated by the solid square).
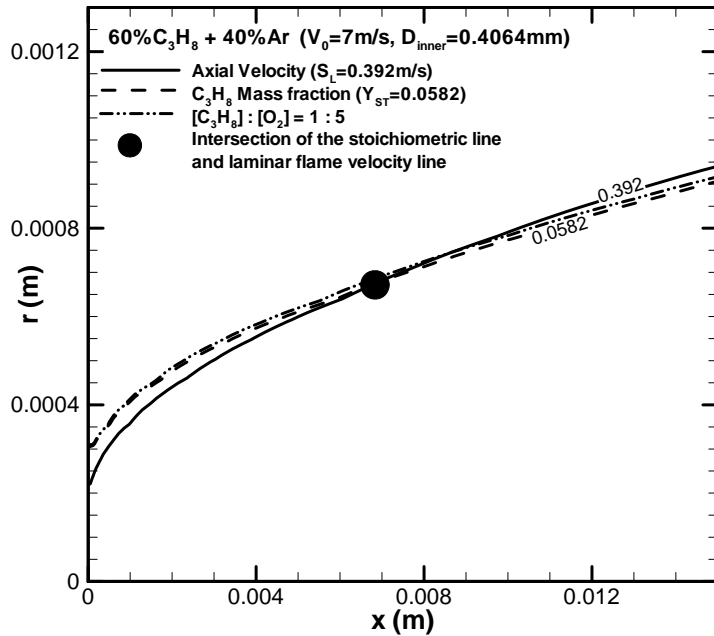
Figure 5.5(b) – Enlarged view of Figure 5.5(a) near the burner exit; the solid dot indicates the intersection of $u = S_L^o$ and the $[C_3H_8]:[O_2] = 1:5$ contours
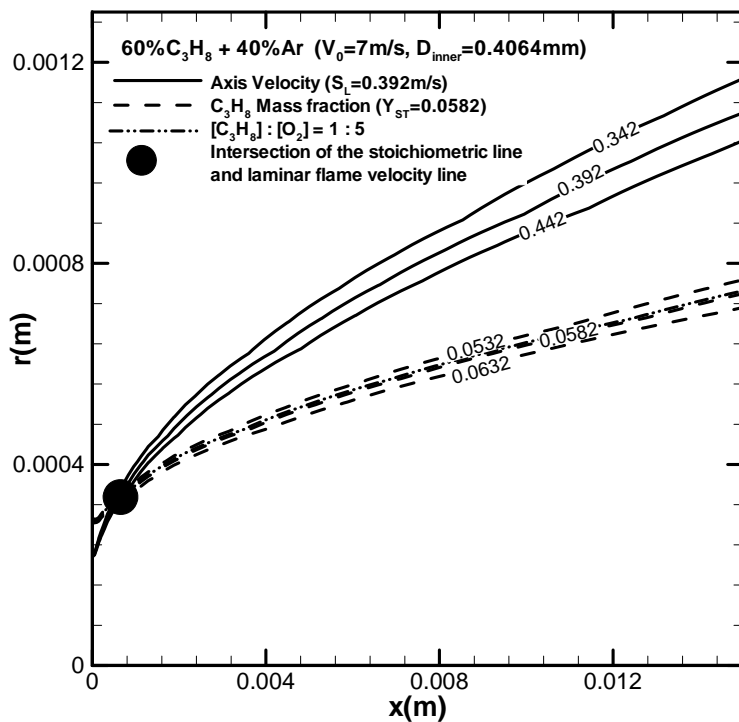
Figure 5.5(c) – Enlarged view of the reacting flow simulation near the burner exit; the solid dot indicates the intersection of $u = S_L^o$ and the $[C_3H_8]:[O_2] = 1:5$ contours
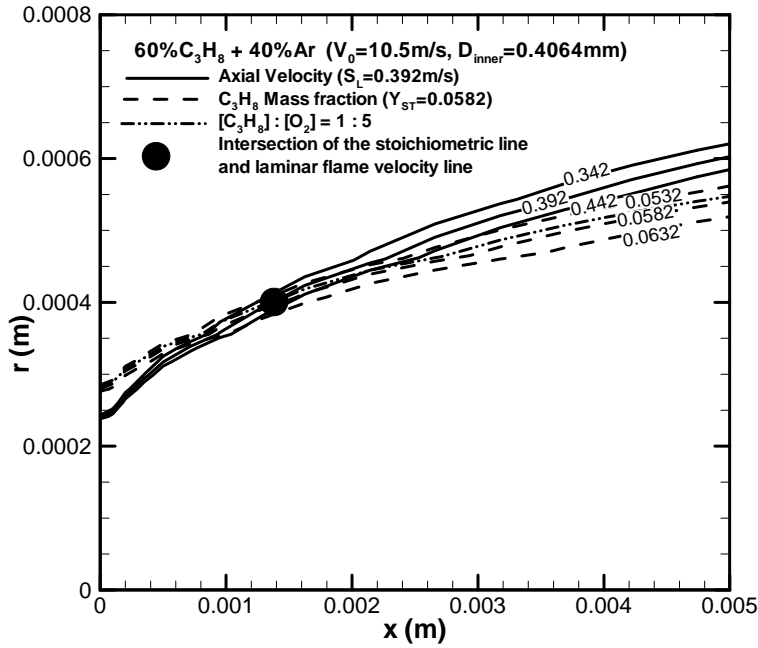
Figure 5.5(d) – Enlarged view of Figure 5.4(h) near the burner exit; the solid dot indicates the intersection of $u = S_L^o$ and the $[C_3H_8]:[O_2] = 1:5$ contours.

As V_0 is increased to 7.0 m/s, the Y_{st} (also the $[C_3H_8]:[O_2] = 1:5$) and iso-velocity contours intersect at $x \approx 0.065$ m (indicated by the black square in the Figure 5.5(a)) and at $x \approx$ 0.0065 m (Figure 5.5(b), an enlarged view of Figure 5.5(a)); between these two locations, the stoichiometric contours lie inside the $u = S_L^o$ contour. The portion of the Y_{st} and $[C_3H_8]:[O_2]$ = 1:5 contours for $x > 0.065$ m lies outside the $u = S_L^o$ contour (i.e., in the low-velocity region), suggesting that the flame base can propagate upstream to $x \approx 0.065$ m. In the region of $x <$ 0.0065 m (see Figure 5.5(b); the solid dot indicates the intersection of $u = S_L^o$ and the $[C_3H_8]:[O_2] = 1:5$ contours), the stoichiometric contour lies in the low-velocity region outside the $u = S_L^o$ contour, suggesting that flame propagation towards the burner lip is possible. Under this condition, an attached flame should be established with the flame base at $x <$ 0.0065 m, which is believed to lie outside the quenching distance from the burner lip. However, this was not observed experimentally; the experimental result is $H_L \approx 0.065$ m. As

will be shown later (Chapter 6), the reacting flow predicts an H_L value close to 0.065m rather than an attached flame. Two possible explanations for these results are that the high velocity gradient in that region extinguished the flame, or that the buoyancy due to heat release causes the flow to accelerate even in the region near the burner lip, altering the velocity and concentration contours that cannot be predicted by cold flow simulations. Figure 5.5(c) is the reacting flow simulation results. It shows that the flow in this region is accelerated and the iso-velocity lines expand outward, thus the intersection moves to $x \approx 0.001$ m, which is located in the quenching distance. The flame lift-off/re-attach hysteresis phenomenon was observed in the experimental section for the pure C_3H_8 flame at $V_0 = 11$ m/s and 12m/s (shown in Figure 4.1(a)), although the lift-off was not predicted by the cold flow simulation for such cases. The co-existence of the near burner lip intersection and a downstream intersection (marked by black squares in the cold flow figures) is a possible explanation for the hysteresis. If the cold flow is ignited below the maximum ignition height (attached flame), the flame base will propagate upstream the stoichiometric line to the burner lip; if the cold flow is ignited above the maximum ignition height (attached flame) but below the maximum ignition height (lift-off flame), the flame will propagate downstream or upstream to the black square intersection and lift off at that position.

For $V_0 = 10.5$ m/s, results are shown in Figure 5.5(d), where $H_L \approx 0.35$ m is predicted. Similar to the case of $V_0 = 7.0$ m/s, the intersection of stoichiometric and the $u = S_L^o$ contours exists in the far field ($x \approx 0.35$ m) and near the burner exit (at $x \approx 0.0013$ m; see Figure 5.5(d)). The region of $x < 0.0013$ m likely lies within the quenching distance and the only location for the flame to stabilize is $x \approx 0.35$ m according to the prediction. It should be noted that the cold flow simulation cannot produce the quenching phenomenon. Therefore, such an explanation helps to reconcile the predicted and the experimental results. For $V_0 = 12.0$ m/s (Figure 5.4(i)), no downstream intersection (indicated by the black square) of the contours can

be seen and both the Y_{st}, the near burner lip intersection is in the distance $x < 0.001$ m, within the quenching distance, and $[C_3H_8]:[O_2] = 1:5$ contours completely lie inside the $u = 0.392$ m/s $(= S_L^o)$ contour above the quenching distance, suggesting flame blow-off.

Similar observations can be made for all the pure C_3H_8 (Figure 5.1), %60C_3H_8 + 40%Ar (Figure 5.4), %40C_3H_8 + 60%Ar (Figure 5.7), %60C_3H_8 +40%He (Figure 5.9) and %80C_3H_8 + 20%He (Figure 5.10) cold flow simulations.

(a)   (b)
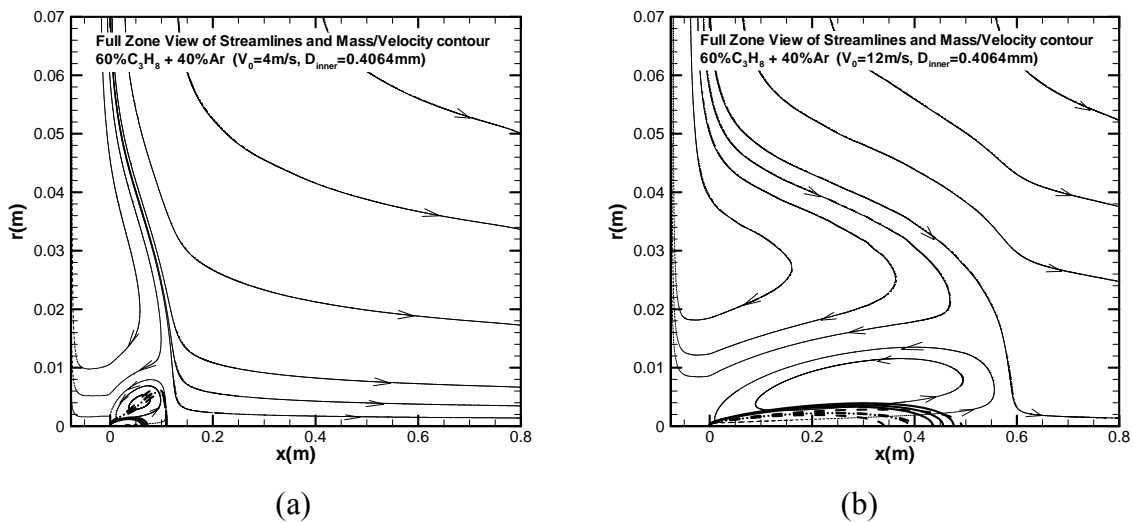
Figure 5.6(a, b) – full view of the stream structure at the computation domain for $V_0 = 4$ m/s and 12m/s

All the 60%C_3H_8 + 40%Ar cold flow results presented above were calculated in Domain (2) (-0.0762m $\leq x \leq$ 0.8m, $0 \leq r \leq$ 0.07m). The streamline structure in Figure 5.6 shows that the three flow regions, which were discussed in Figure 5.2(b2), also exists in the 60%C_3H_8 + 40%Ar flow in the jet velocity ranged we calculated, even when the flame blow-off occurs at $V_0 = 12$ m/s. Thus the calculation Domain (2) doesn't lead to early blow-off, as that discussed for Figure 5.2(b1).

Cold flow simulation results for 40%C_3H_8 + 60%Ar are shown in Figure 5.7(a-e). In these figures, axial velocity (represented by solid lines) and C_3H_8 mass fraction (represented by broad dashed lines) are plotted. One of the constant-velocity lines ($u = S_L^o$) represents the stoichiometric laminar flame velocity. All of these figures have the similar zero velocity line and streamline structure (represented in Figure 5.7(d)) as that in the pure C_3H_8 figures (except for Figure 5.1 (n), V_0 = 19 m/s) and the 60%C_3H_8 + 40%Ar figures.
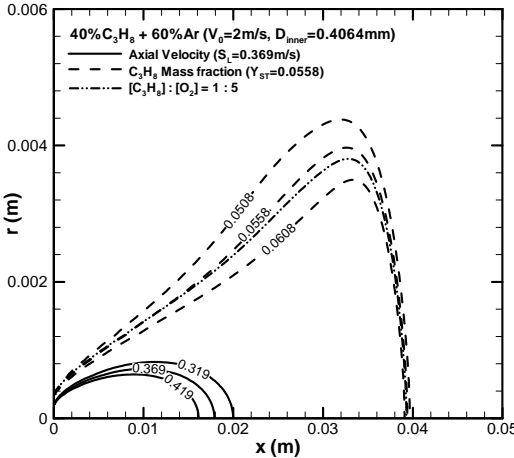
(a)
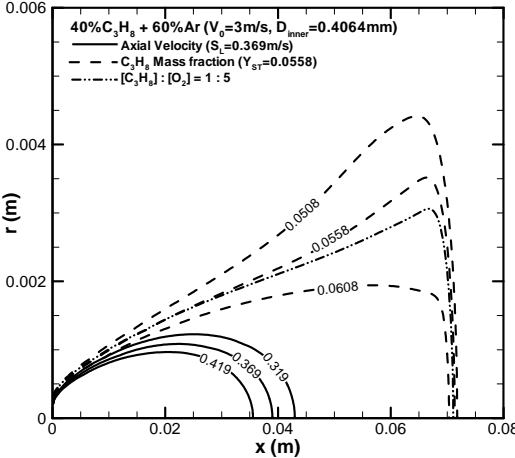
(b)
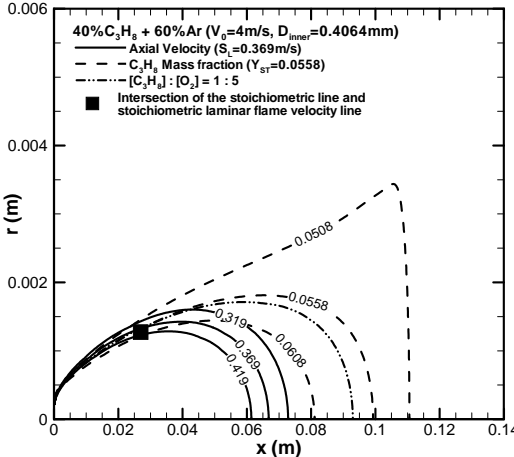
(c)
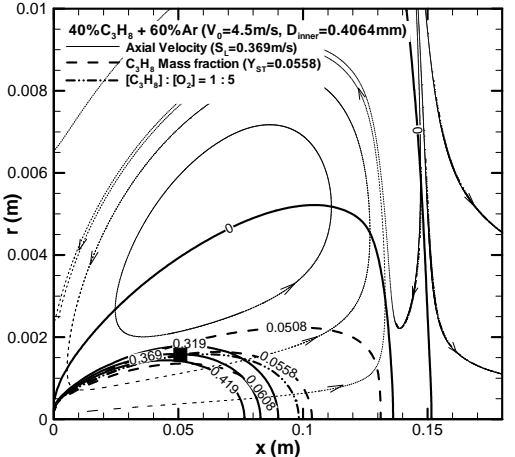
(d)

Figure 5.7(a - e) – Contours of constant velocity and concentration for 40%C_3H_8 + 60%Ar cold flow CFD simulation
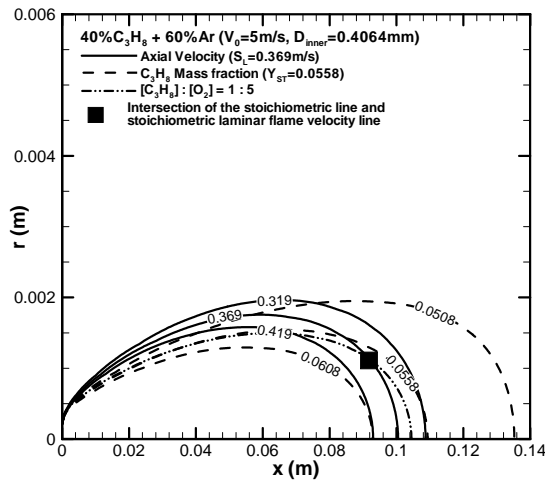
(e)

Figure 5.7(a - e) – (continued)

Table 5.3 – Lift-off height (H_L), maximum ignition height (H_I) comparison between the experimental data and cold flow simulation for $40\%C_3H_8 + 60\%Ar$

V_0 (m/s)	2.0	3.0	4.0	4.5	5.0	5.5
H_L (cm)-exp	N	N	2.0	3.0	blow	
H_L (cm)-CFD		N	2.5	5.0	9.0	blow
H_I (cm)-exp	2.0	3.5	4.5	5	Blow	
H_I (cm)-CFD	3.8 [a]	7 [a]	9 [a]	10 [a]	10.5 [a]	

Refer: [a] – maximum height for the stoichiometric line

From Table 5.3, the predicted lift-off speed (V_0 = 4 m/s) for $40\%C_3H_8 + 60\%Ar$ cold flow CFD simulation equals the experimental data, the predicted blow-off velocity is 5.5m/s, which is slightly higher than the experimental velocity 5.9 m/s. The maximum ignition height predictions are approximately twice the experimental values for low speed cases (V_0 < 4.5 m/s), it is probably because of the drop in the flammability due to the 60%Ar dilution.
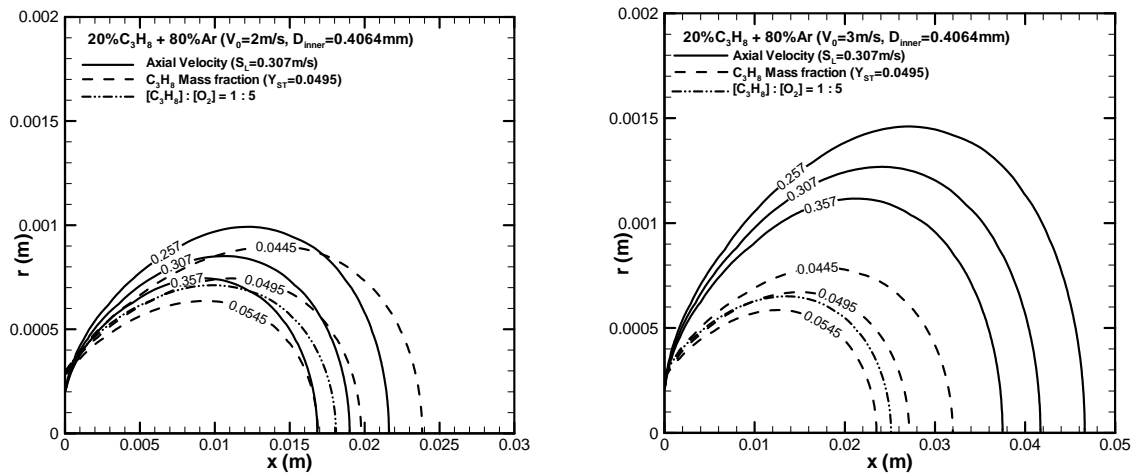
Figure 5.8(a, b) – Cold-flow prediction of 20%C_3H_8-80%Ar mixture with V_0 = 2.0 m/s and 3.0m/s; flame blows (experimentally this mixture is not ignitable).

With 80% Ar dilution, the conclusion regarding the C_3H_8 flame liftoff differs when using Y_{st} = 0.0495 and [C_3H_8]:[O_2] = 1:5 contours. The binary diffusion coefficients between Ar and air is higher than that between C_3H_8 and air, D_{Ar-O2} = D_{Ar-N2} = 2 x 10^{-5} m^2/s, and $D_{C3H8-O2}$ = $D_{C3H8-N2}$ = 1.1 x 10^{-5} m^2/s (298.15K, 1atm), so the Ar species diffuses to the outward at a faster rate than the C_3H_8 species. Thus the mass fraction of C_3H_8 in the [C_3H_8]:[O_2] = 1:5 contours is higher than Y_{st} = 0.0495 (the stoichiometric C_3H_8 mass fraction for C_3H_8 in the 20%C_3H_8 + 80%Ar / air pre-mixture), the Y_{st} = 0.0495 contours lies outside of the [C_3H_8]:[O_2] = 1:5 contours. Their separation is not apparent when the Ar dilution was 40% and 60%, but as the Ar dilution increases to 80%, their segregation becomes clear in Figure 5.8.

Experimentally, this C_3H_8-Ar mixture could not be ignited at all. Figure 5.8(a) shows that for V_0 = 2.0 m/s, the Y_{st} = 0.0495 and u = 0.307 m/s (= S_L^o) contours intersect at $x \approx 0.018$ m and 0.0005 m. The flame in the near-lip region is expected to extinguish due to quenching, leaving the only possible flame stabilizing location at, and thus the lift-off height of, 0.018 m. However, the [C_3H_8]:[O_2] = 1:5 contour lies within the $u = S_L^o$ = 0.307 m/s contour, suggesting that the flame either blows out or does not exist. No flame can be ignited and

61

stabilized for V_0 = 2.0 m/s. For V_0 = 3.0 m/s (Figure 5.8(b)), both the Y_{st} and $[C_3H_8]:[O_2]$ =

1:5 contours lie within the u = 0.307 m/s contour, indicating blowout or non-existence of the

flame, as experimentally observed. Although not shown here, reacting flow calculations were

conducted to verify the existence of a lifted flame for 80% Ar dilution. In accordance with

the experimental result, no flame could be established for either V_0 = 2.0 m/s or V_0 = 3.0 m/s

and by including reaction and the associated heat release and buoyancy effects.

5.3 Helium diluted propane

Cold flow simulation results for $60\%C_3H_8 + 40\%He$ are shown in Figure 5.9(a-n). In these figures, axial velocity (represented by solid lines) and C_3H_8 mass fraction (represented by broad dashed lines) are plotted. The dashed lines with arrows denote the streamlines.
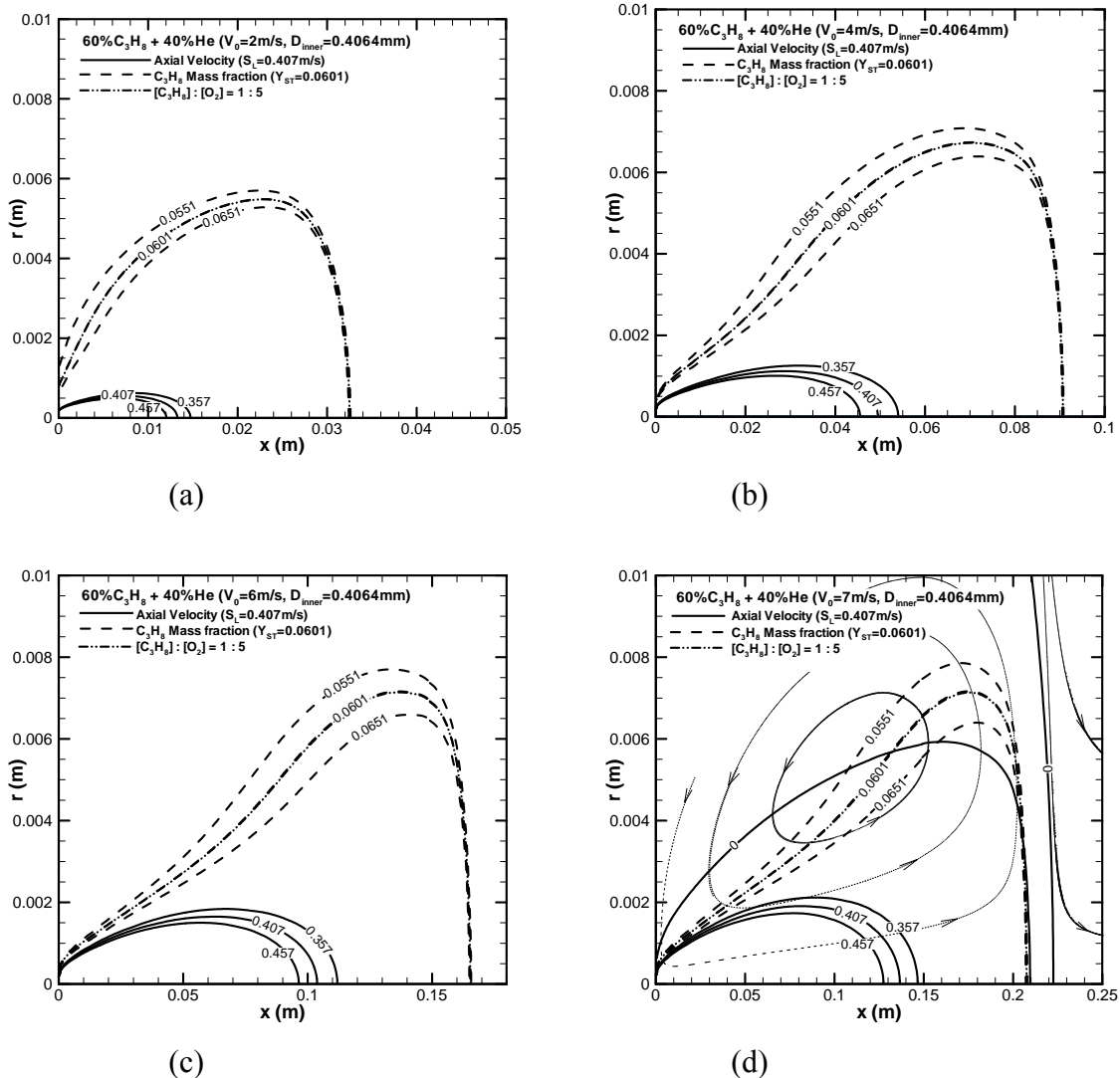
Figure 5.9(a-n) – Contours of constant velocity and concentration for $60\%C_3H_8 + 40\%He$ cold flow CFD simulation. For simplicity, the zero axial velocity lines and streamlines are only showed in Figure 5.9(d), but they exist and have the similar structure for all the cases in Figure 5.9(a-n).
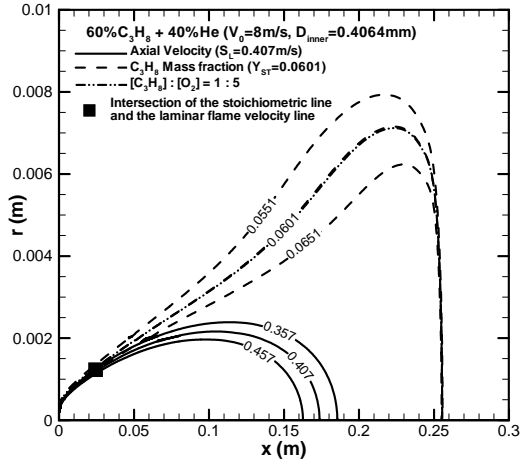
(e)
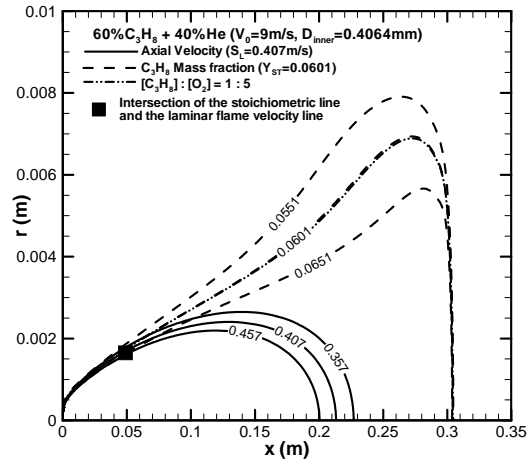
(f)
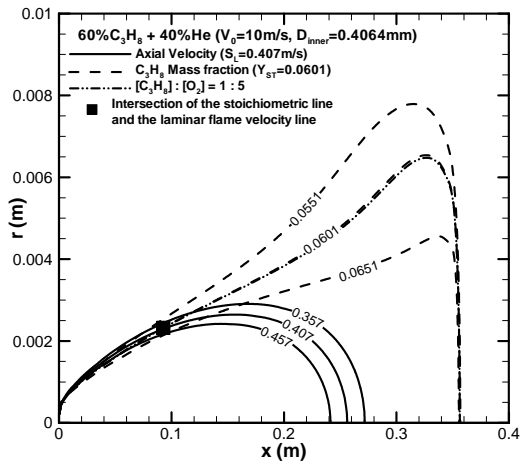
(g)
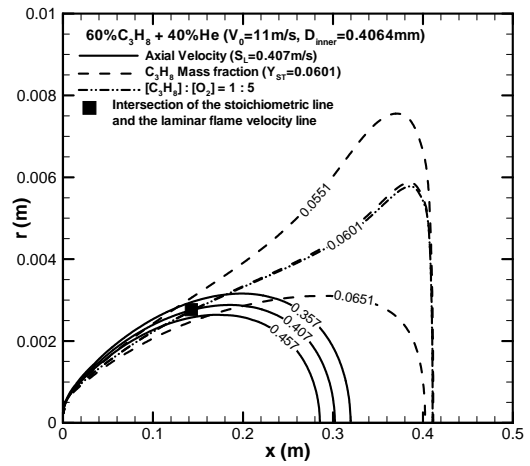
(h)
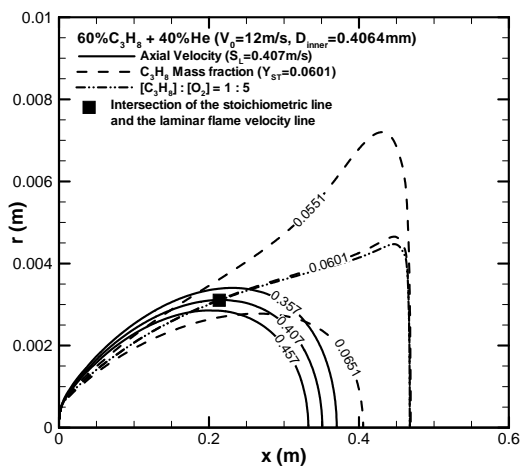
(i)
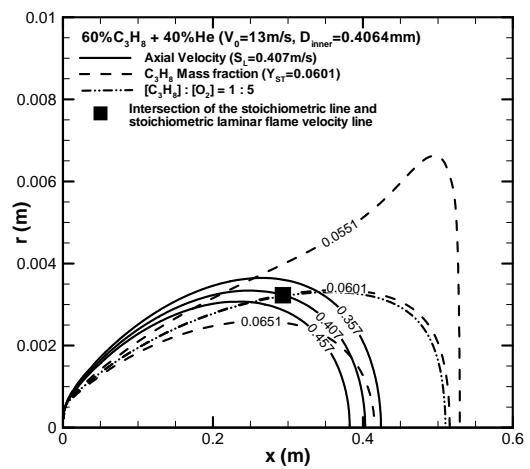
(j)

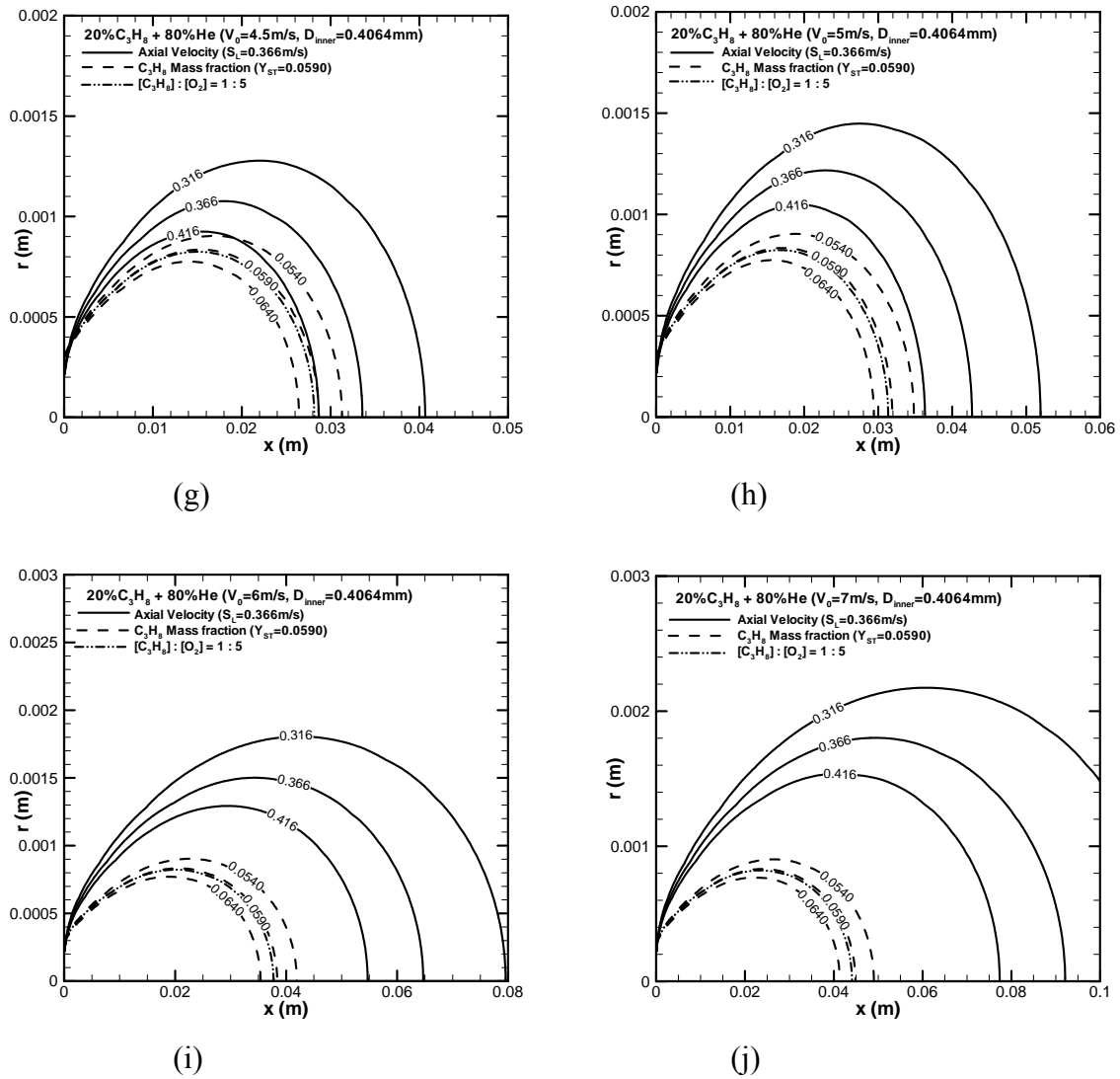Figure 5.9(a-n) – (continued)

(k)

(l)

(m)

(n)
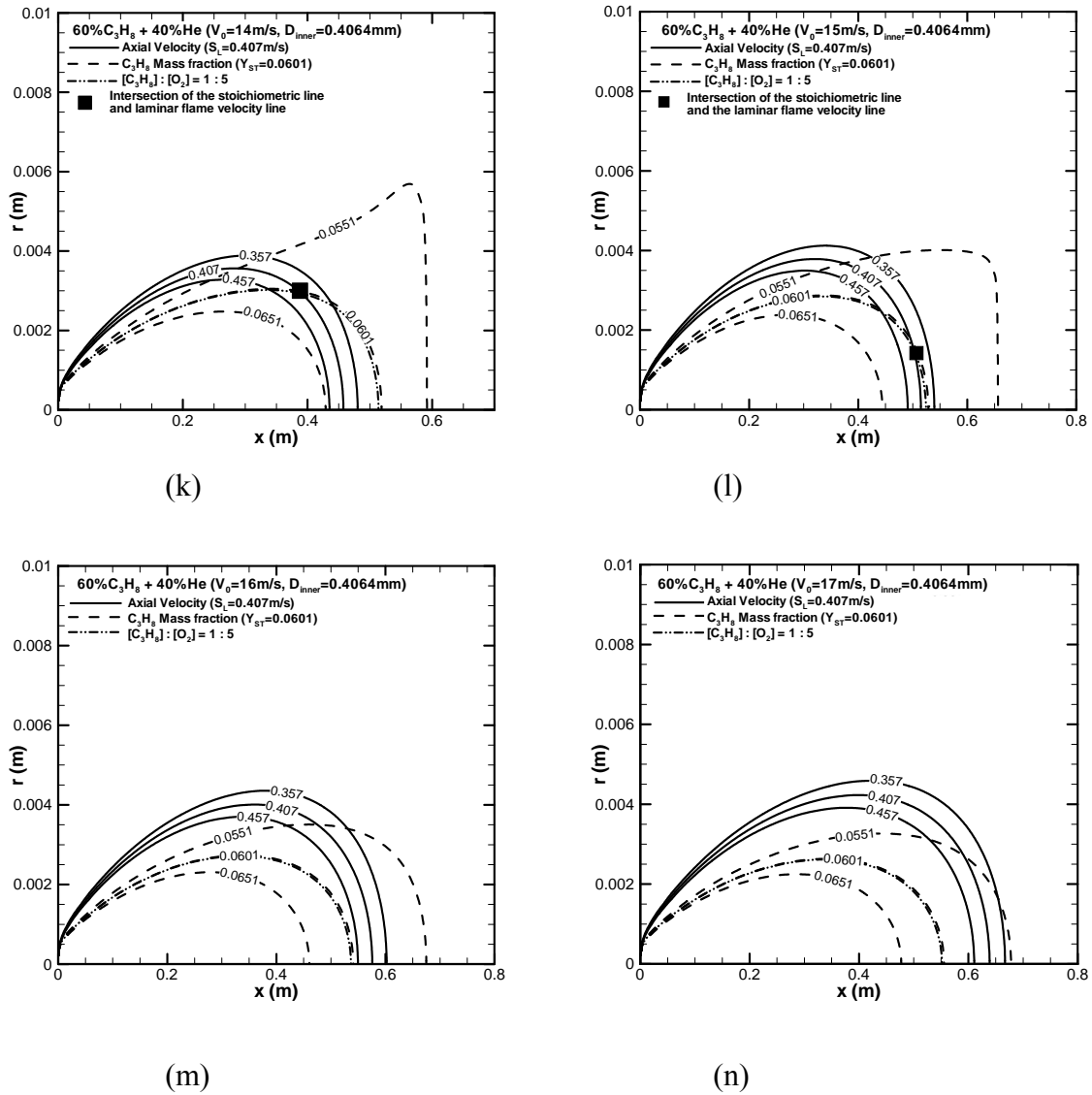
Figure 5.9(a-n) – (continued)

Table 5.4 – Lift-off height(H_L), maximum ignition height(H_I) comparison between the experimental data and cold flow simulation for $60\%C_3H_8 + 40\%He$(the data for 8m/s or higher was calculated in the larger domain; for 7m/s or lower velocity, medium domain and larger domain results are coincident).

V_0 (m/s)	2.0	4.0	6.0	7.0	8.0	9.0	10	11	12	13	14	15	16
H_L (cm)-exp	N	N	1.0	1.8	3.5	5.5	8.0	10.5	17.0	Blow	-	-	-
H_L (cm)-CFD	N	N	N	N	2.0	5.0	9.0	14	21	29	38	50	N
H_I (cm)-exp	2.5	7.0	11	12	13.5	15	17	18	19	Blow	-	-	-
H_I (cm)-CFD	3.2[a]	9.0[a]	16[a]	21[a]	25[a]	30[a]	35[a]	40[a]	46[a]	51[a]			

Refer: [a] – maximum height for the stoichiometric line

For 60%C_3H_8-40%He flames (Figures 5.9a – 5.9n and Table 5.4; $V_{BO} \approx$ 17.0 m/s), S_L^o = 0.407 m/s and Y_{st} = 0.0601 while the stoichiometric ratio [C_3H_8]:[O_2] remains to be 1:5. These two concentration contours nearly overlap for V_0 up to V_{BO}. The binary diffusion coefficients between He and air is higher than that between C_3H_8 and air, D_{He-O2}= 7.6 x 10^{-5} m^2/s, D_{He-N2} = 7.3 x 10^{-5} m^2/s, and $D_{C3H8-O2}$ = $D_{C3H8-N2}$ = 1.1 x 10^{-5} m^2/s (298.15K, 1atm), so the He species diffuses to the outward at a faster rate than the C_3H_8 species. Thus the mass fraction of C_3H_8 in the [C_3H_8]:[O_2] = 1:5 contours is higher than Y_{st} = 0.0601 (the stoichiometric C_3H_8 mass fraction for C_3H_8 in the 60%C_3H_8 + 40%He / air pre-mixture), the Y_{st} = 0.0601 contours lies outside of the [C_3H_8]:[O_2] = 1:5 contours. Their segregation is not apparent when the He dilution is 40%, however it will become clear as He dilution increases to 80% in Figure 5.10.

Figure 5.9a shows that for V_0 = 2.0 m/s, the flame is attached; that is, the stoichiometric contour lies entirely in the low-velocity region outside the $u = S_L^o$ contour and the flame can be stabilized as close to the burner as the quenching distance allows. It can be seen that $H_L \approx$ 0.14 m for V_0 = 11.0 m/s and $H_L \approx$ 0.50 m for V_0 = 15.0 m/s. For V_0 = 11.0 m/s and V_0 = 15.0 m/s, both the Y_{st} and the [C_3H_8]:[O_2] = 1:5 contours lie outside the contour in regions of x < 0.001 m near the burner exit (no enlarged views of regions near burner exit are shown here for brevity), where the quenching effect may cause the flame to extinguish. Therefore, the stabilization locations for these two cases are at their respective values of x = H_L. The flame blows off for V_0 = 17.0 m/s. The H_L near the blow-off limit for this flame is larger than that for the 60%C_3H_8-40%Ar flame; this flame also had a larger V_{BO} (approximately 17.0 m/s vs. 12.0 m/s). Such differences can be attributed to the differential diffusion effects of mass and viscous transports. The CFD predicted maximum ignition height (Table 5.4) for the low velocity flows (V_0 < 6.0 m/s) approximately match to the experiment

data. Although not presented, C_3H_8 flames with 60% He dilution also achieved stable lift-off prior to reaching their V_{BO} (10.5 m/s).

With 80% He dilution, results are shown in Figure 5.10(a-j). For $V_0 = 3.8$ m/s (Figure 5.10e), either the $Y_{st} = 0.0495$ or $[C_3H_8]:[O_2] = 1:5$ contour intersects with the $u = S_L^o$ contour at two locations – one at $x \approx 0.018$ m and the other at $x < 0.001$ m. Similar to the results shown in Figure 5.5(d) for the 60%C_3H_8 + 40%Ar case, it is believed that no flame could exist in the region of $x < 0.001$ m due to quenching. It is also possible that that the buoyancy effect, similar to that discussed along with Figure 5.5(b), may cause the near-field concentration in such a way that the intersection of contours shrinks from an above-quenching-distance region ($x > 0.005$ m) to the quenching region of $x < 0.001$ m. Therefore, the flame liftoff height is $H_L \approx 0.018$m. The liftoff phenomenon was experimentally observed, although with a somewhat smaller liftoff height of approximately 1.0 cm. For $V_0 = 4.0$ m/s, as shown in Figure 5.10(f), the predicted intersection of the contours is located only at $x \approx 0.001$ m, with the stoichiometric contour lying outside the $u = S_L^o$ contour for $x = 0 - 0.001$ m. Again this is a possible location for flame to anchor. However, no stable flame can be established in this region of $x = 0 - 0.001$ m due to quenching; such an explanation is in agreement with experimental observation.
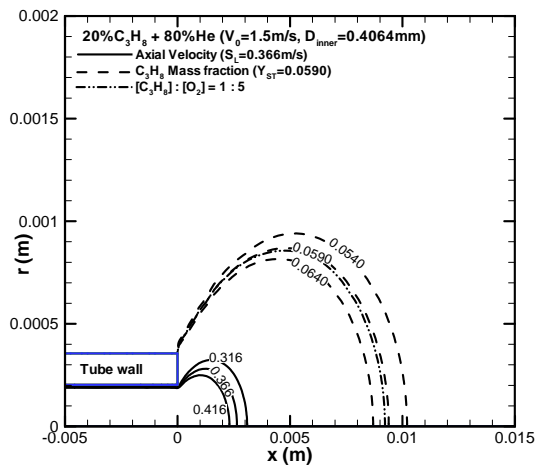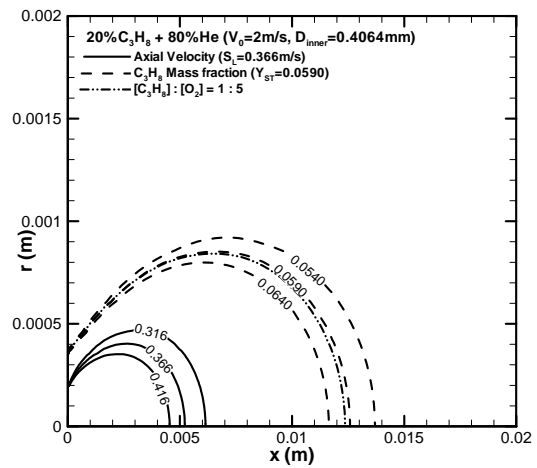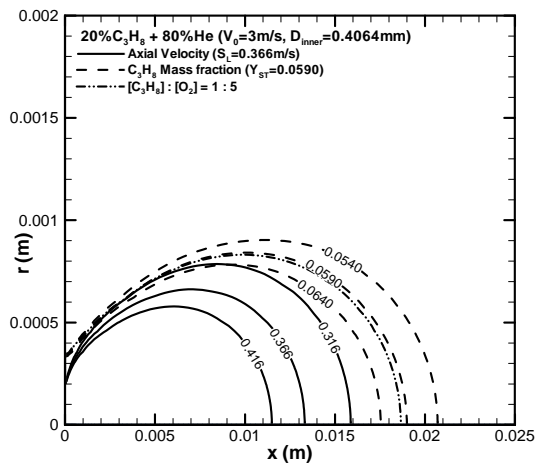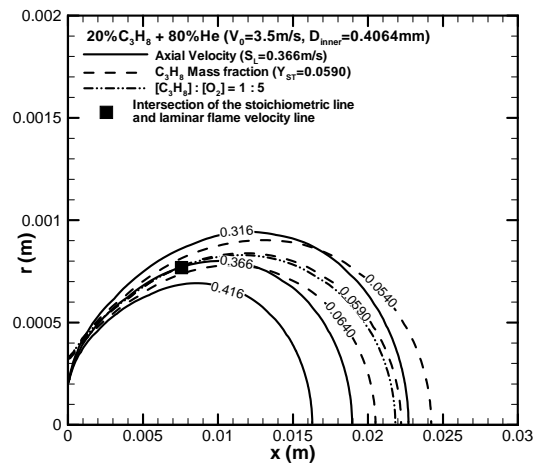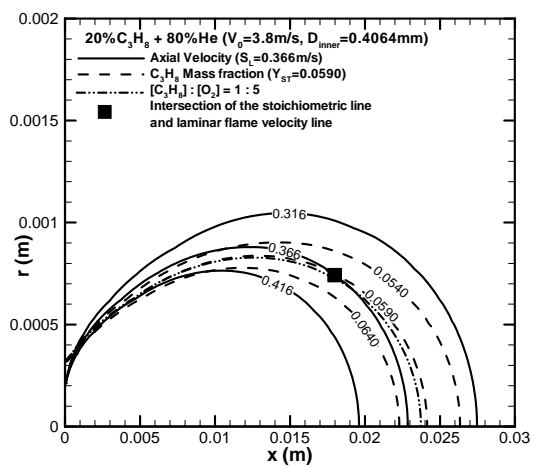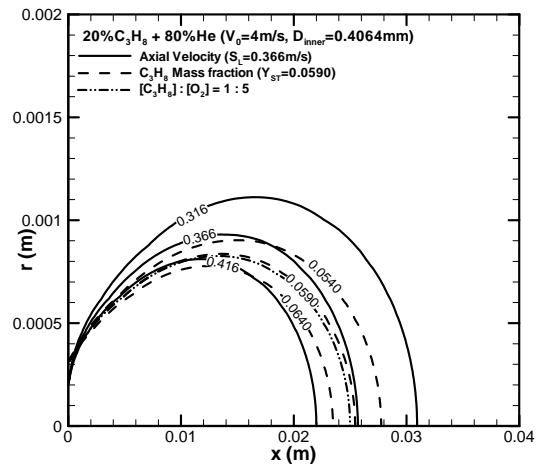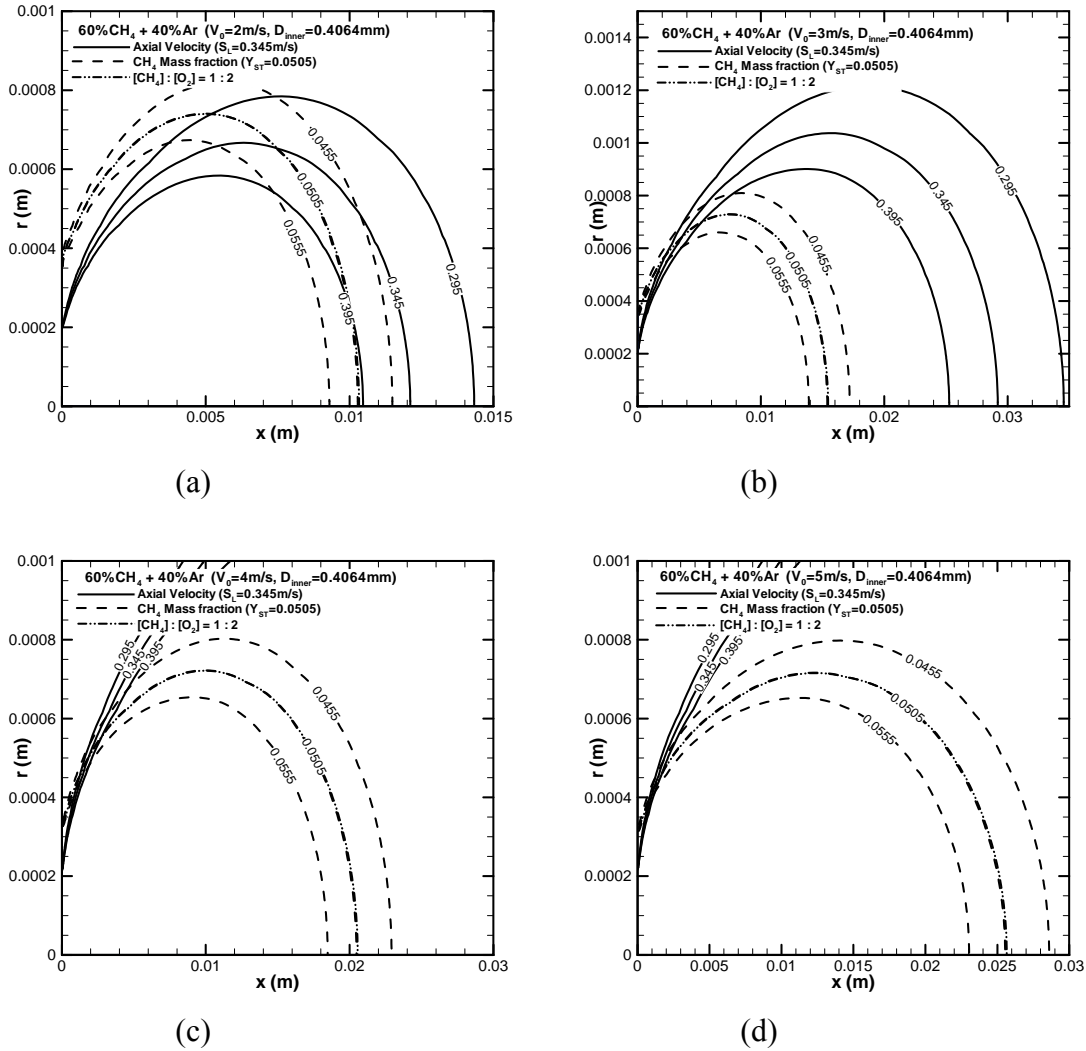
Figure 5.10(a - j) – Contours of constant velocity and concentration for $20\%C_3H_8 + 80\%He$ cold flow CFD simulation

(g)

(h)

(i)

(j)

Figure 5.10(a-j) – (continued)

Table 5.5 – Lift-off height(H_L), maximum ignition height(H_I) comparison between the experimental data and cold flow simulation for 20%C_3H_8 + 80%He

V_0 (m/s)	1.5	2.0	3.0	3.5	3.8	4.0	4.5	5.0	6	7
H_L (cm)-exp	N	N	0.25	-	-	0.6	0.9	1.2	2.4	blow
H_L (cm)-CFD	N	N	N	0.7	1.8	2.4	blow			
H_I (cm)-exp	0.3	0.4	0.6			1.0	1.3	2	3	blow
H_I (cm)-CFD	0.9[a]	1.25[a]	1.9[a]	2.2[a]		2.5[a]	blow			

Refer: [a] – maximum height for the stoichiometric line

Table 5.5 shows the predicted maximum ignition heights are about 3 times as the experimental values even for the low velocity case (V_0 < 4 m/s), similar to that situation in Table 5.3, it is assumed that the C_3H_8 flammability is depressed due to the 80%He dilution.
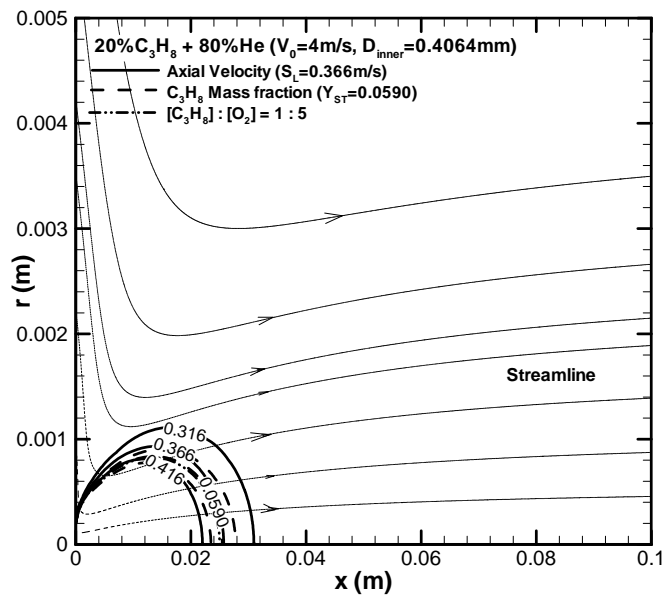
Figure 5.11 – A typical streamline and contours of constant velocity and concentration for 20%C$_3$H$_8$ + 80%He cold flow CFD simulation

Figure 5.11 indicates the typical streamline and velocity structure of the 20%C$_3$H$_8$ + 80%He cold flow simulations, differential from the other Ar/He/C$_3$H$_8$ compositions (Figure 5.1, 5.4, 5.7, 5.8. 5.9), there is no zero velocity contour and no stagnation level (introduced in Figure 5.3 (b2)), the jet fuel flow blows to the top boundary directly. An explanation is that the density of the 80%He diluted C$_3$H$_8$ is lighter than the air, thus there is no gravity induced negative buoyancy effect as other fuel compositions (pure C$_3$H$_8$, 60%C$_3$H$_8$ + 40%Ar, 40%C$_3$H$_8$ + 60%Ar, 20%C$_3$H$_8$ + 80%Ar, 60%C$_3$H$_8$ + 40%He).

5.4 Methane-inert mixtures

Cold-flow predictions for CH$_4$ with all dilution levels which are in the experimental flammable range are investigated. These pure CH$_4$, and CH$_4$ with 20% or 40% of He or Ar dilutions, do not show stable flame lift-off prior to blow out.
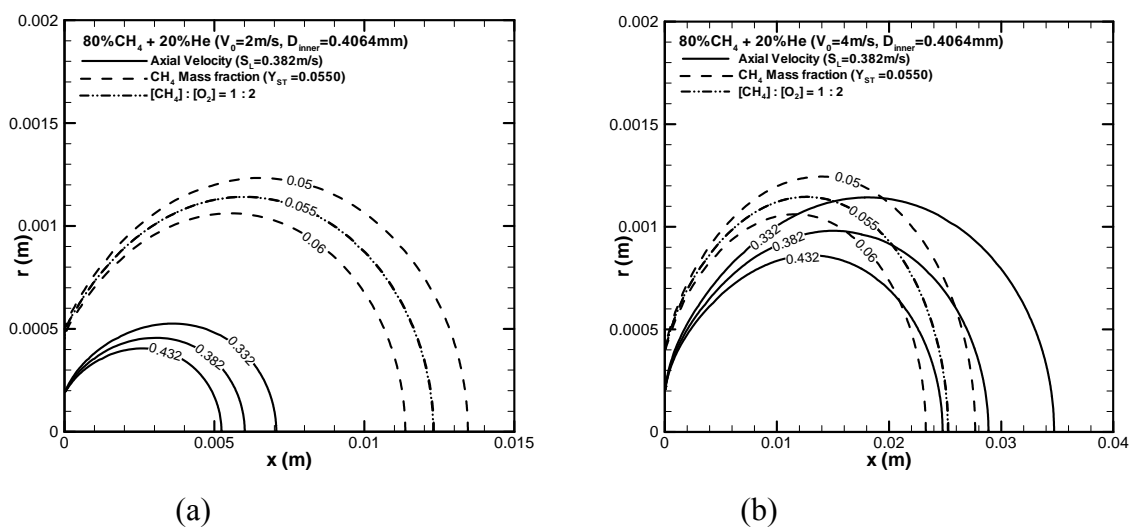

(a)

(b)

(b)

(d)
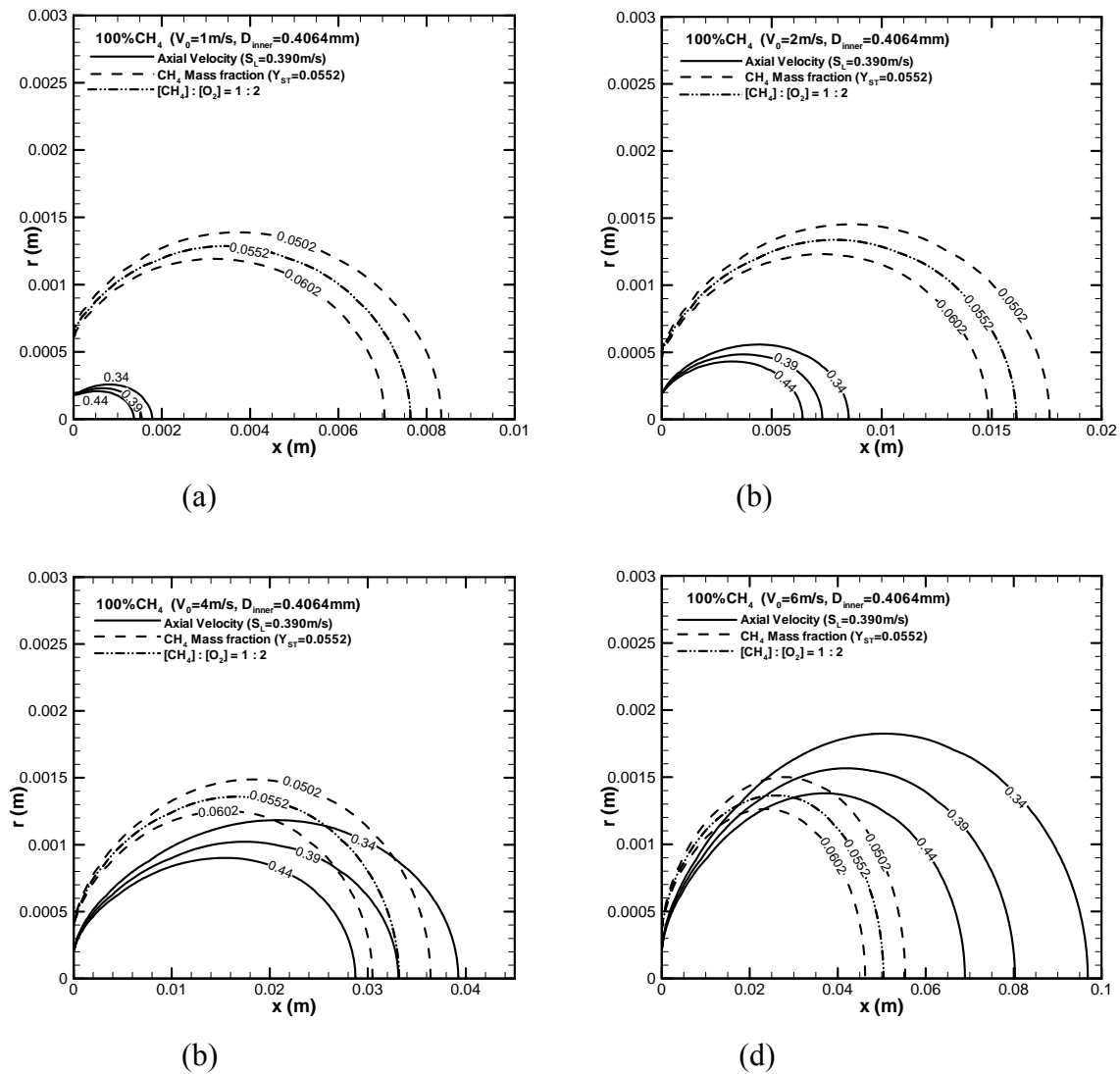
Figure 5.12(a - i) – Contours of constant velocity and concentration for pure CH$_4$ cold flow CFD simulation
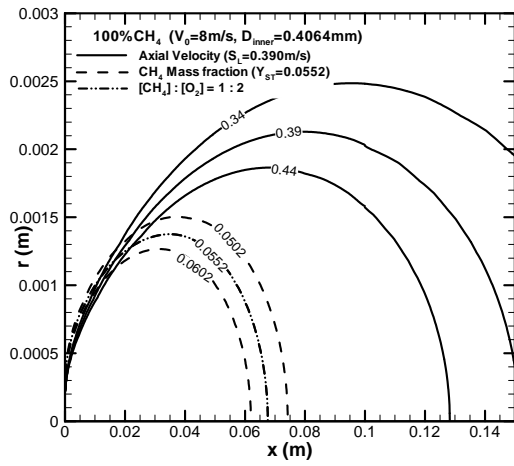
(e)
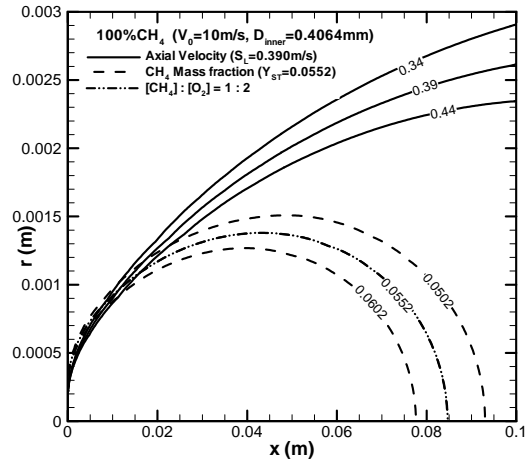
(f)
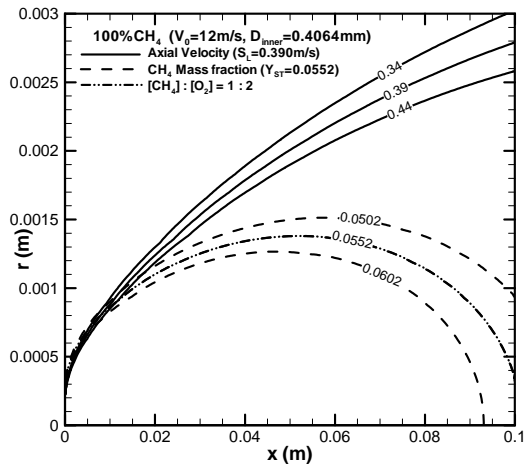
(g)
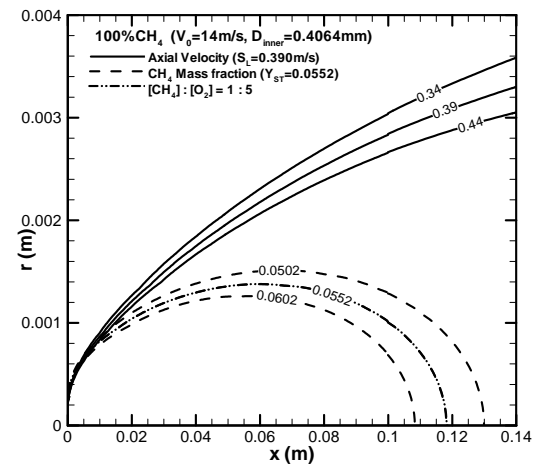
(h)
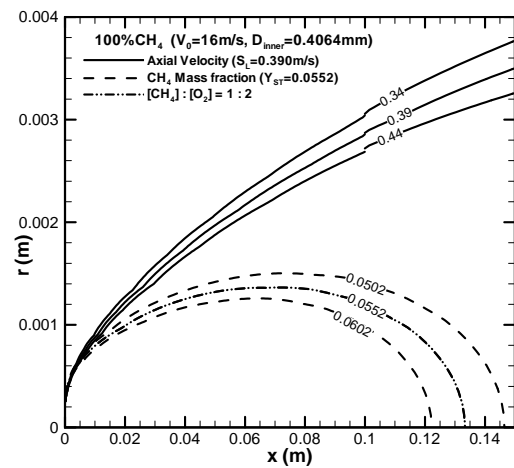
(i)

Figure 5.12(a - i) – (continued)

Table 5.6 –Maximum ignition height (H_I) comparison between the experimental data and cold flow simulation for pure CH_4

V_0 (m/s)	1	2	4	6	8	10	12	14	15.5	16
H_I(cm)-exp	0.7	1.5	2.5	2.9	3.3	4	5	3	1	Blow out
H_I (cm)-CFD	0.76[a]	1.6[a]	3.3[a]	5.0[a]	6.7[a]	8.5[a]	10.2[a]	11.8[a]	-	13.4[a]
H_I (cm)-CFD	N	N	3.3[b]	2.4[b]	1.7[b]	1.2[b]	1.0[b]	0.7[b]	-	0.3[b]

Refer: [a] – maximum height for the stoichiometric line
[b] – Intersection of the stoichiometric line and laminar flame velocity line

For the pure CH_4 flow, the stoichiometric $[CH_4]:[O_2]$ = 1:2 contour intersects with the stoichiometric laminar flame velocity ($u = S_L^o$) contour for all the flows with $V_0 >4$ m/s. It can be seen from Figure 5.12(d) (V_0 = 6 m/s) that the Y_{st} = 0.0552 and the stoichiometric line $[CH_4]:[O_2]$ = 1:2 are identical, lie outside of the u = 0.390 m/s contour between the burner exit ($x = 0$) and the intersection (x = 0.024 m), and lie inside of the velocity contour above the intersection ($x > 0.024$ m). In the experiment, the cold flow is ignitable below the maximum ignition height (H_I), if ignited below H_I = 2.9 cm (Table 5.6), the flame base will travel along the stoichiometric line upstream until attaching to the burner lip.

For the $V_0 < 4$ m/s flows, the experimental maximum ignition height is close to the maximum height for the stoichiometric line, the disturbances for the low spend flow is relatively small. As the flow velocity increases, the intersection of the stoichiometric line and stoichiometric laminar flame velocity contour thus emerges and shrinks from 3.3 cm at V_0 = 4 m/s to 0.3 cm at V_0 = 16 m/s, However, due to the ignition spark energy influence and flow stagnation effect upstream of the ignition wire, the cold flow usually can be ignited from a higher ignition height proportional to the intersection height, it is based on the assumption that the pulse of spark can generate a buoyancy and disturbance which can push the flame to propagate upstream to cross the obstacle distance between the maximum ignition height and the intersection of the stoichiometric line and the stoichiometric laminar velocity line. The results in Table 5.6 show that the experimental maximum ignition height (H_I) is about 4 times of the CFD predicted intersection of the stoichiometric line the stoichiometric laminar flame

velocity contour (from 10 m/s to 15.5 m/s). For the $V_0 = 16$ m/s flow, the intersection shrinks

to $x = 0.3$ cm, it is close to the burner lip quenching distance, thus blow-out. The quenching

distance for stoichiometric methane-air flame was reported to be 2mm [28].

(a)

(b)

(c)

(d)
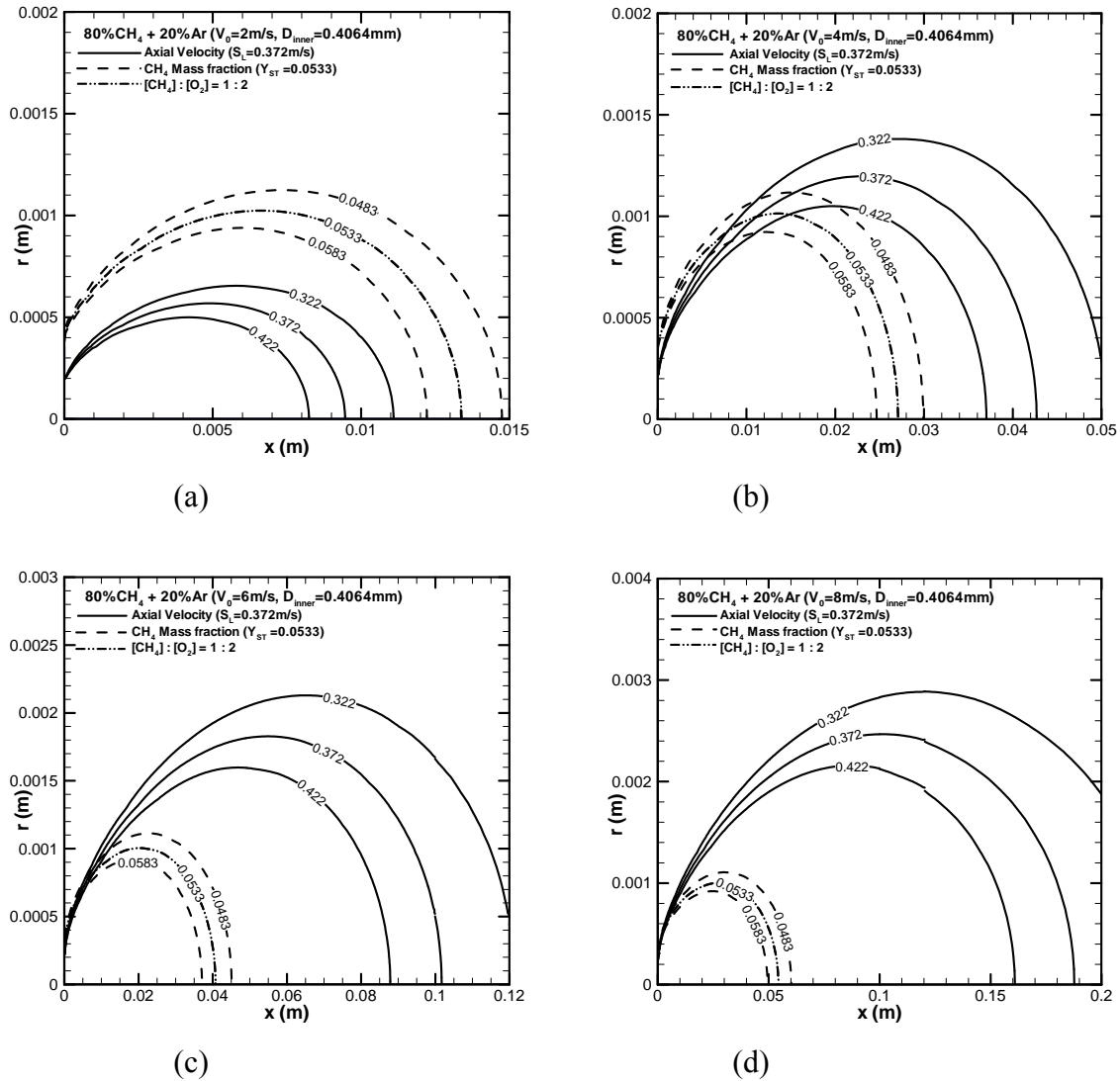
Figure 5.13(a - i) – Contours of constant velocity and concentration for pure 80%CH$_4$ + 20%Ar cold flow CFD simulation

Table 5.7 – Maximum ignition height (H_I) comparison between the experimental data and cold flow simulation for 80%CH$_4$ + 20%Ar

V_0 (m/s)	2	4	6	8	9
H_I(cm)-exp	1.5	2.5	3	1	Blow out
H_I (cm)-CFD	1.35[a]	2.7[a]	4.0[a]	5.4[a]	
H_I (cm)-CFD	N	1.2[b]	0.75[b]	0.25[b]	

Refer: [a] – maximum height for the stoichiometric line

[b] – Intersection of the stoichiometric line and laminar flame velocity line

From Figure 5.13 and Table 5.7, the 80%CH$_4$ + 20%Ar cold flow accurately predicted the maximum ignition height (H_I) for the $V_0 < 4$ m/s cases. For the higher speed cases, $V_0 > 6$ m/s, the experimental maximum ignition height is approximately 4 times of the height for the intersection of the stoichiometric line and the stoichiometric laminar flame velocity line. The blow-out velocity of $V_0 = 9$ m/s is also predicted by the quenching distance theory.

(a)

(b)

(c)

(d)

Figure 5.14(a - g) – Contours of constant velocity and concentration for pure 60%CH$_4$ + 40%Ar cold flow CFD simulation ((f) and (g) are the full view graph for (c) and (d), respectively)
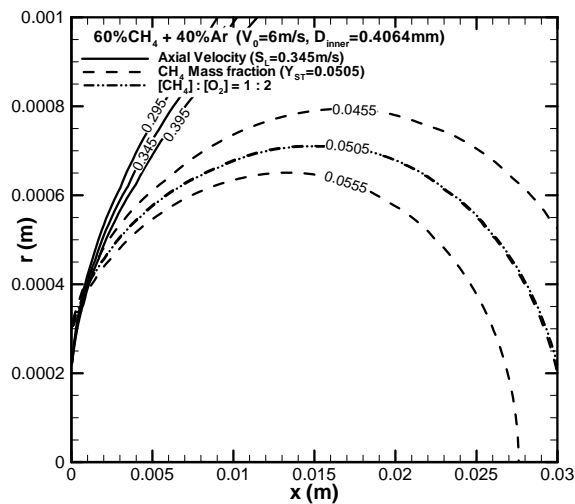
(e)
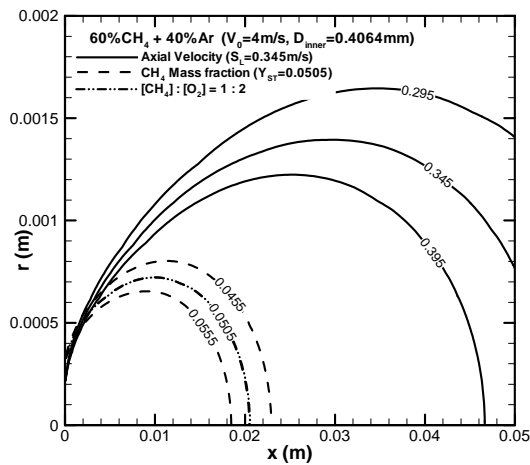
(f)
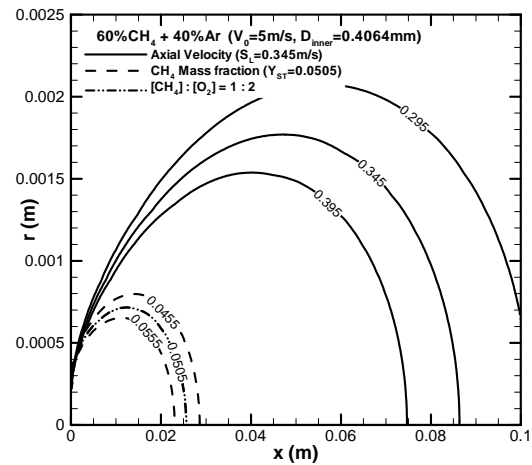
(g)

Figure 5.14(a-g) – (continued)

Table 5.8 – Maximum ignition height (H_I) comparison between the experimental data and cold flow simulation for 60%CH_4 + 40%Ar

V_0 (m/s)	2	3	4	5	6
H_I (cm)-exp	1	1.3	1	blow	blow
H_I (cm)-CFD	1.0[a]	1.5[a]	2.0[a]	2.6[a]	
H_I (cm)-CFD	0.7[b]	0.35[b]	0.25[b]	0.1[b]	

Refer: [a] – maximum height for the stoichiometric line

[b] – Intersection of the stoichiometric line and stoichiometric laminar flame velocity line

For the 60%CH$_4$-40%Ar flame, results for V_0 = 2.0 m/s, 3.0 m/s, 4 m/s, 5 m/s and 6.0 m/s are shown in Figure 5.14(a-e). For this flame, Y_{st} = 0.0505 and S_L^o = 0.345 m/s. It can be seen from Figure 5.14a (V_0 = 2.0 m/s) that both the Y_{st} = 0.0505 and the stoichiometric [CH$_4$]:[O$_2$] = 1:2 contours (nearly identical) lie outside the $u = S_L^o$ contour near the burner exit (x = 0), suggesting an attached flame. For V_0 = 3.0 m/s (Figure 5.14b), these concentration contours near x = 0 still lie outside the $u = S_L^o$ contour. However, the portion of the stoichiometric contour lying outside the $u = S_L^o$ contour shrinks toward the burner exit, to $x \approx 0.0035$ m (Table 5.8) from ≈ 0.007 m for V_0 = 2.0 m/s. For V_0 = 5.0 m/s (Figure 5.14g, with expanded near-field view shown in Figure 5.14d) this portion (the flame stabilization zone) has shrunk to $x \approx 0.001$ m (Table 5.8), where heat loss to the burner lip is expected to be significant and should cause the flame to blowout for similar reasons given to explain flame blowout results shown in Figure 5.5d. Current and previous experiments [9] showed that the 60%CH$_4$-40%Ar flame did not have stable liftoff prior to reaching the blowout limit $V_{BO} \approx 5.0$ m/s.

(a)   (b)

Figure 5.15(a - f) – Contours of constant velocity and concentration for pure %80CH$_4$ + 20%He cold flow CFD simulation
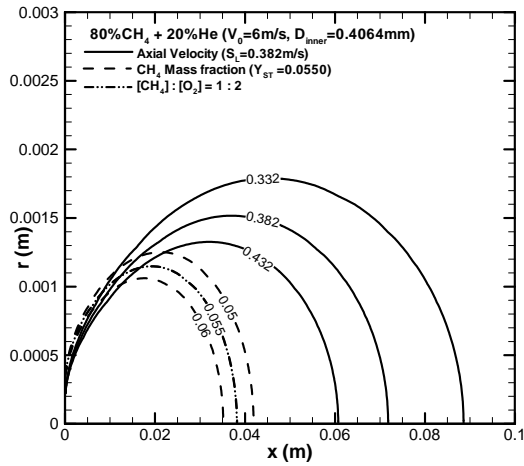
(c)
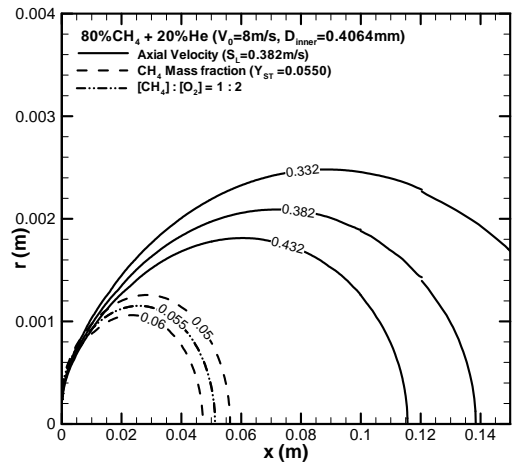
(d)
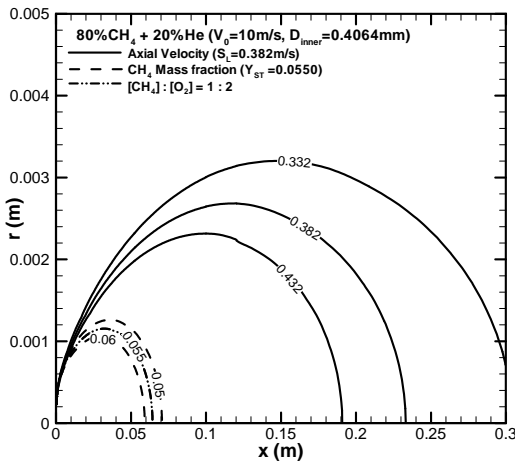
(e)
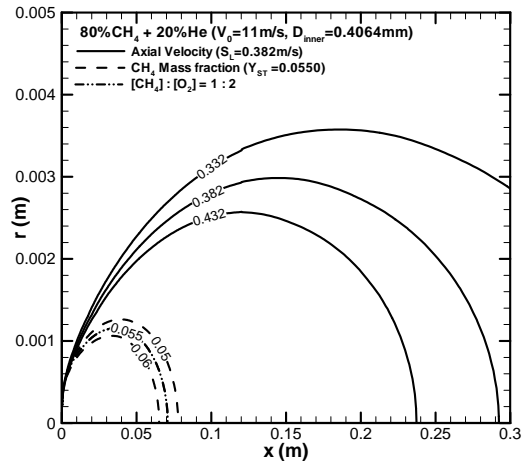
(f)

Figure 5.15(a - f) – (continued)

Table 5.9 – Maximum ignition height (H_I) and Lift-off height (H_L) comparison between the experimental data and cold flow simulation for 80%CH_4 + 20%He

V_0 (m/s)	2	4	6	8	10	11
H_L (cm)- exp	N	N	N	0.1	0.9	Blow off
H_I (cm)- exp	1.5	2.8	3.8	5.0	3.0	Blow off
H_I (cm)- CFD	1.2[a]	2.5[a]	3.8[a]	5.1[a]	6.3[a]	7.0[a]
H_I (cm)- CFD	N	2.1[b]	1.5[b]	1.0[b]	0.4[b]	0.2[b]

Refer: [a] – maximum height for the stoichiometric line

[b] – Intersection of the stoichiometric line and stoichiometric laminar flame velocity line

Figure 5.15(a-i) present the cold flow CFD results for $80\%CH_4 + 20\%He$ ($Y_{st} = 0.0550$ and $S_L^o = 0.382$ m/s). The heights for intersection of the stoichiometric line and stoichiometric laminar flame velocity line (Table 5.9) for $V_0 = 2$ m/s, 4 m/s, 6 m/s, 8 m/s and 10 m/s are above the quenching distance [28], indicate attached flames. While the intersection height for $V_0 = 11$ m/s is located in $x = 0.2$ cm, within the quenching distance from the burner lip, leds to blow out. However, the experimental results show the lift-off phenomenon for $V_0 = 10$ m/s, with a lift-off height of 0.9 cm. For the low jet flow velocities, $V_0 < 8$ m/s, the experimental maximum ignition heights coincided with the maximum heights of the stoichiometric line.
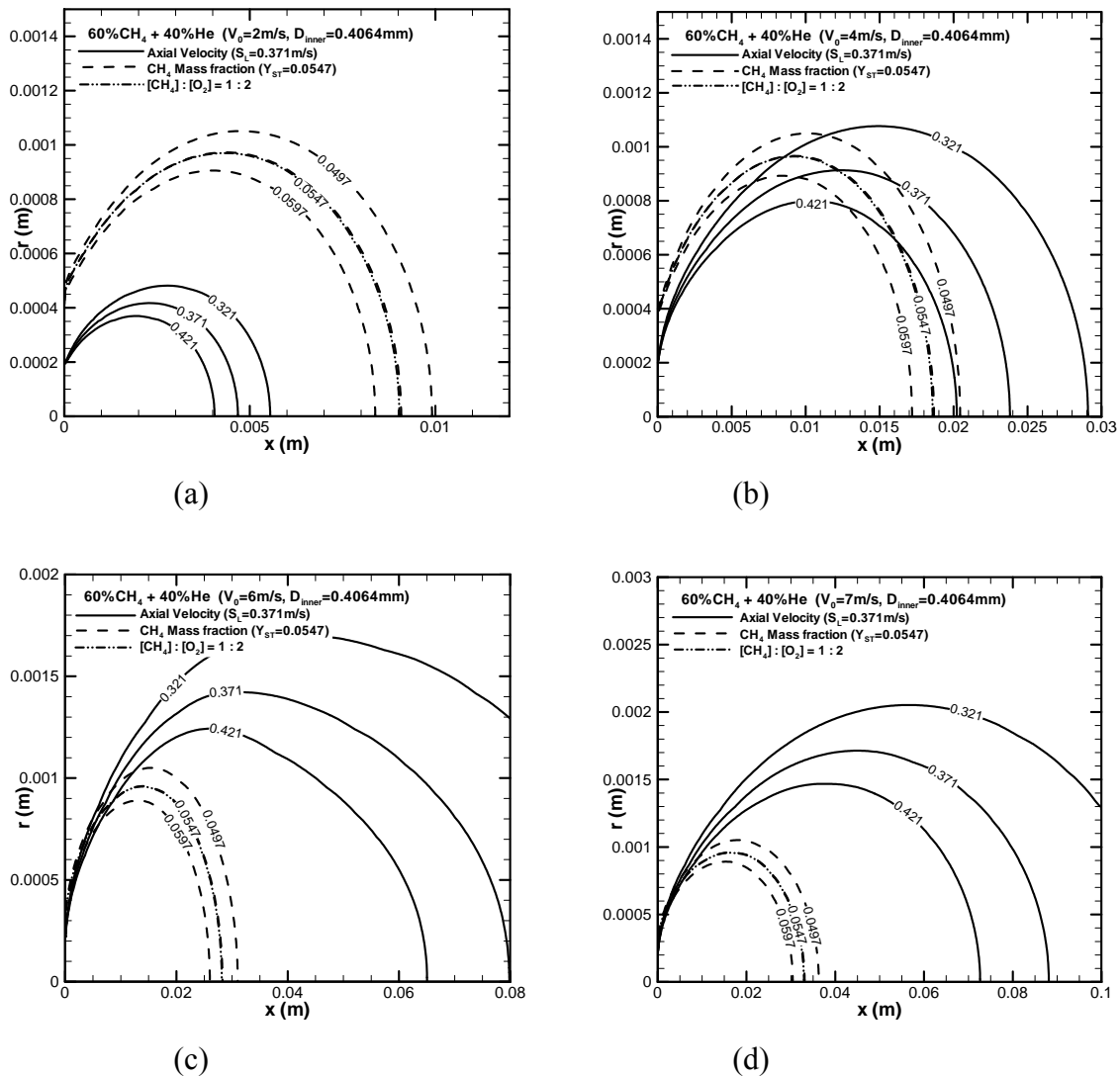
Figure 5.16(a - e) – Contours of constant velocity and concentration for pure %60CH₄ + 40%He cold flow CFD simulation

(e)
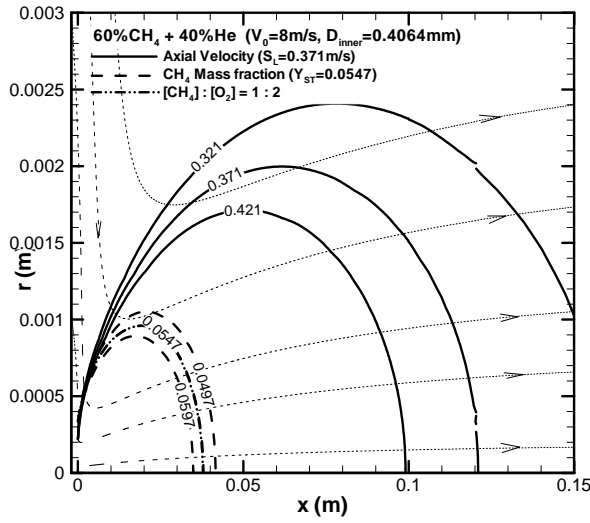
Figure 5.16(a – e) – (continued)

Table 5.10 – Maximum ignition height (H_I) and Lift-off height (H_L) comparison between the experimental data and cold flow simulation for 60%CH_4 + 40%He

V_0 (m/s)	2	4	6	7	7.5	8
H_L (cm)- exp	N	N	0.5	1	1.5	Blow off
H_I (cm)- exp	1.2	2.2	2.7	2.5	2	Blow off
H_I (cm)- CFD	0.9[a]	1.9[a]	2.8[a]	3.5[a]	-	3.8[a]
H_I (cm)- CFD	N	1.2[b]	0.6[b]	0.35[b]	-	0.2[b]

Refer: [a] – maximum height for the stoichiometric line
[b] – Intersection of the stoichiometric line and stoichiometric laminar flame velocity line

The cold-flow results of 60%CH_4-40%He (Y_{st} = 0.0547 and S_L^o = 0.371 m/s) are presented in Figure 5.16(a-e), V_0 = 2.0 m/s, 4.0 m/s, 6.0 m/s 7 m/s and 8.0 m/s, respectively. Following similar observations as for 60%CH_4 + 40%Ar, the flame stabilization zone near the burner exit can be seen to shrink, from $x \approx 0.012$ m (Figure 5.16b), to $x \approx 0.006$ m (Figure 5.16c for V_0 = 6.0 m/s) to $x \approx 0.002$ m (Figure 5.16i) while V_0 was increased from 4.0 m/s to 8.0 m/s. The flame for V_0 = 4.0 m/s (Figure 5.16b) is therefore stable and attached. Similarly, for V_0 = 6.0 m/s the flame base can propagate to as close to the burner lip as the quenching

80

distance allows, and thus the flame is attached. These cold-flow calculations for $V_0 = 8.0$ m/s predict a possible flame stabilization region $x < 0.002$ (Figure 5.16e, Table 5.10). If this region lies within the quenching distance, the flame will blow out. Otherwise, an attached flame is established. The streamlines in Figure 5.16e show the air entrainment without the back flow region which was shown in Figure 5.2(b1), the similar streamline distribution exists in all the above pure CH_4 and 20%-40% Ar/He diluted CH_4 cold flows, this streamline distribution is similar to that shown in Figure 5.11 for 80%He diluted C_3H_8, the average density for these fuel compositions are lighter than the air and the other C_3H_8/dilution composition, thus there is no gravity induced negative buoyancy effect.

Experimentally the 60%CH_4-40%He flame exhibited stable lifted configuration in the velocity range of Figures 5.16c and 5.16d. To understand the disagreement between the predicted and experimental results, the effect due to combustion was investigated, with the details given in the Chapter 6.

5.5 Summary

The cold flow calculations including multi-component diffusivities successfully predicted the lift-off and blow-off / blow-out phenomenon for the pure C_3H_8, Ar / He diluted C_3H_8, pure CH_4 and Ar diluted CH_4 flames. It also indicated the ignition properties for the low speed fuel jet flows.

The comparison for C_3H_8 and 60%C_3H_8-40%Ar/He mixture between the calculated cold flow and experimental flame lift-off height (H_L) is graphed in Figure 5.17. The agreement between calculated and experimental values of H_L for pure propane is much less satisfactory, with H_L significantly being under-predicted, and the lift-off velocity $V_{lift-off}$ is 2 m/s higher than the experimental value, $V_0 = 11$ m/s. The reason for these results is not known, although it might be attributed to the increased buoyancy effect in the flame of pure fuel compared to diluted fuels. It was decided to obtain reacting flow results for H_L, which are shown in Chapter 6.
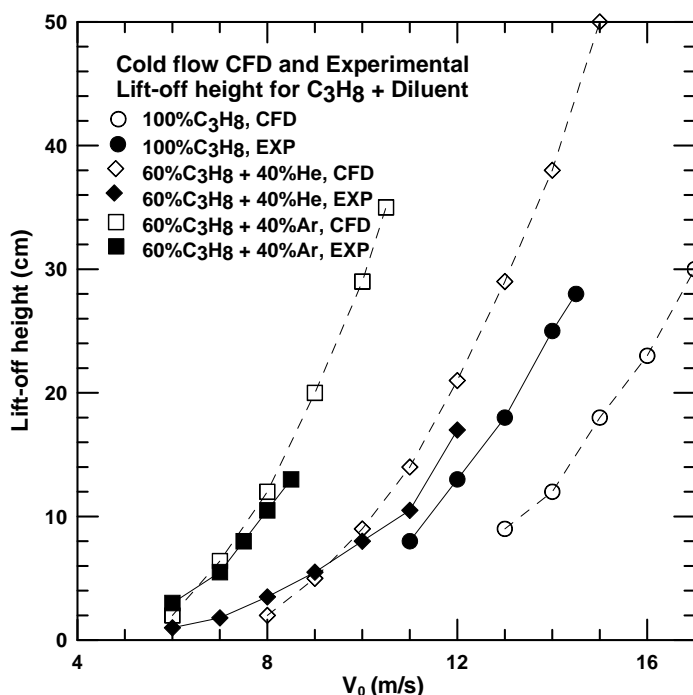
Figure 5.17 – Calculated cold flow and experimental flame lift off height (H_L) as a function of V_0 for C_3H_8 and 60%C_3H_8-40%Ar/He mixture.

CHAPTER 6: REACTING FLOW

This chapter reports and discusses the reacting flow CFD simulation results for the pure C_3H_8, 40%Ar diluted C_3H_8, 40%He diluted C_3H_8, and 40%He diluted CH_4 flames; analyzes their lift-off height, flame length, flame width and stretch rate; and analyzes the effect of the stretch rate on the propagation speed of the tribrachial flame base.

6.1 Pure C_3H_8 flame

Reacting flows of pure C_3H_8 at 4 different jet velocities (10, 12, 14 and 15m/s) were simulated using the propane-air total reaction mechanism, described in Chapter 3. The full and enlarged views of contours of concentration, axial velocity, temperature, and reaction rate are shown in Figure 6.1(a-d). The tribrachial structure of Arrhenius reaction rate contour verified the tribrachial flame structure introduced in Chapter 1: a lean premixed flame in the outside, a diffusion flame in the stoichiometric line and a rich premixed flame in the inside, all extending from a single location. The value of lift-off height (H_L) is the foremost location where the reaction rate exceeds 0.02 kmol/m^{3}s; the value of flame length (L_F) is equal to the distance between the top of the diffusion flame and the base of the flame; the flame width (W_F) is equal to the maximum radius of the lean premixed flame. All these data for every jet velocity are statistically listed in Table 6.1.

For each jet velocity, the flame stretch rate along a variety of isotherms (310K, 350K, 500K, 1000K, 1500K and 2000K) are interpolated. To calculate the flame stretch, 5 points were selected along the isotherms around the stoichiometric point (the intersection of the stoichiometric line and the isotherm). The stretch rate is equal to the slope of the V_t (tangential velocity over the isotherm, or written as V_η in the curvilinear orthogonal system in Figure 6.2) versus curve distance from the first point, P1. This detail will be introduced in the following

paragraph. Figure A.1 to Figure A.4 (in the Appendix) show the intersections of the streamlines and these isotherms for each jet velocity.
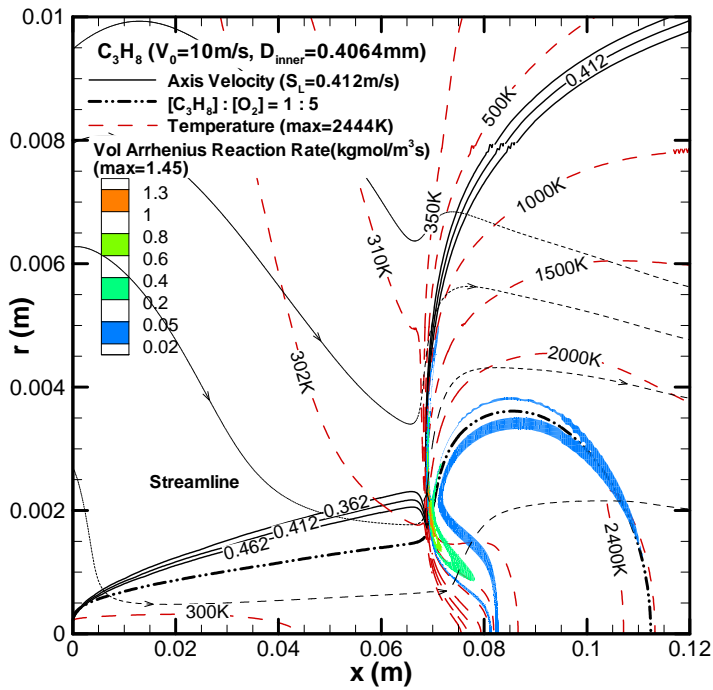
(a1) full view of $V_0 =10$ m/s
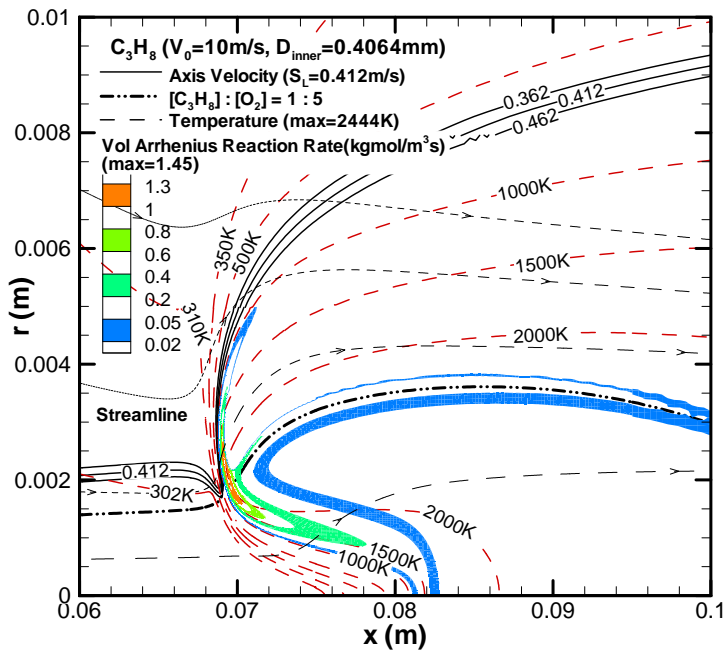
(a2) enlarged view of $V_0 =10$ m/s

Figure 6.1(a, b, c, d) – Full size and enlarged views of contours of axial velocity, stoichiometric line, temperature and reaction rate for pure C_3H_8 at 4 different jet velocities (10, 12, 14 and 15 m/s).
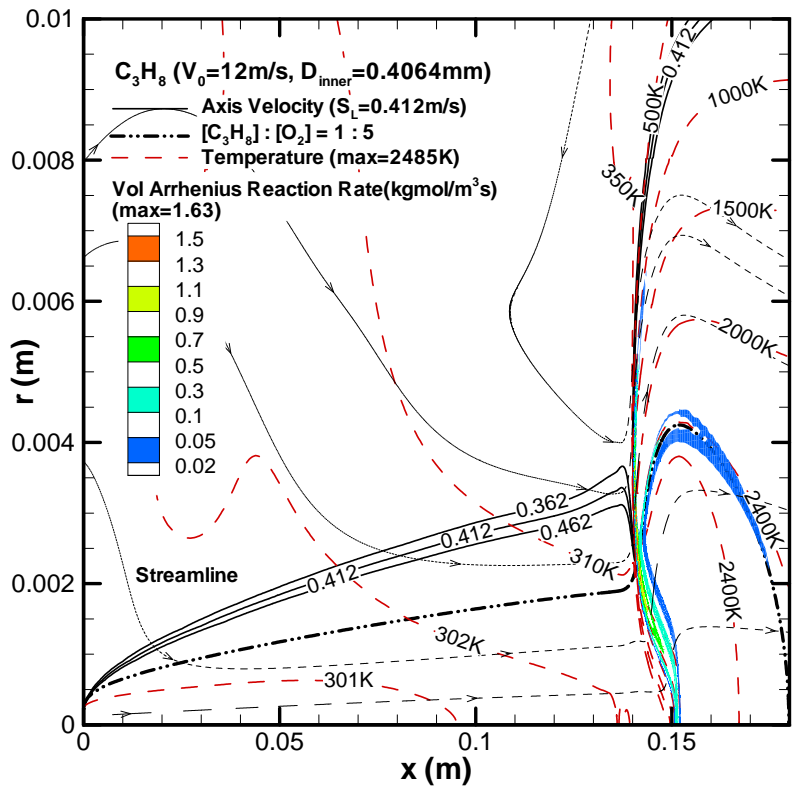
(b1) full view of V_0 =12 m/s
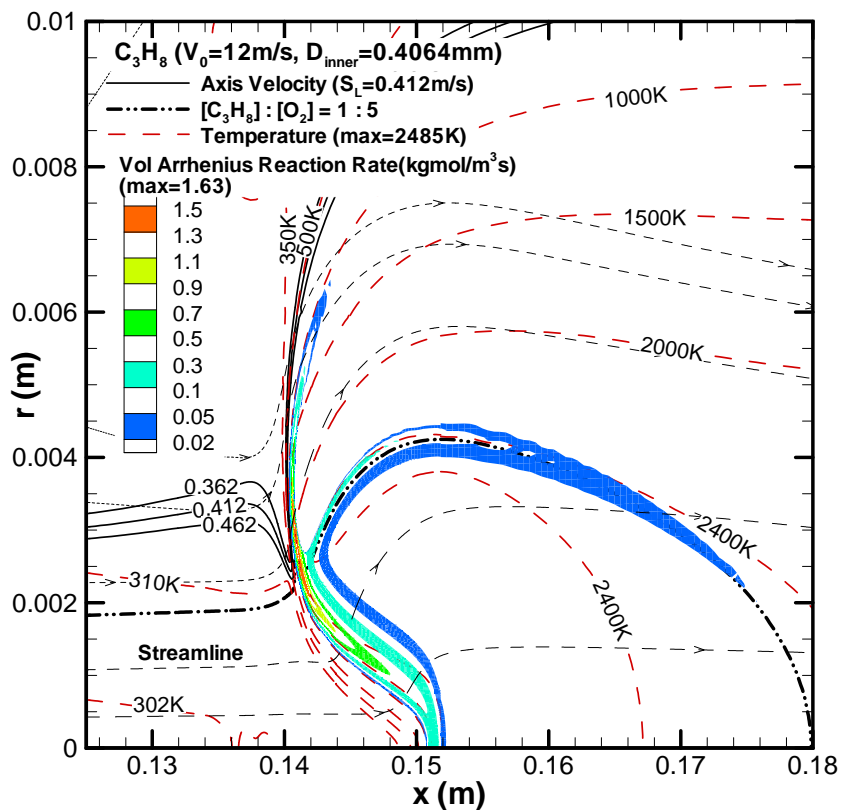
(b2) enlarged view of V_0 =12 m/s

Figure 6.1(a, b, c, d) – (continued)
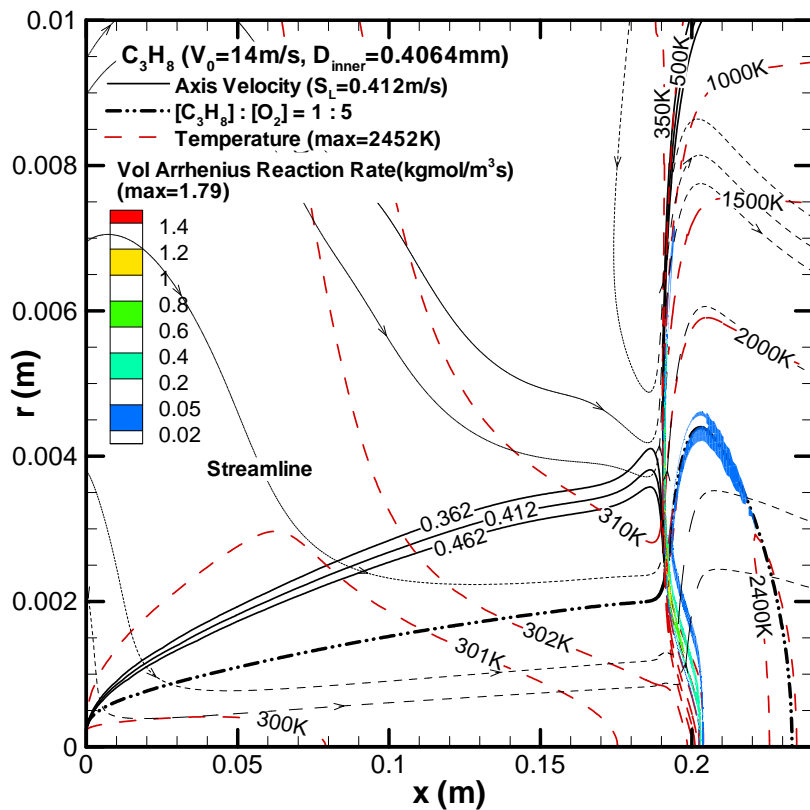
(c1) full view of $V_0 = 14$ m/s
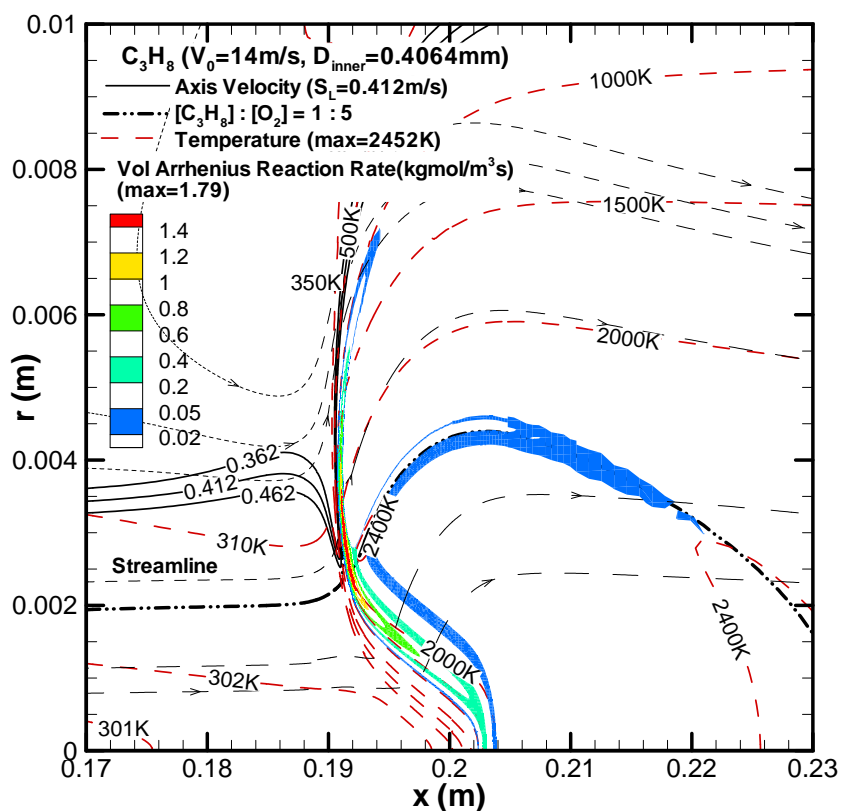
(c2) enlarged view of $V_0 = 14$ m/s

Figure 6.1(a, b, c, d) – (continued)
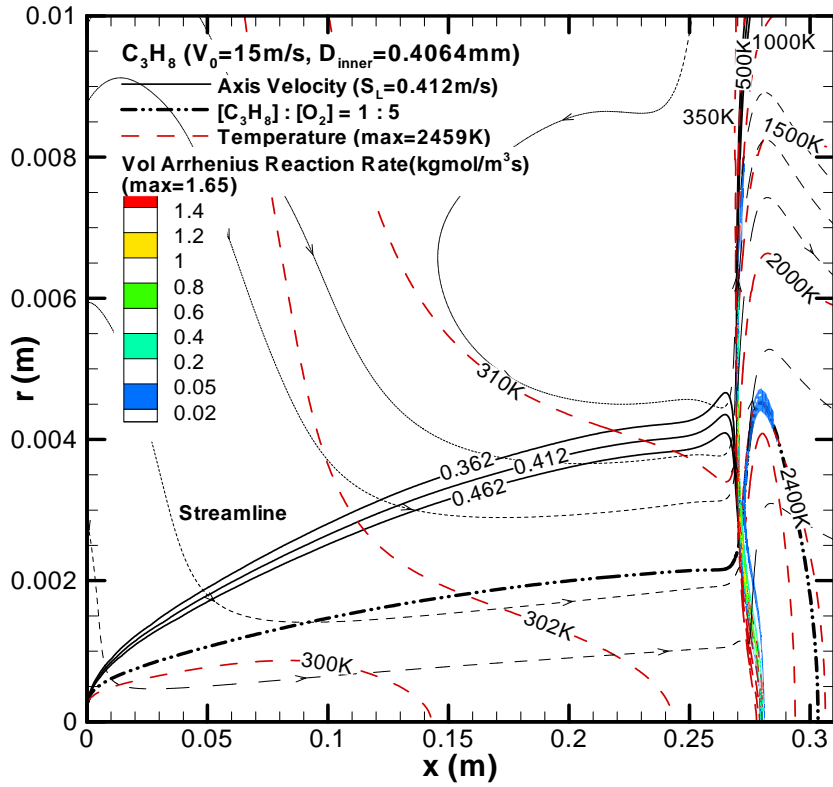
(d1) full view of $V_0 = 15$ m/s
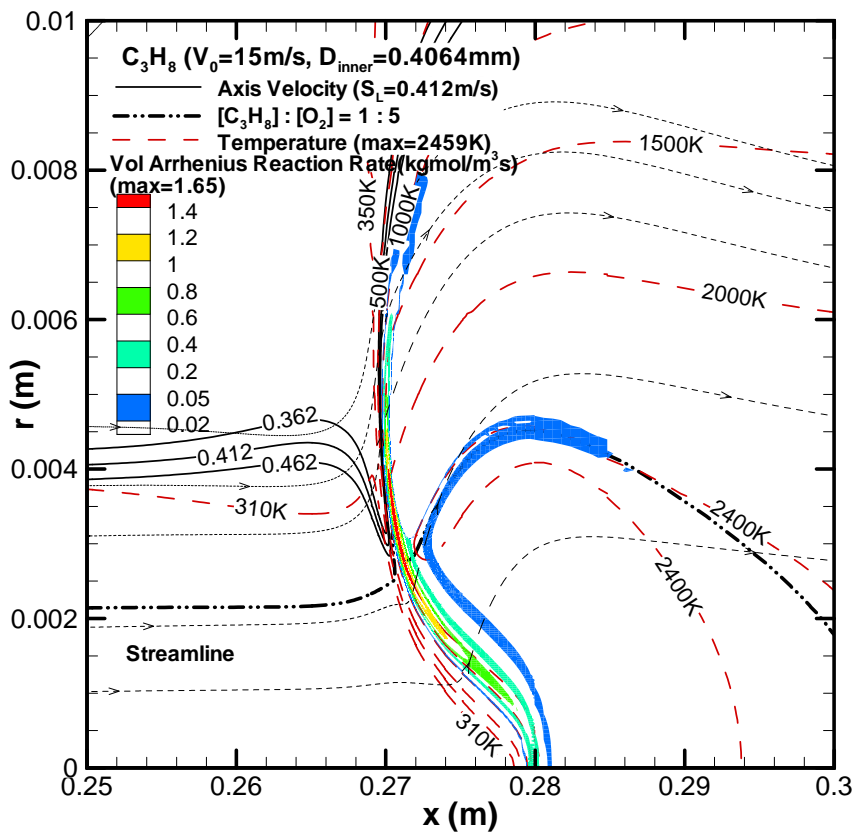
(d2) enlarged view of $V_0 = 15$ m/s

Figure 6.1(a, b, c, d) – (continued)

According to Chung and Law, the flame stretch rate (k) is given as [29]

$$k = \frac{1}{A}\frac{dA}{dt} = \nabla_t \cdot v_t + (v_{flame} \cdot n)(\nabla \cdot n),$$

where ∇_t and v_t are the tangential gradient operator and tangential velocity over the flame surface, respectively, v_{flame} is flame displacement velocity, and n is the normal unit vector of the flame surface. For our static flames, v_{flame} is zero, so the second term in the RHS of the equation is to be neglected, then the stretch rate can be represented by $k = \nabla_t \cdot v_t = (dv_\eta / d\eta)$, and $dv_\eta / d\eta$ can be estimated from the tangential velocity gradient along the flame surface in Figure 6.2. The flame stretch rates can be calculated by linear fit for the slope of the tangential velocity on the orthogonal coordinate of v_η vs η.
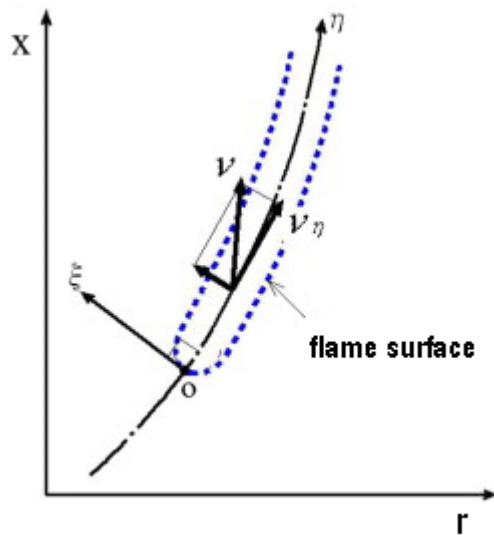
Figure 6.2 – A curvilinear orthogonal system of coordinates along the flame surface. [30]

In Figure A.1(a1), the isotherms are approximately parallel to the flame base. Five points, marked as P1 - P5, are selected along the T =310 K isotherm and the third point is located in the intersection of the stoichiometric line and the isotherm. The curve distance (η) from the first point P1 and the magnitude of velocity (V_m) at each point are recorded, the angle θ between the direction of the velocity (streamline) and the T = 310K isotherm is measured by

the protractor. The tangential velocity ($V_t = v_\eta$) at each point is equal to $V_m cos(\theta)$ at that point. Then V_t vs distance (η) for each point are plotted in Figure A.1(a2): the slope can be calculated by linearly fitting, which is equal to 628.4 /s in Figure A.1(a2). The same method is used for the other isotherms and jet velocities (Figure A.1 to Figure A.4). The results of flame length (L_F), flame width (W_F), lift-off height (H_L), stretch rate (k), perpendicular velocity over the isotherm (V_P), axial velocity (V_X), C_3H_8 mass fraction (Y_{c3h8}) and volumetric Arrhenius reaction rate (RR, unit: $kgmol/m^3s$) for a variety of isotherms at each specific jet velocity are tabulated in Table 6.1.

Table 6.1 shows the reacting flow prediction of H_L demonstrated a better agreement with the experimental data than the cold flow results (Figure 5.17). The reacting flow flame begins to lift off at $V_{lift-off}$ = 10m/s, which is only 1m/s lower than the experimental $V_{lift-off}$ =11 m/s (lift-off speed), while the cold flow simulation in Chapter 5 predicted a higher $V_{lift-off}$ = 13 m/s and smaller H_L than the experimental data at each specific V_0 value (Figure 5.17). L_F and W_F are also accessible for the reacting simulation, the predicted L_F matches well with the experimental data from V_0 = 11m/s to 14m/s. W_F increases linearly while V_0 increases; this phenomenon is qualitatively verified from the experimental observation. However, the experimental flame width wasn't recorded because the flame base oscillation from the disturbance in the room environment made it difficult to determine the flame base width. This tendency can be explained: as V_0 increases, H_L increases, the fuel and air are better premixed upstream of the flame base. Thus, the diffusion flame branch becomes shorter and the lean flame branch becomes wider; it also is an indication of weakened flame stretch.

Table 6.1 - L_F (flame length), W_F (flame width), H_L (lift-off height), and k (the stretch rate), V_P (perpendicular velocity to the isotherm), V_X (axial velocity), Y_{c3h8} (C_3H_8 mass fraction) and RR (volumetric Arrhenius reaction rate, unit: kgmol/m3s) for a variety of isotherms at each specific jet velocity (V_0) for pure propane flame.

V_0	L_F (exp)	L_F cfd	W_F cfd	H_L (exp)	H_L cfd	310K	350K	500K	1000K	1500K	2000K
10 m/s	-	4.0cm	5.0mm	attach	6.8cm						
k (/s)						628.4	698.1	747.7	947.6	1280.4	1684.6
Vp (cm/s)					41.1	40.4	40.5	49.7	83.7	119.2	152.1
Vx (cm/s)						51.0	45.5	44.2	62.0	90.2	119.7
Y_{c3h8}					0.0603	0.0601	0.0594	0.0562	0.0436	0.0294	0.0139
RR						6.1×10^{-16}	1.9×10^{-13}	4.8×10^{-8}	0.020	0.65	1.32
11 m/s	3.5cm	-		8.0cm	-						
12 m/s	3.0cm	3.4cm	6.2mm	14.0cm	14.0cm						
k (/s)						271.0	580.2	619.5	818.9	998.5	1252.4
Vp (cm/s)					41.1	39.8	42.7	54.4	95.6	138.8	180.0
Vx (cm/s)						58.2	51.5	52.2	75.3	109.1	144.0
Y_{c3h8}					0.0603	0.0602	0.0595	0.0564	0.0443	0.0304	0.0152
RR						6.0×10^{-16}	2.0×10^{-13}	6.0×10^{-8}	0.020	0.68	1.49
13 m/s	2.0cm	-		18.0cm	-						
14 m/s	1.2cm	2.0cm	7.1mm	25.0cm	19.1cm						
k (/s)						547.2	604.5	671.5	767.7	923.9	1192.6
Vp (cm/s)					41.1	46.8	47.5	59.5	104.4	152.8	199.5
Vx (cm/s)						59.1	54.5	55.1	81.1	120.7	162.3
Y_{c3h8}					0.0603	0.0602	0.0596	0.0567	0.0449	0.0315	0.0166
RR						6.2×10^{-16}	2.4×10^{-13}	1.1×10^{-7}	0.024	0.73	1.74
14.5 m/s	0.5cm	-		28.0cm	-						
15 m/s	-	1.2cm	8.0mm	blow	27.0cm						
k (/s)						383.0	438.6	497.9	570.9	659.1	742.5
Vp (cm/s)					41.1	42.6	42.9	56.3	101.1	148.8	193.8
Vx(cm/s)						61.1	58.1	58.0	81.5	118.8	155.9
Y_{c3h8}					0.0603	0.0602	0.0596	0.0565	0.0445	0.0307	0.0156
RR						5.9×10^{-16}	2.2×10^{-13}	7.7×10^{-8}	0.024	0.70	1.54

Values of k and V_P along the stoichiometric line at each isotherm are listed in Table 6.1. For each flame, k and V_P increase monotonously with the isotherm temperature for each V_0 illustrated in Table 6.1. Along the stoichiometric line ($[C_3H_8]:[O_2] = 1:5$), in the intersection with the 1000K isotherm, Y_{c3h8} is approximately only 75% of Y_{ST} ($Y_{ST} = 0.0603$ for stoichiometric premixed C_3H_8 /air); in the intersection with the 1500K isotherm, Y_{c3h8} (C_3H_8 mass fraction) is approximately 50% of Y_{ST} ; in the intersection with the 2000K isotherm, Y_{c3h8} is approximately 25% of Y_{ST}. However, RR (volumetric Arrhenius reaction rate, unit: kgmol/m^{3}s) increases from 0.020 at the 1000K isotherm intersection to 1.32 at the 2000K isotherm intersection (RR data are taken from the V_0 = 10 m/s flame in Table 6.1).

The flame base is defined along the stoichiometric contour where RR = 0.02 kgmol/m^{3}s. From the contours at Figure 6.1 and the data at Table 6.1, the RR = 0.02 kgmol/m^{3}s contour approximately coincides with the T = 1000K isotherm at the flame base. To the upstream of the 1000K isotherm, the reaction rate is negligible; thus we define the bottom of this RR = 0.02 kgmol/m^{3}s contour or 1000K isotherm as the boundary of the reacting zone and the pre-heating zone.

Table 6.2 - For one-dimensional stoichiometric C_3H_8 / Air pre-mixed flame, C3 full mechanism, CHEMKIN calculation results

T (K)	298.15	310	350	500	1000	1500	1673	2000	2275(max)
V (cm/s)	41.1	43.0	48.8	70.4	145.0	224.0	250.8	295.5	330.4
H_{DOT}(J/s/cc)	2.0 x10^{-11}	4.0 x10^{-3}	1.3 x10^{-1}	4.2	5.0 x10^2	4.6 x10^3	6.07x10^3 (max)	2.6x10^2	1.9 x10^{-2}

H_{DOT}: heat generation rate.

RR is corresponding to H_{DOT} (heat generation rate) in the 1-dimensional C3 full mechanism simulation result in Table 6.2. For the full mechanism, the heat generation rate generally represents the sum of the reacting rates of all these reactions. The maximum product

temperature of the C3 full mechanism is 2275 K, which is about 190 K below the maximum temperature points (2444 K – 2485 K) of the 2-dimentional one-step total reaction simulations (Figure 6.1(a-d)). The predicted temperature in the maximum H_{DOT} (6.07 x10^3 J/s/cc) position (Table 6.2) is 1673 K, while the interpolated temperature of the maximum RR position (Figure A.1(f1), Figure A.2(f1), Figure A.3(f1) and Figure A.4(f1)) along the stoichiometric line ([C_3H_8]:[O_2] = 1:5) is 1850 K. This indicates our one-step total reaction simplified simulation over-predicted about 10% (190 K / (2275 K – 298.15 K) ≈ 10%) of the heat release effect.

Along each isotherm (T = 1000 K, 1500 K and 2000 K), k decreases monotonously when V_0 increases from 10m/s to 15m/s. The same tendency is also observed in the He/Ar diluted C_3H_8 flames in the following sections (Table 6.3 and Table 6.5) when V_0 increases from the lift-off velocity to the blow-off velocity. There should be a critical k for each fuel composition prior to its blow-off. For the 1000 K isotherm, k decreases monotonously from 947.6 /s at V_0 = 10 m/s, 818.9 /s at V_0 = 12 m/s, 767.7 /s at V_0 = 14 m/s to 570.9 /s at V_0 = 15 m/s. On the other hand, V_P increases from 83.7 cm/s at V_0 = 10m/s to 101.1 cm/s at V_0 = 15m/s, which are between 2 and 2.5 times of the stoichiometric laminar flame velocity at 298.15 K (41.1 cm/s, Table 6.2), or 0.58 to 0.70 times of the stoichiometric laminar flame velocity at 1000K (145.0 cm/s, Table 6.2).

For the 1500K isotherm, k decreases monotonously from 1280.4 /s at V_0 = 10 m/s, 998.5 /s at V_0 = 12 m/s, 923.9 /s at V_0 = 14 m/s to 659.1 /s at V_0 = 15 m/s; the value of V_P increases from 119.2 cm/s at V_0 = 10m/s to 148.8 cm/s at V_0 = 15m/s, which are between 2.9 and 3.5 times of the stoichiometric laminar flame velocity 41.1 cm/s, or 0.53 to 0.66 times of the stoichiometric laminar flame velocity 224 cm/s at 1500 K (Table 6.2).

So it can be said that as V_0 increases, k decreases and V_P increases at the flame base. This is consistent with results of Chung [6] and Ju [18], in that the flame base moves downstream to find a new stabilization location as V_0 increases.

The typical simulated reacting flow fields for H_L determination (containing iso-velocity contour, streamlines, isotherms, and the stoichiometric concentration contour) are shown in Figure 6.1b and 6.1d for pure C_3H_8, V_0 = 12 m/s and 15 m/s, respectively. Their cold flow results are shown in Figure 5.1g and Figure 5.1j, respectively. For the V_0 = 12 m/s flow, in Figure 5.1g, the stoichiometric line is located outside of the stoichiometric laminar flame velocity contour; the attached flame is predicted in the cold flow simulation. In Figure 6.1(b1), the stoichiometric laminar flame velocity contour ($u = S_L^o$ = 0.412 m/s) lies outside of the stoichiometric line ($[C_3H_8]$: $[O_2]$ = 1:5) in the region between the flame base and jet lip quenching distance ($x \approx 0.002$ m); the reacting flow predicted H_L = 14.0 cm coincides with the experimental results. Figure 6.1(b2) shows the $u = S_L^o$ contour sharply bends toward the jet centerline immediately below the flame base, then bends outward due to the heat expansion acceleration; the stoichiometric line ($[C_3H_8]$: $[O_2]$ = 1:5) also bends outward ahead of the flame base to intersect the velocity contour. However, the 1 mm X 1 mm enlarged Figure A.2(b1) indicates that the $u = S_L^o$ contour doesn't intersect with the stoichiometric line even though they are very close.

For the V_0 = 15 m/s flow, Figure 5.1j indicates an intersection of the stoichiometric line ($[C_3H_8]$: $[O_2]$ = 1:5) and the $u = S_L^o$ at x = 0.18 m. The $u = S_L^o$ contour lies outside of the stoichiometric line below that intersection; a lift-off height of H_L = 0.18 m is predicted by the cold flow simulation, while H_L = 0.25 m for V_0 = 14.5 m/s and blow off for V_0 = 15 m/s (Table 6.1) are observed in the experiment. Figure 6.1(d1) shows the stoichiometric line lies inside of the $u = S_L^o$ contour between the jet lip quenching distance ($x \approx 0.002$ m) and the

flame base $x = 0.27$ m. Similar to that in Figure 6.1(b2), the $u = S_L^o$ contour and the stoichiometric line immediately bend to each other ahead of the flame base. The 1 mm X 1 mm enlarged Figure A.4(b1) also shows that the $u = S_L^o$ contour doesn't intersect with the stoichiometric line even though they are very close to each other, and the streamlines also show a strong flow re-direction ahead of the flame base. The reacting flow result predicts a relatively more accurate lift off height ($H_L = 0.27$ m) by comparing it with the cold flow result and experiment value.

Taking into account the buoyancy force and gas expansion (i.e., flow re-direction) due to the heat release effect, reacting flow simulations are more consistent with the experiment reality by comparison to the cold flow results in Chapter 5. However, the previous theory of intersection of stoichiometric line and stoichiometric laminar flame velocity contour in the analytical criterion and cold flow simulation can no longer be applied to the reacting flow due to the heat acceleration and re-direction of the flow below the flame base. This will also be verified in the 40%Ar/He diluted propane reacting flow.

6.2 60%C$_3$H$_8$ + 40%Ar flame

Reacting flows of 40%Ar diluted C$_3$H$_8$ with at 3 different V_0 (6 m/s, 7 m/s and 8 m/s) are calculated using the propane-air total reaction mechanism, described in Chapter 3. The full size and enlarged view contours of concentration, axial velocity, temperature, and reaction rate are shown in Figure 6.3(a - c). For each V_0, the flame stretch rate along a variety of isotherms (302K/310K, 350K, 500K, 1000K, 1500K and 2000K) are interpolated with the same method in Section 6.1. Figure A.5(a - f) to Figure A.7(a - f) show the isotherm interpolations for each jet velocity. Flame length (L_F), flame width (W_F), lift-off height (H_L), stretch rate (k), perpendicular velocity to the isotherm (V_P), axial velocity (V_X), C$_3$H$_8$ mass fraction and volumetric Arrhenius reaction rate (RR) for a variety of isotherms at each specific jet velocity are concluded in Table 6.3. The 1-dimensional, C3 full mechanism simulated results for the velocity and heat generation rate corresponding to each specific temperature value are also listed in Table 6.4. Their values will be compared with these parameters located in the stoichiometric line in the 2-dimensional simulation results.

A typical simulated reacting flow field for H_L determination (containing iso-velocity contour, streamlines, isotherms, and the stoichiometric concentration contour) are shown in Figure 6.3b for 40%Ar diluted C$_3$H$_8$ with V_0 = 7 m/s. The cold flow result is shown in Figure 5.5a. Figure 5.5a indicates an intersection of the stoichiometric line ([C$_3$H$_8$]: [O$_2$] = 1:5) and the $u = S_L^o$ at x = 0.065 m. The $u = S_L^o$ contour lies outside of the stoichiometric line below that intersection, thus a lift-off height of H_L = 0.065 m is predicted by the cold flow simulation, while H_L = 0.055 m for V_0 = 7 m/s (Table 6.3) are observed in the experiment. Figure 6.3(b1) shows the stoichiometric line lies inside of the $u = S_L^o$ contour between the jet lip quenching distance ($x \approx$ 0.002 m) and the flame base (x = 0.058 m). Similar to that in

Figure 6.1(b2), the $u = S_L^o$ contour and the stoichiometric line immediately bend to each other

ahead of the flame base. The 1 mm X 1 mm enlarged Figure A.6(b1) shows that the $u = S_L^o$

contour doesn't intersect with the stoichiometric line even though they are very close to each

other. The reacting flow prediction (H_L = 0.058 m) is closer to the experiment data (H_L =

0.055 m) compared with the cold flow result (H_L = 0.065 m). This phenomenon verified the

conclusion in the previous section.
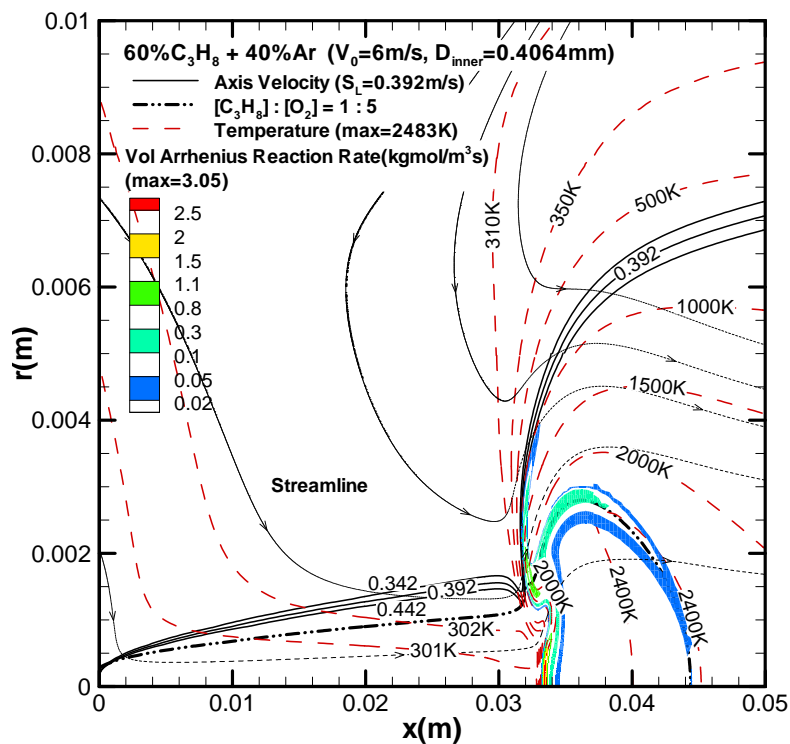
(a1) full view of V_0 = 6 m/s
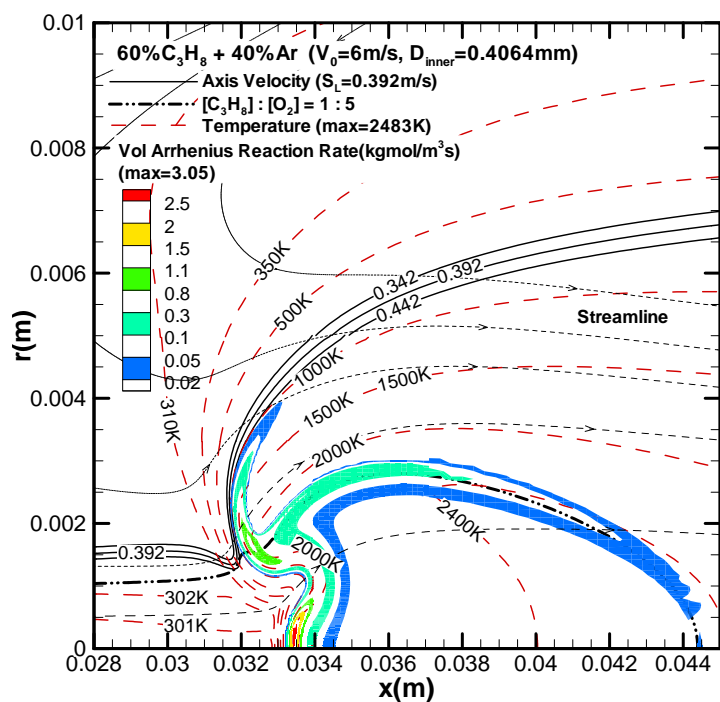
(a2) enlarged view of V_0 = 6 m/s

Figure 6.3(a, b, c) – Full size and enlarged view of contours of axial velocity, stoichiometric line, temperature and reaction rate for 60% C_3H_8 with 40% Ar dilution at 3 different jet velocities (6 m/s, 7 m/s and 8 m/s).
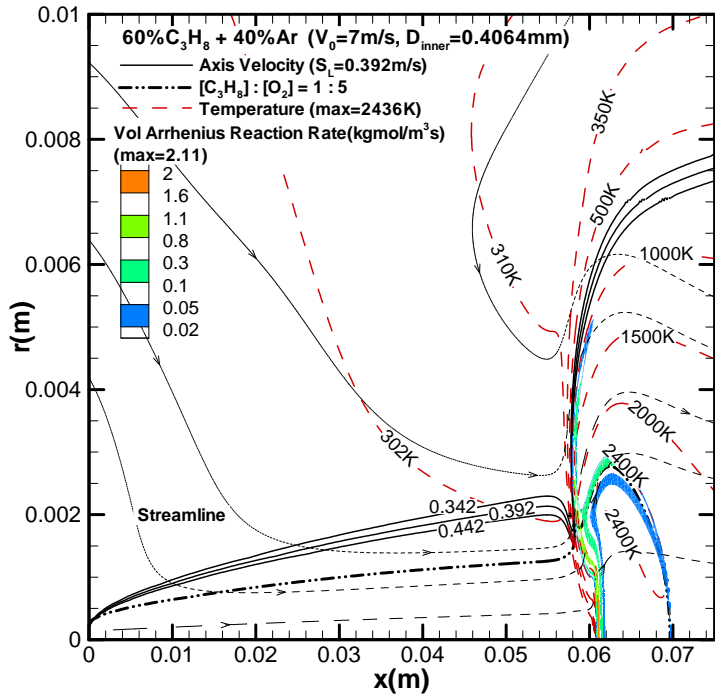
(b1) full view of $V_0 = 7$ m/s
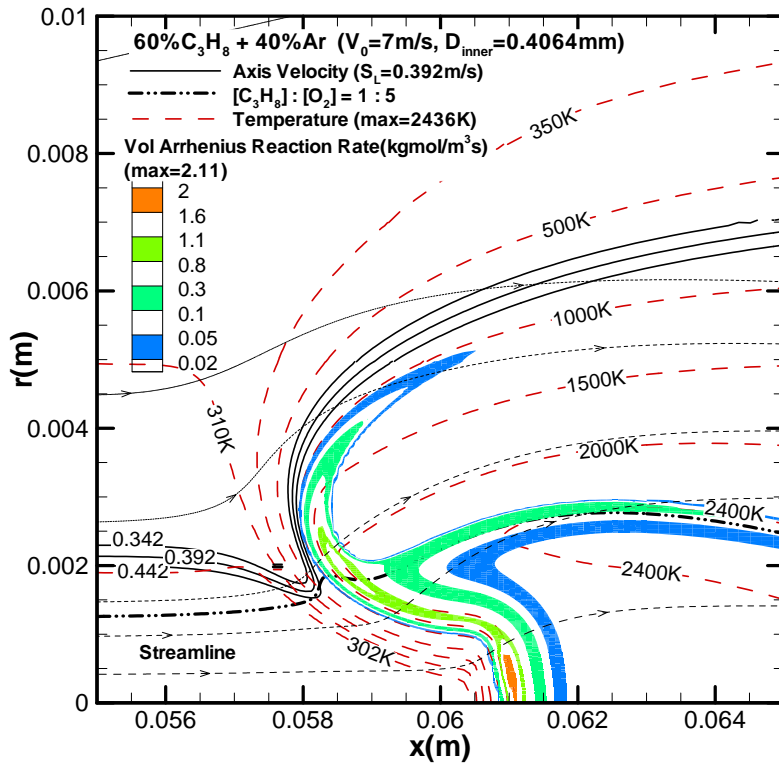
(b2) enlarged view of $V_0 = 7$ m/s

Figure 6.3(a, b, c) – (continued)
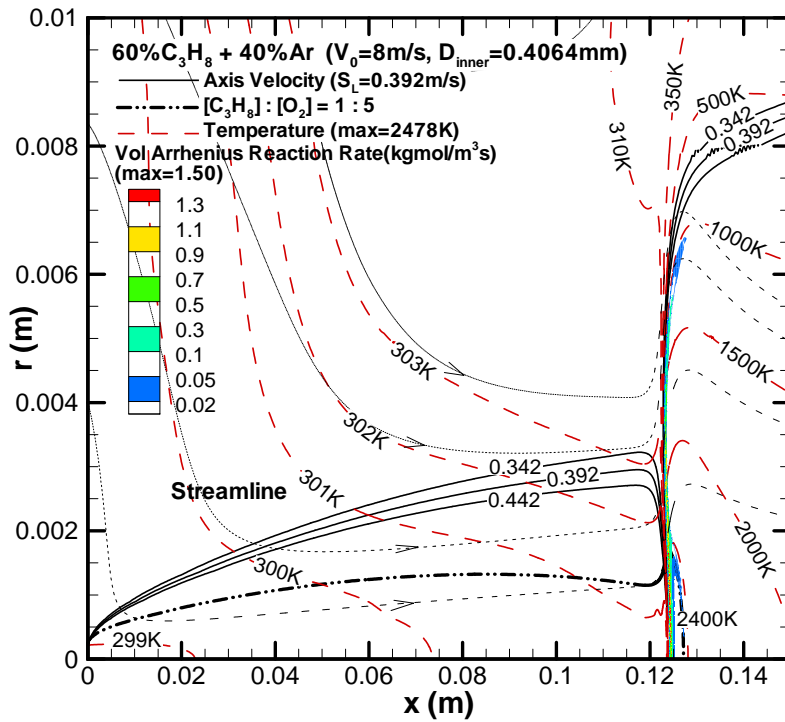
(c1) full view of $V_0 = 8$ m/s
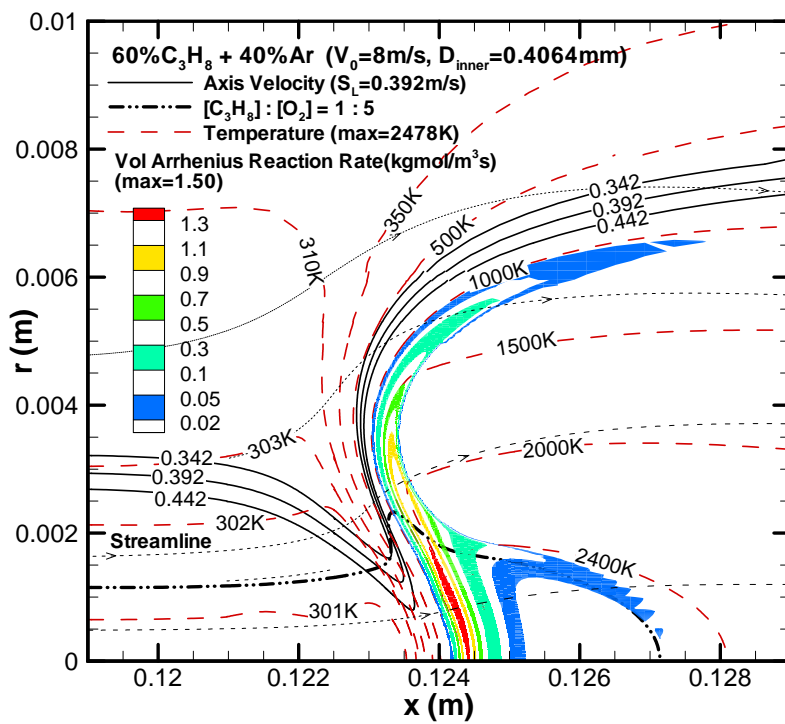
(c2) enlarged view of $V_0 = 8$ m/s

Figure 6.3(a, b, c) – (continued)

Table 6.3 - L_F (flame length), W_F (flame width), H_L (lift-off height), and k (the stretch rate), V_P (perpendicular velocity to the isotherm), V_X (axial velocity), Y_{c3h8} (C_3H_8 mass fraction) and RR (volumetric Arrhenius reaction rate, unit: kgmol/m^{3}s) for a variety of isotherms at each specific jet velocity for 40%Ar diluted propane flame.

V_0	L_F EXP	L_F CFD	W_F CFD	H_L EXP	H_L CFD	302K	310K	350K	500K	1000K	1500K	2000K
6 m/s	1.2cm	1.2cm	4.0mm	3.0cm	3.2cm							
k (/s)						-	555.8	636.0	701.1	922.7	1240.1	2236.8
Vp(cm/s)					39.2		38.0	38.3	45.7	73.1	101.9	126.0
Vx(cm/s)							51.1	44.2	41.6	54.1	75.1	94.0
Y_{c3h8}					0.0582		0.0578	0.0568	0.0537	0.0413	0.0273	0.0122
RR							7.1 x10^{-16}	3.5 x10^{-12}	6.2 x10^{-7}	0.033	0.58	1.03
7 m/s	1.1cm	1.15cm	5.1mm	5.5cm	5.8cm							
k (/s)						305.5	-	508.6	576.4	744.0	911.4	1199.8
Vp(cm/s)					39.2	41.6		40.4	49.7	82.6	117.8	152.7
Vx(cm/s)						54.2		43.6	42.6	61.1	88.3	116.8
Y_{c3h8}					0.0582	0.0582		0.0576	0.0540	0.0418	0.0284	0.0131
RR						1.7 x10^{-16}		2.0 x10^{-12}	3.8 x10^{-6}	0.043	0.60	1.13
8 m/s	0.5cm	0.4cm	6.5mm	10.5cm	12.3cm							
k (/s)						69.4	-	119.6	224.9	302.8	333.5	289.2
Vp(cm/s)					39.2	41.1		40.0	49.8	86.1	128.9	175.6
Vx(cm/s)						39.0		34.1	39.7	70.0	110.4	156.8
Y_{c3h8}					0.0582	0.0587		0.0578	0.0546	0.0420	0.0279	0.0137
RR						1.7 x10^{-16}		2.3 x10^{-13}	5.6 x10^{-8}	0.018	0.61	1.23

Table 6.3 indicates that these predicted values of H_L and L_F for the 40%Ar diluted propane reacting flow are essentially identical with the experimental values for all three jet velocities ($V_0 = 6$ m/s, 7 m/s and 8 m/s). The accuracy in the prediction of H_L and L_F for 40%Ar diluted propane flame seems to be much better than that for the pure propane (Table 6.1) and 40%He diluted propane (Table 6.5 in the following section). It is assumed that experimental disturbance for the 40%Ar diluted propane flame are relatively smaller than the other flames because these lift off velocities (6 m/s – 8 m/s) and the lift off heights (0.03 m – 0.11 m) are relatively low, so the distortion from the constant pressure condition assumption(1 atm, 79%N_2 + 21%O_2) in the boundary simulation domain is nearly negligible compared with the high V_0 and high H_L in pure propane simulation (Table 6.1).

Table 6.3 shows k in each isotherm monotonously decreases when V_0 increases from 6m/s to 8m/s. In the 1000K isotherm, k decreases from 922.7 /s at $V_0 = 6$ m/s, 744.0 /s at $V_0 = 7$ m/s to 302.8 /s at $V_0 = 8$ m/s; on the other hand, the value of V_P increases from 73.1 cm/s at $V_0 = 6$ m/s, 82.6 cm/s at $V_0 = 7$ m/s to 86.1 cm/s at $V_0 = 8$ m/s, which is 1.8 - 2.2 times of the stoichiometric laminar flame velocity $S_L^o = 39.2$ cm/s (Table 6.4). If further increase V_0 to 9m/s, k will continue to decrease below 300 /s, then blow-off. Thus it is assumed $k = 300$ /s is the critical stretch rate for lifted flame stabilization. Table 6.5 (in the following section) also indicates the critical stretch rate of 300 /s in the $V_0 = 12$m/s 40%He diluted propane flame base (1000K isotherm).

Table 6.4 - For 1-dimensional stoichiometric 40%Ar diluted C_3H_8 / Air pre-mixed flame, C3 full mechanism, CHEMKIN calculation results

T (K)	298.15	302	310	350	500	1000	1500	1682	2000	2258(max)
V (cm/s)	39.2	39.8	41.0	46.4	67.0	137.9	212.6	239.5	280.7	311.6
H_{DOT}(J/s/cc)	2.0×10^{-13}	2.5×10^{-4}	3.4×10^{-3}	1.1×10^{-1}	3.4	4.2×10^2	4.2×10^3	5.52×10^3 (max)	2.0×10^2	2.2×10^{-2}

H_{DOT}: heat generation rate.

The higher k in the flame base, the more stable the tribrachial flame exists. The experimental results show the $V_0 = 8$ m/s flame for 40%Ar diluted propane and $V_0 = 12$ m/s flame for 40%He diluted propane approach to their blow-off velocities. Both their CFD and experimental L_F are merely 0.4 cm to 0.6 cm, so they are vulnerable to any disturbance; it is experimentally observed that even small disturbances from the environment can blow off these flames. Simply by observing the flame shape of these two flames in Figure 6.3(c2) and 6.4(d2), their flame bases become flatter and wider compared with their lower V_0 flames; thus even small oscillation and disturbance can blow off these flames.

Table 6.1 shows the V_0 = 15m/s flame for pure propane experimentally blow off, while the reacting flow CFD simulated H_L is 27.0 cm, L_F is 1.2 cm, and k is 570.9 /s; all these values are higher than those values in the 40%Ar and 40%He diluted propane. It is assumed that the oscillation and disturbance for the V_0 = 15m/s flame at H_L = 27.0 cm position are much higher than the oscillation and disturbance for the V_0 = 8 m/s flame for 40%Ar diluted propane at H_L = 12.3 cm and the V_0 = 12 m/s flame for 40%He diluted propane at H_L = 15.2 cm. Thus the V_0 = 15 m/s pure propane flame requires a higher stability potential to resist the oscillation and disturbance, so the critical stretch rate limit is increased to 570.9 /s for the pure propane flame.

6.3 60%C_3H_8 + 40%He flame

Reacting flows of 40%He diluted C_3H_8 at 4 different V_0 (6 m/s, 8 m/s, 10 m/s and 12 m/s) are calculated using the propane-air total reaction mechanism, described in Chapter 3. The full size and enlarged view contours of concentration, axial velocity, temperature, and reaction rate are shown in Figure 6.4(a - d). For each V_0, the flame stretch rate along a variety of isotherms (310K, 350K, 500K, 1000K, 1500K and 2000K) are interpolated with the same method in Section 6.1. Figure A.8(a - f) to Figure A.11(a – f) show the isotherm interpolations for each jet velocity. Flame length (L_F), flame width (W_F), lift-off height (H_L), stretch rate (k), perpendicular velocity to the isotherm (V_P), axial velocity (V_X), C_3H_8 mass fraction and volumetric Arrhenius reaction rate (RR) for a variety of isotherms at each specific jet velocity are concluded in Table 6.5. The 1-dimensional, C3 full mechanism simulated results for the velocity and heat generation rate corresponding to each specific temperature value are also listed in Table 6.6. Their values will be compared with these parameters in the stoichiometric line in the 2-dimensional simulation results.
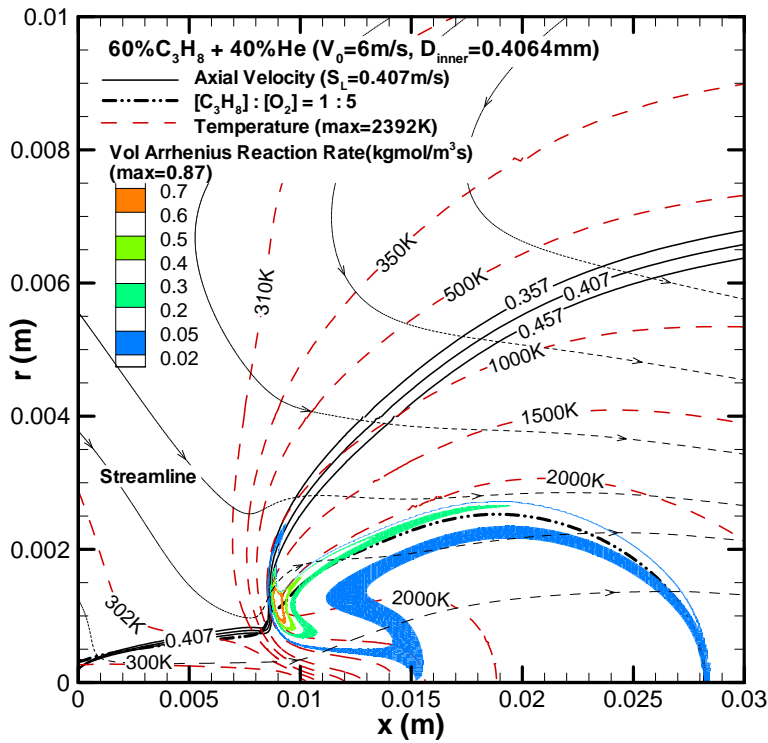
(a1) full view of V_0 = 6 m/s
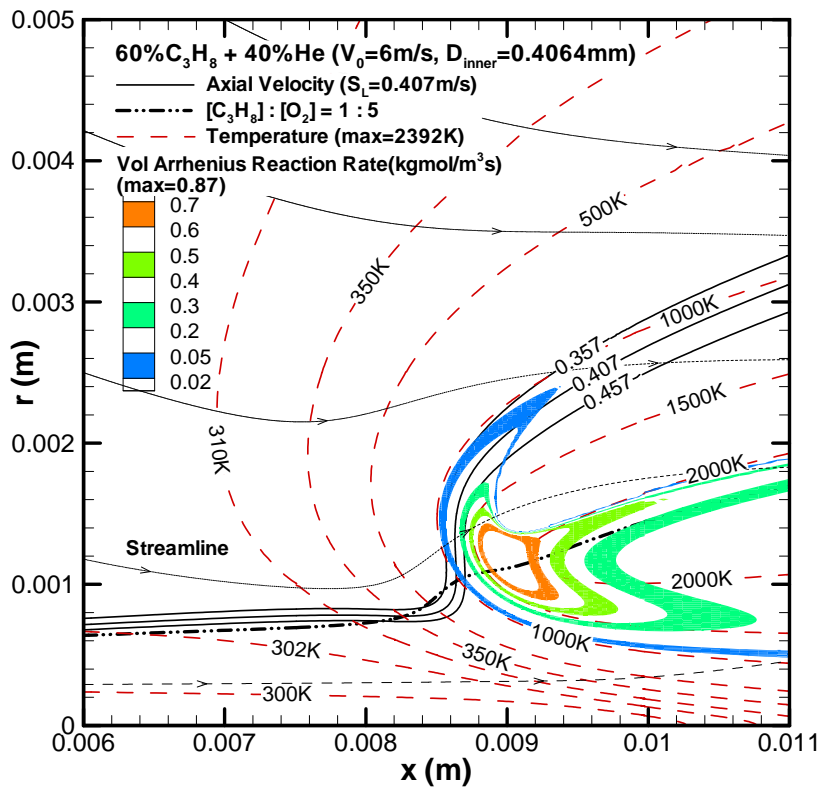
(a2) enlarged view of V_0 = 6 m/s

Figure 6.4(a - d) – Full size and enlarged view of contours of axial velocity, stoichiometric line, temperature and reaction rate for 60% C_3H_8 with 40% He dilution at 4 different jet velocities (6 m/s, 8 m/s, 10 m/s and 12 m/s).
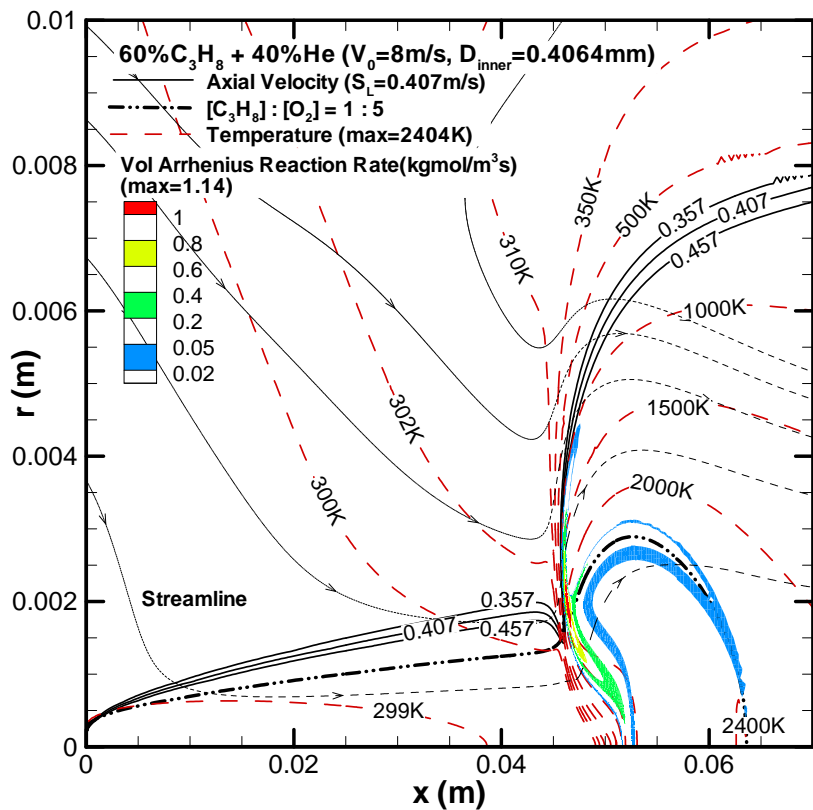
(b1) full view of V_0 = 8 m/s
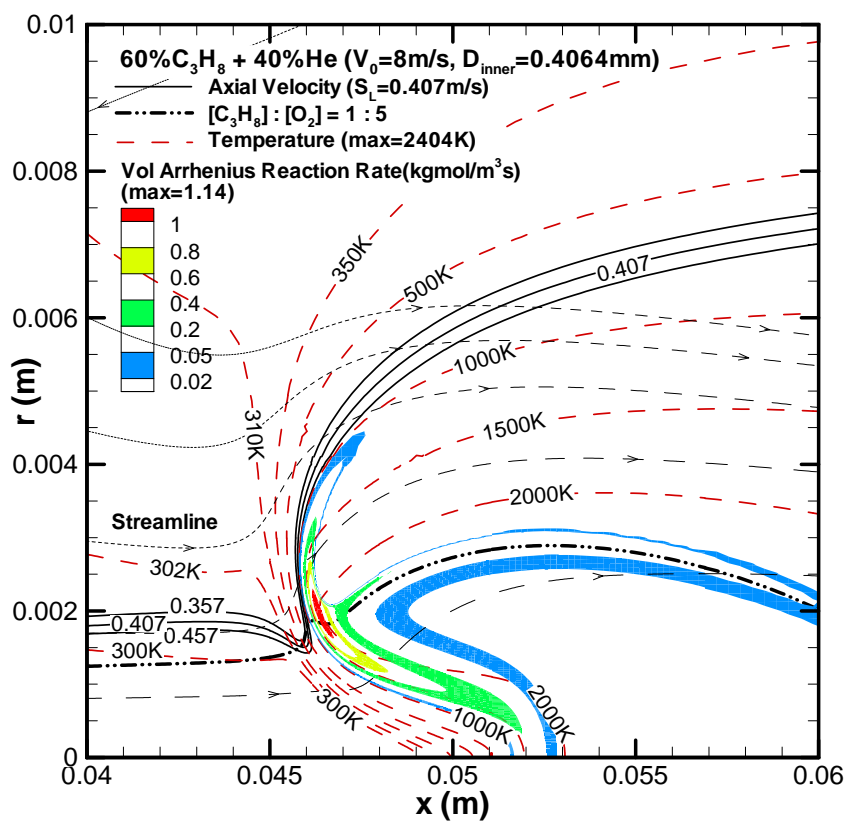
(b2) enlarged view of V_0 = 8 m/s

Figure 6.4(a - d) – (continued)
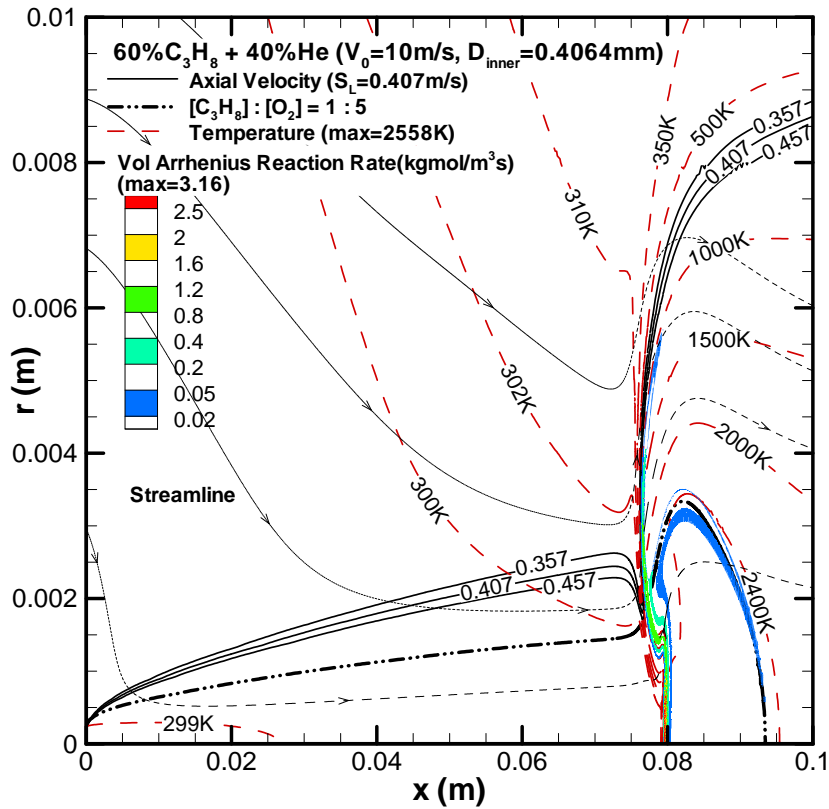
(c1) full view of V_0 = 10 m/s
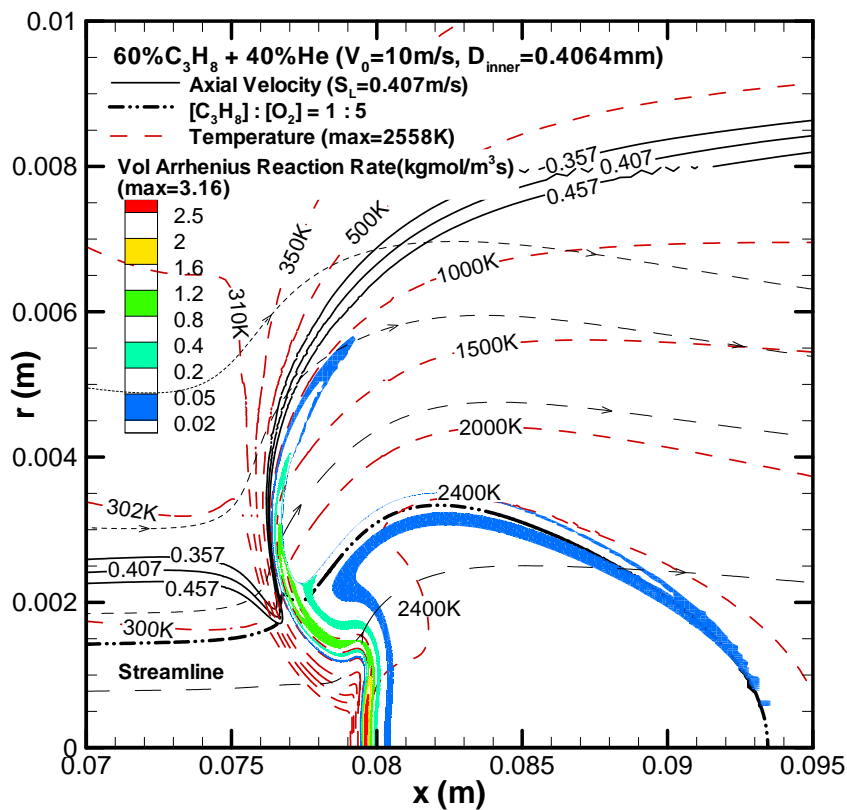
(c2) enlarged view of V_0 = 10 m/s

Figure 6.4(a - d) – (continued)
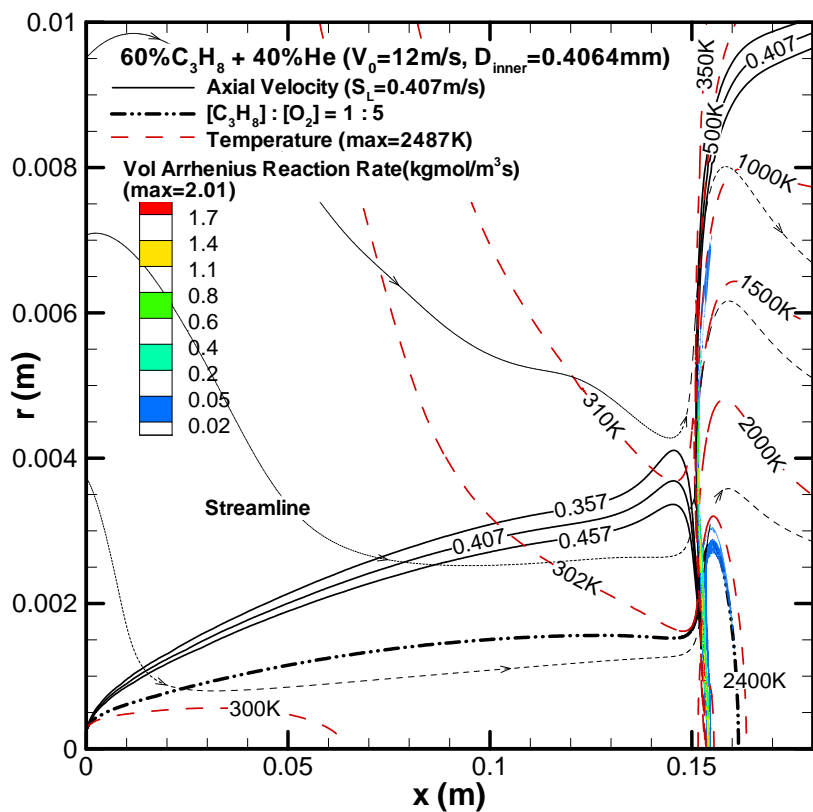
(d1) full view of V_0 = 12 m/s
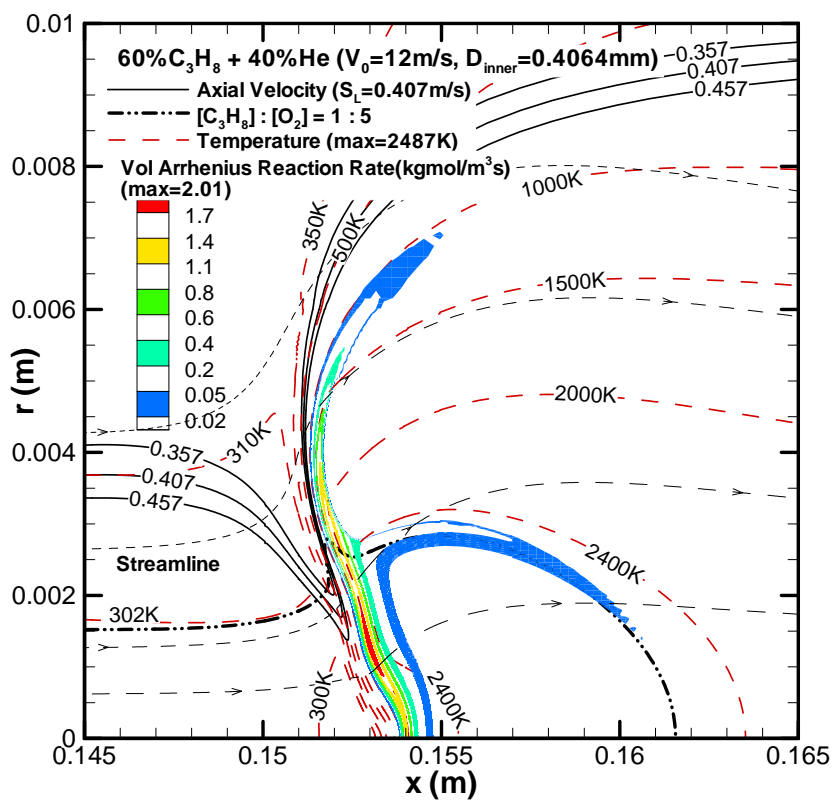
(d2) enlarged view of V_0 = 12 m/s

Figure 6.4(a - d) – (continued)

Table 6.5 - L_F (flame length), W_F (flame width), H_L (lift-off height), and k (the stretch rate), V_P (perpendicular velocity to the isotherm), V_X (axial velocity), Y_{c3h8} (C_3H_8 mass fraction) and RR (volumetric Arrhenius reaction rate, unit: kgmol/m^{3}s) for a variety of isotherms at each specific jet velocity for 40%He diluted propane flame.

V_0	F_L (exp)	F_L cfd	W_F CFD	H_L (exp)	H_L cfd	310K	350K	500K	1000K	1500K	2000K
6 m/s	1.6cm	1.7cm	2.5mm	1.0cm	0.9cm						
k (/s)						639.0	649.6	666.9	850.4	1368.3	4535.6
Vp(cm/s)					40.7	22.5	26.0	33.2	50.1	68.3	83.7
Vx(cm/s)						48.8	41.0	34.5	42.0	59.2	77.4
Y_{c3h8}					0.0601	0.0597	0.0592	0.0556	0.0420	0.0266	0.0098
RR						5.4×10^{-16}	1.2×10^{-13}	2.8×10^{-8}	0.015	0.50	0.65
8m/s	1.5cm	1.7cm	4.4mm	3.5cm	4.5cm						
k (/s)						473.1	534.1	589.0	701.2	996.0	1574.0
Vp(cm/s)						35.9	36.3	43.8	71.7	102.5	130.8
Vx(cm/s)						42.3	37.4	36.2	51.8	76.6	101.9
Y_{c3h8}						0.0600	0.0593	0.0559	0.0428	0.0280	0.0123
RR						6.6×10^{-16}	3.6×10^{-13}	5.9×10^{-8}	0.019	0.58	0.98
10m/s	1.0cm	1.3cm	5.6mm	8.0cm	7.7cm						
k (/s)						495.1	537.9	577.2	687.8	927.2	1217.8
Vp(cm/s)					40.7	39.5	39.8	49.9	85.2	122.5	158.8
Vx(cm/s)						46.3	42.5	42.5	62.4	91.6	121.5
Y_{c3h8}					0.0601	0.0601	0.0594	0.0561	0.0435	0.0294	0.0139
RR						5.9×10^{-16}	1.9×10^{-13}	5.0×10^{-8}	0.020	0.62	1.25
12m/s	0.4cm	0.6cm	7.0mm	17.0cm	15.2cm						
k (/s)						94.8	134.7	225.3	376.7	508.8	412.1
Vp(cm/s)					40.7	40.4	42.4	54.6	95.5	142.9	193.9
Vx(cm/s)						34.4	32.4	37.2	66.4	105.3	149.8
Y_{c3h8}					0.0601	0.0601	0.0594	0.0562	0.0440	0.0298	0.0152
RR						6.2×10^{-16}	2.8×10^{-13}	7.2×10^{-8}	0.021	0.67	1.46

Table 6.6 - For 1-dimensional stoichiometric 40%He diluted C_3H_8 / Air pre-mixed flame, C3 full mechanism, CHEMKIN calculation results

T (K)	298.15	310	350	500	1000	1500	1678	2000	2258(max)
V (cm/s)	40.7	42.2	47.9	69.1	142.1	219.4	246.7	289.8	321.7
H_{DOT}(J/s/cc)	4.6×10^{-16}	1.7×10^{-3}	8.4×10^{-2}	3.0	4.0×10^2	4.2×10^3	5.86×10^3	2.1×10^2	2.4×10^{-2}

H_{DOT}: heat generation rate.

Table 6.5 shows k in each isotherm monotonously decreases when V_0 increases from 6 m/s to 12 m/s. In the 1000K isotherm, k decreases from 850.4 /s at $V_0 = 6$ m/s, 701.2 /s at $V_0 = 8$ m/s to 376.7 /s at $V_0 = 12$ m/s. On the other hand, the value of V_P increases from 50.1 cm/s at $V_0 = 6$ m/s, 71.7 cm/s at $V_0 = 8$ m/s to 95.5 cm/s at $V_0 = 12$ m/s, which are 1.25 - 2.35 times of the stoichiometric laminar flame velocity 40.7 cm/s (298.15 K), or 0.5 - 0.68 times of the stoichiometric laminar flame velocity 142.1 cm/s at 1000 K isotherm; if further increase to $V_0 = 13$ m/s, k will continue to decrease below 300 /s and blow-off.

It is noticed that, generally, k increases with the isotherm temperature for each specified V_0 with specified fuel composition. However, for the 12 m/s 40%He diluted propane, and 8 m/s 40%Ar diluted propane, their k at 2000 K isotherm are below that at 1500 K isotherm. When they are approaching the blow off limit, the length of their diffusion flame branches (L_F) drop to 0.6cm (Table 6.5) and 0.4 cm (Table 6.3), their lift off heights (H_L) reach the maximum, so the flames are better premixed compared to their lower velocity flames.

Figure 6.4(a2), (b2) and (d2) shows that the $u = S_L^o = 0.407$ m/s contour intersects with the stoichiometric contour ([C_3H_8]: [O_2] = 1:5) twice immediately ahead of the flame base for the 40%He diluted propane flame at $V_0 = 6$ m/s, 8 m/s and 12 m/s. Their detailed structures can be seen in the 1 mm X 1 mm enlarged graph at Figure A.8(c1), Figure A.9(c1) and Figure A.11(b1). Between these two intersections, the $u = S_L^o$ contour lies inside of the stoichiometric contour. However, the region between these two intersections are merely 0.3 mm; below these intersections, the $u = S_L^o$ contour lies outside of the stoichiometric contour. However, for the 40%He diluted propane flame at $V_0 = 10$ m/s, the 1 mm X 1 mm enlarged Figure A.10(b1) indicates that the $u = S_L^o$ contour doesn't intersect with the stoichiometric line even though they are very close.

Based on the laminar flame velocity contour ($u = S_L^o$) and stoichiometric contour structure for the reacting flow simulations in Figure 6.1, Figure 6.3, and Figure 6.4, as discussed in

Section 6.1, Section 6.2 and the previous paragraph, the necessary condition for the flame base stabilization point (the intersection of the stoichiometric line and the laminar flame velocity), which was defined for the similarity analysis and cold flow predictions, is not strictly necessary. However, the velocity line must lie outside of the stoichiometric line, and they must tend to close up or intersect with each other in order to keep the lifted flame base from attaching to the jet exit. Other mechanisms such as the flame kernel coupled with the Damkohler number at the flame base [12 - 14] might provide alternative explanations for the predicted results. Furthermore, due to the gas expansion and acceleration, the flow speed ahead of the flame base can be greater than the 1-dimensional value of S_L^o. There have been reports that the flow speed at the flame base is in the range of $u = 1.85\, S_L^o$ - 3.0 S_L^o [5, 7, 25]. But if the 1- dimensional value of S_L^o was converted into the stoichiometric laminar flame velocity at the corresponding isotherm, the perpendicular velocity at such point turns to 0.52 to 0.70 times of the 1 – dimensional S_L^o value.

The reacting flow results for H_L are shown in Figure 6.5, comparing with the cold flow results in Figure 5.17, both for the pure propane and for the 40% He/Ar diluted propane, the agreements of the H_L are significantly improved between calculated and experimental values. These results suggest the need to properly model the effects of buoyancy due to heat-releasing reaction, even though the one-step reaction model over-predicted 10% of the heat release. It is believed that the gas expansion and buoyancy effects accounts for better prediction for the pure C_3H_8 flame. These effects will be further discussed in the next section along with the reacting flow predictions of CH_4 flames.

110
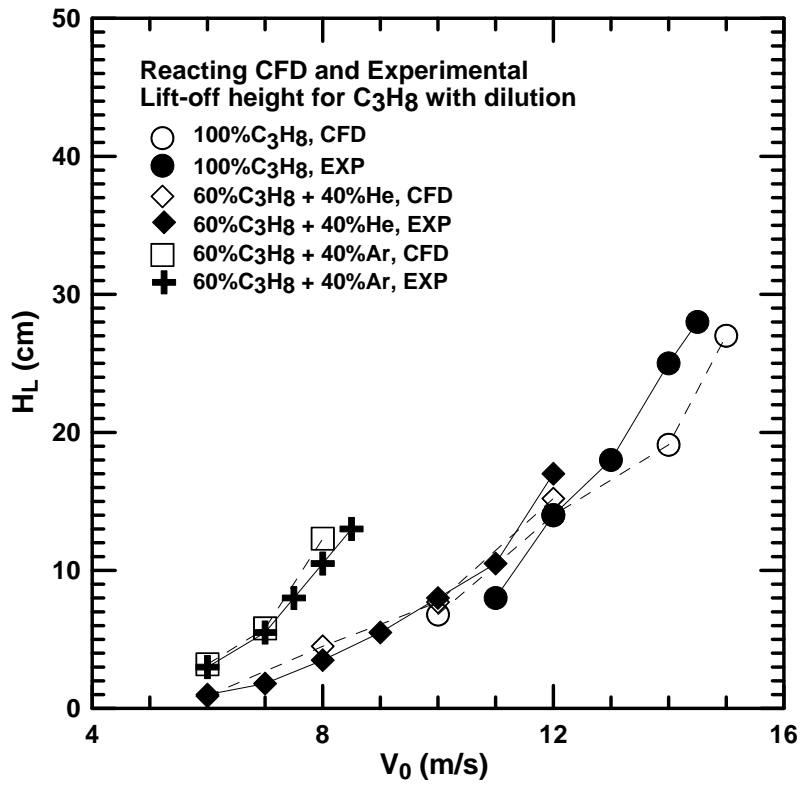
Figure 6.5 – Calculated reacting flow and experimental flame lift of height (H_L) as a function of V_0 for C_3H_8 and $60\%C_3H_8$-$40\%Ar/He$ mixture.

6.4 60%CH$_4$ + 40%He flame

Anticipating effects of the buoyancy force and gas expansion (i.e., flow re-direction) due to heat release, reacting flow calculations were conducted for the 60%CH$_4$-40%He mixture at V_0 = 6.0 m/s. The results for the 60%CH$_4$-40%He mixture are shown in Figures 6.6b and 6.6c. It can be seen that the [CH$_4$]: [O$_2$] = 1: 2 contours in the cold-flow and reacting flow predictions are nearly identical for $x \leq 0.017$ m (see Figure 6.6a and 6.6b). The cold flow prediction indicated an attached flame in this region. For $x <$ 0.017 m in the reacting flow results (Figure 6.6b), the stoichiometric [CH$_4$]: [O$_2$] = 1: 2 contour lies within the $u = S_L^o$ = 0.371 m/s contour, suggesting no flame stabilization is possible in this $x <$ 0.017 m region according to the criterion used in the similarity analyses. However, at $x \approx 0.0195$ m in the reacting flow, the $u = S_L^o$ contour sharply bends toward the jet centerline immediately upstream of the high-temperature reaction zone in Figure 6.6b, which is an enlarged view of Figure 6.6c), indicating a shrinkage of the high-velocity region and slowdown of the gas flow near the jet centerline region, where the gas velocity should be the greatest without reaction. On the other hand, the stoichiometric contour and the streamline in this region bend away from the jet centerline (see Figure 6.6), which is not seen in the cold flow prediction. The bending of the stoichiometric and $u = S_L^o$ contours results in their two intersections (at $x \approx$ 0.0190 m and $x \approx$ 0.0196 m, Figure 6.6c) that is also not seen in the cold-flow prediction (Figure 6.6a). It appears that the radially outward bending is associated with gas expansion and the flow re-direction ahead of the flame base. However, this may still not guarantee a flame stabilization point. The axial velocity component undergoes deceleration then acceleration, as suggested by its gradient in the x-direction. At the first intersection of $u = S_L^o$ and stoichiometric contours, $(x, r) \approx$ (0.0190 m, 0.001 m), the temperature is about 302 K,

suggesting no reaction. At the second intersection of $u = S_L^o$ and stoichiometric contours, (x, r) $\approx$ (0.0196 m, 0.001 m), the temperature is about 600 K, it is still in the preheating zone. Between these two intersections, the axial velocity is below the $u = S_L^o$. It can be seen in Figure 6.6c the most upstream location of the flame base is located at $(x, r) \approx$ (0.0197 m, 0.0017 m), where the temperature is greater than 1,000 K and $u > S_L^o$. These computational results suggest that the flame base location cannot be determined in a like manner as in the cold-flow similarity or numerical predictions.
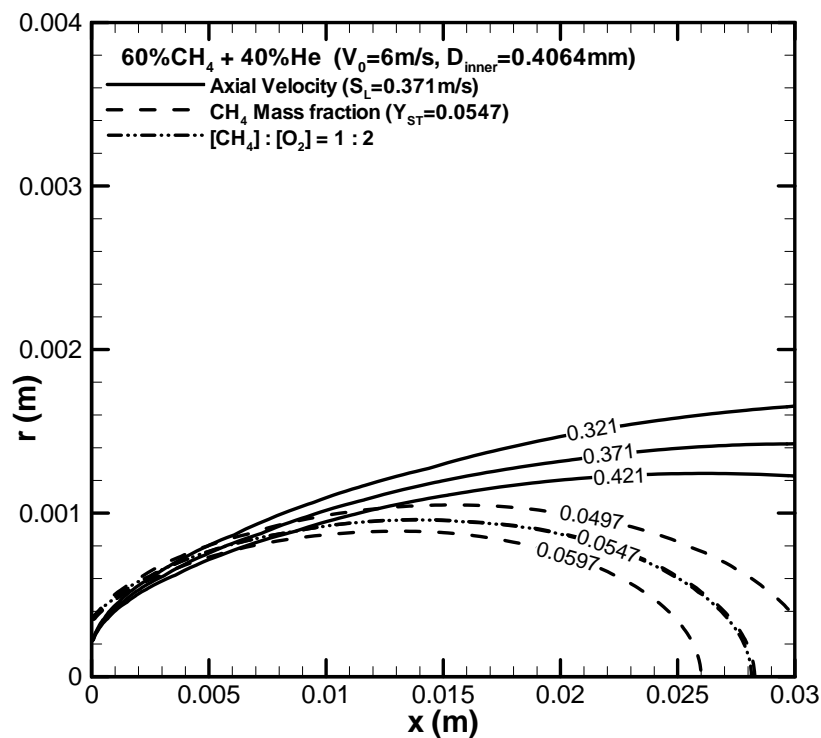
Figure 6.6(a) - Cold-flow prediction of 60%CH₄-40%He mixture at $V_0 = 6.0$ m/s; flame may blow out possibly due to quenching/heat loss at the burner lip ($x < 0.002$ m).
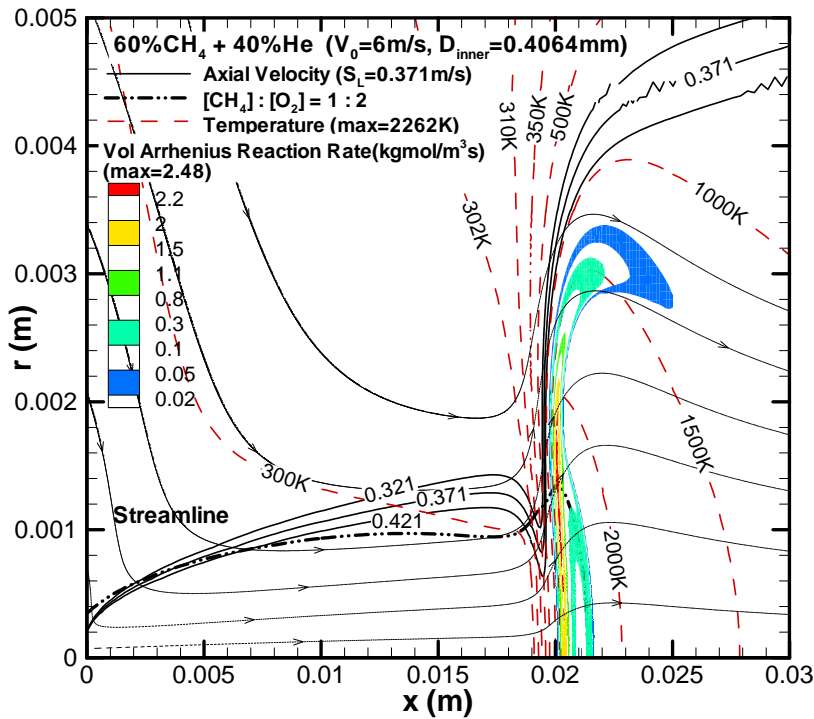
Figure 6.6(b) - Full view of Reacting flow: contours of axial velocity, stoichiometric line, temperature and reaction rate for 60%CH_4-40%He mixture at V_0 = 6 m/s.
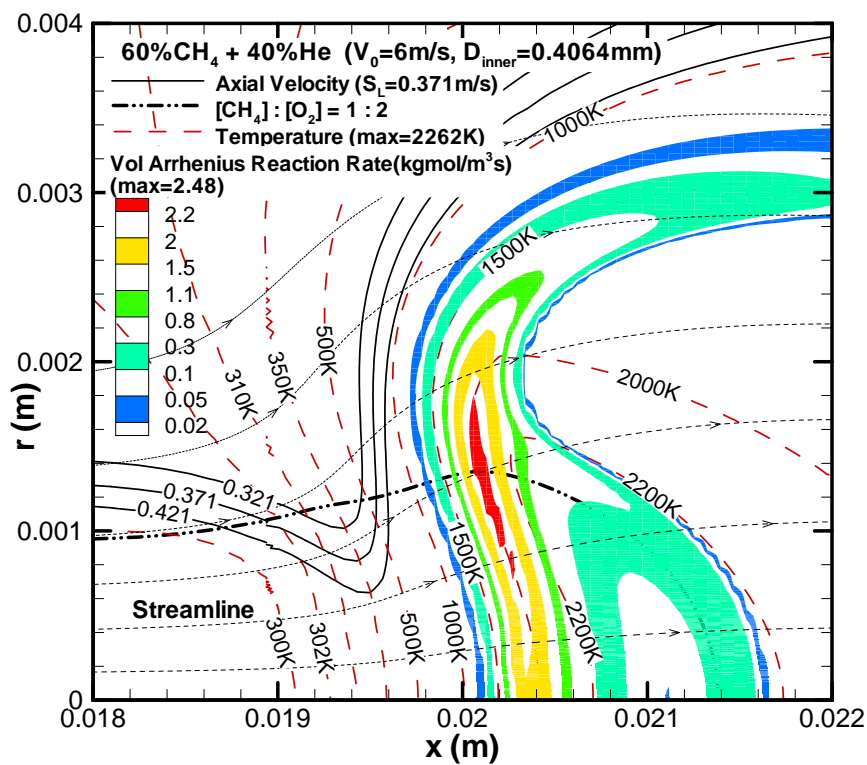
Figure 6.6(c) - Enlarged view of Reacting flow: contours of axial velocity, stoichiometric line, temperature, and reaction rate for 60%CH_4-40%He mixture at V_0 = 6 m/s.

114

Table 6.7 - L_F (flame length), W_F (flame width), H_L (lift-off height), and k (the stretch rate), V_P (perpendicular velocity to the isotherm), V_X (axial velocity), Y_{c3h8} (C_3H_8 mass fraction) and RR (volumetric Arrhenius reaction rate, unit: $kgmol/m^3 s$) for a variety of isotherms at each specific jet velocity for 40%He diluted CH_4 flame.

V_0	L_F (EXP)	L_F CFD	W_F CFD	H_L (EXP)	H_L CFD	310K	350K	500K	1000K	1500K	2000K
6 m/s	0.6cm	0.4cm	3.4mm	0.5cm	2.0cm						
k (/s)						62.5	108.7	188.5	334.7	435.3	659.1
Vp(cm/s)					37.1	35.1	35.0	41.9	65.8	86.7	105.7
Vx(cm/s)						31.2	29.0	33.8	56.9	78.5	98.9
Y_{ch4}					0.0547	0.0549	0.0542	0.0511	0.0384	0.0241	0.0093
RR						0	1.9×10^{-20}	2.5×10^{-12}	2.2×10^{-3}	0.39	2.25
7 m/s	0.6cm	blow		1.0cm	blow						
7.5 m/s	0.5cm	-		1.5cm	-						

Table 6.8 - For 1 -dimensional stoichiometric 40%He diluted CH_4 / Air pre-mixed flame, GRI-Mech3.0 mechanism, CHEMKIN calculation results

T (K)	298.15	310	350	500	1000	1500	1672	2000	2187(max)
V (cm/s)	37.1	38.8	43.8	62.9	127.5	193.0	215.6	253.5	273.7
H_{DOT}(J/s/cc)	3.1×10^{-15}	2.1×10^{-3}	5.9×10^{-2}	3.1	3.2×10^2	2.8×10^3	3.77×10^3 (max)	6.3×10^1	5.02×10^{-3}

HDOT: heat generation rate.

Table 6.7 shows k (the stretch rate) monotonously increases with the isotherm temperature value. And $k = 334.7$ /s is the critical stretch rate on the 1000K isotherm for maximum V_0 lift-off flame; the tribrachial flame cannot be lifted against a lower stretch rate. The perpendicular velocity (V_P) in the intersection of the $[CH_4]$: $[O_2]$ = 1: 2 contour and the 1000 K isotherm is 65.8 m/s, which is 1.8 times of S_L^o (37.1 cm/s). Table 6.8 shows the GRI-Mech3.0 mechanism simulated 1-dimensional flame adiabatic temperature (2187 K) is close to the one-step irreversible reaction, 2-dimensional maximum flame temperature of 2262 K.
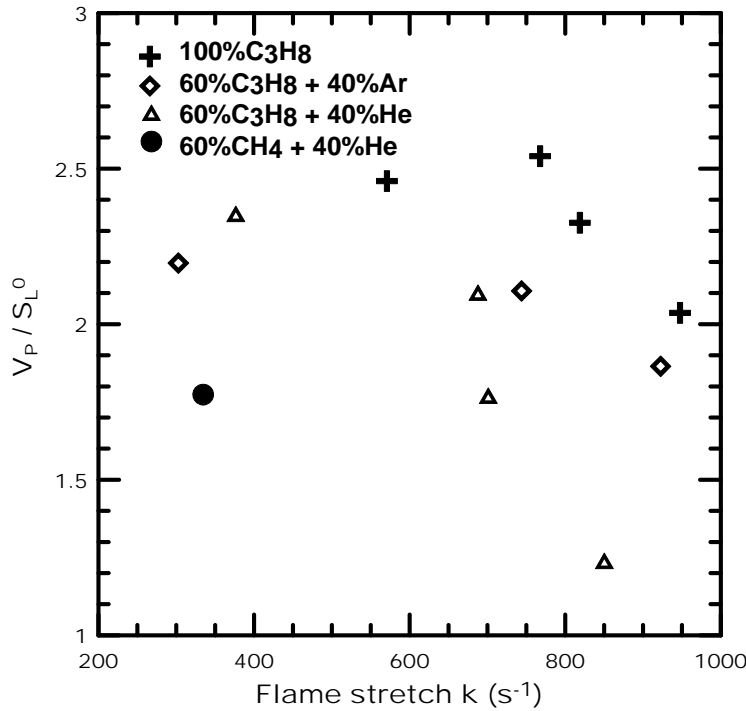
Figure 6.7 - Perpendicular velocities (V_P / S_L^o) in the intersection of stoichiometric line and 1000 K isotherm versus flame stretch

Figure 6.7 shows the values of V_P / S_L^o at different flame stretch rate for all the reacting flows in this chapter. It is noticed that the pure propane flame base has a higher V_P / S_L^o than the 40% Ar / He diluted propane flame base. The value of V_P / S_L^o for pure propane and 40%Ar/He diluted propane increases when the flame stretch decreases. The values of V_P / S_L^o ranges from 1.25 to 2.5, and the maximum V_P / S_L^o is reached when the flame is approaching its blow-off velocity. The only exception is the $V_0 = 15$m/s ($k = 570$ /s) propane flame, which is blow-off experimentally (Table 6.1). Ko and Chung [6] experimentally measured the unsteady tribrachial flame base stretch rate for pure methane, their $V_P / S_L^o = 0.775$ m/s / 0.390 m/s = 1.99 at $k = 334$ /s. Figure 6.7 shows V_P is 1.8 times of S_L^o for the 40%He diluted methane steady lifted flame at $k = 334$ /s, this prediction is generally verified by their experimental measurement.

116

CHAPTER 7: CONCLUSIONS AND FUTURE WORK

7.1 Conclusions

Numerical solutions of laminar fuel jets were obtained for predicting jet flame liftoff. The cold-flow prediction included effects of buoyancy (due to molecular weights of fuels and fuel-inert mixtures) and multi-component diffusivities. One-step irreversible heat release reaction was added to further include the effects of buoyancy force and gas expansion due to combustion reaction. The following were found.

(1) No Schmidt number criterion based similarity solutions or numerical cold-flow simulations could consistently predict the flame lift-off. This is attributable to the multi-component diffusion and the buoyancy and gas expansion effects not included in similarity and cold-flow numerical analyses.

(2) Heat release due to combustion reaction was found to significantly alter the velocity and concentration contours in the immediate upstream vicinity of the flame base. The results suggest that, for the CH_4 and C_3H_8 flames studied, the flame stabilization locations do not coincide with the intersection of the $u = S_L^o$ and stoichiometric contours, if such intersections exist. The flame stabilization and lift-off do not require such intersections as necessary conditions. Including the heat release effect helps to predict lift-off for the 60%CH_4-40%He flame, which cold-flow solutions fail to accomplish; it also improves the prediction of the lift-off height in pure and diluted C_3H_8 flames.

(3) The stretch rate k (1000 K isotherm) has a minimum value of 300 /s as the condition for the flame to be stabilized in the lifted fuel jet. The perpendicular velocity (V_P) in the flame base (intersection of the stoichiometric line and 1000 K isotherm) increases as the jet velocity V_0 increases until blow-off (k monotonously decreases to 300 /s). This is an automatic adjustment for the tribrachial flame to stand against the increased upstream jet flow velocity.

For other potential fuel-inert mixtures and blended fuels, the results of this study suggest that effects of strong heat release, multi-component diffusion, heat release, buoyancy, and gas expansion would have to be included for complete flame lift-off prediction.

7.2 Future work

Full C3 mechanism for C_3H_8 flames and GRI-Mech3.0 mechanism for CH_4 flames are great challenges to overcome. Including the intermediate reactions and species, the basic structures in the flame base will be more similar to the physical realities. The intrinsic relationship between the fuel / oxygen fractions, the stretch rate, and the flame speed can be further observed.

The maximum ignition height prediction for the low speed flames can be further analyzed by adding the transitional heat and momentum disturbance from the ignition wire to the converged cold flow simulation results. The flammable range for the stoichiometric ratio and the flame speed at each specific ratio should also be applied to the cold flow analysis.
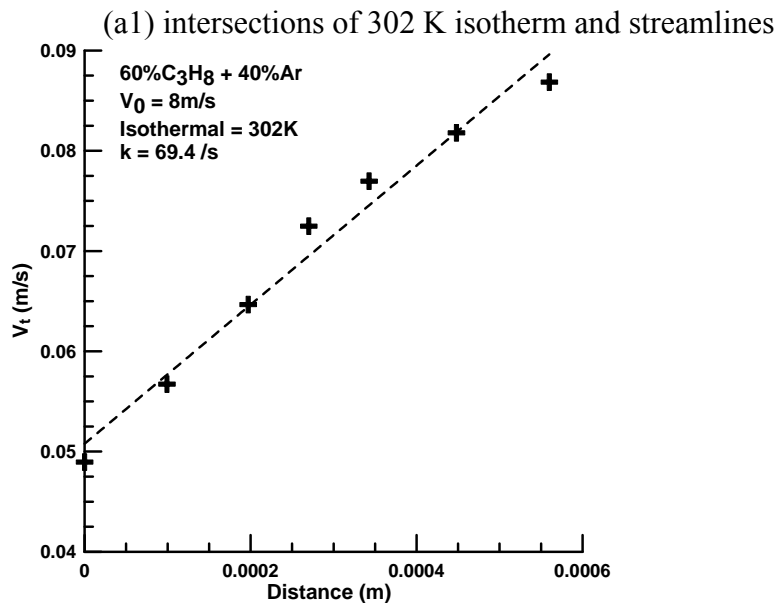
APPENDIX: ADDITIONAL FIGURES
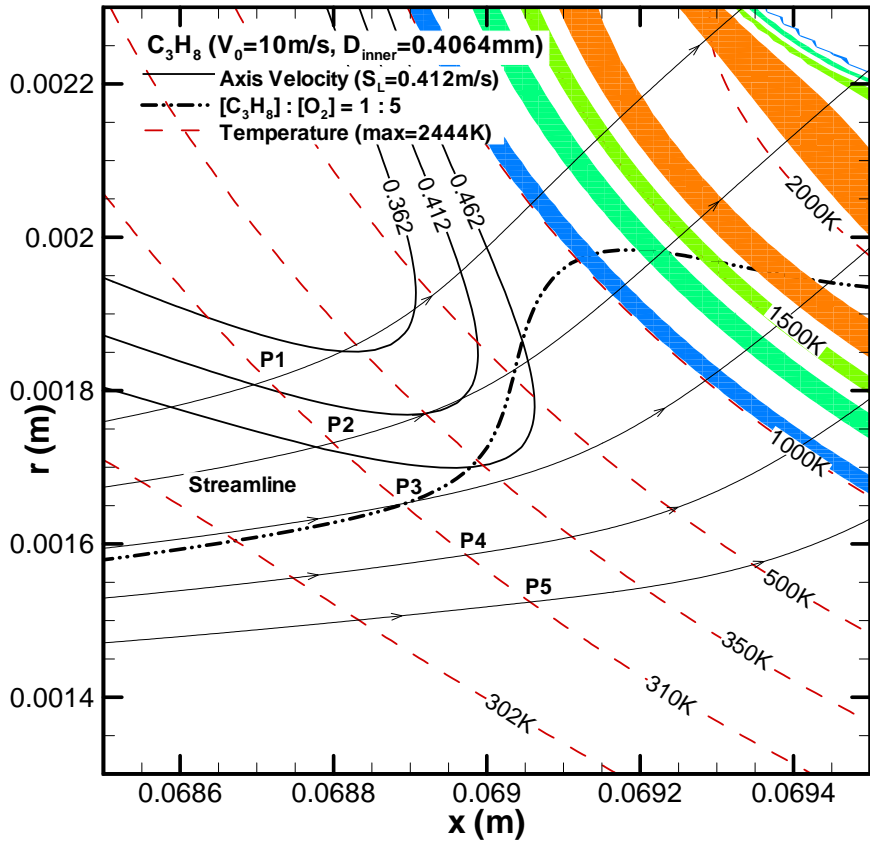
(a1) intersections of 310 K isotherm and streamlines
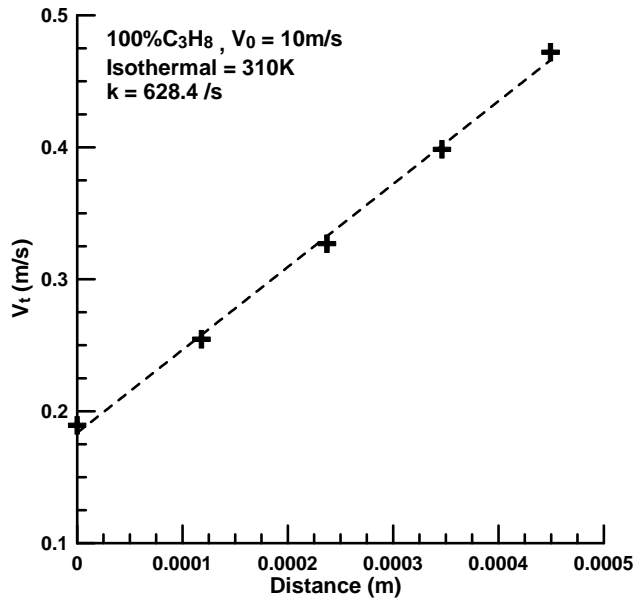
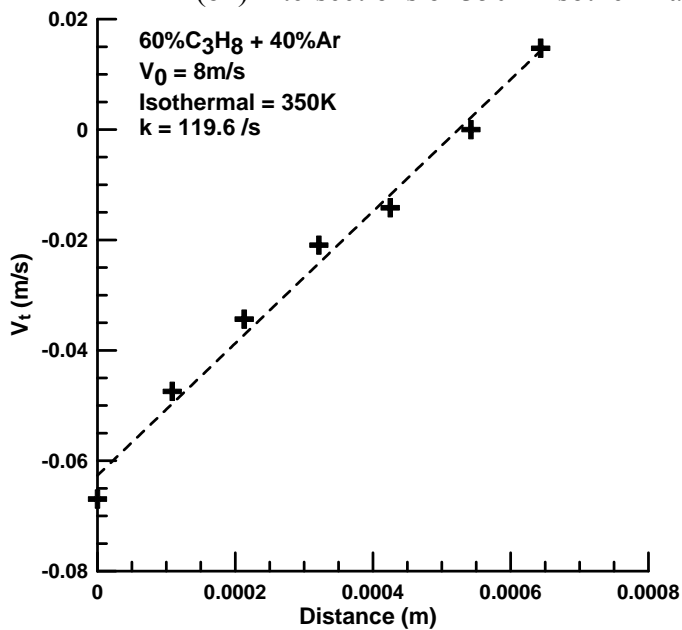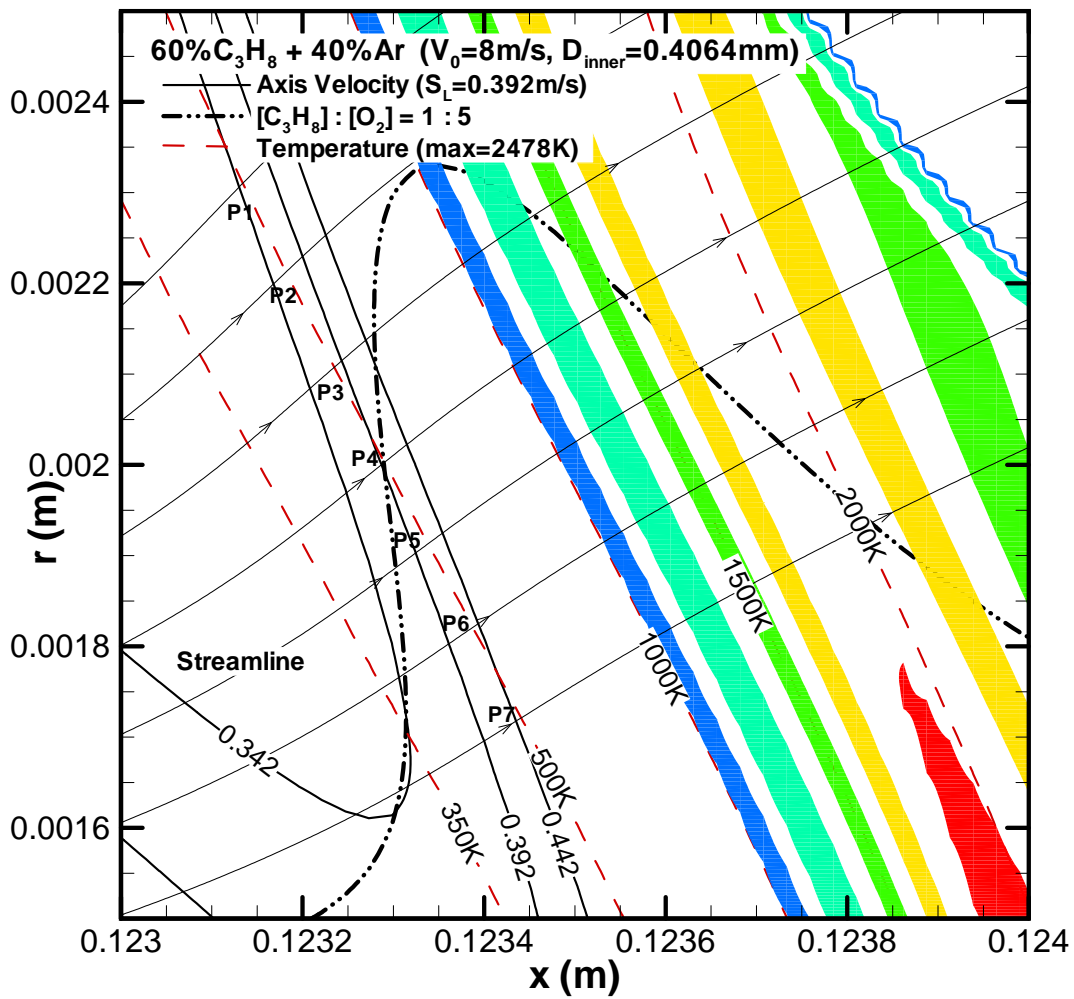(a2) stretch rate fit along 310 K isotherm

Figure A.1 (a - f) –Interpolation around the stoichiometric line and the stretch rate fit for a variety of isotherms (310K, 350K, 500K, 1000K, 1500K and 2000K) for pure C_3H_8 at jet velocity of 10 m/s.
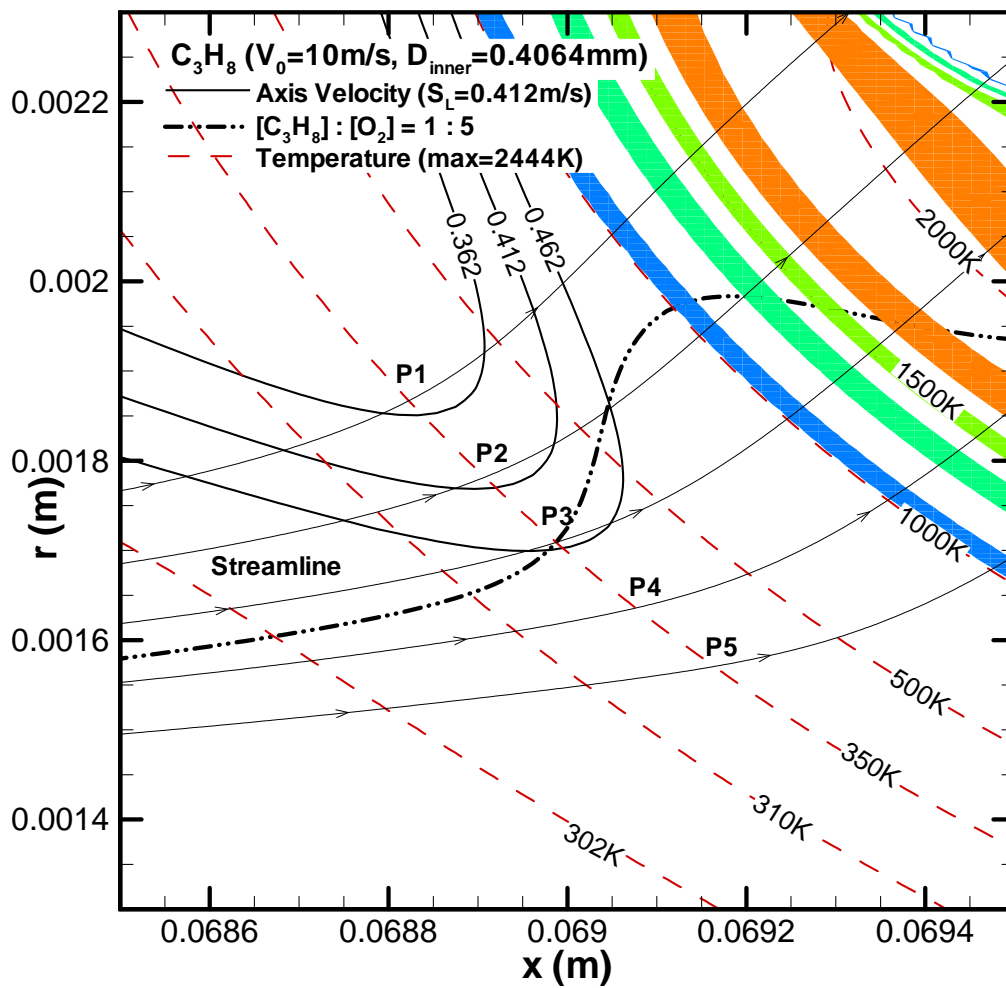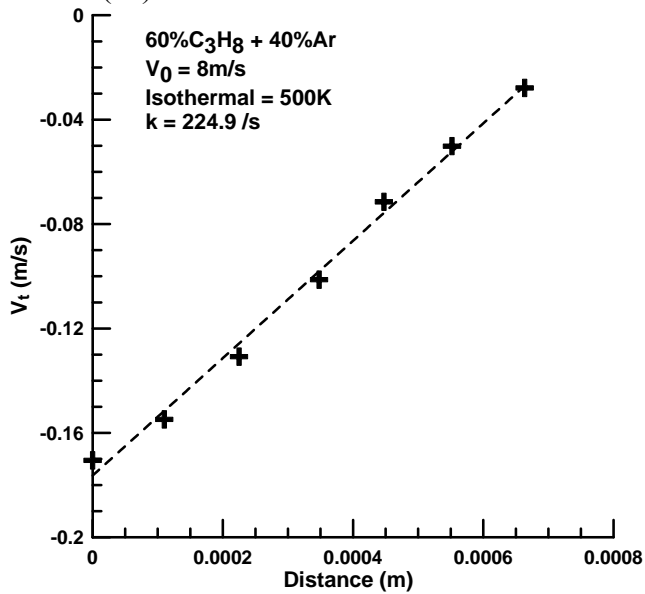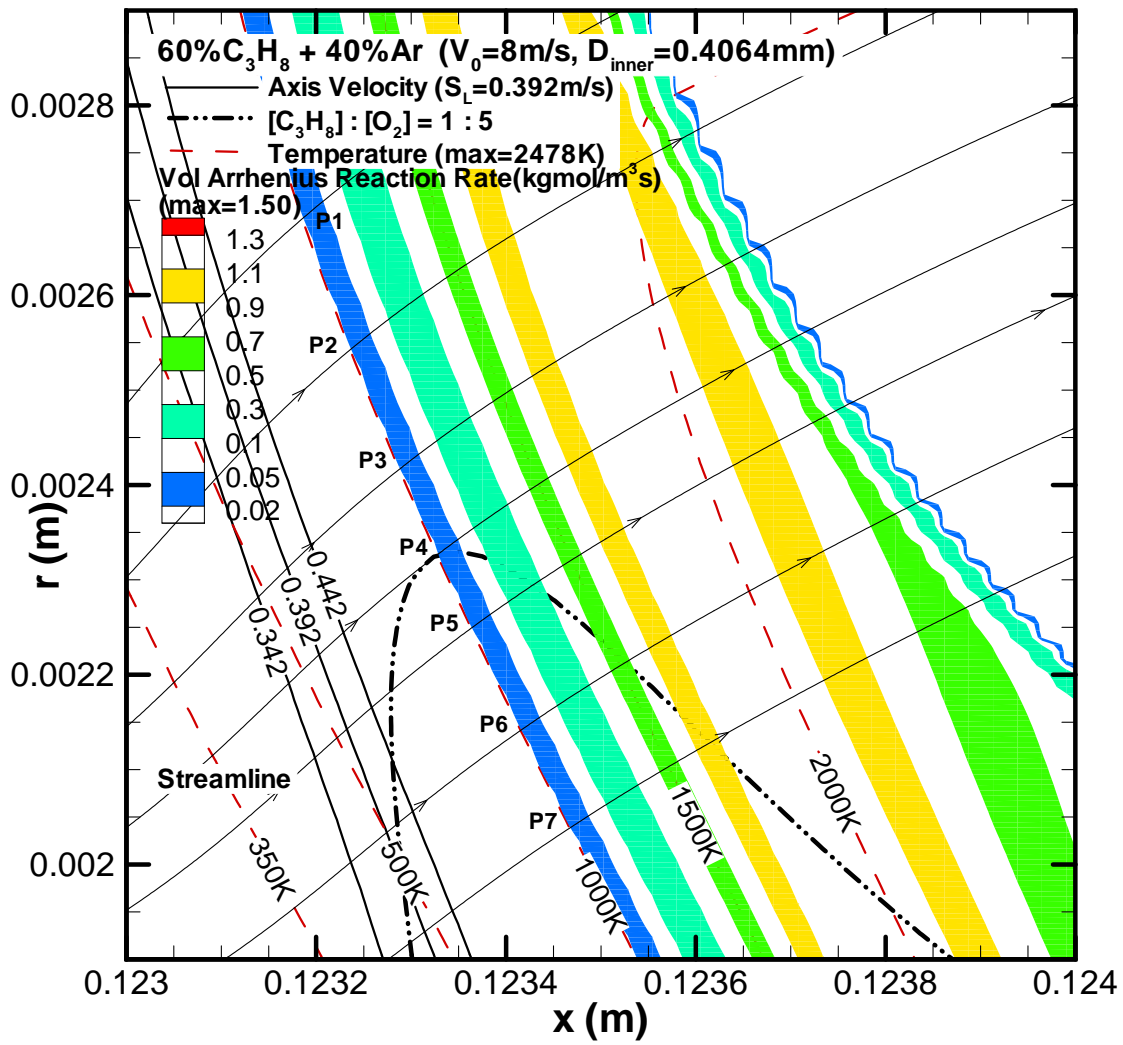
(b1) intersections of 350 K isotherm and streamlines
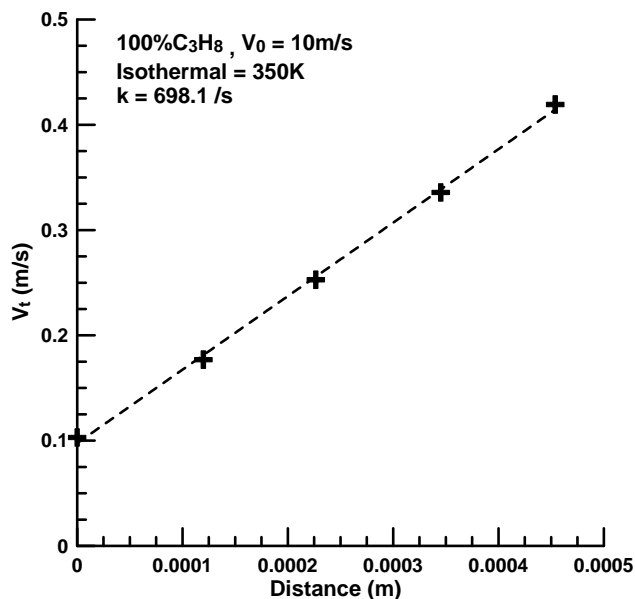
(b2) stretch rate fit along 350 K isotherm

Figure A.1 (a - f) – (continued)
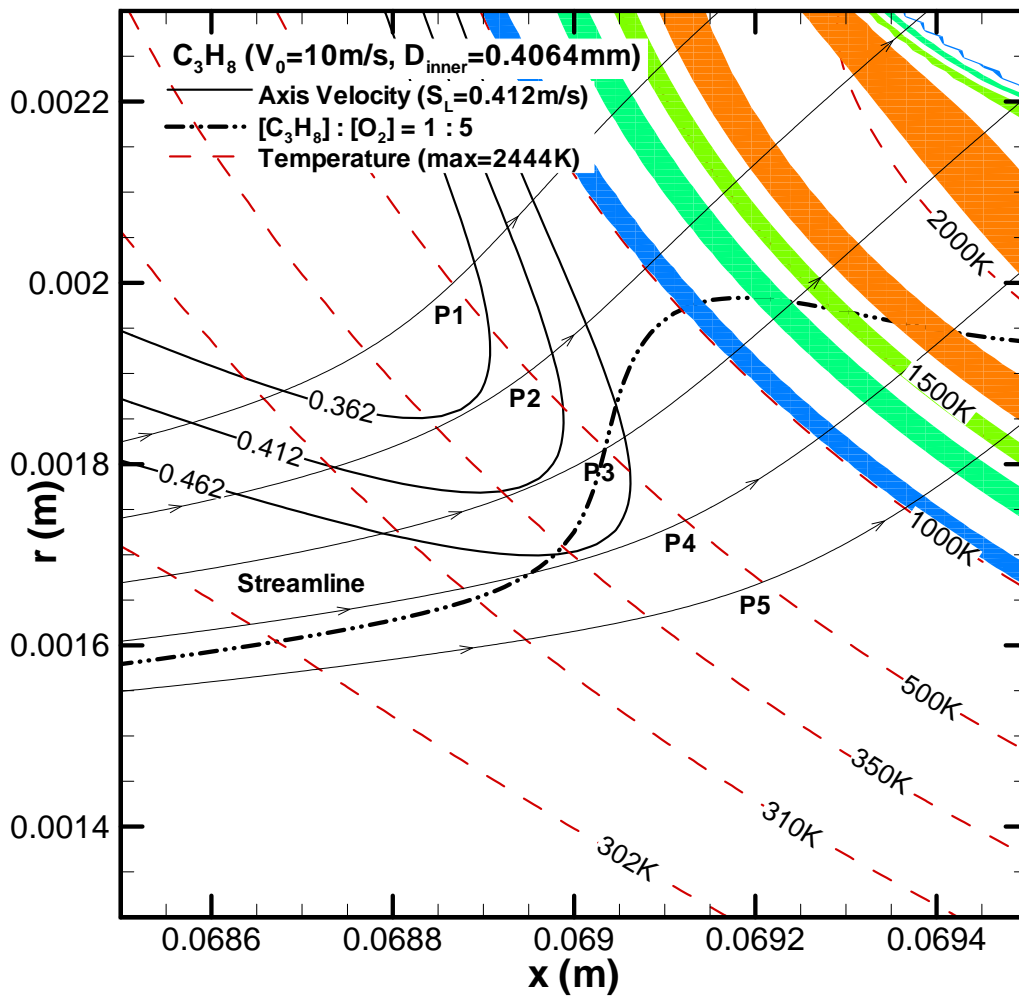
(c1) intersections of 500 K isotherm and streamlines
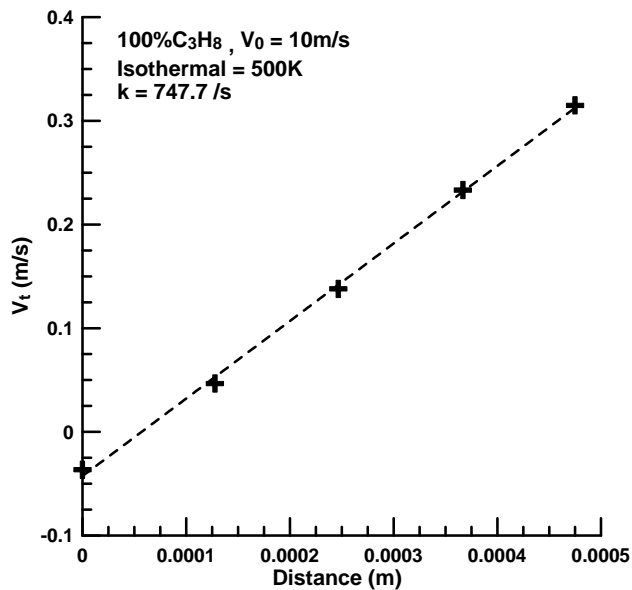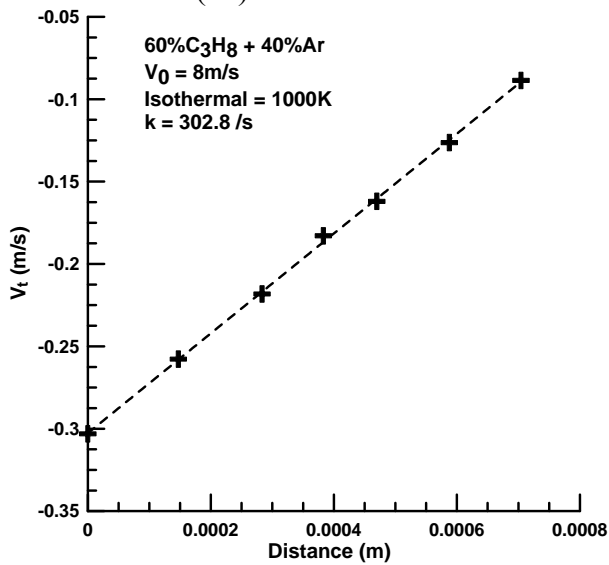

(c2) stretch rate fit along 500 K isotherm
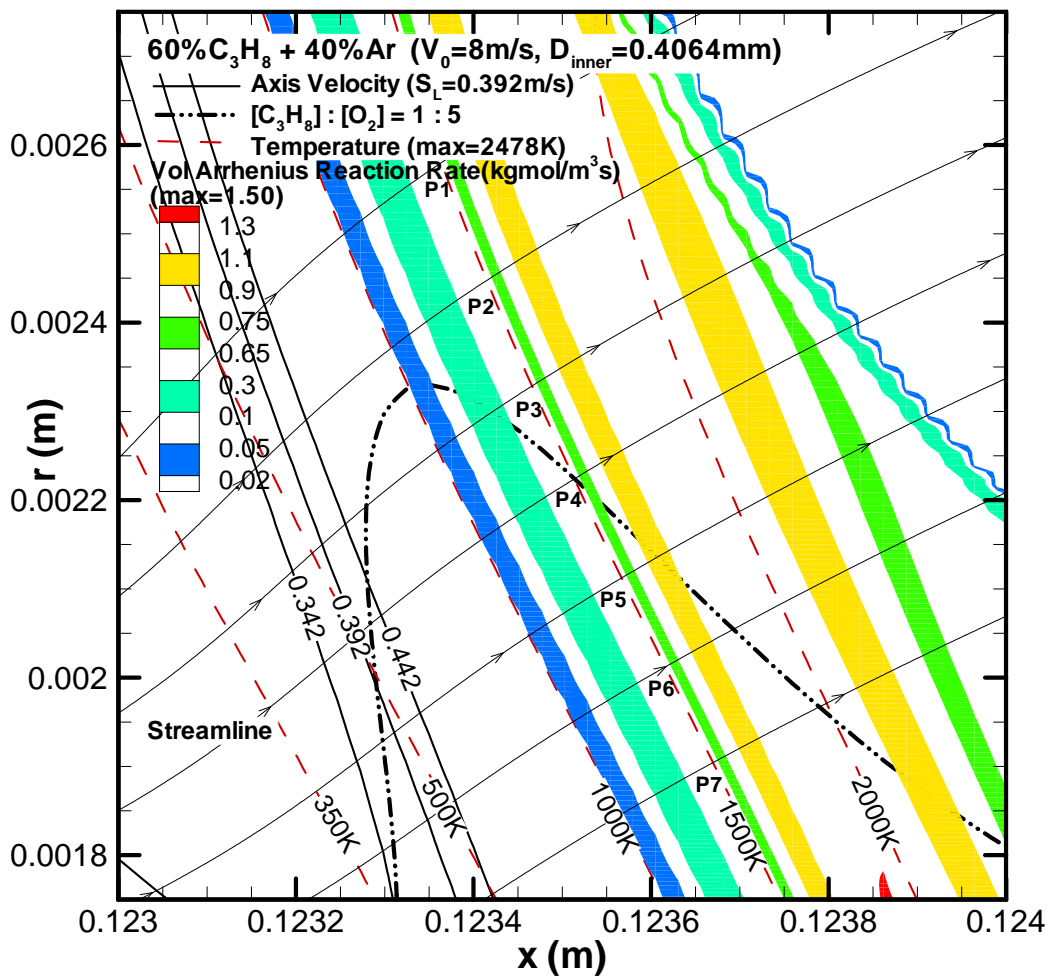
Figure A.1 (a - f) – (continued)
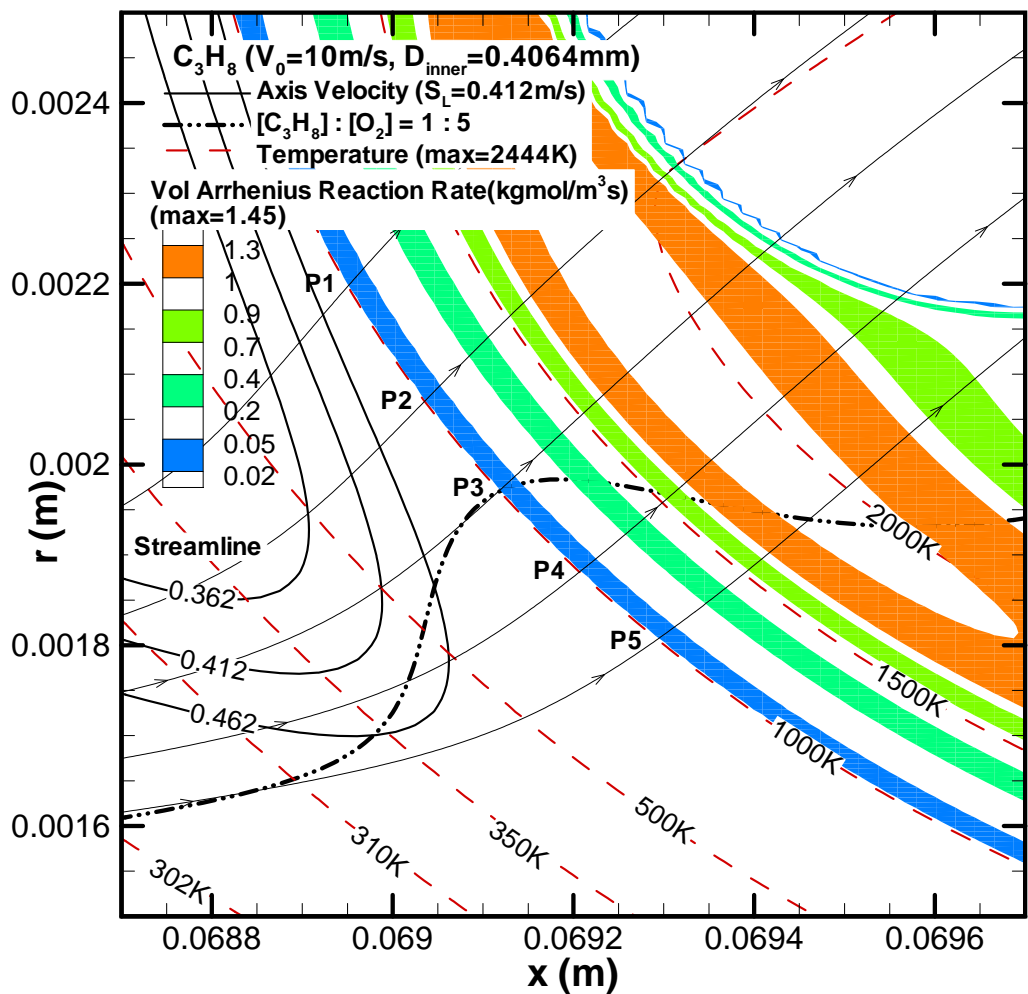
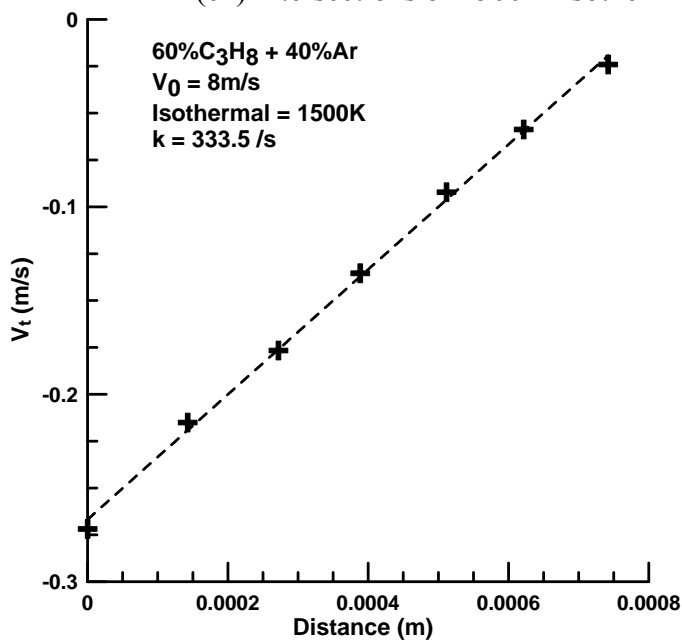(d1) intersections of 1000 K isotherm and streamlines
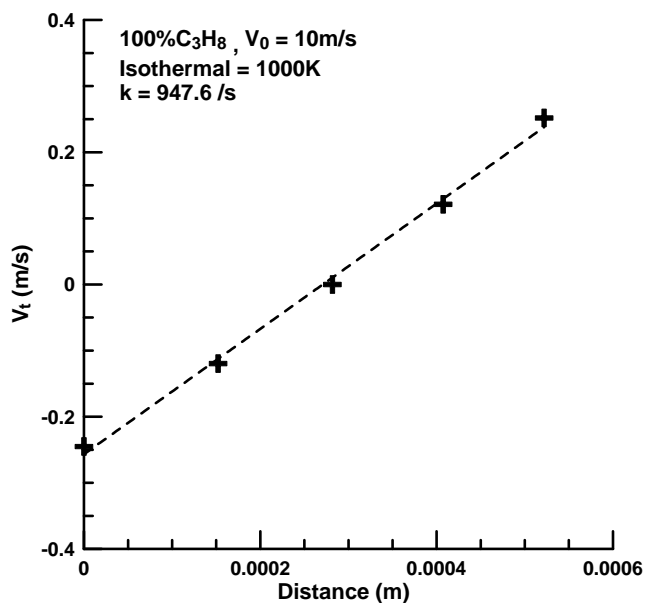
(d2) stretch rate fit along 1000 K isotherm
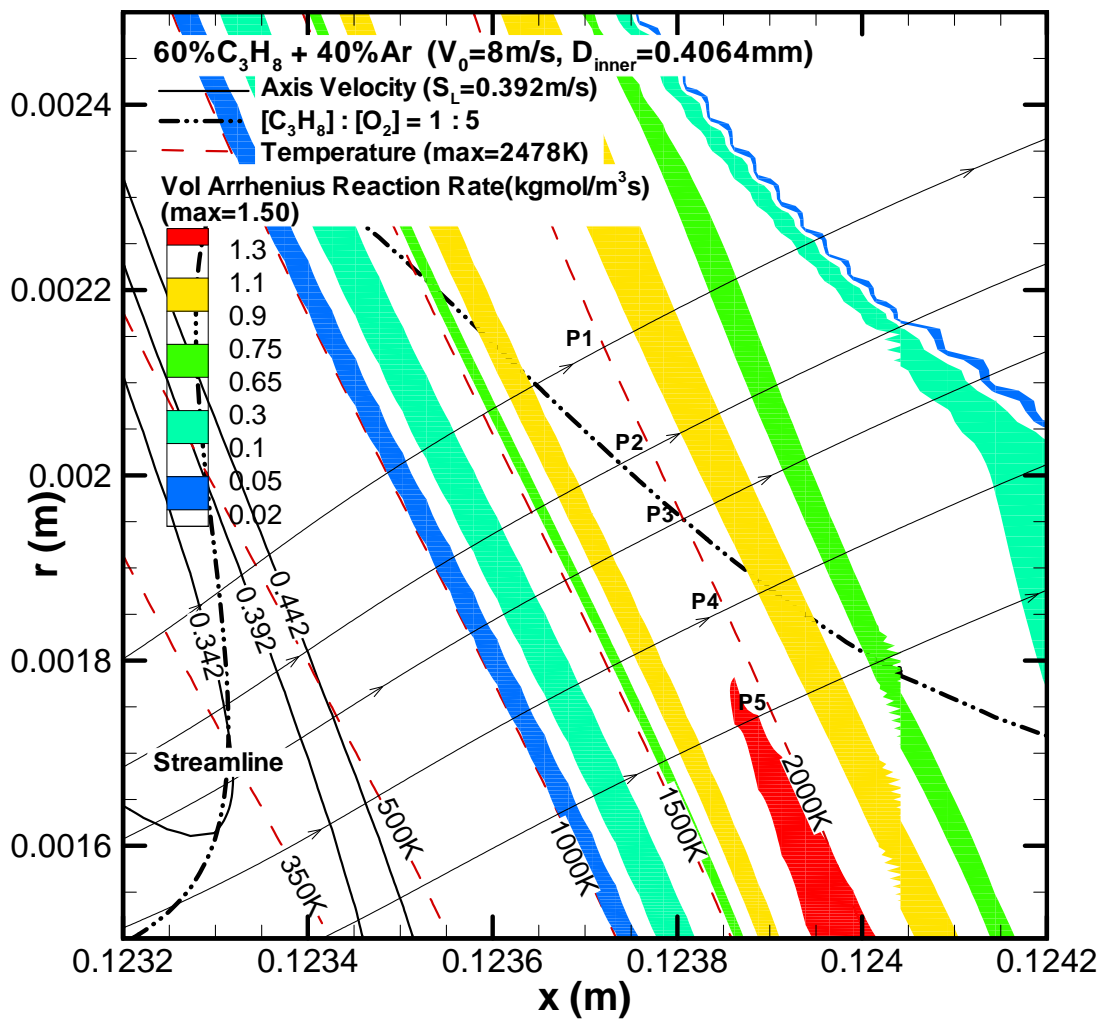
Figure A.1 (a - f) – (continued)
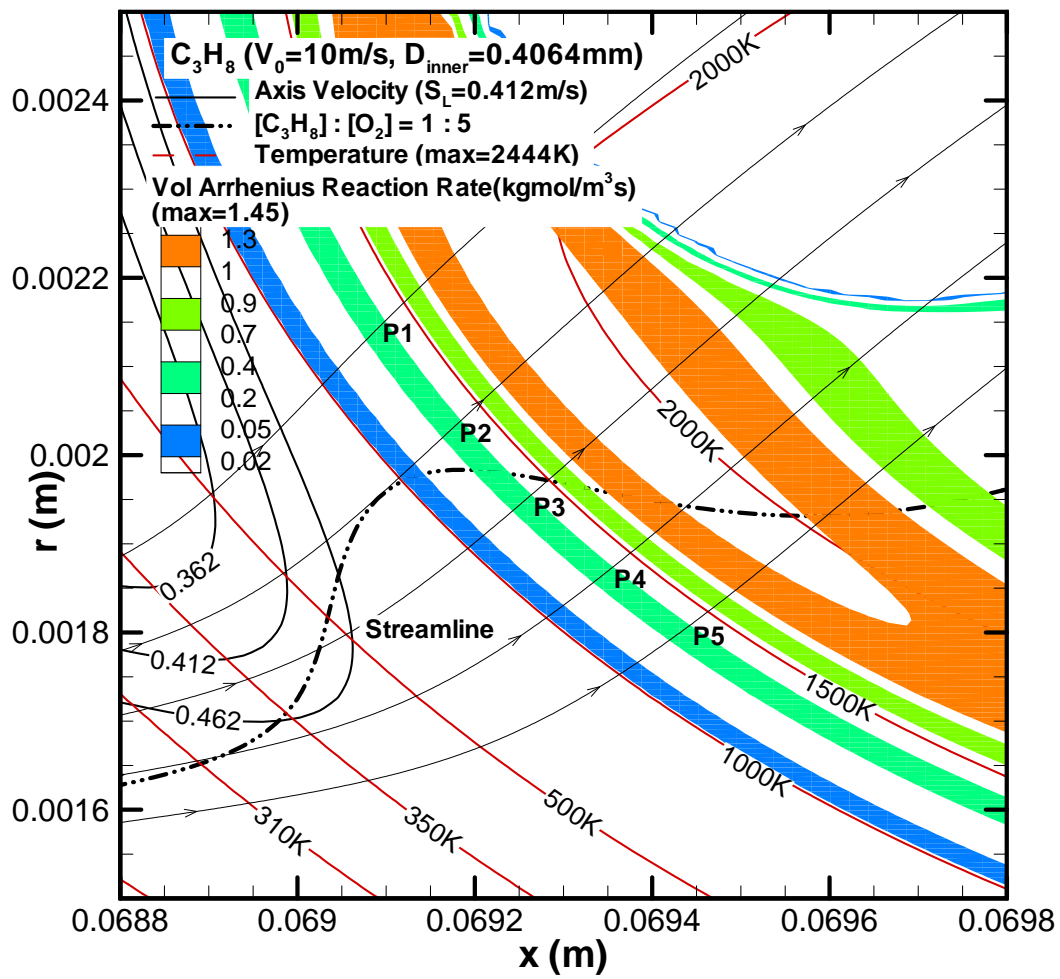
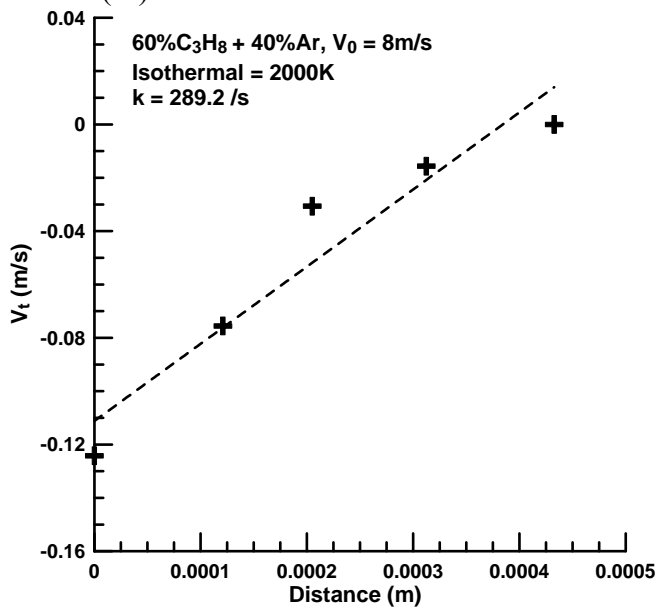(e1) intersections of 1500 K isotherm and streamlines
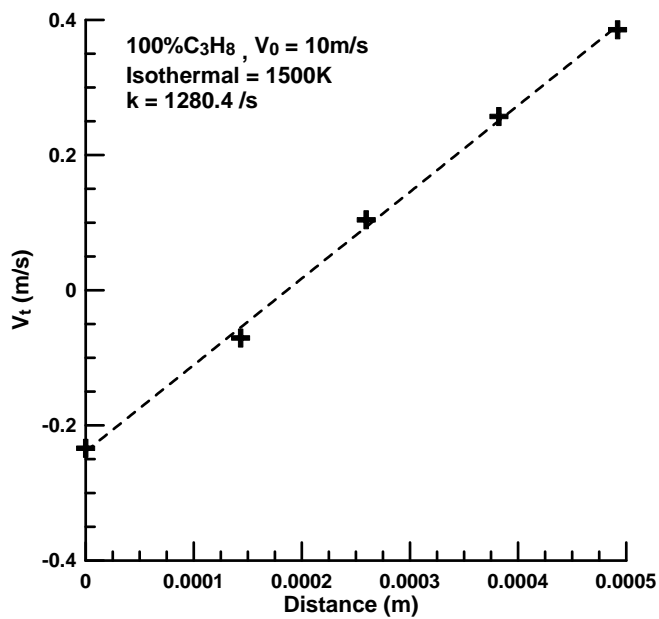
(e2) stretch rate fit along 1500 K isotherm
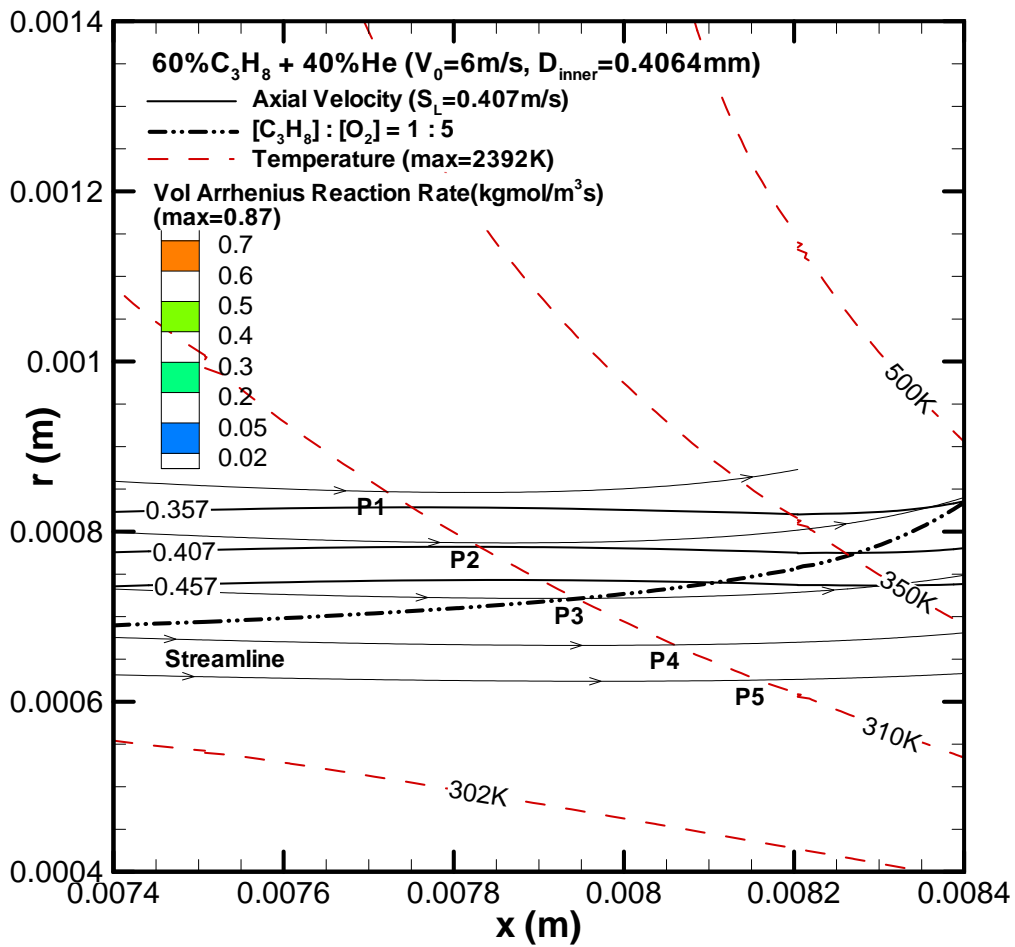
Figure A.1 (a - f) – (continued)
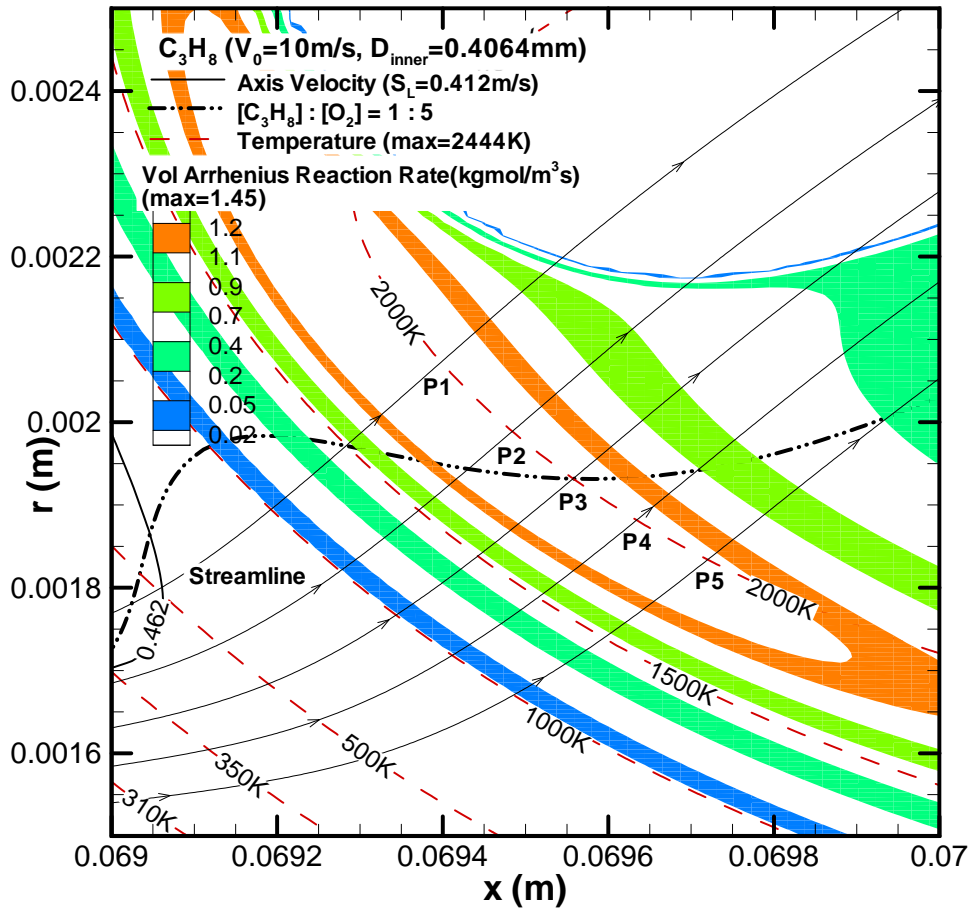
(f1) intersections of 2000 K isotherm and streamlines
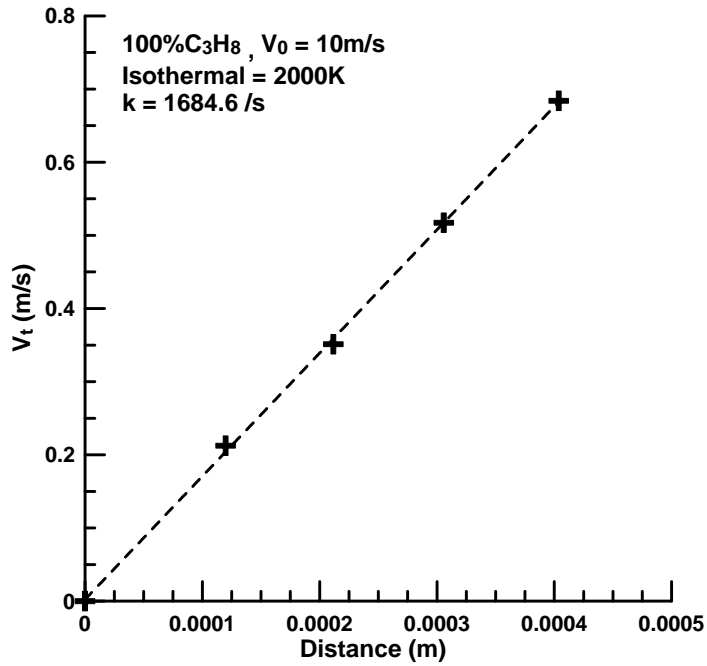
(f2) stretch rate fit along 2000 K isotherm

Figure A.1 (a - f) – (continued)
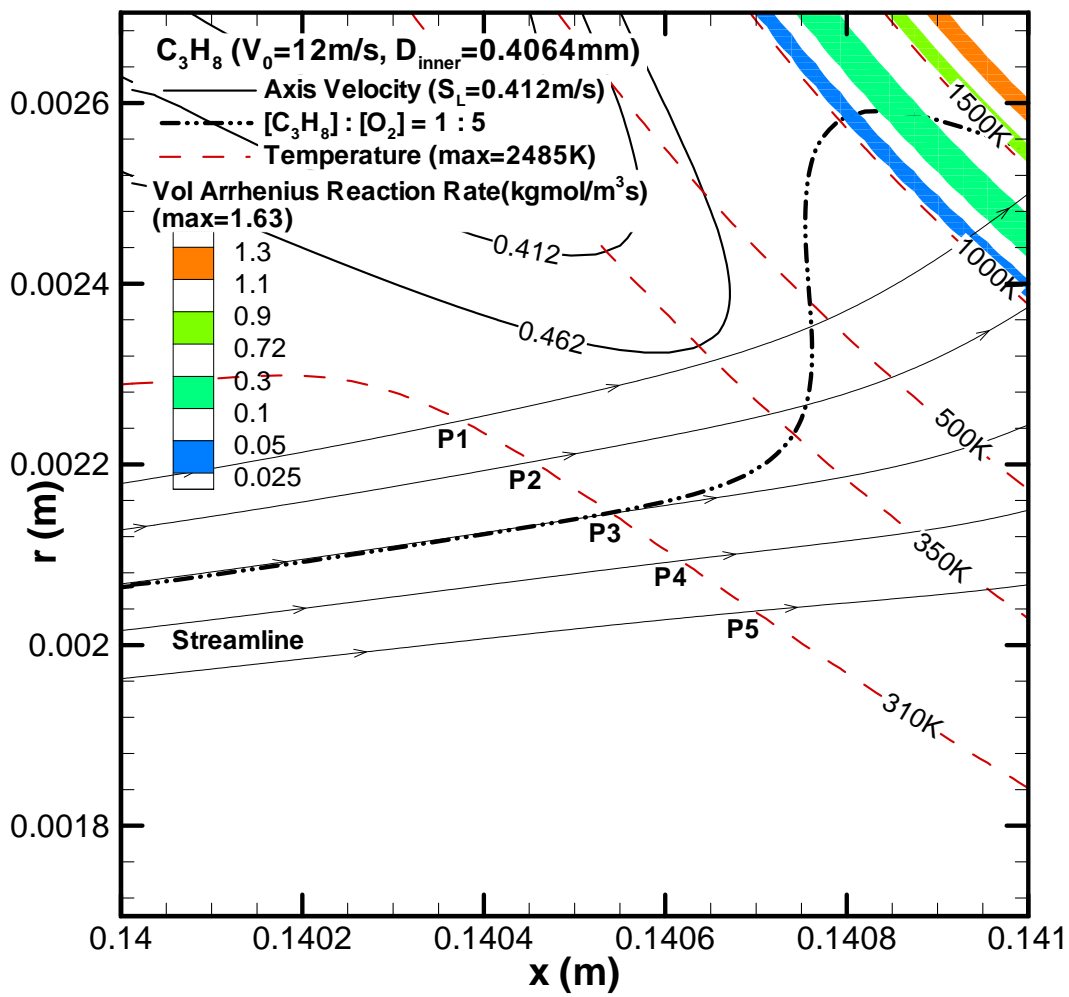
(a1) intersections of 310 K isotherm and streamlines
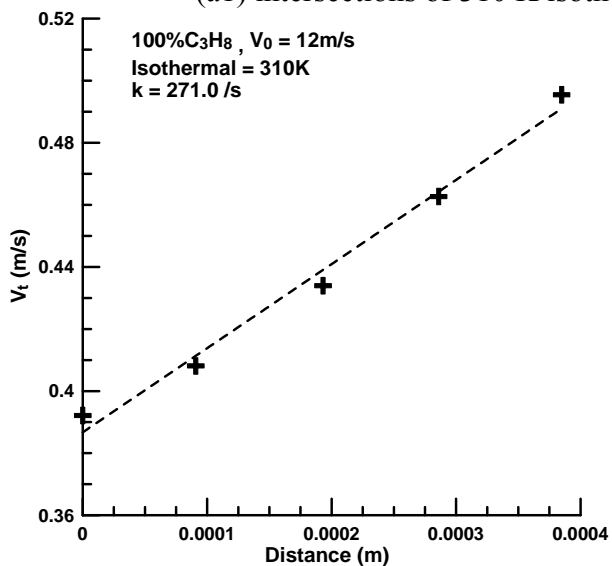
(a2) stretch rate fit along 310 K isotherm

Figure A.2 (a - f) –Interpolation around the stoichiometric line and the stretch rate fit for a variety of isotherms (310K, 350K, 500K, 1000K, 1500K and 2000K) for pure C_3H_8 at jet velocity of 12 m/s.
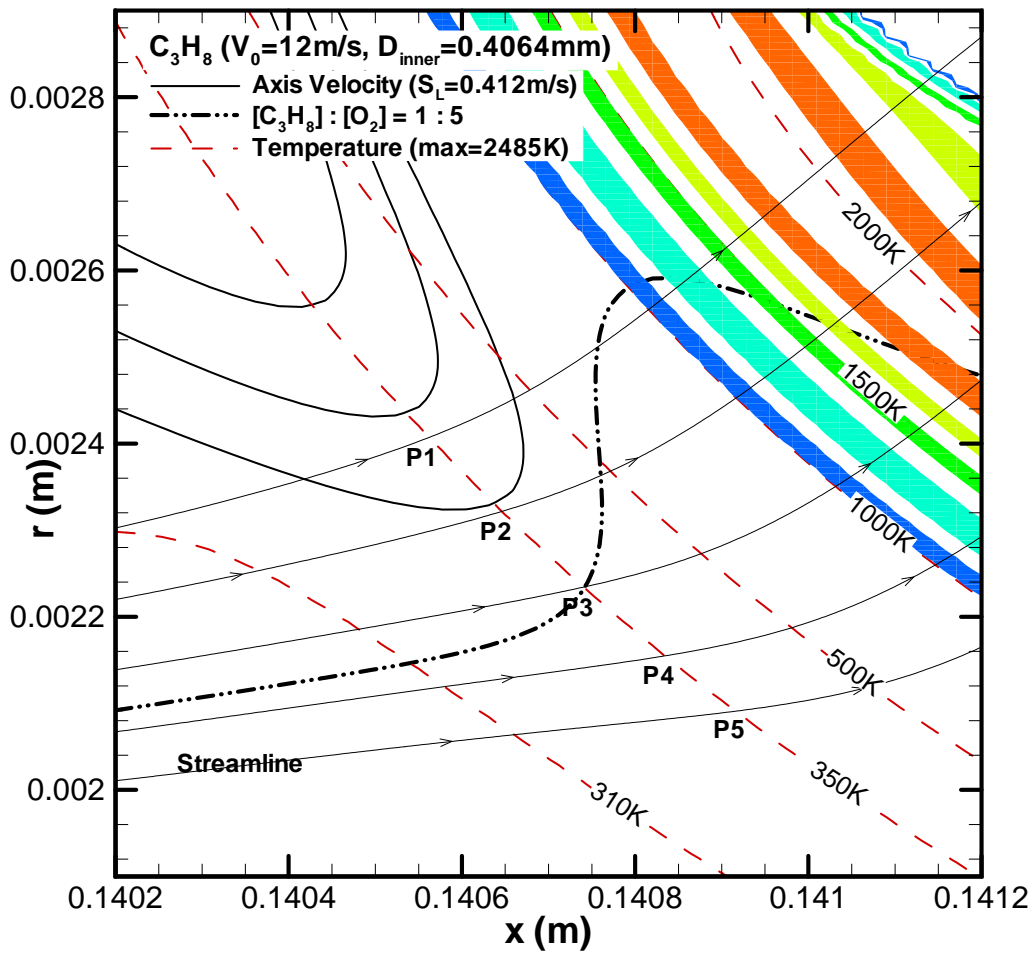
(b1) intersections of 350 K isotherm and streamlines
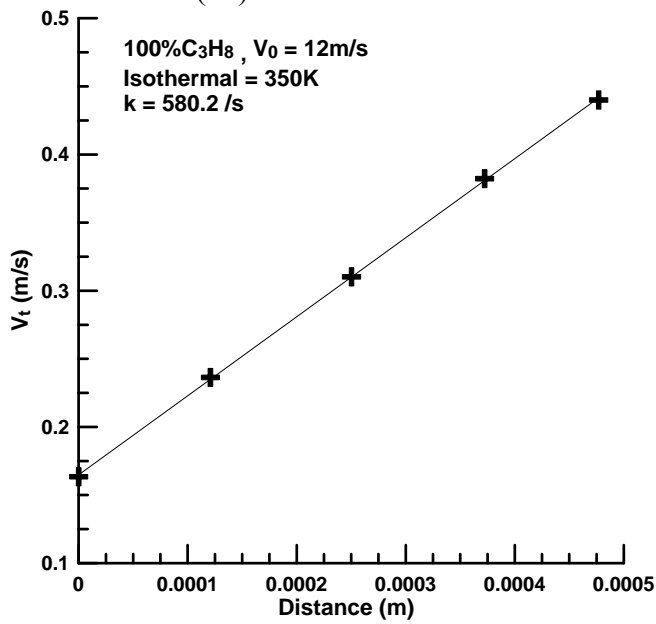
(b2) stretch rate fit along 350 K isotherm

Figure A.2 (a - f) – (continued)
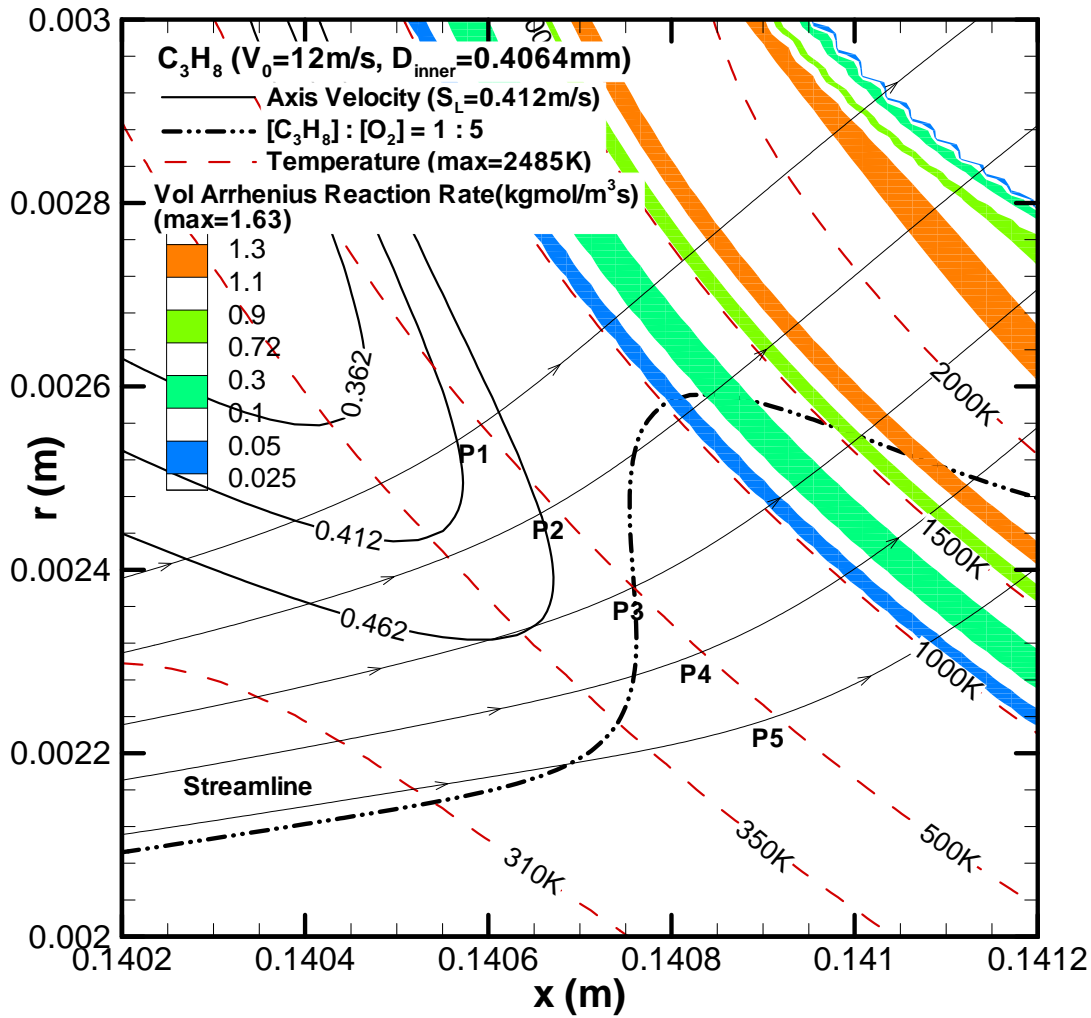
(c1) intersections of 500 K isotherm and streamlines
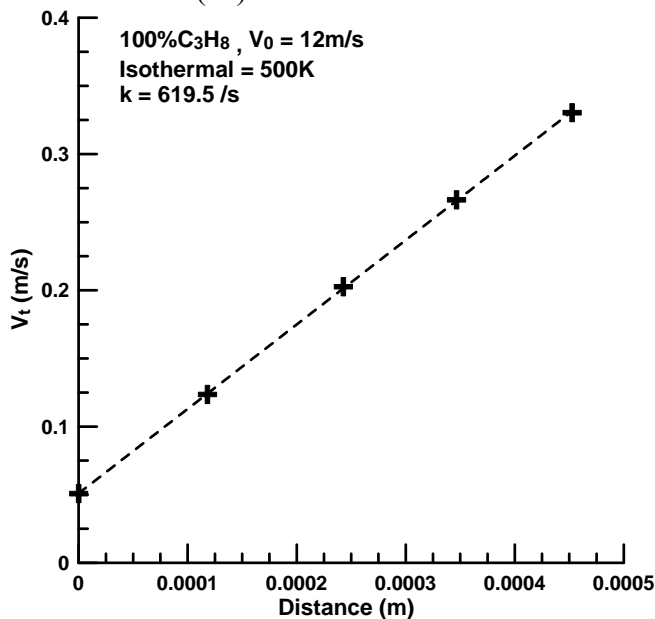
(c2) stretch rate fit along 500 K isotherm

Figure A.2 (a - f) – (continued)
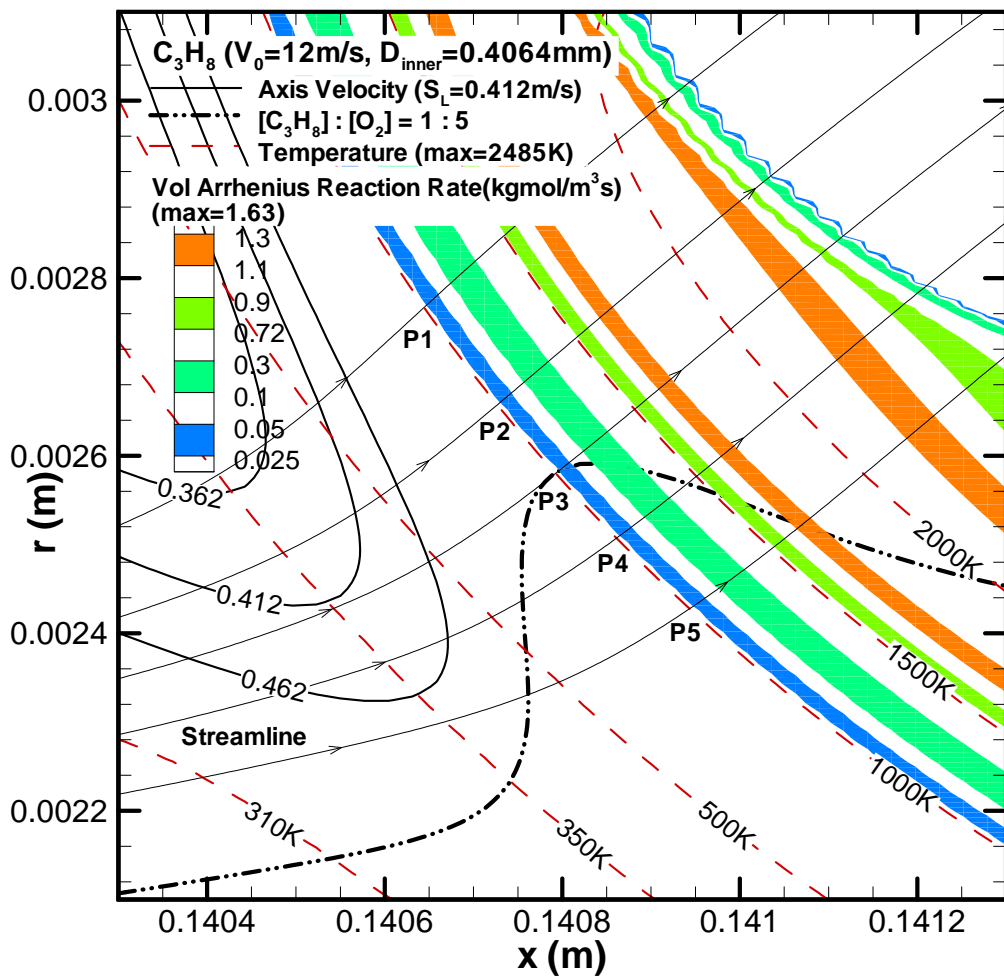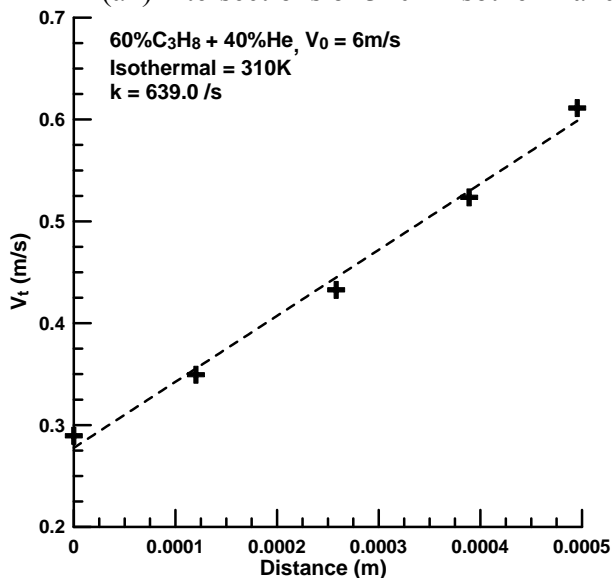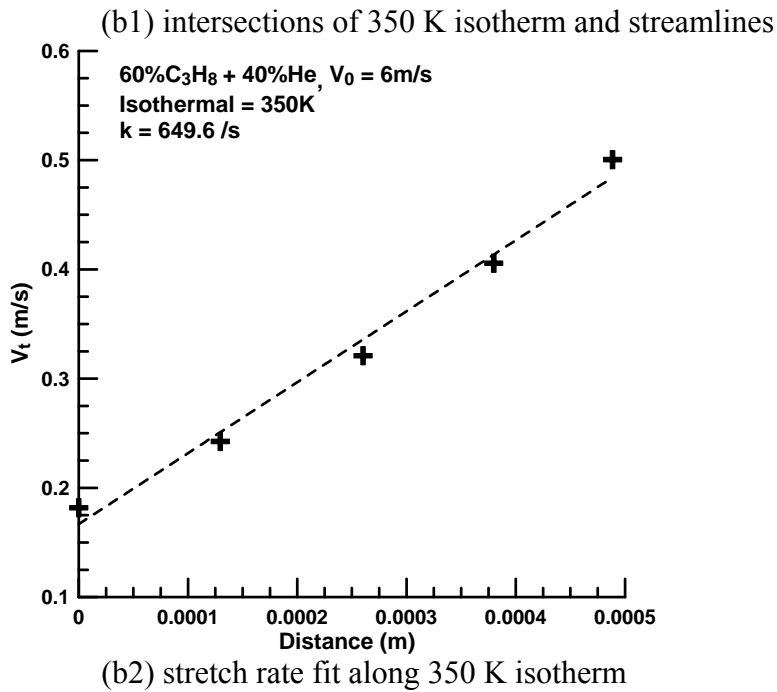
(d1) intersections of 1000 K isotherm and streamlines
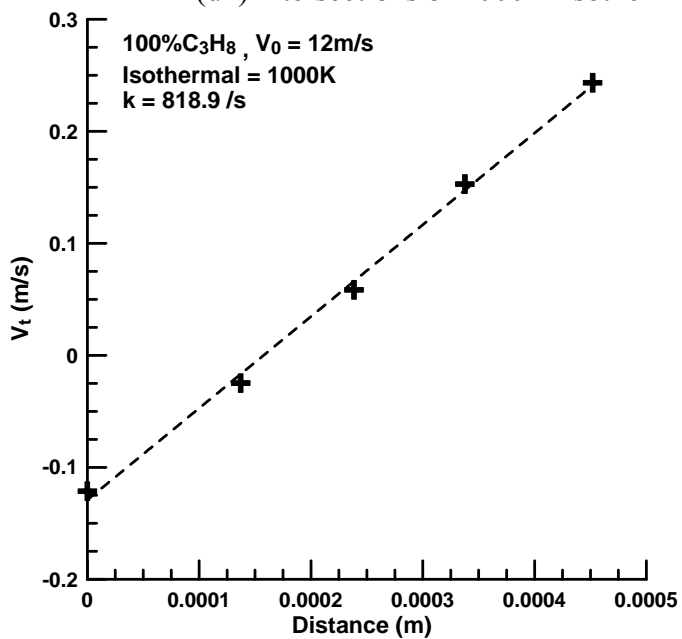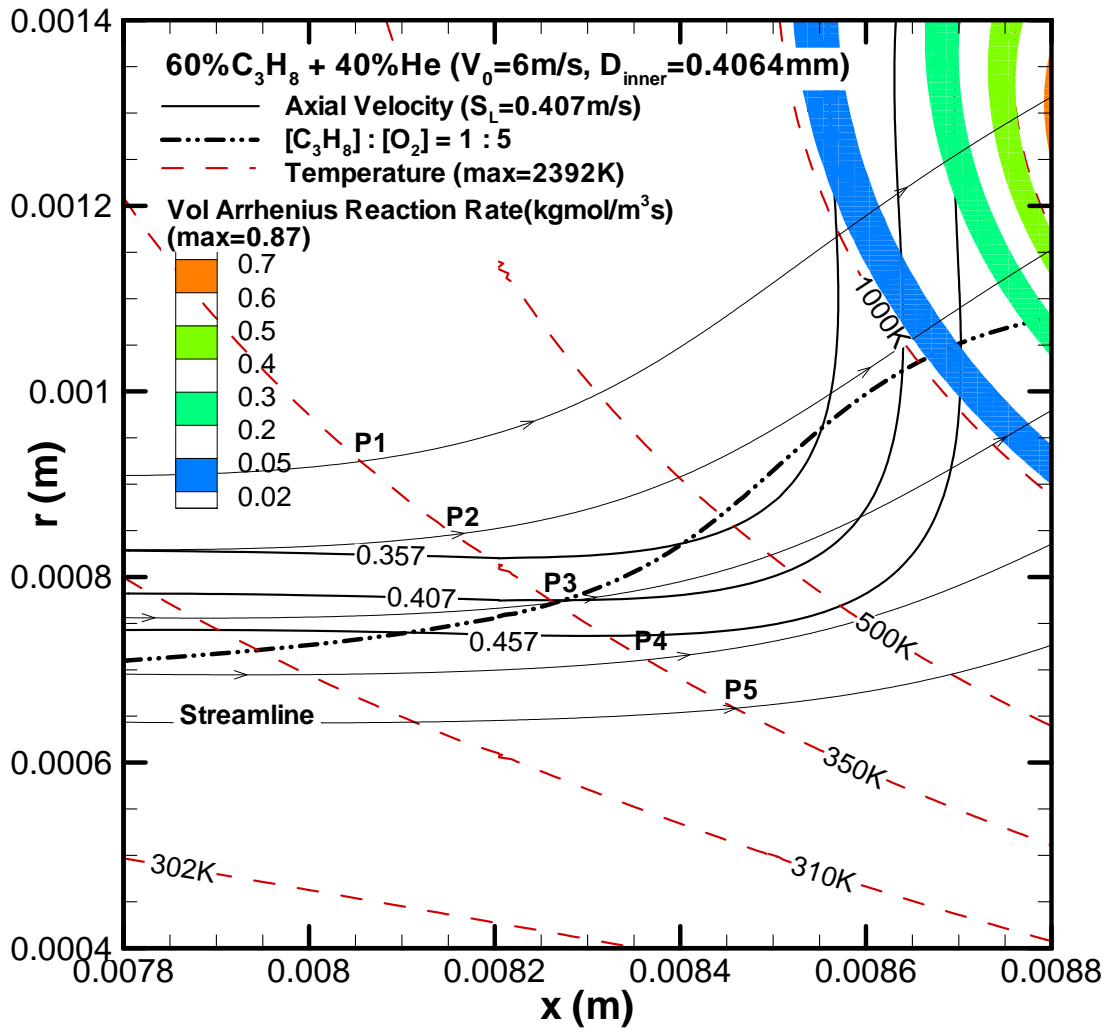

(d2) stretch rate fit along 1000 K isotherm

Figure A.2 (a - f) – (continued)
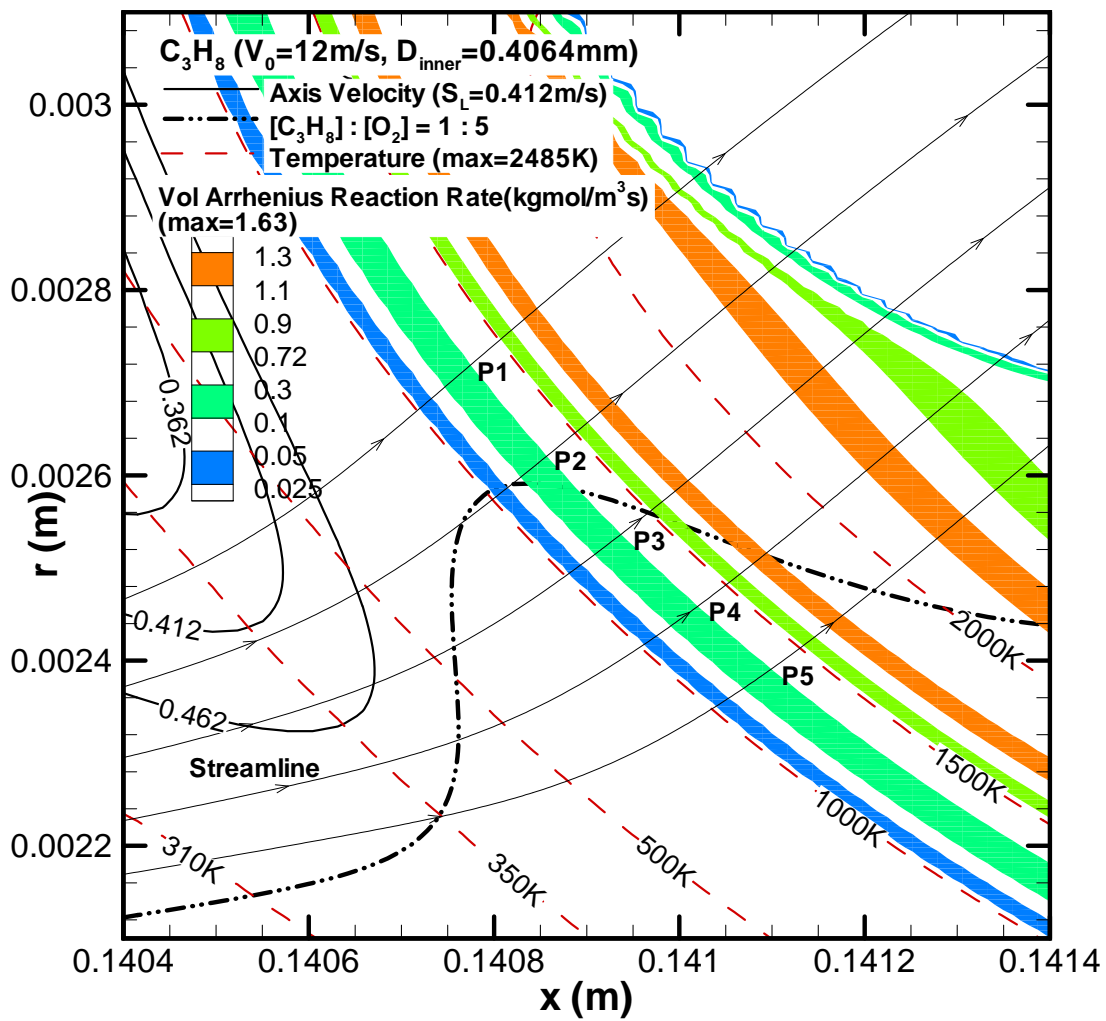
(e1) intersections of 1500 K isotherm and streamlines
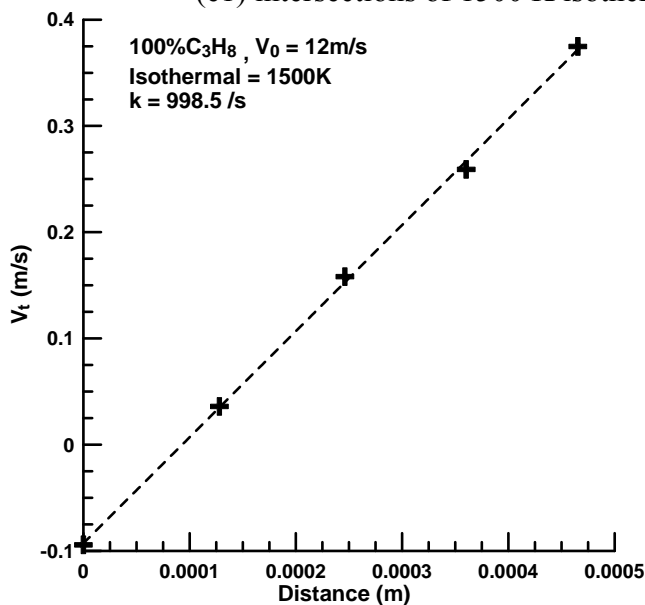
(e2) stretch rate fit along 1500 K isotherm

Figure A.2 (a - f) – (continued)
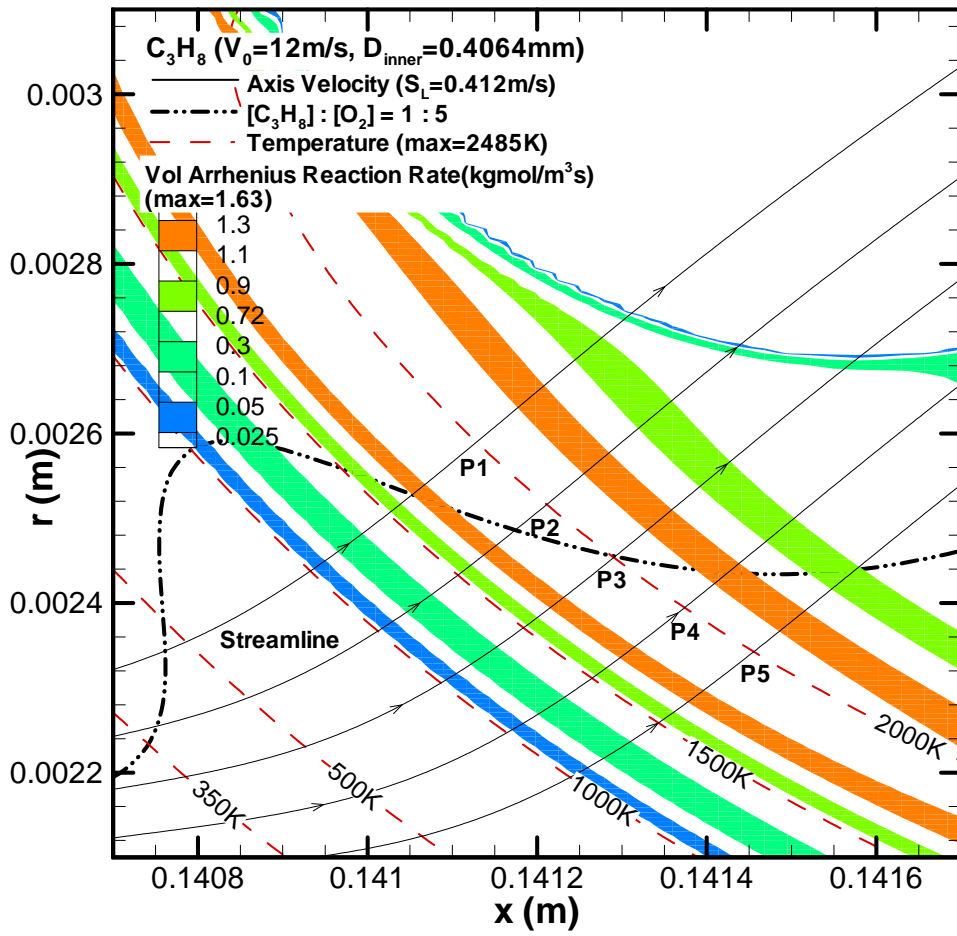
(f1) intersections of 2000 K isotherm and streamlines
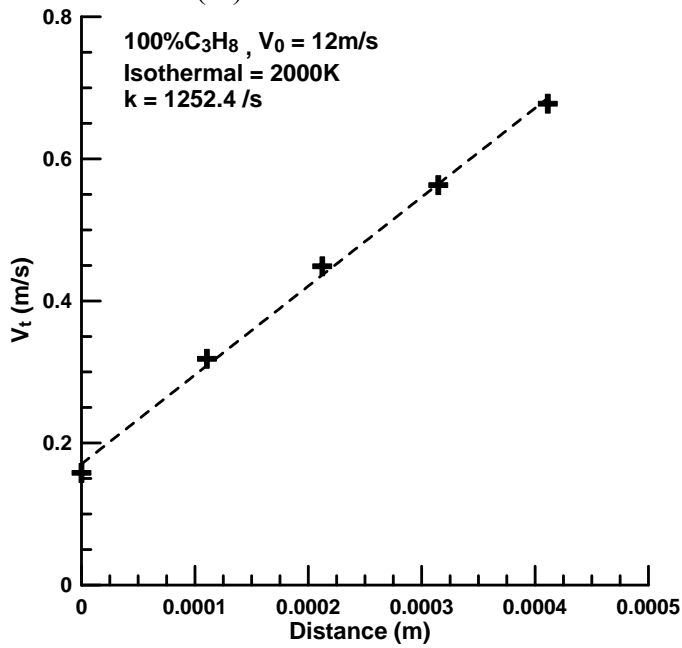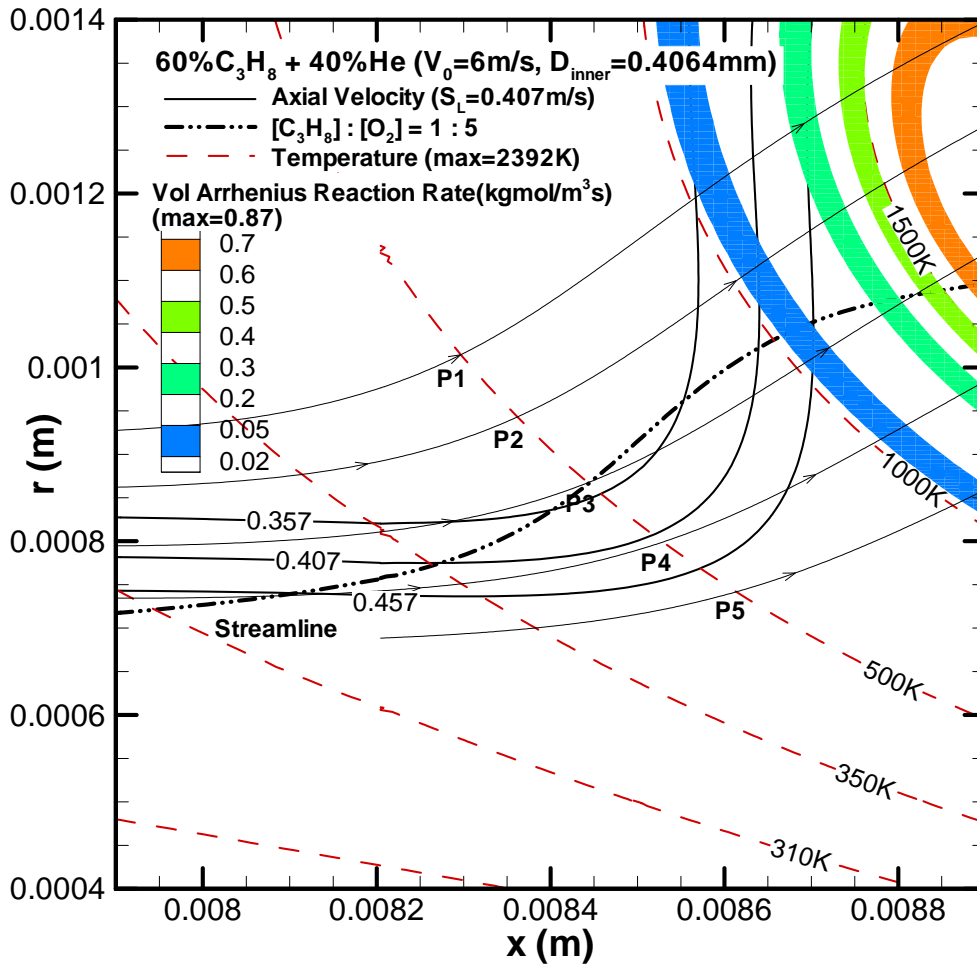

(f2) stretch rate fit along 2000 K isotherm

Figure A.2 (a - f) – (continued)
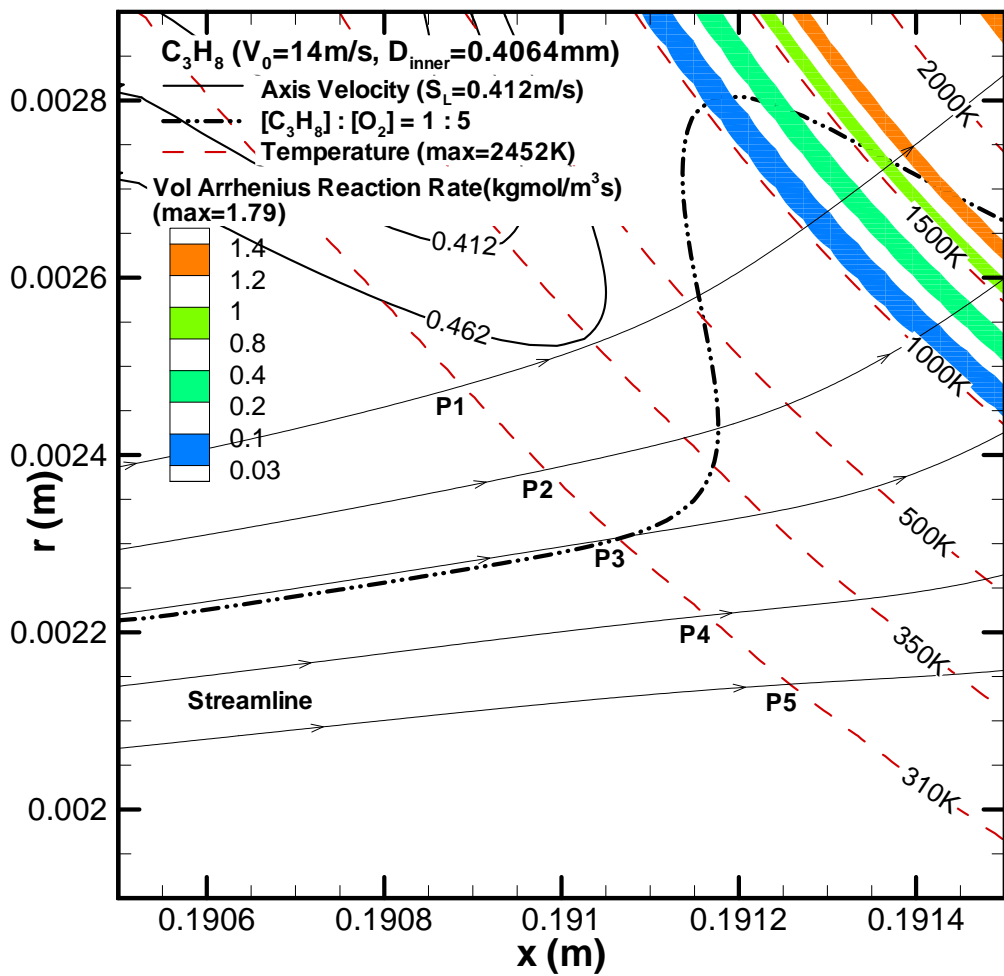
(a1) intersections of 310 K isotherm and streamlines
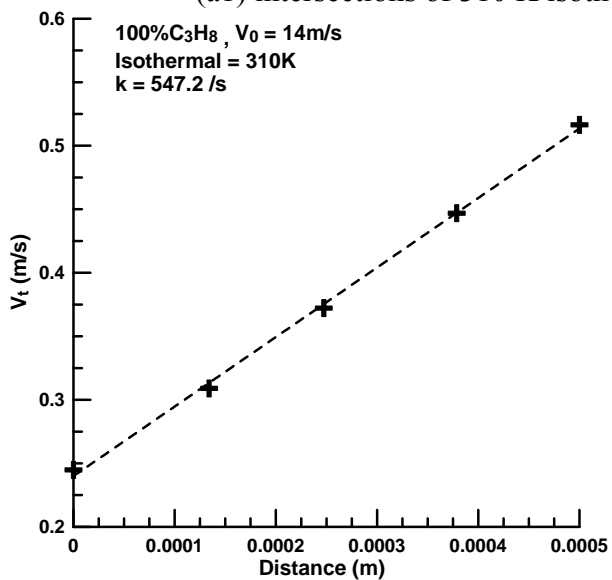
(a2) stretch rate fit along 310 K isotherm

Figure A.3 (a - f) – Interpolation around the stoichiometric line and the stretch rate fit for a variety of isotherms (310K, 350K, 500K, 1000K, 1500K and 2000K) for pure C_3H_8 at jet velocity of 14 m/s.
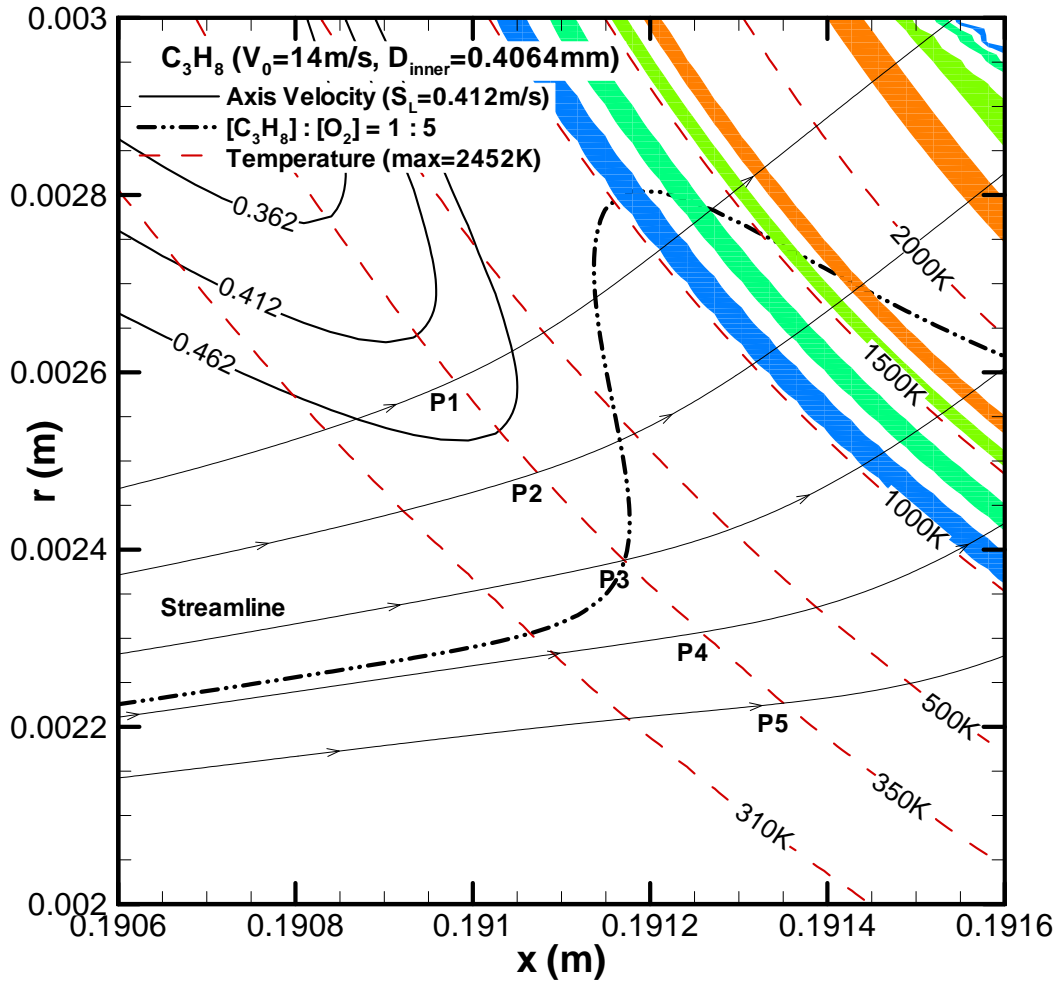
(b1) intersections of 350 K isotherm and streamlines
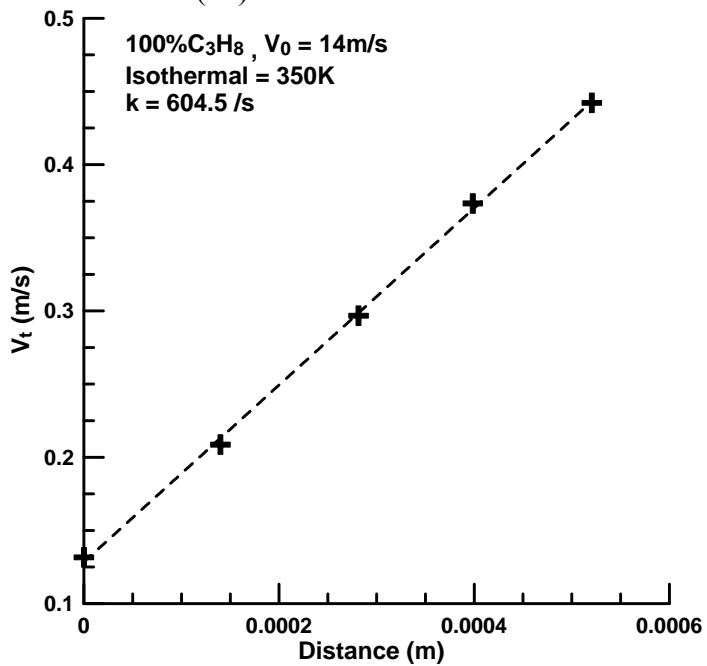
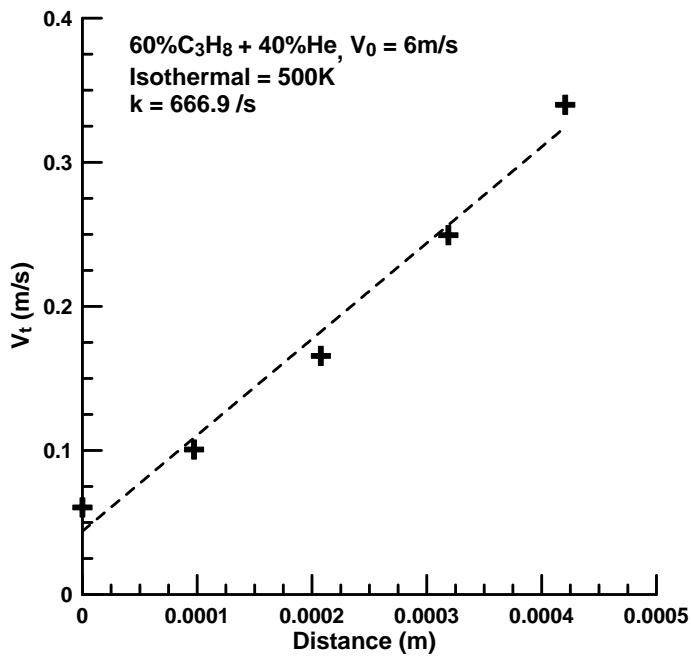(b2) stretch rate fit along 350 K isotherm

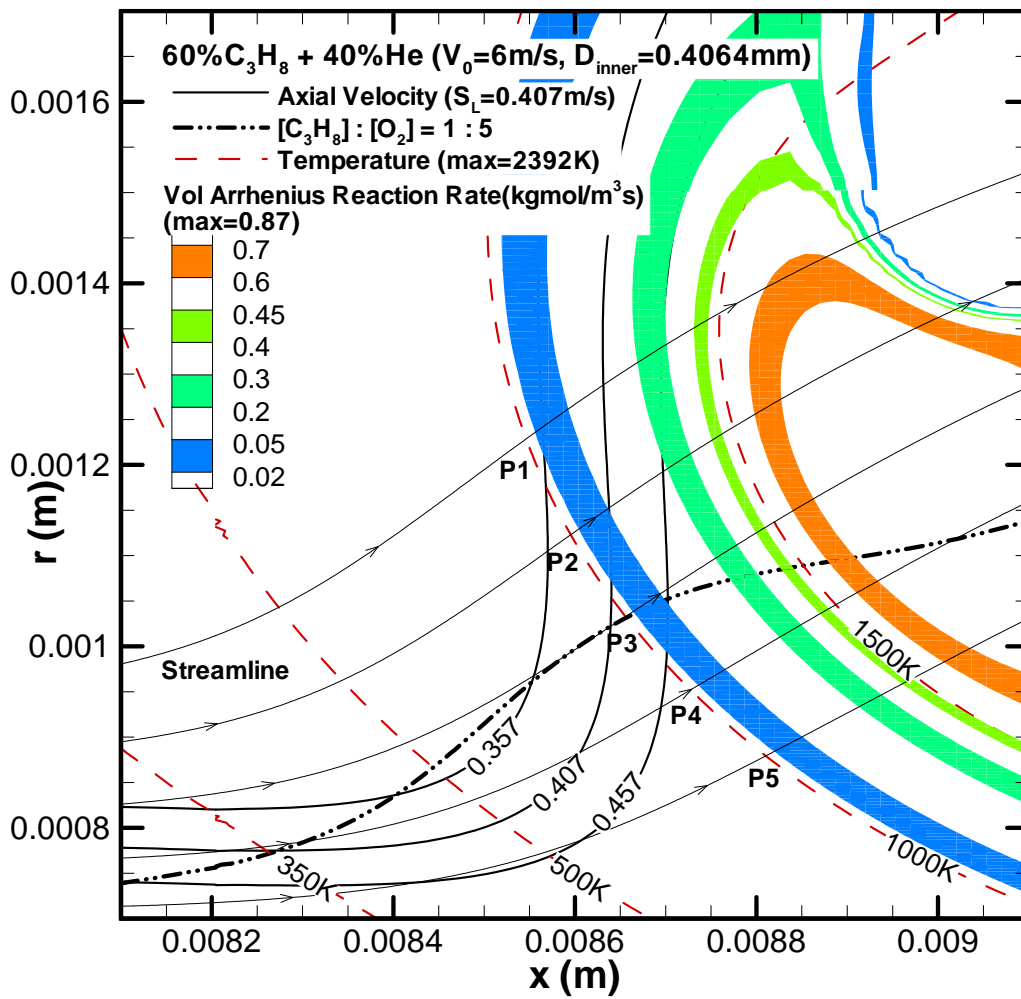Figure A.3 (a - f) – (continued)
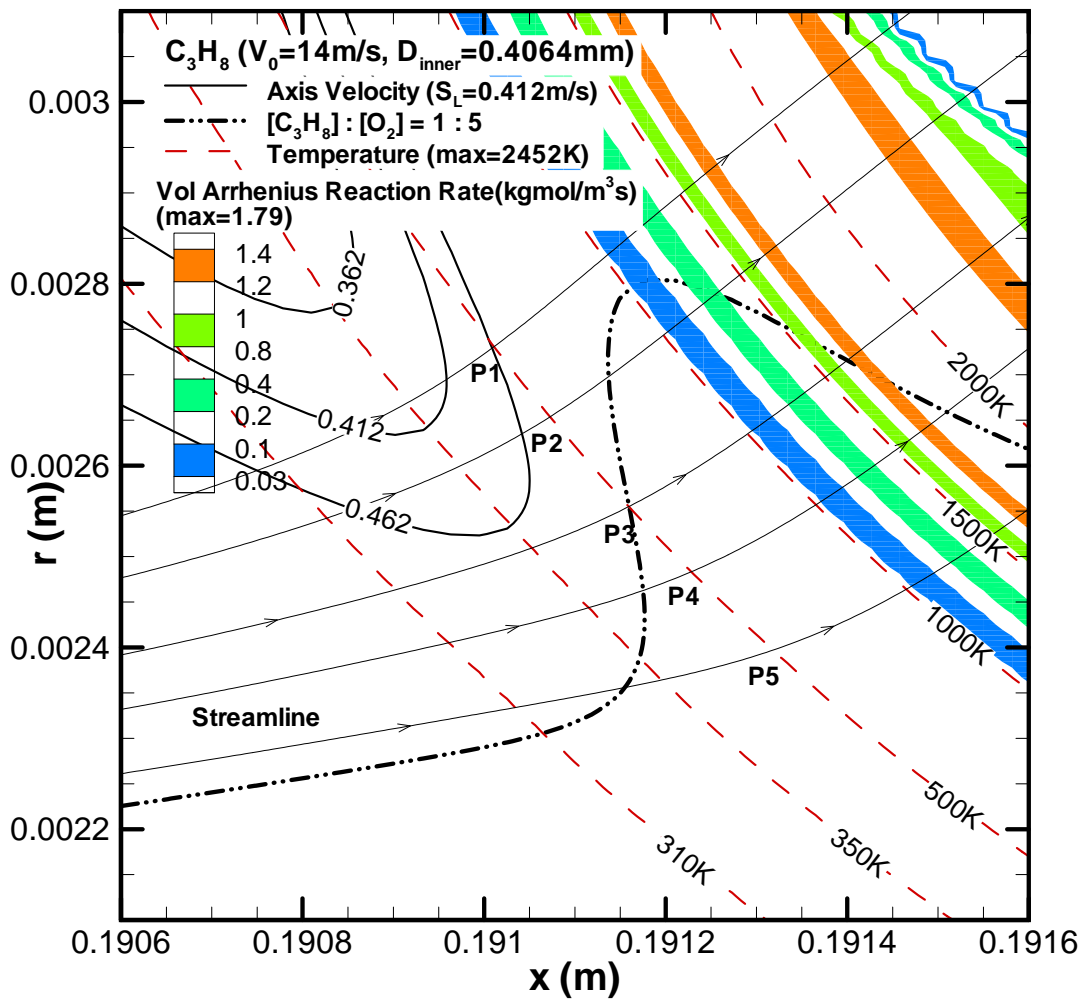
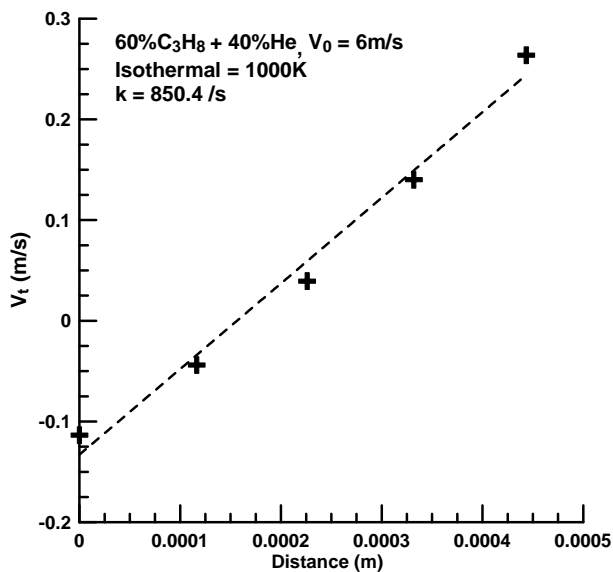(c1) intersections of 500 K isotherm and streamlines
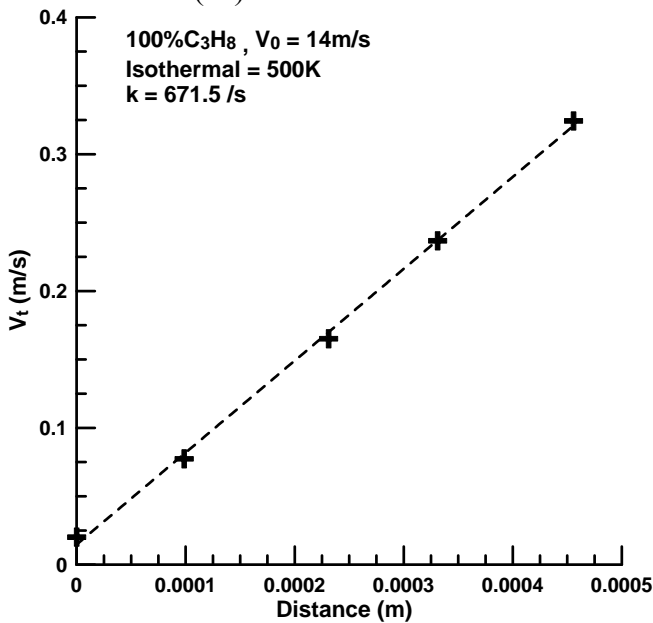
(c2) stretch rate fit along 500 K isotherm
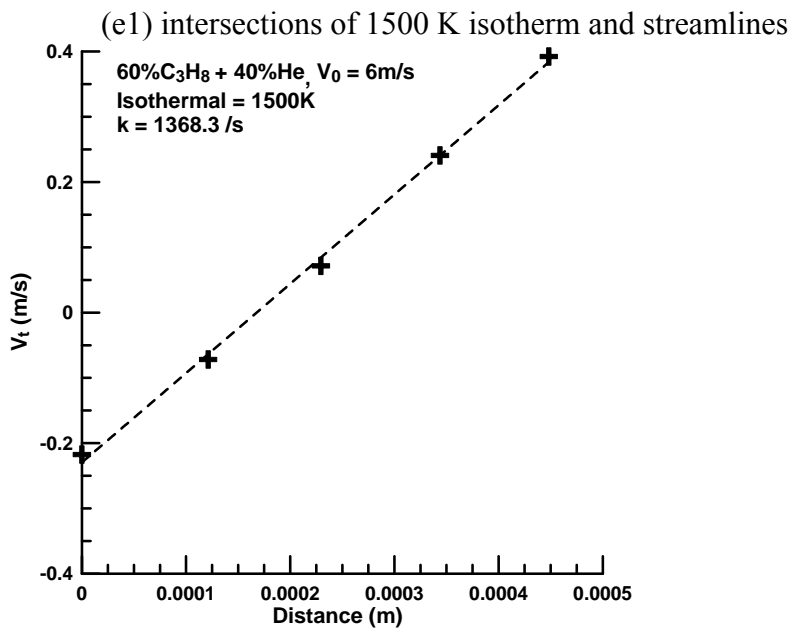
Figure A.3 (a - f) – (continued)
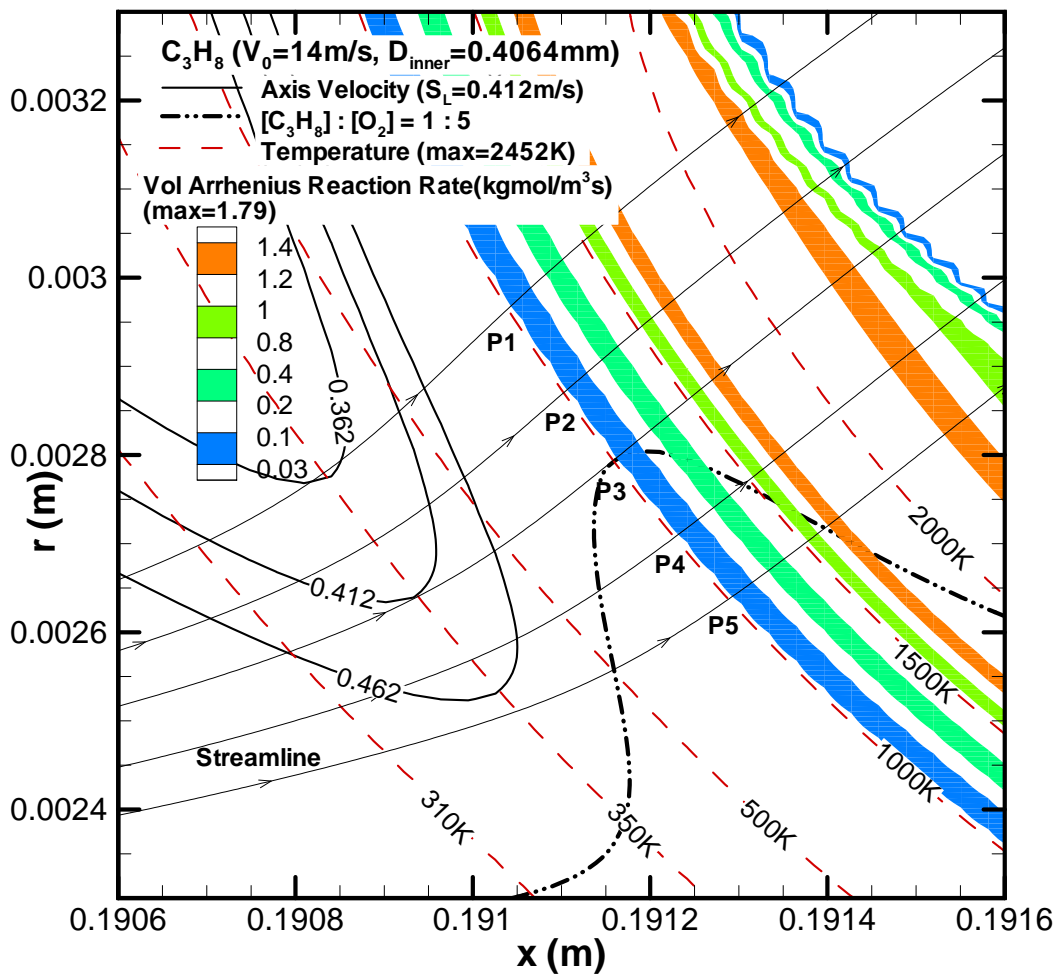
(d1) intersections of 1000 K isotherm and streamlines
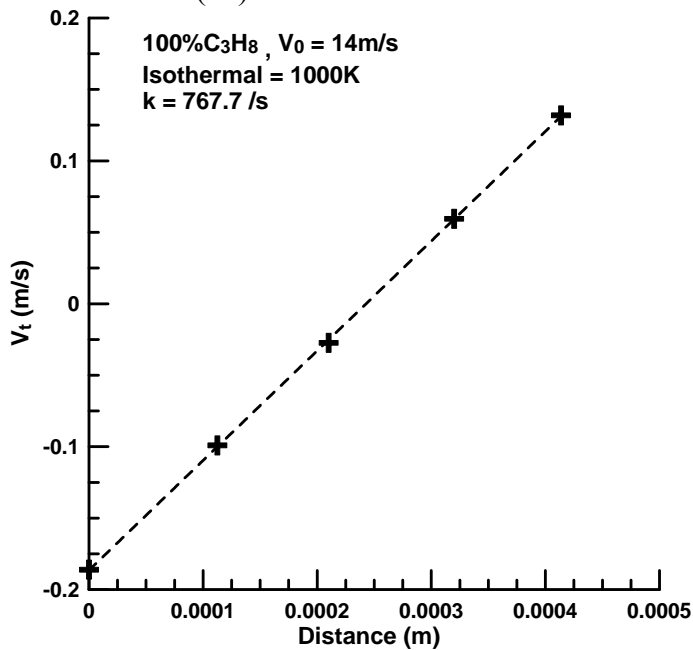
(d2) stretch rate fit along 1000 K isotherm

Figure A.3 (a - f) – (continued)
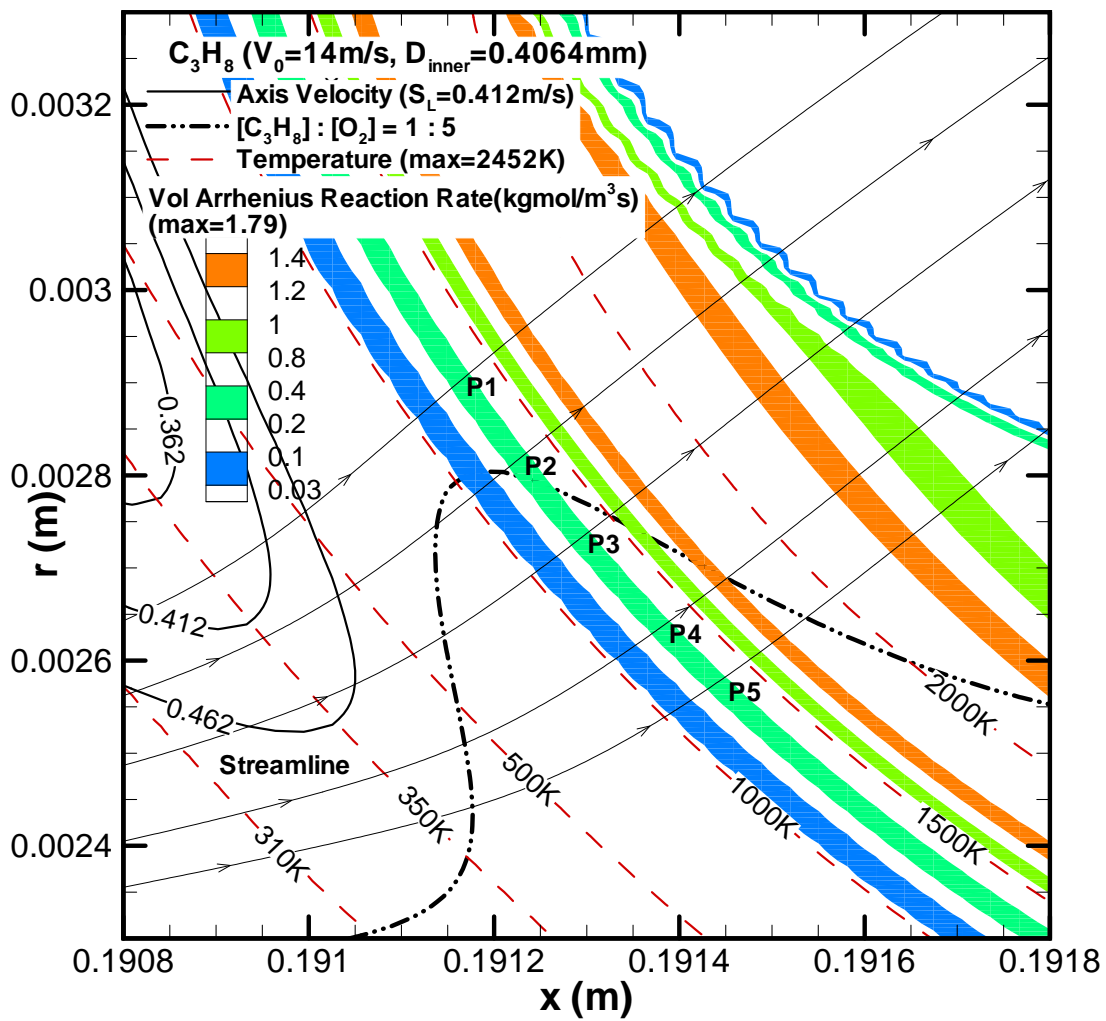
(e1) intersections of 1500 K isotherm and streamlines
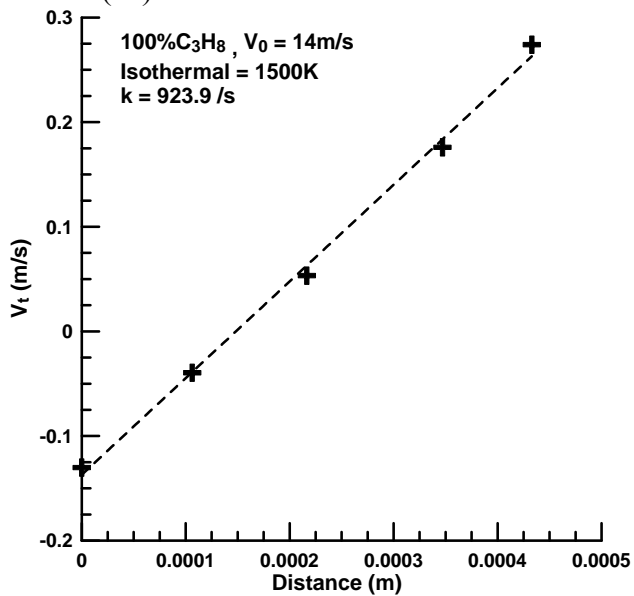
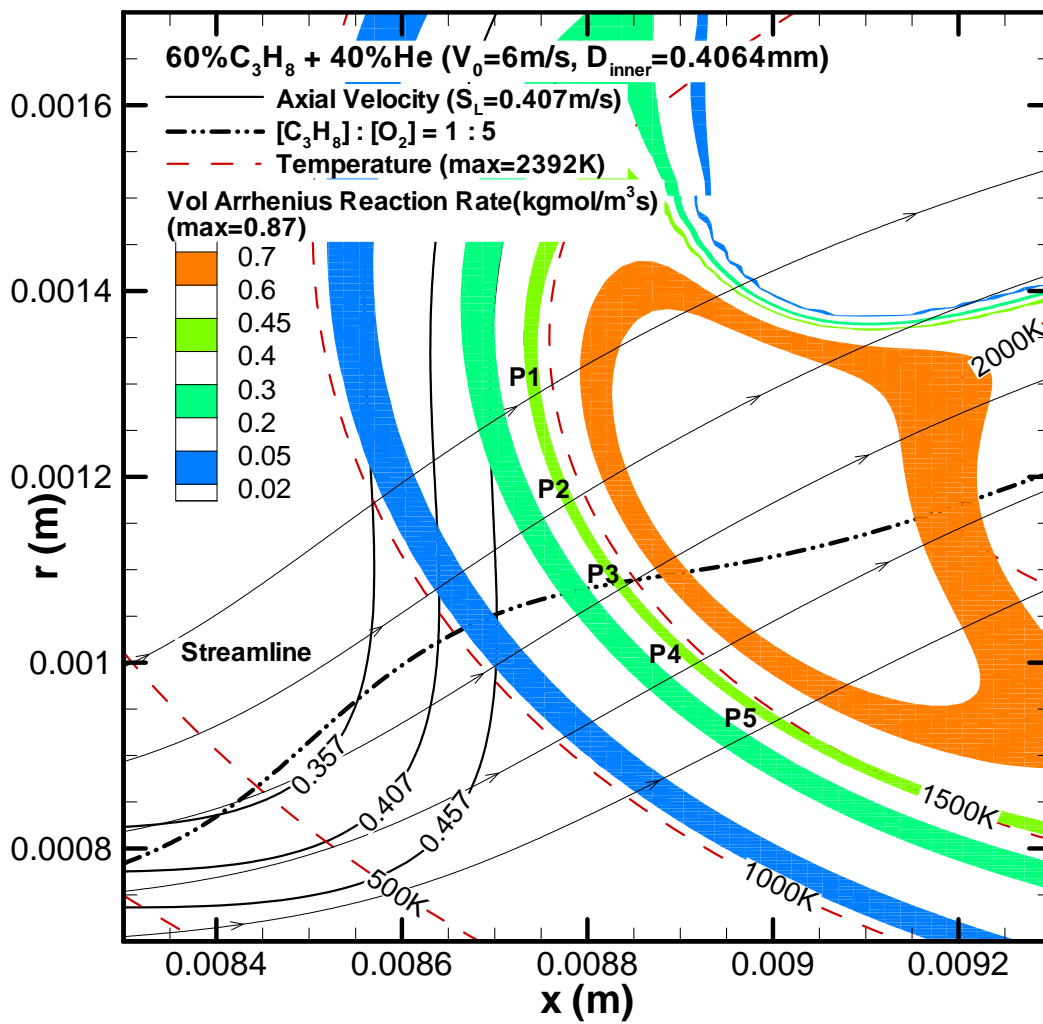(e2) stretch rate fit along 1500 K isotherm

Figure A.3 (a - f) – (continued)
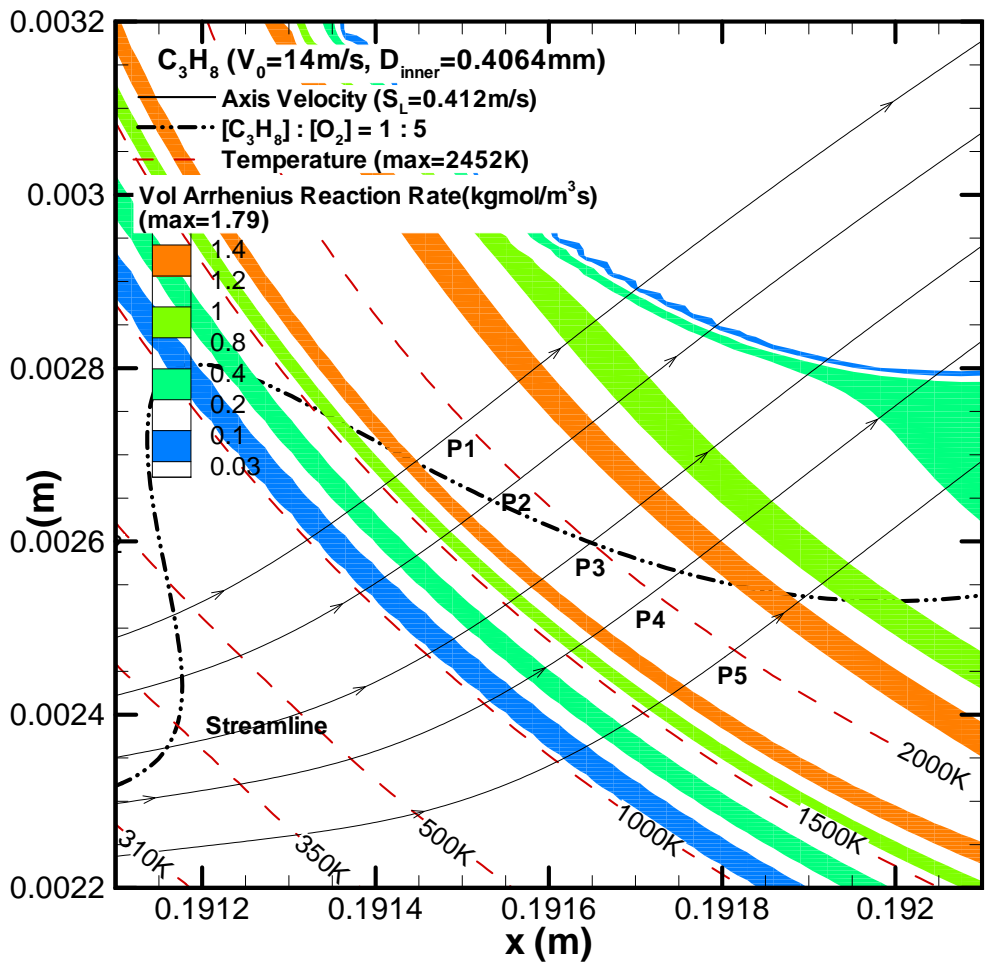
(f1) intersections of 2000 K isotherm and streamlines
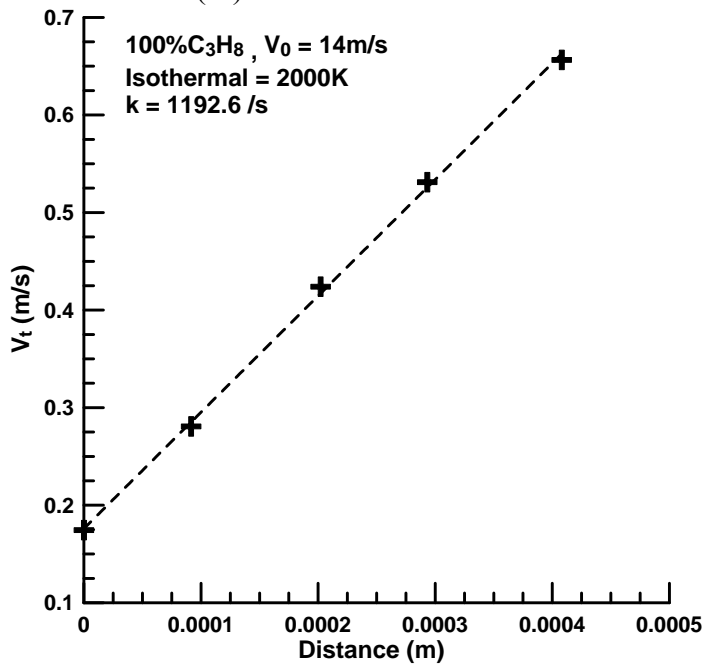
(f2) stretch rate fit along 2000 K isotherm

Figure A.3 (a - f) – (continued)
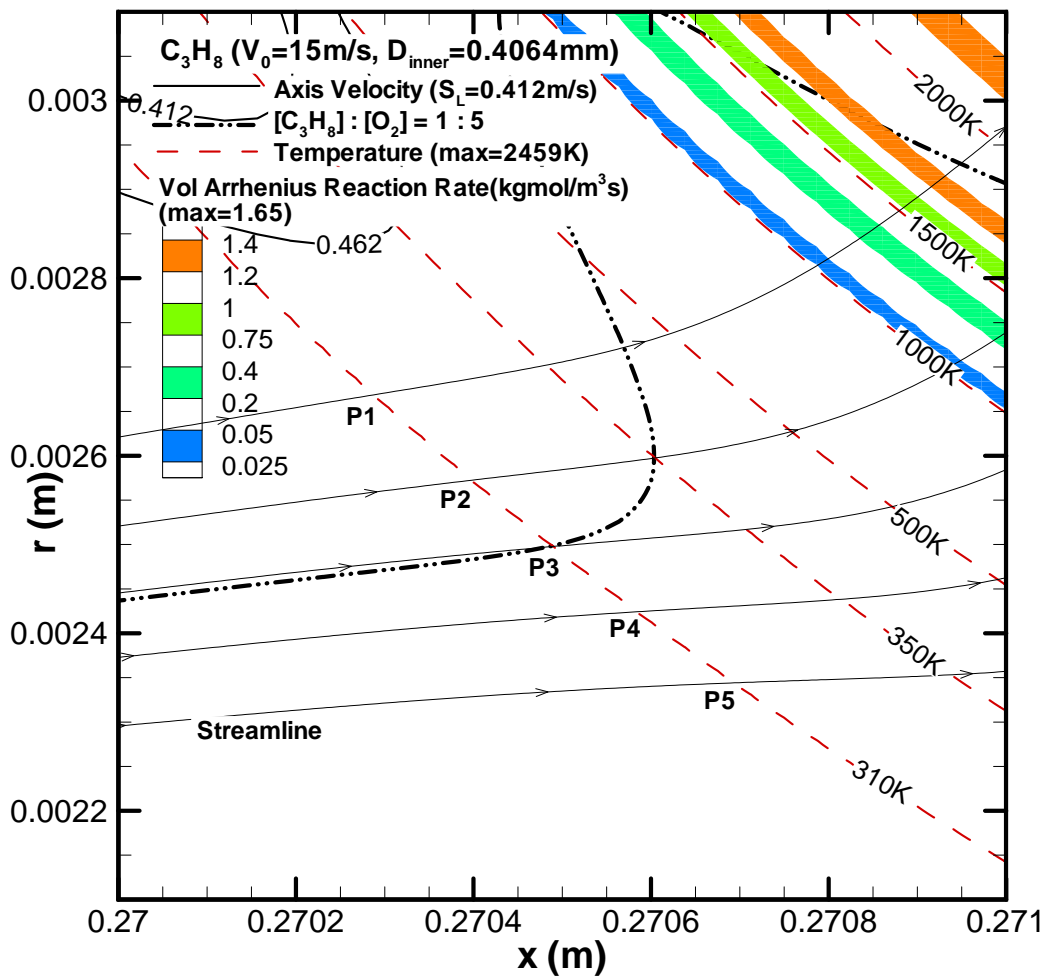
(a1) intersections of 310 K isotherm and streamlines
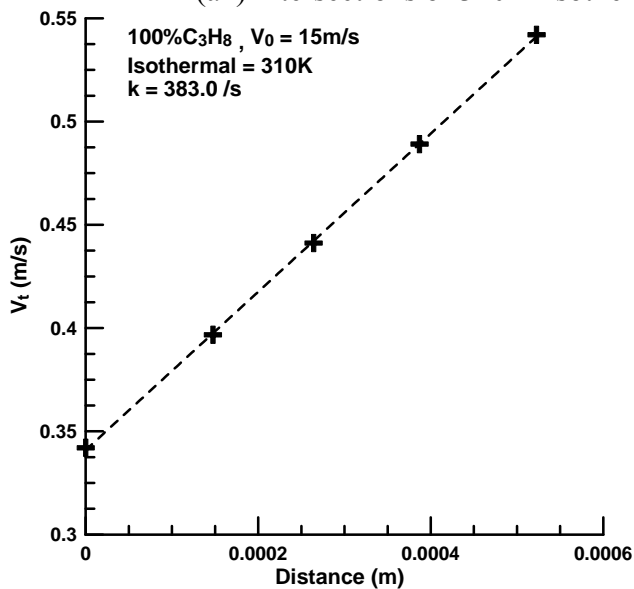
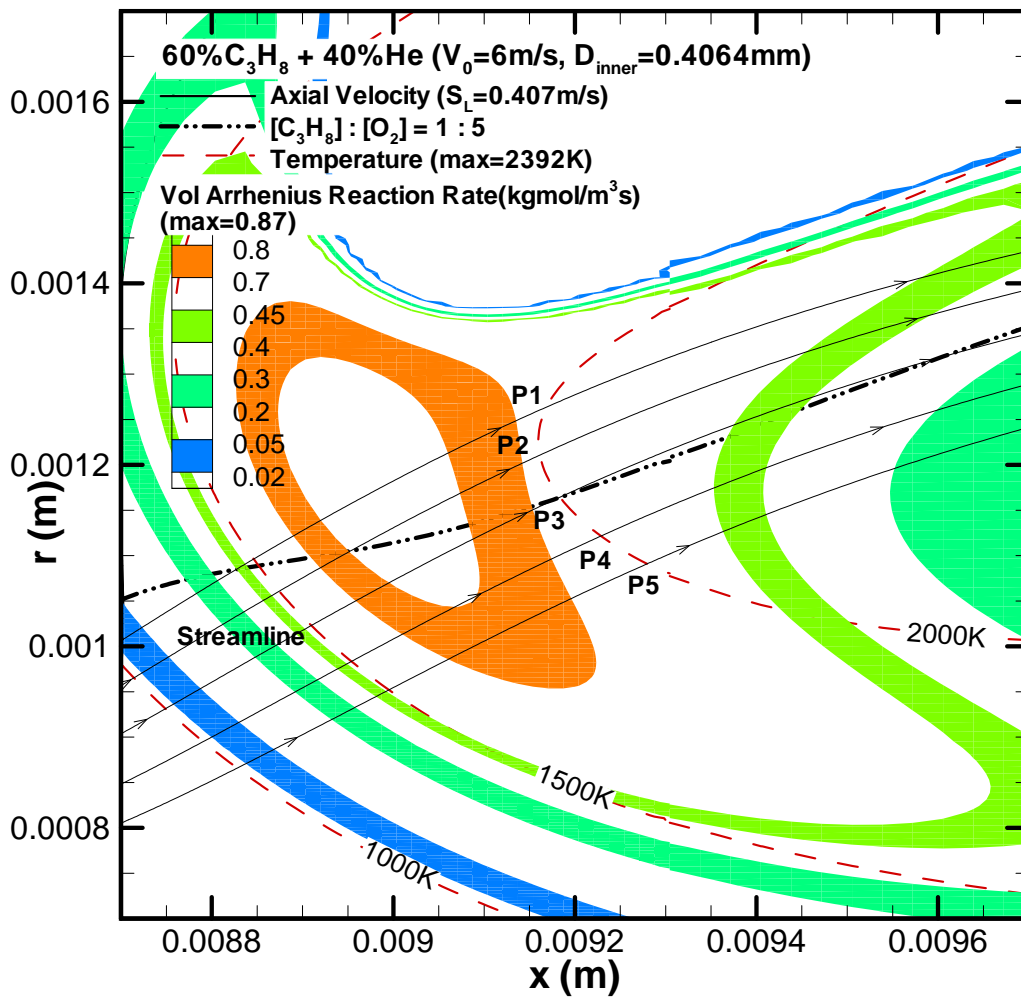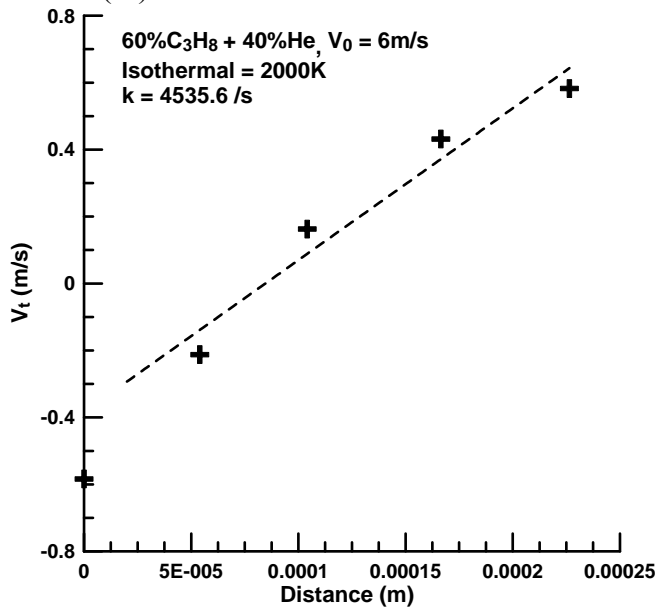(a2) stretch rate fit along 310 K isotherm

Figure A.4 (a - f) – Interpolation around the stoichiometric line and the stretch rate fit for a variety of isotherms (310K, 350K, 500K, 1000K, 1500K and 2000K) for pure C_3H_8 at jet velocity of 15 m/s.
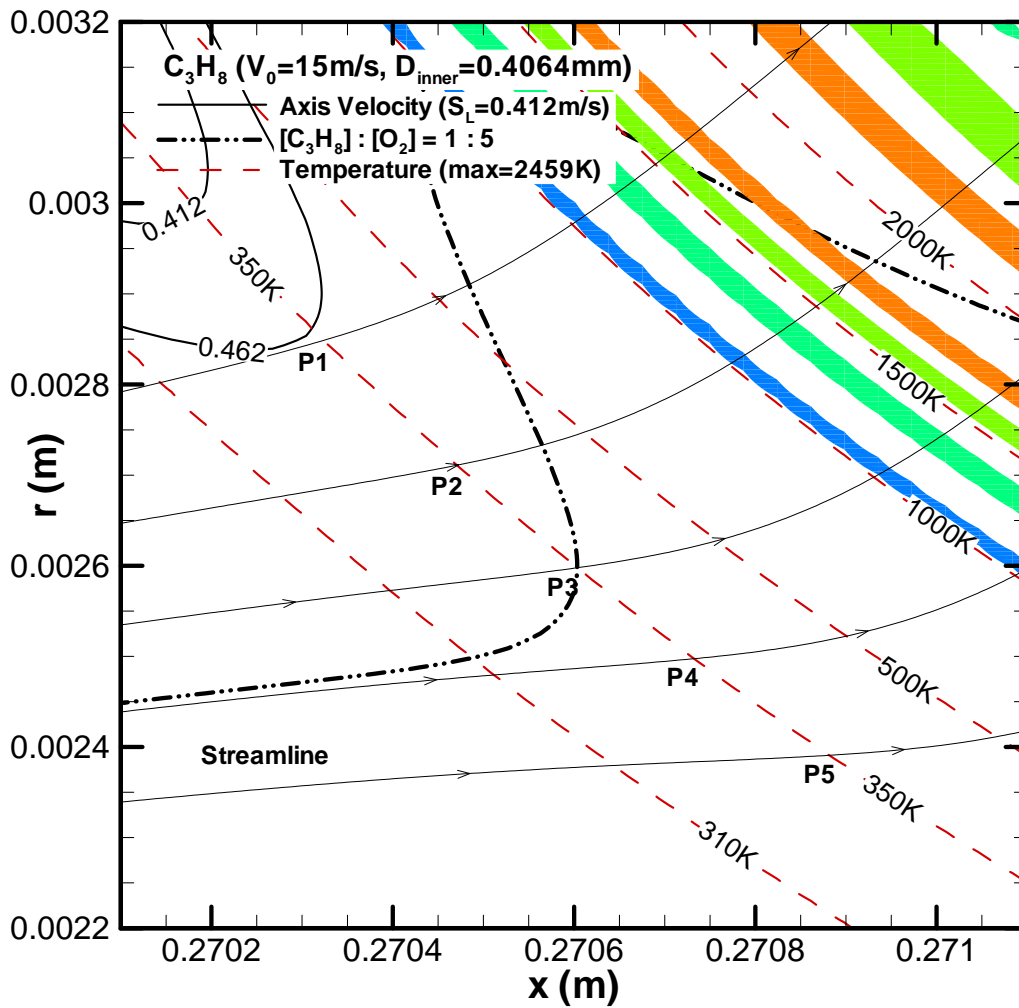
(b1) intersections of 350 K isotherm and streamlines
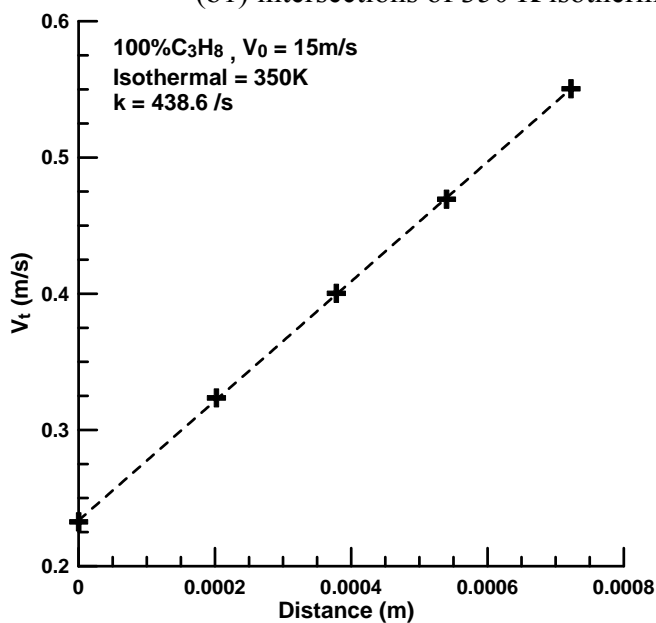
(b2) stretch rate fit along 350 K isotherm

Figure A.4 (a - f) – (continued)
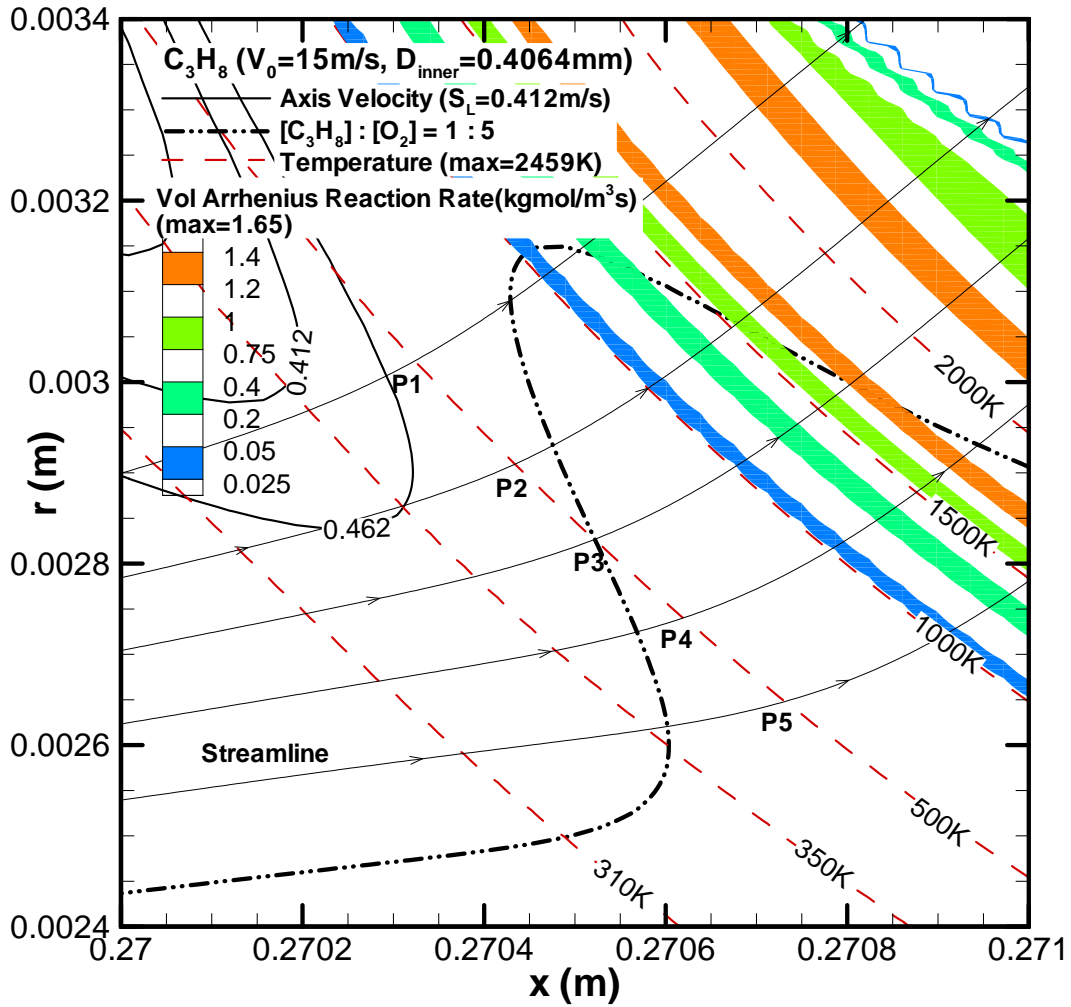
(c1) intersections of 500 K isotherm and streamlines
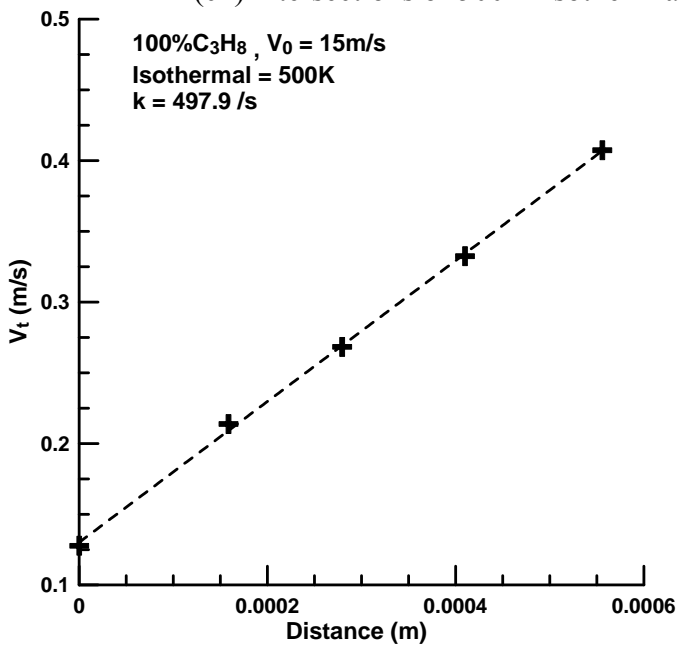
(c2) stretch rate fit along 500 K isotherm
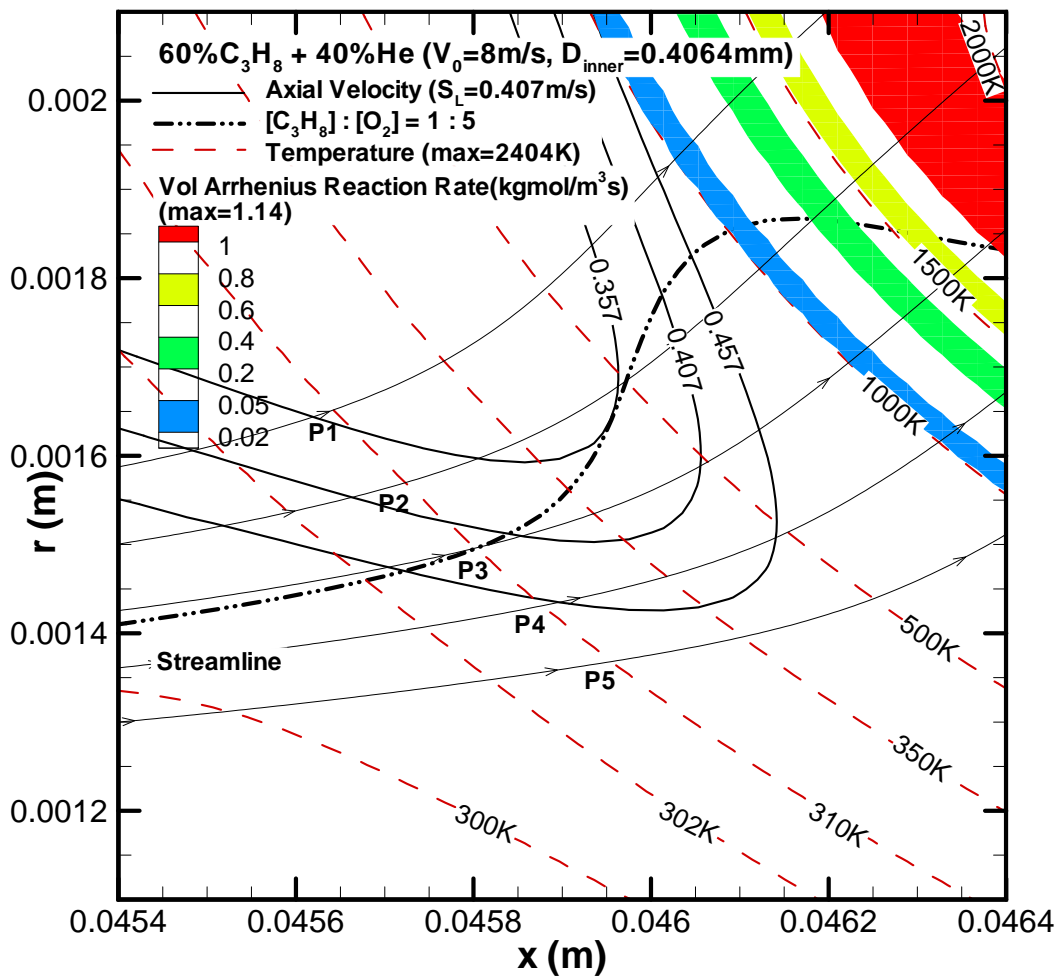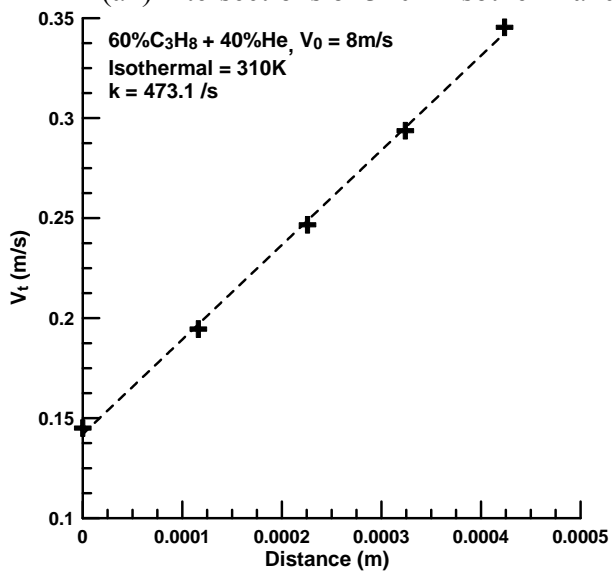
Figure A.4 (a - f) – (continued)
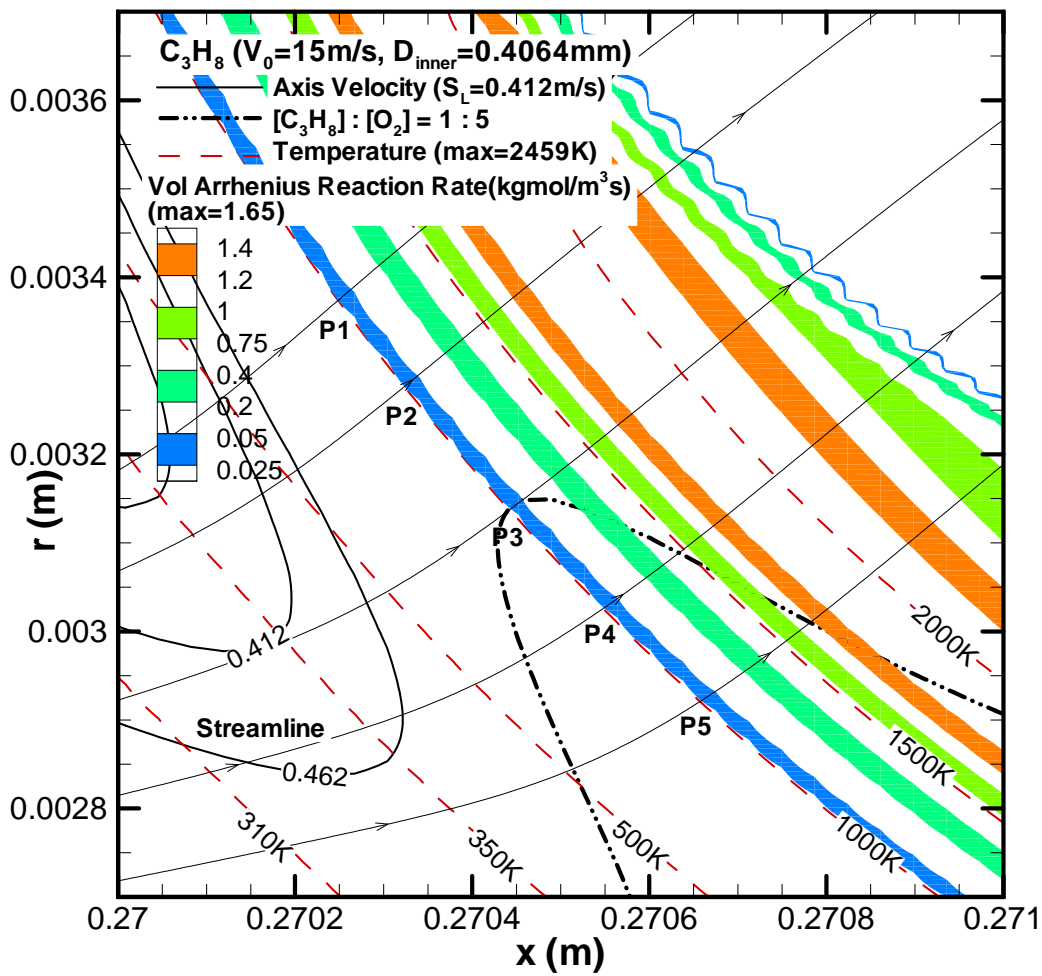
(d1) intersections of 1000 K isotherm and streamlines
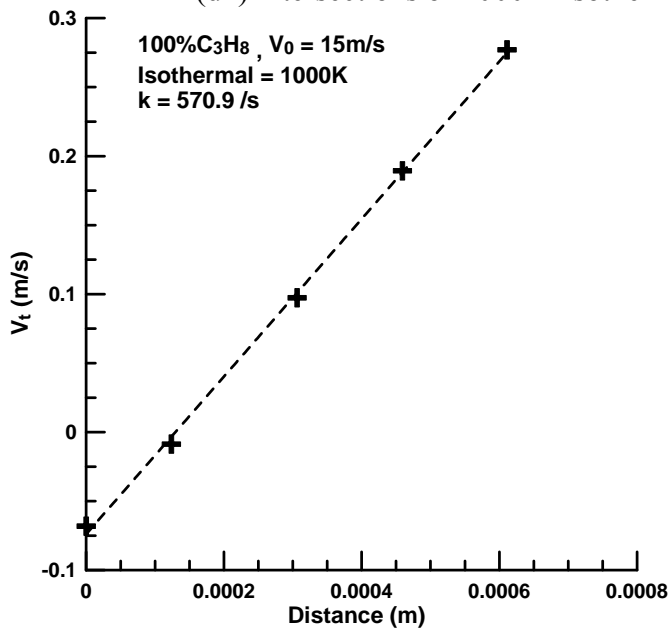
(d2) stretch rate fit along 1000 K isotherm

Figure A.4 (a - f) – (continued)
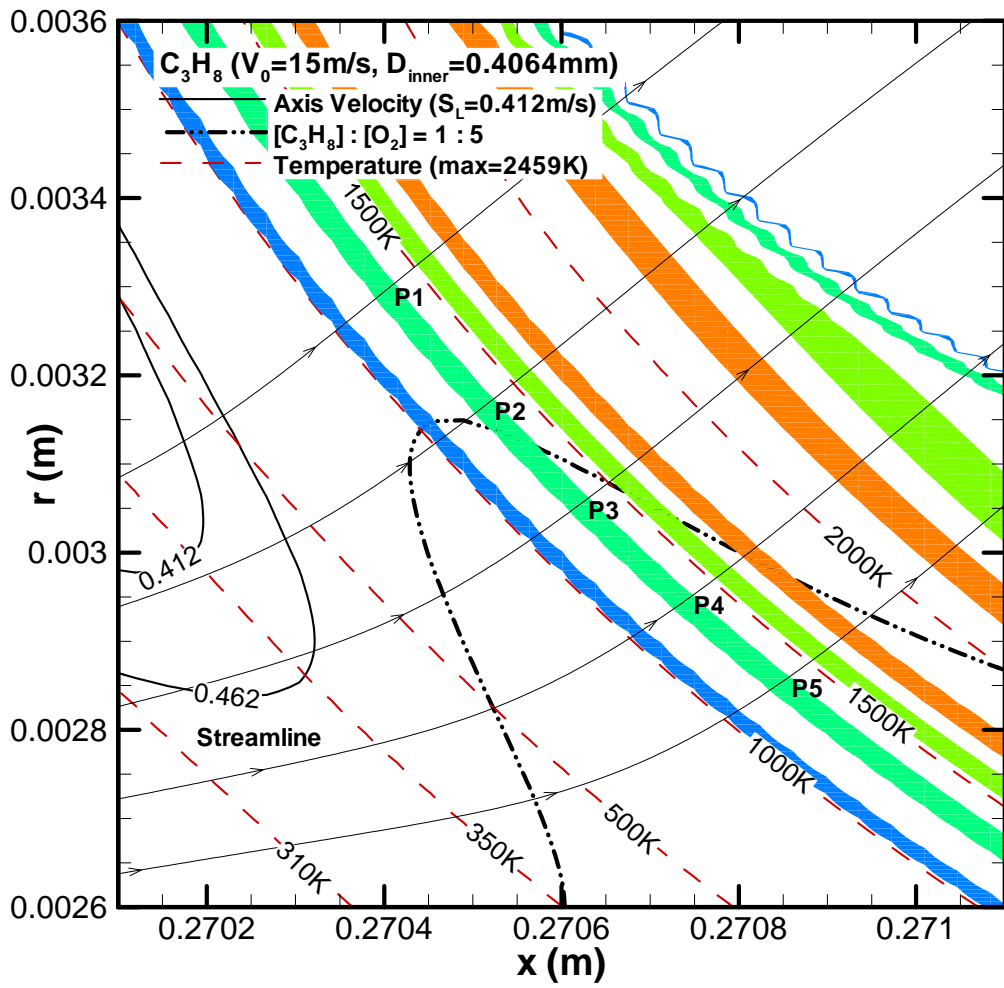
(e1) intersections of 1500 K isotherm and streamlines
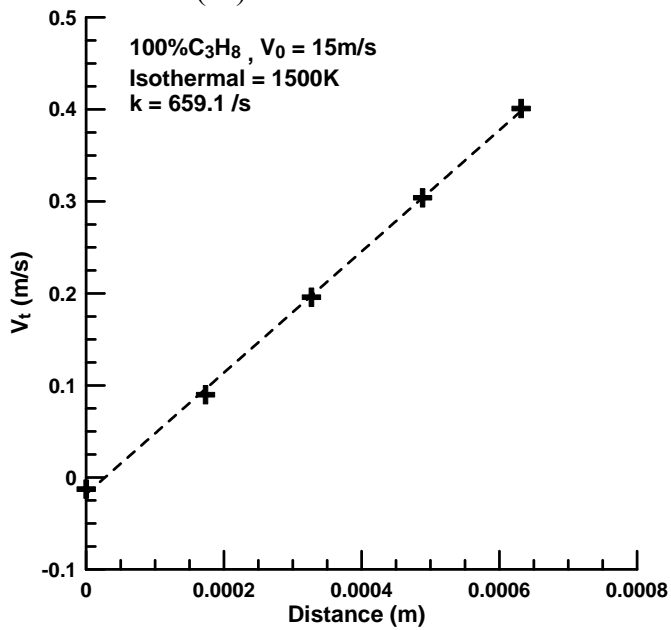
(e2) stretch rate fit along 1500 K isotherm

Figure A.4 (a - f) – (continued)
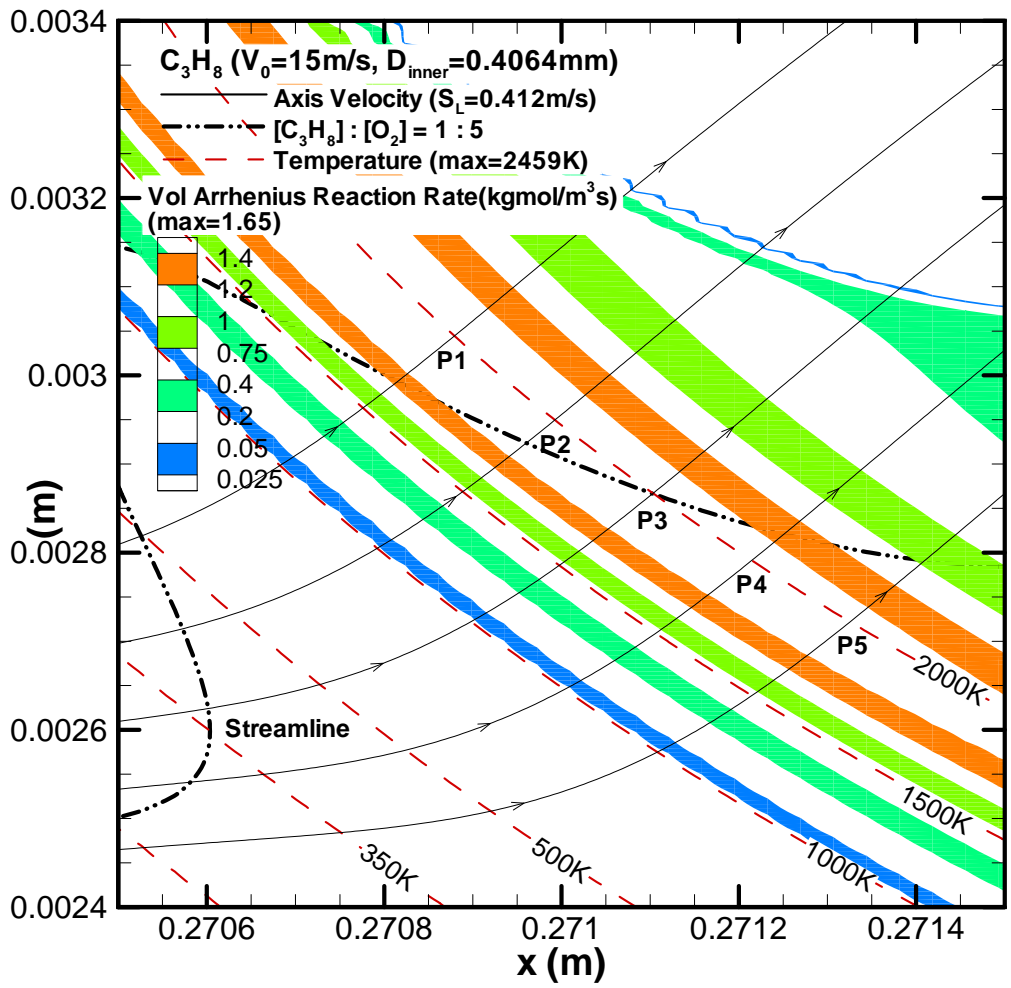
(f1) intersections of 2000 K isotherm and streamlines
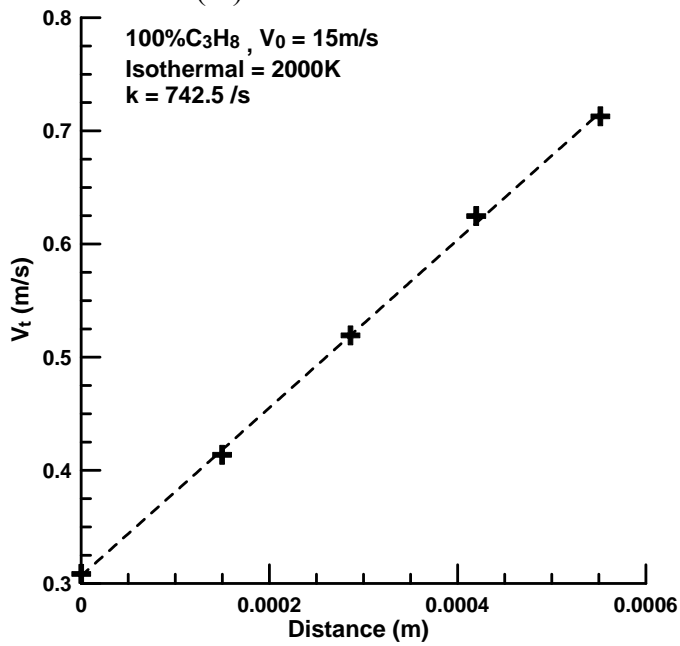
(f2) stretch rate fit along 2000 K isotherm

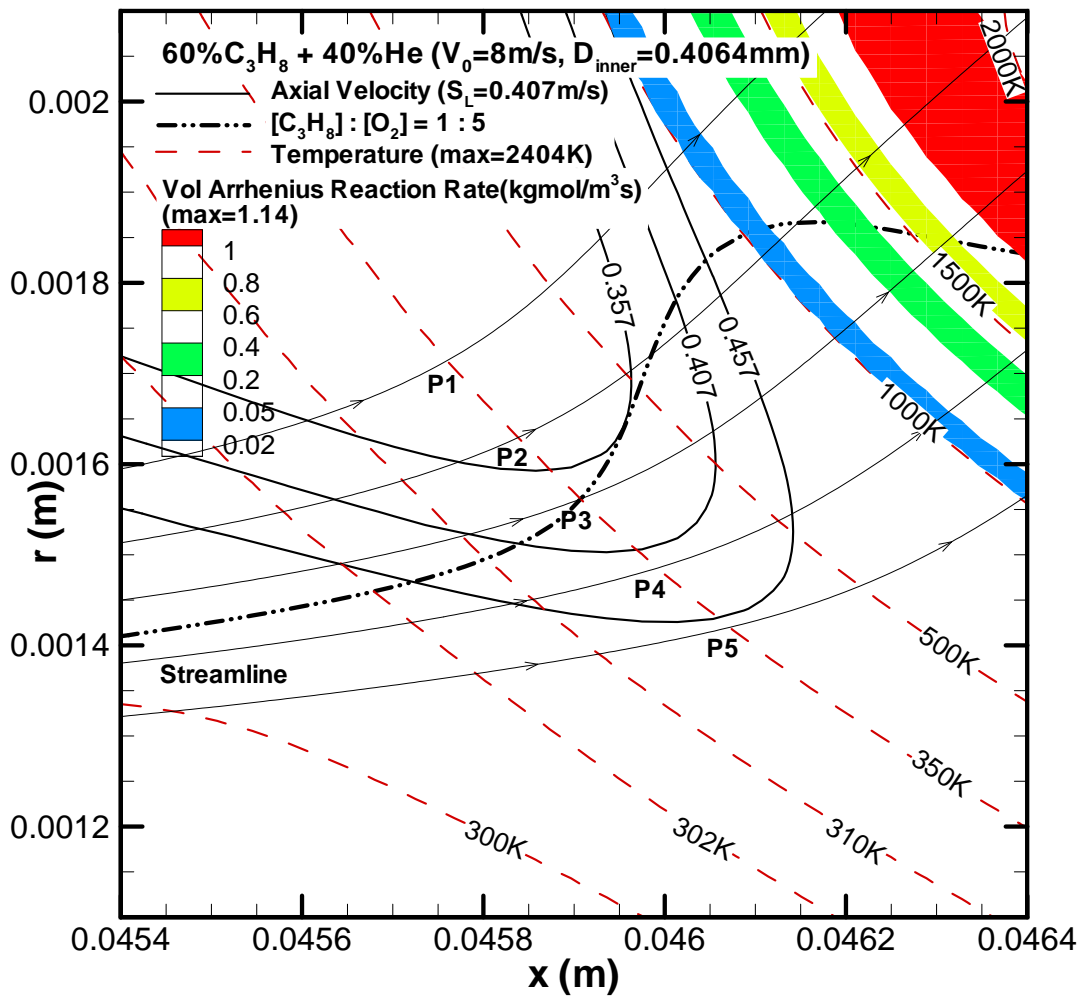Figure A.4 (a - f) – (continued)
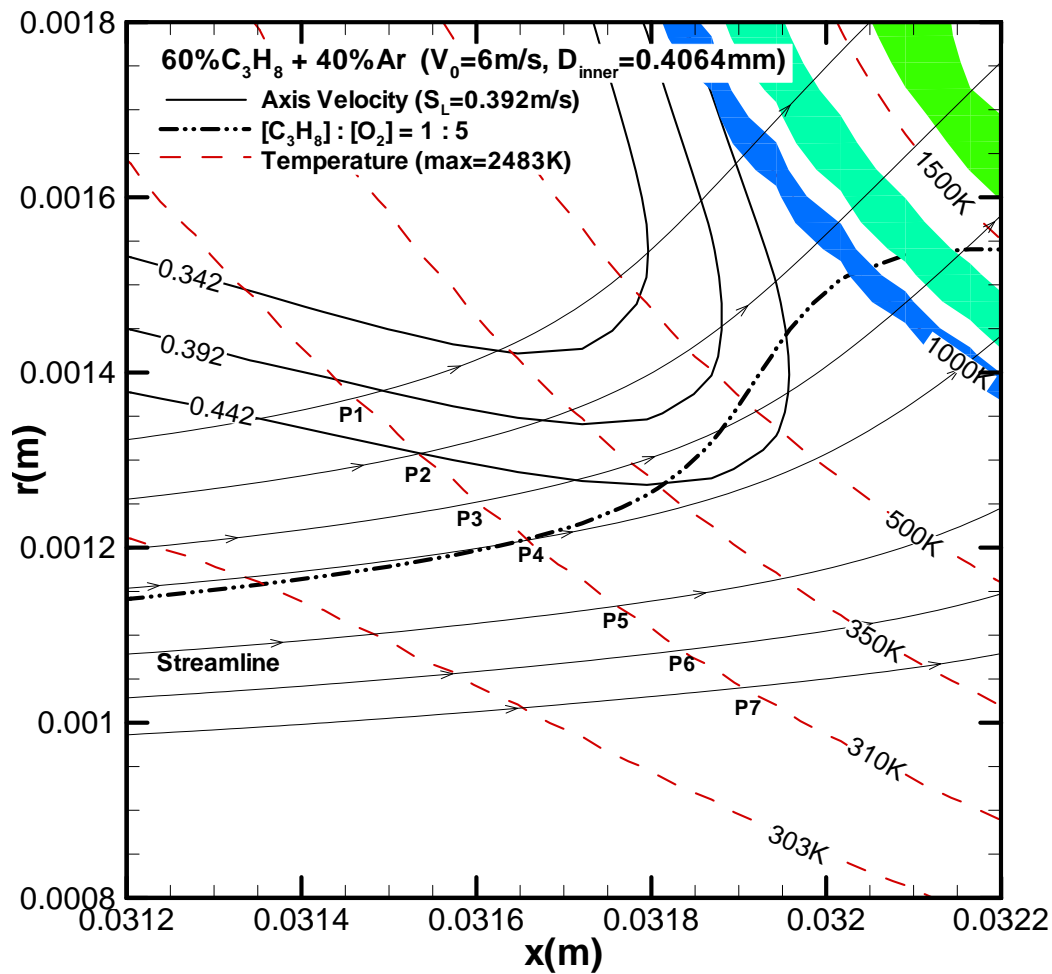
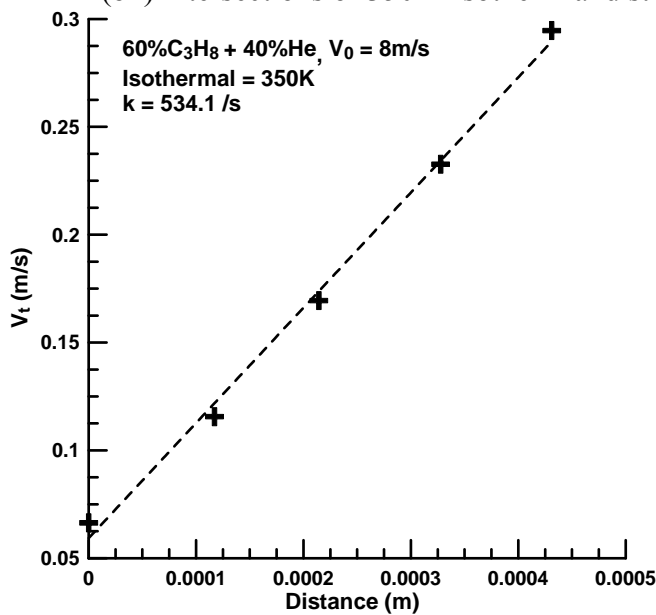(a1) intersections of 310 K isotherm and streamlines
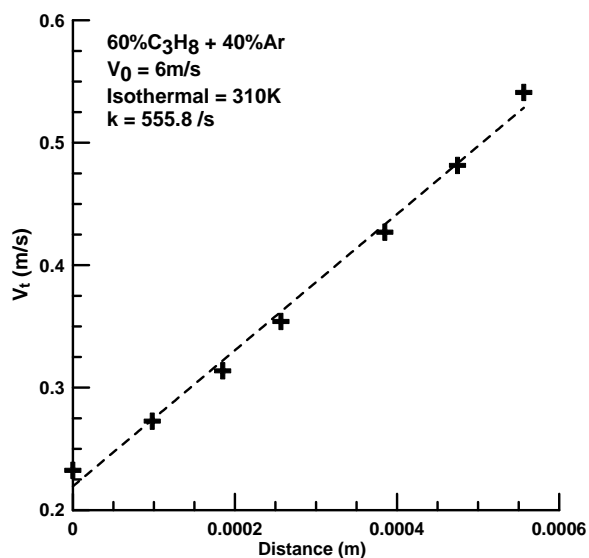
(a2) stretch rate fit along 310 K isotherm

Figure A.5 (a - f) – Interpolation around the stoichiometric line and the stretch rate fit for a variety of isotherms (310K, 350K, 500K, 1000K, 1500K and 2000K) for 60% C_3H_8 with 40% Ar dilution at jet velocity of 6 m/s.
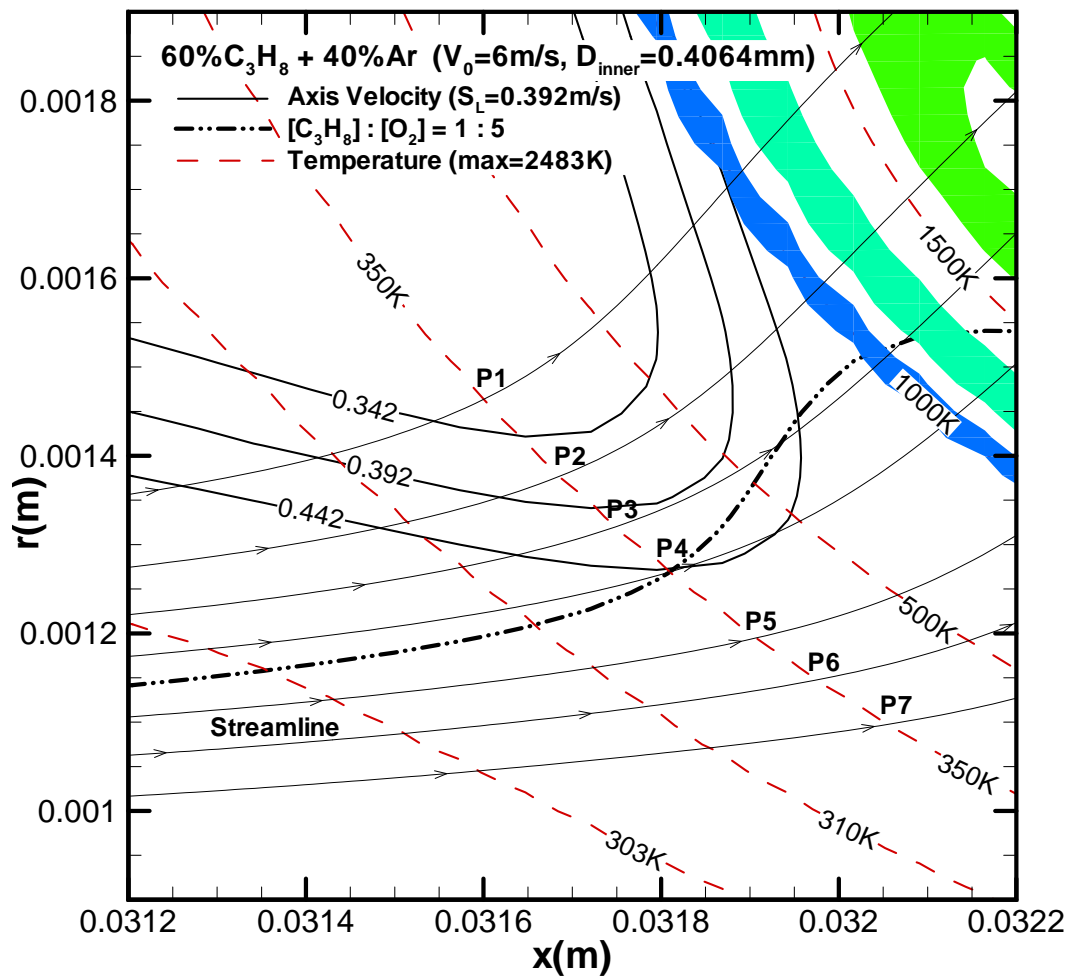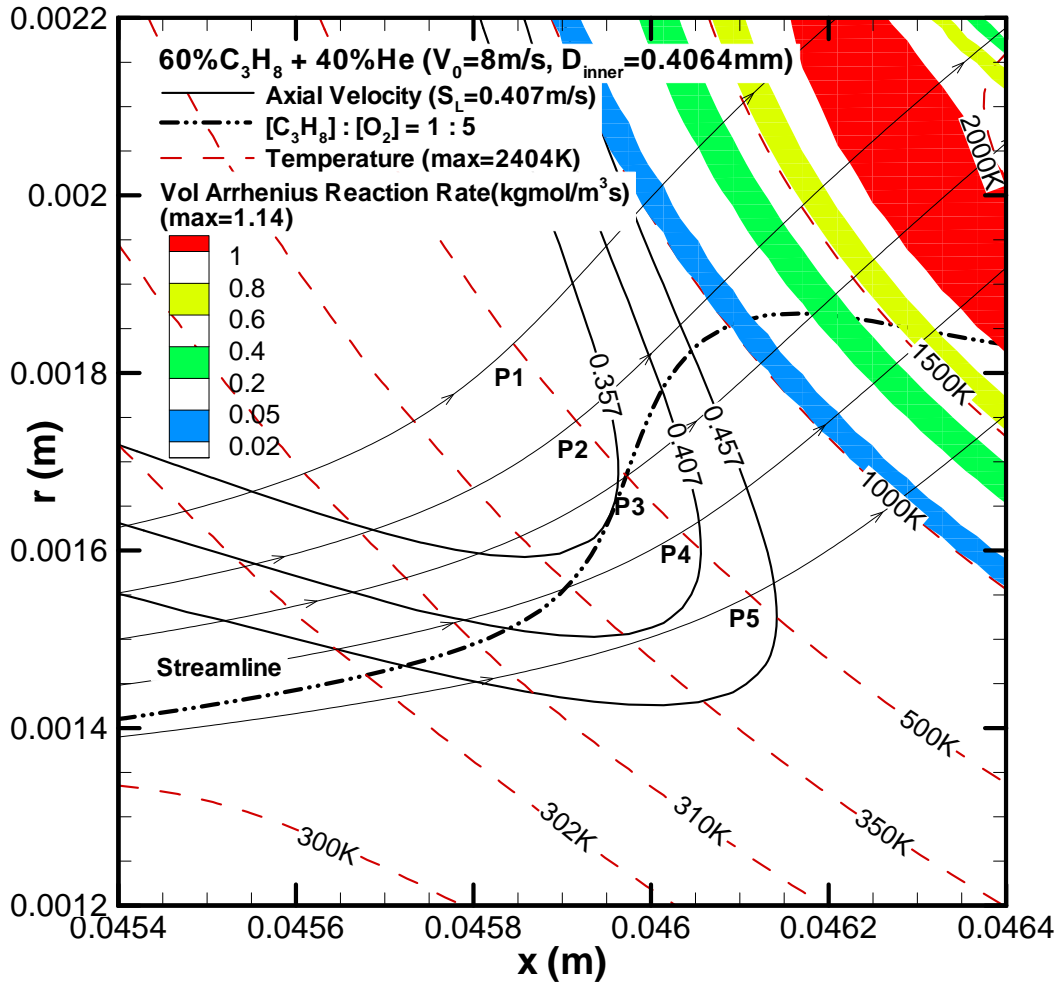
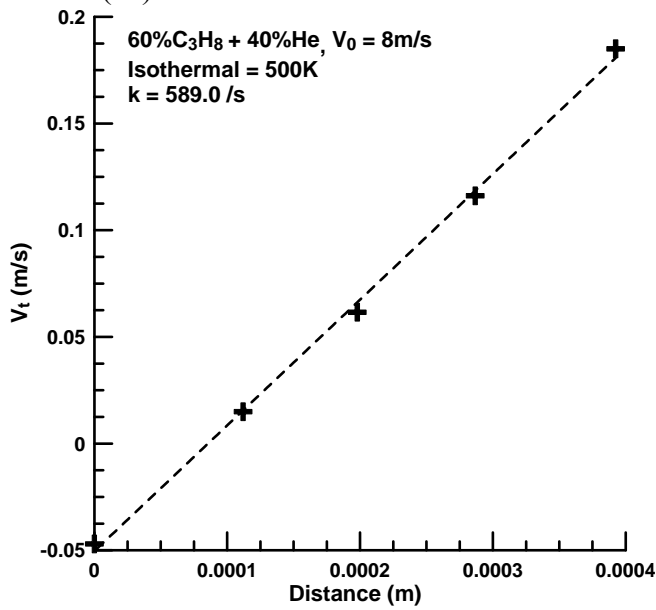(b1) intersections of 350 K isotherm and streamlines
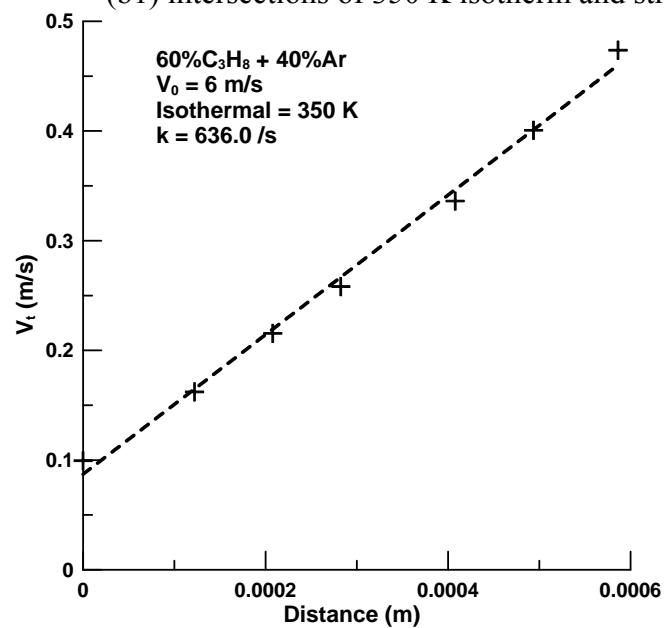
(b2) stretch rate fit along 350 K isotherm
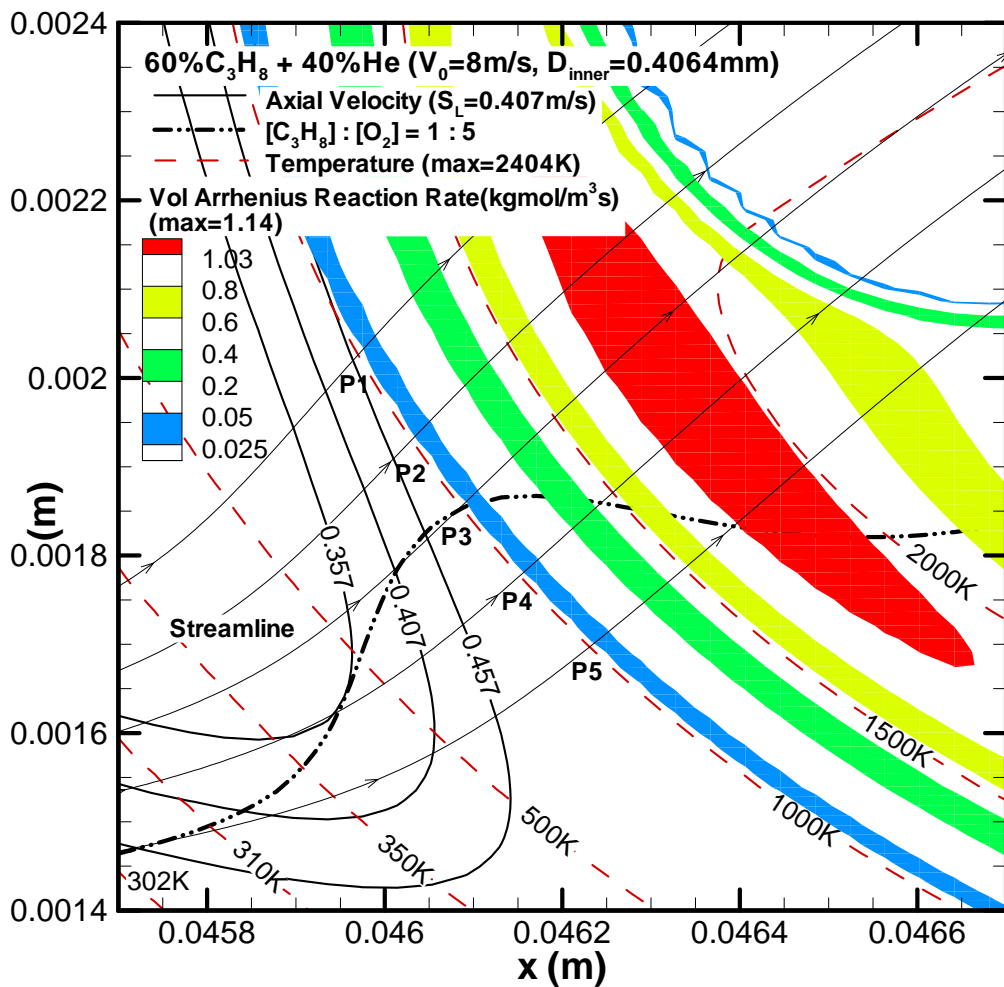
Figure A.5 (a - f) – (continued)
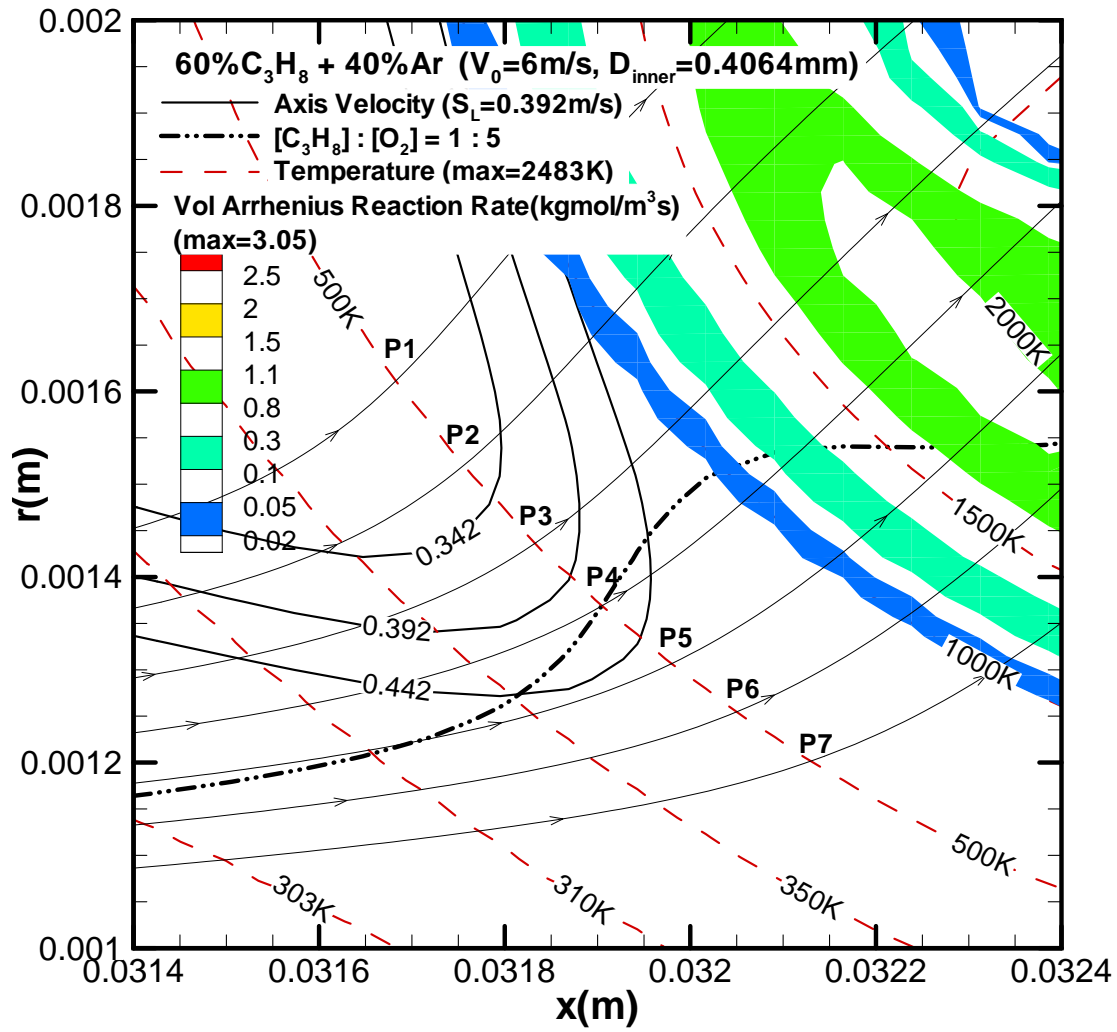
(c1) intersections of 500 K isotherm and streamlines
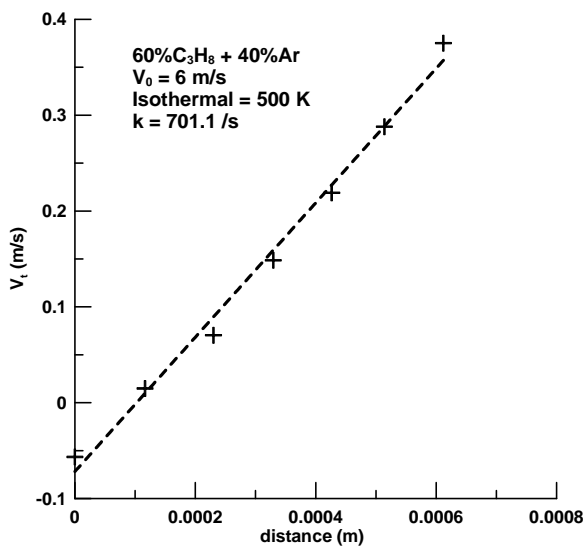
(c2) stretch rate fit along 500 K isotherm

Figure A.5 (a - f) – (continued)
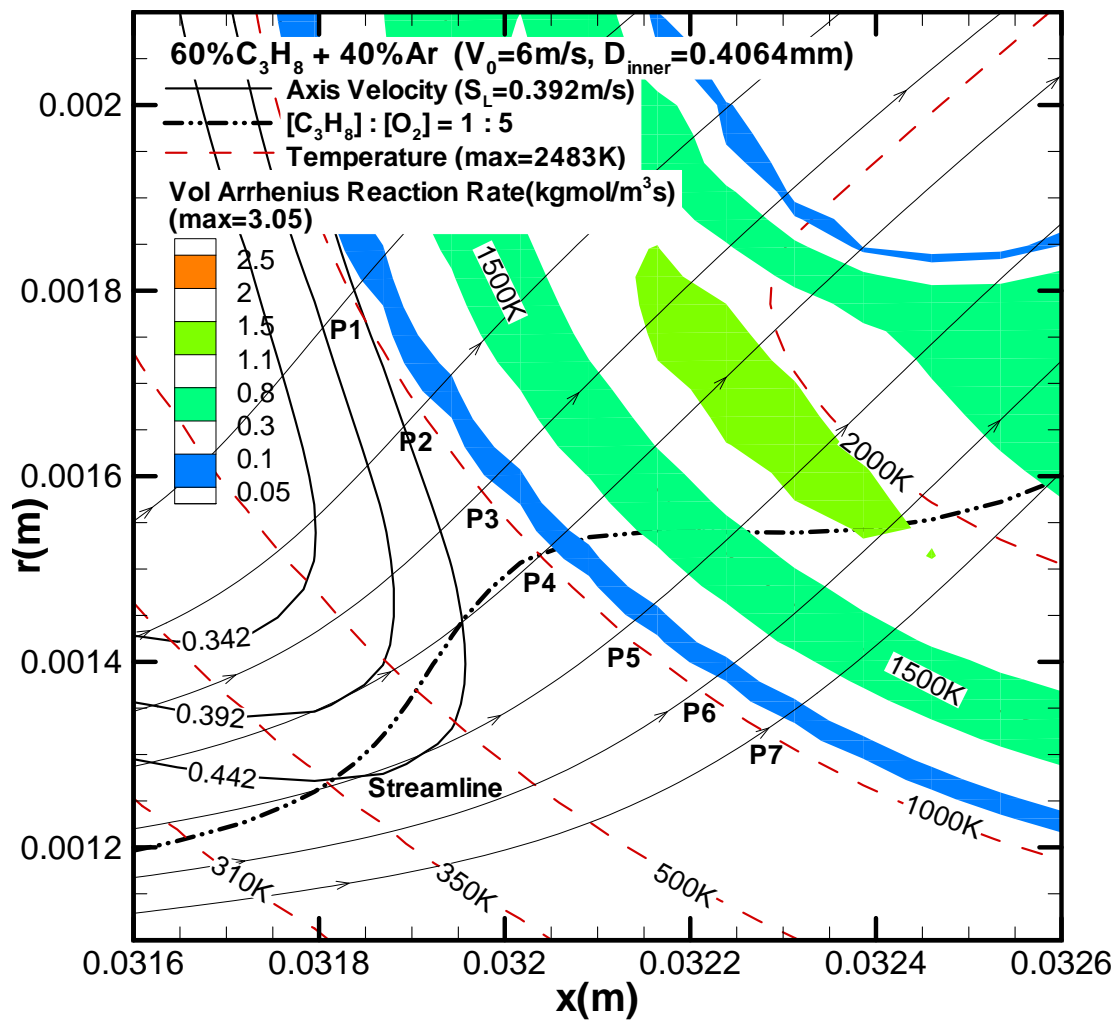
(d1) intersections of 1000 K isotherm and streamlines
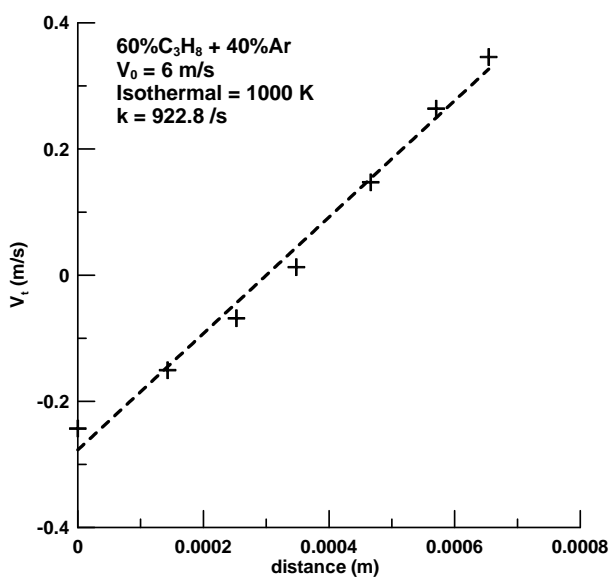
(d2) stretch rate fit along 1000 K isotherm

Figure A.5 (a - f) – (continued)
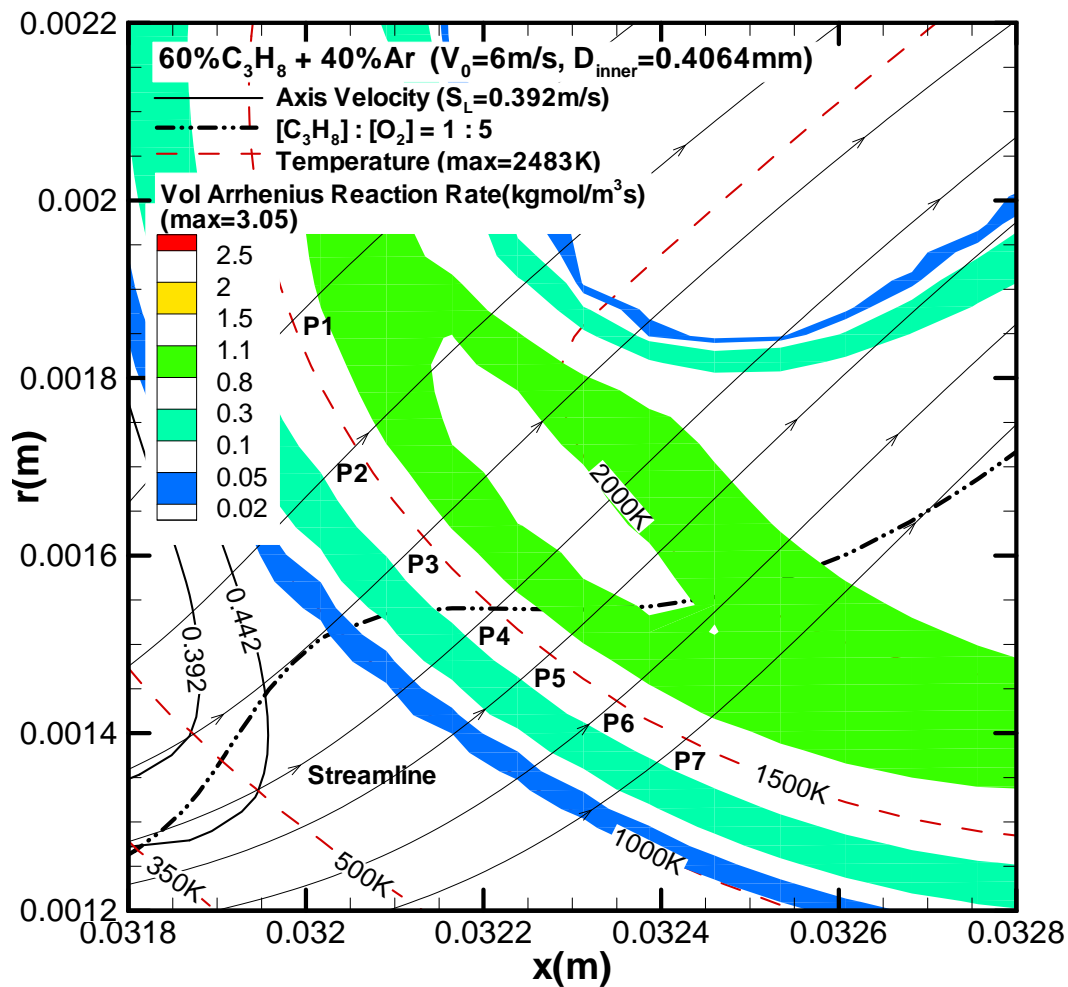
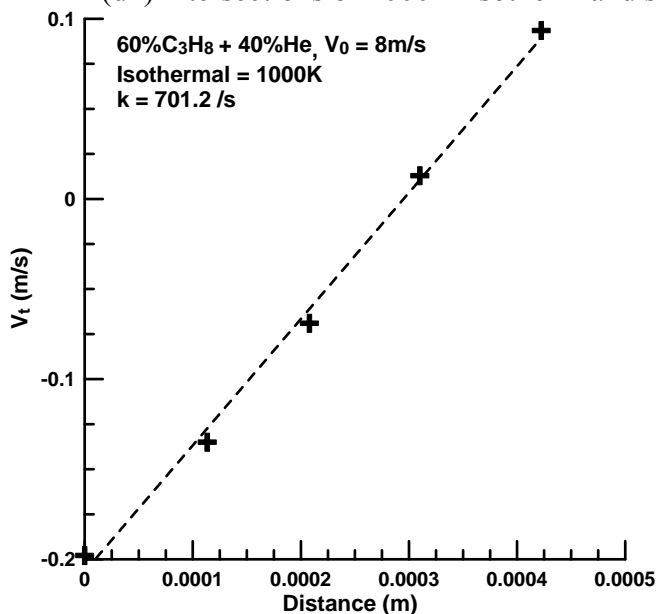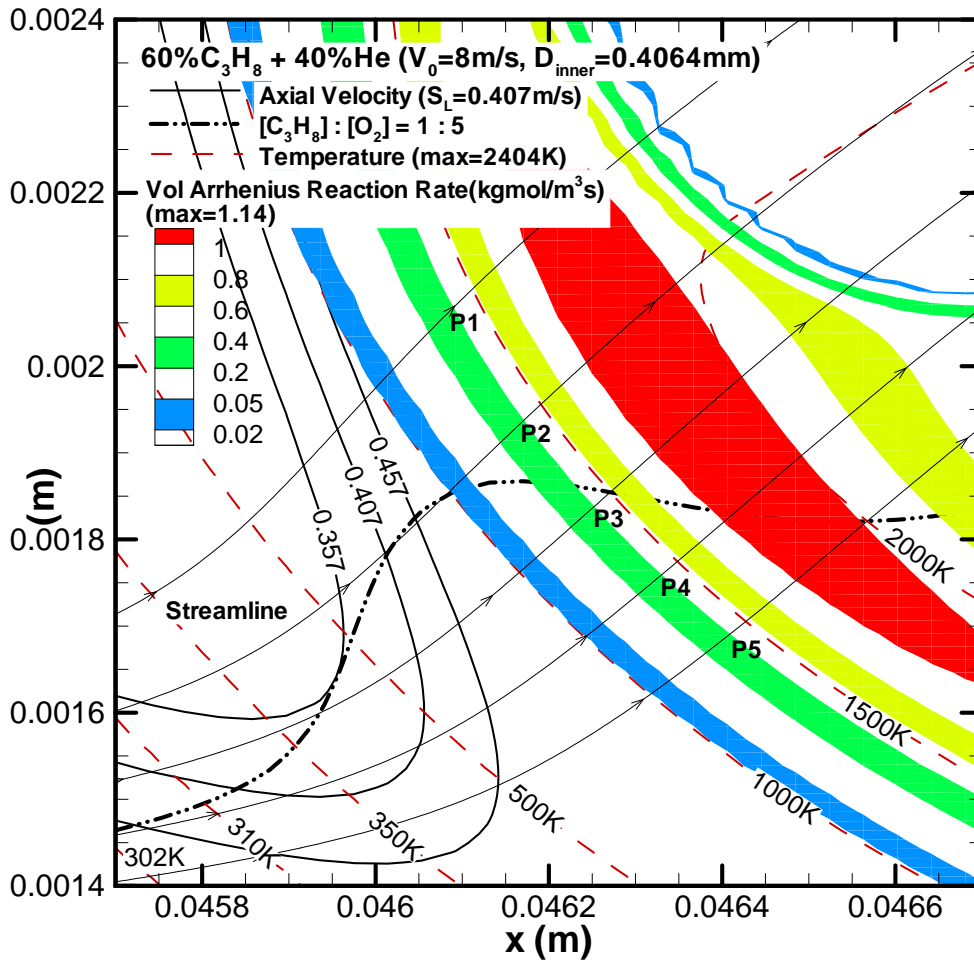(e1) intersections of 1500 K isotherm and streamlines
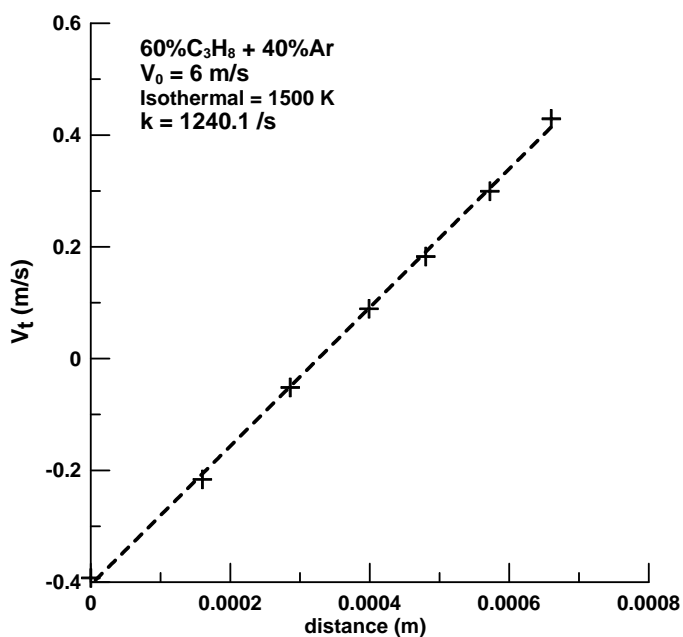
(e2) stretch rate fit along 1500 K isotherm

Figure A.5 (a - f) – (continued)
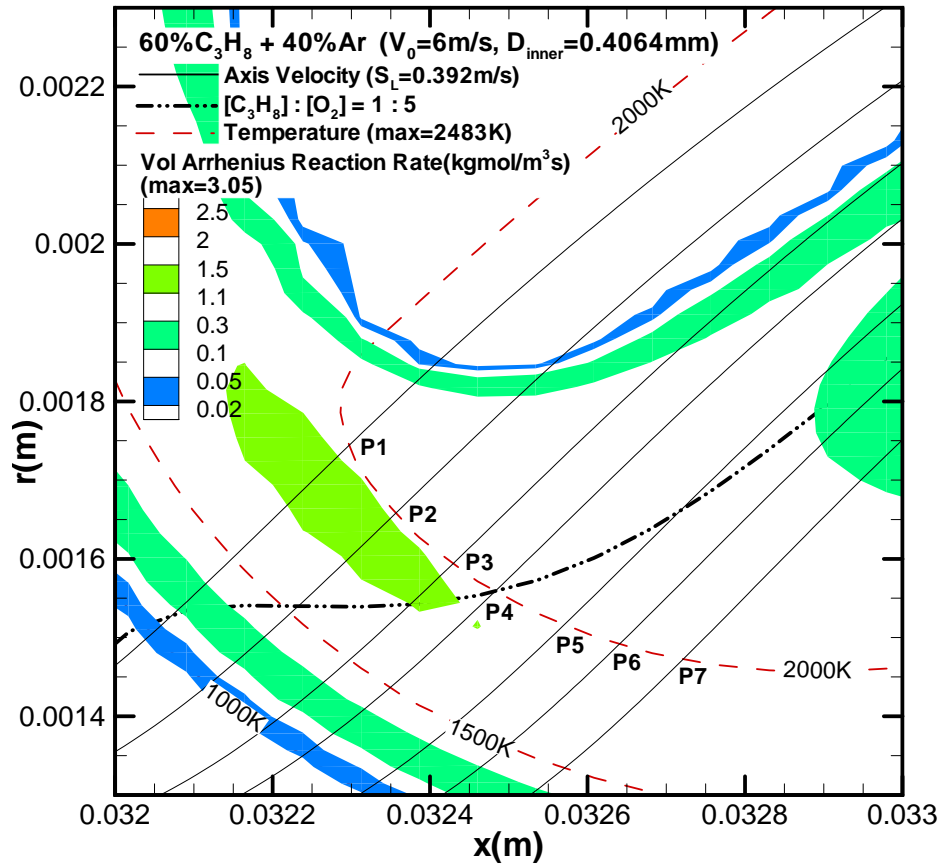
(f1) intersections of 2000 K isotherm and streamlines
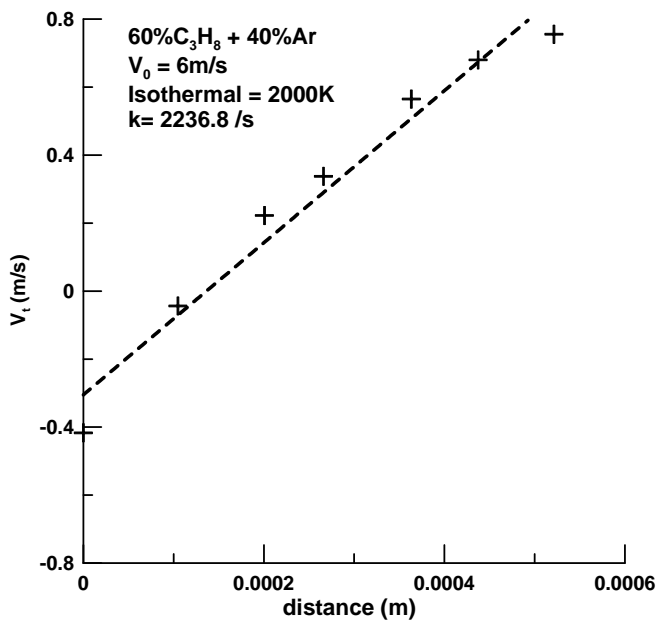
(f2) stretch rate fit along 2000 K isotherm

Figure A.5 (a – f) - (continued)
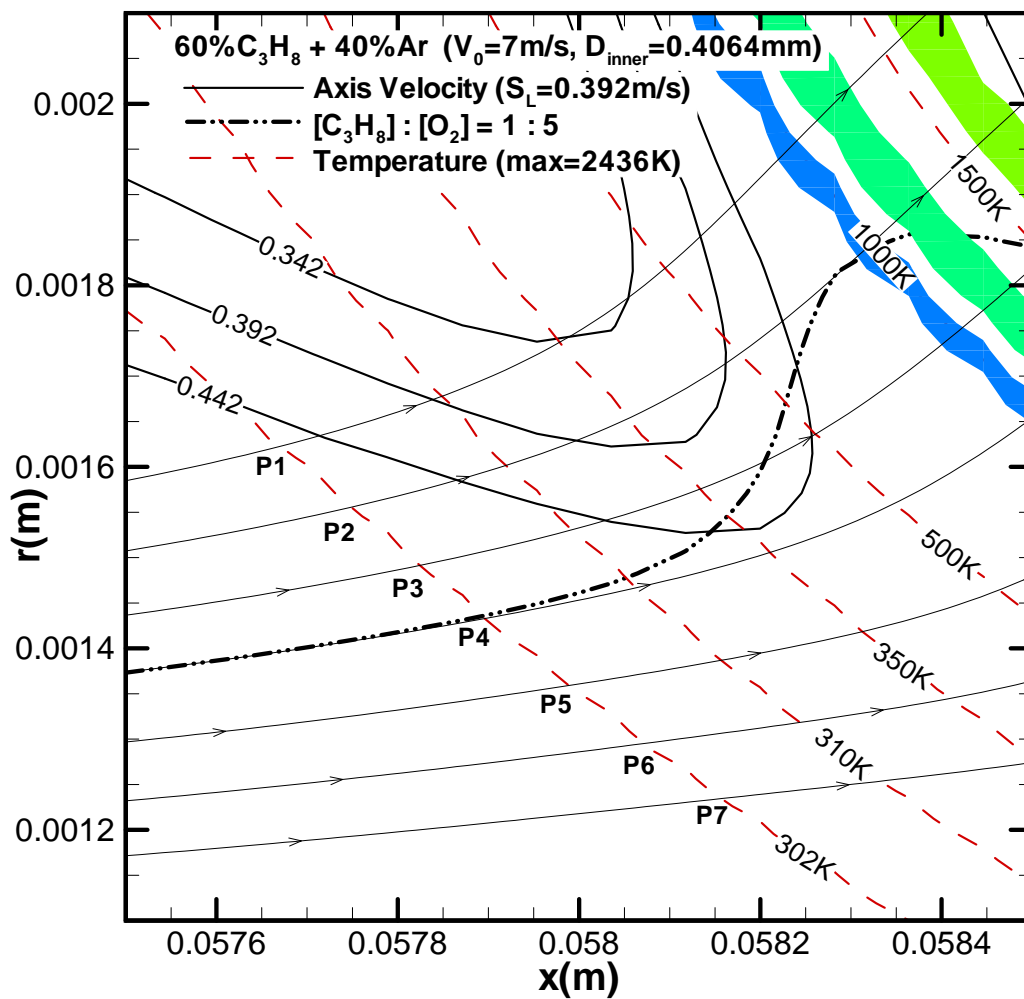
(a1) intersections of 302 K isotherm and streamlines
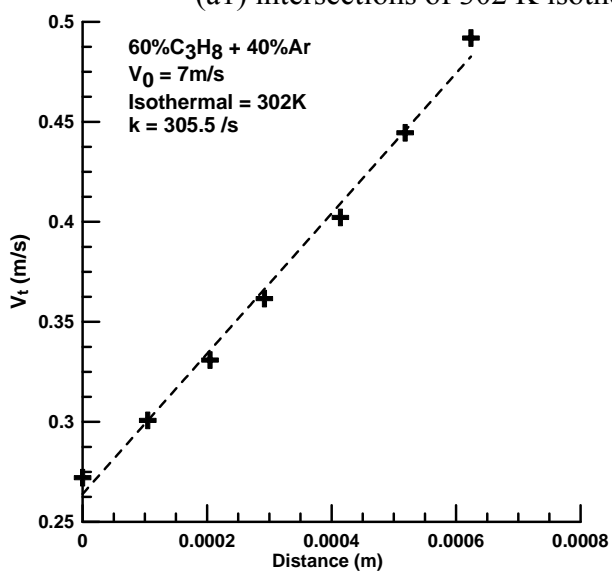
(a2) stretch rate fit along 302 K isotherm

Figure A.6 (a - f) – Interpolation around the stoichiometric line and the stretch rate fit for a variety of isotherms (302K, 350K, 500K, 1000K, 1500K and 2000K) for 60% C_3H_8 with 40% Ar dilution at jet velocity of 7 m/s.
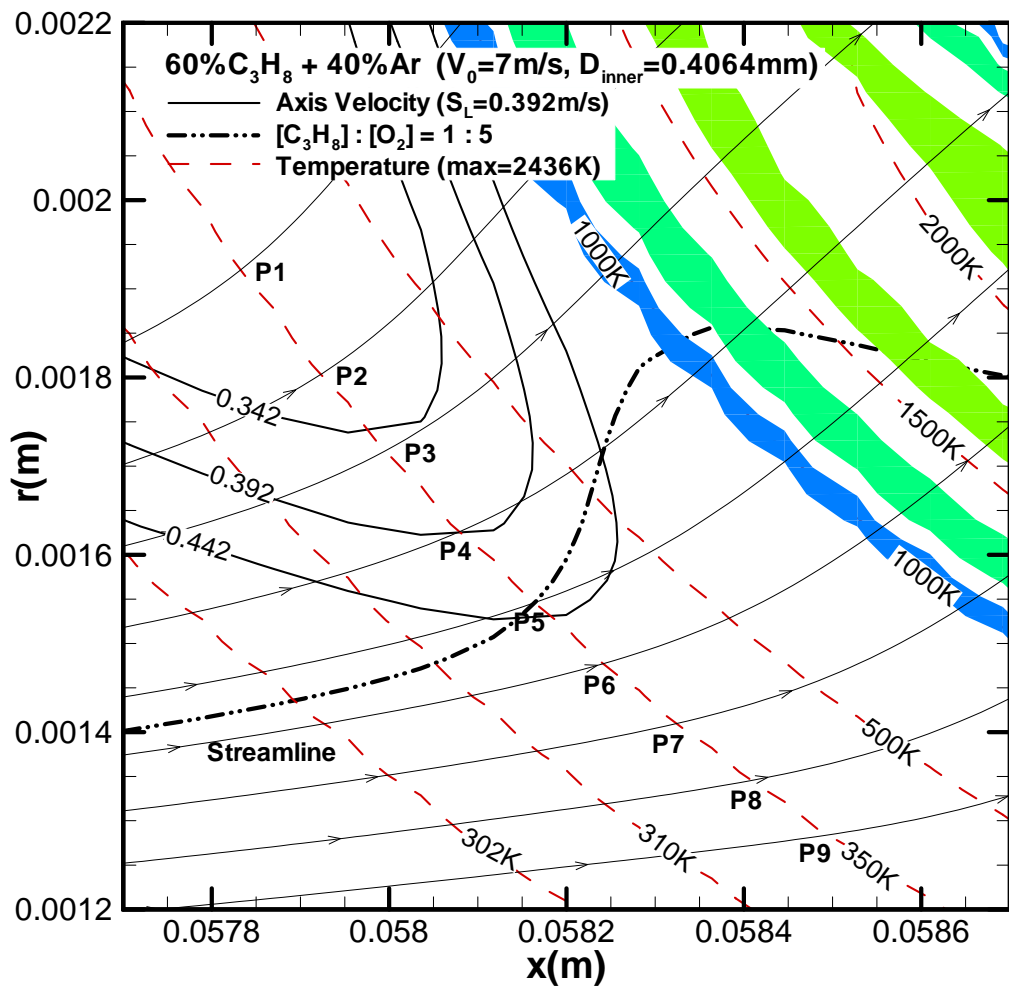
(b1) intersections of 350 K isotherm and streamlines
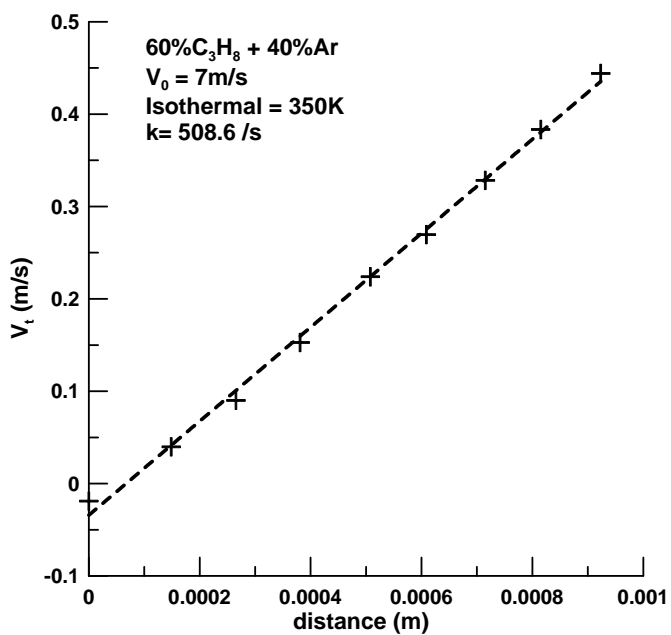
(b2) stretch rate fit along 350 K isotherm

Figure A.6 (a - f) – (continued)
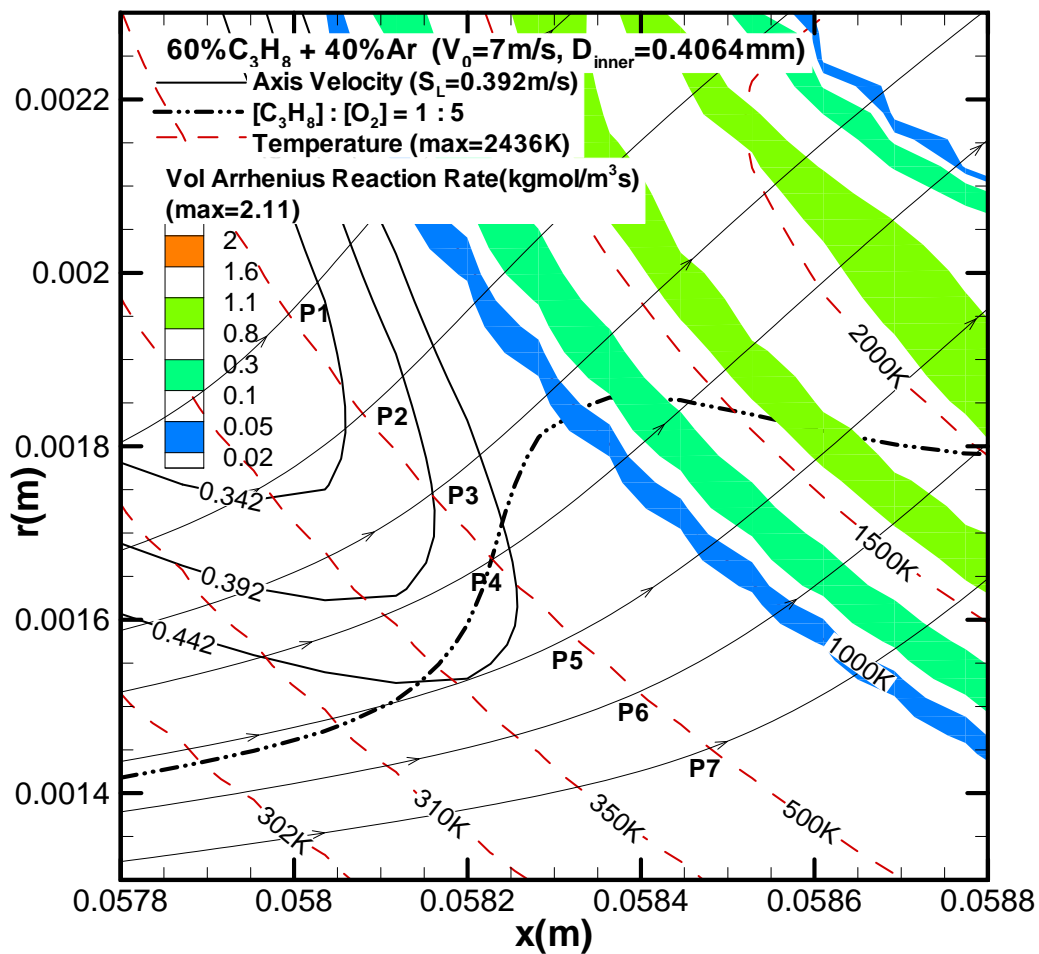
(c1) intersections of 500 K isotherm and streamlines
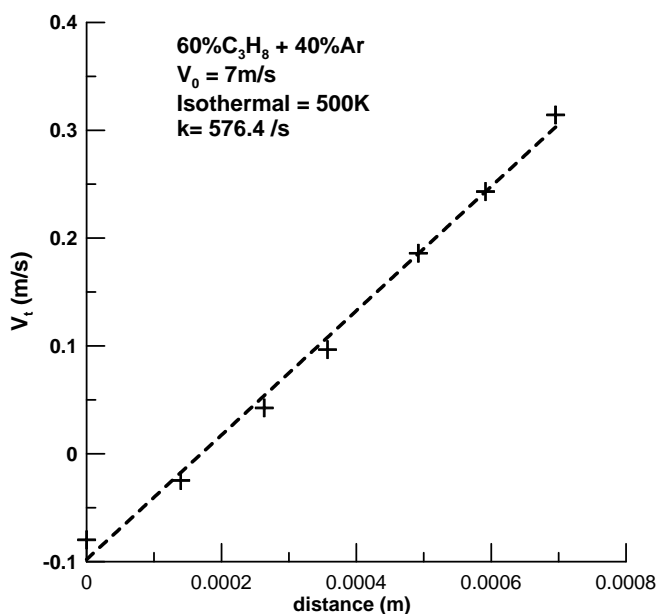
(c2) stretch rate fit along 500 K isotherm

Figure A.6 (a - f) – (continued)
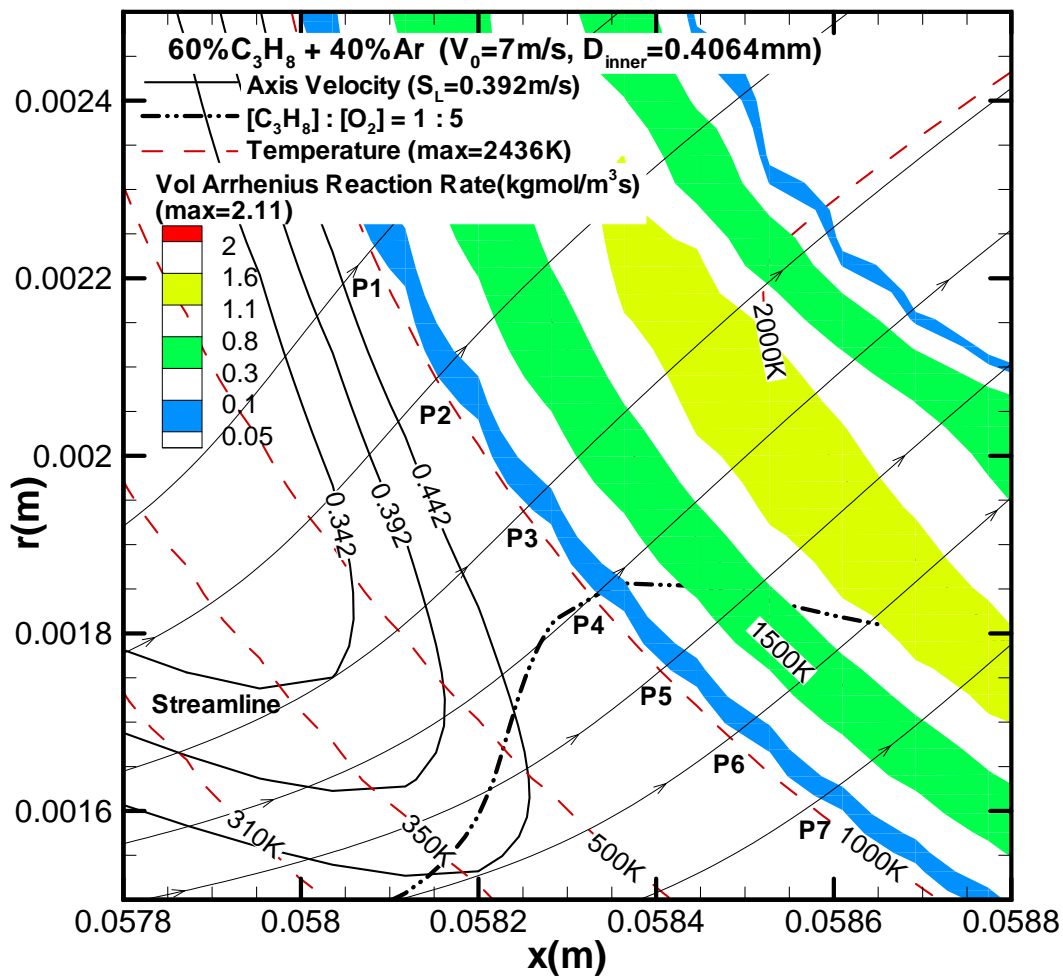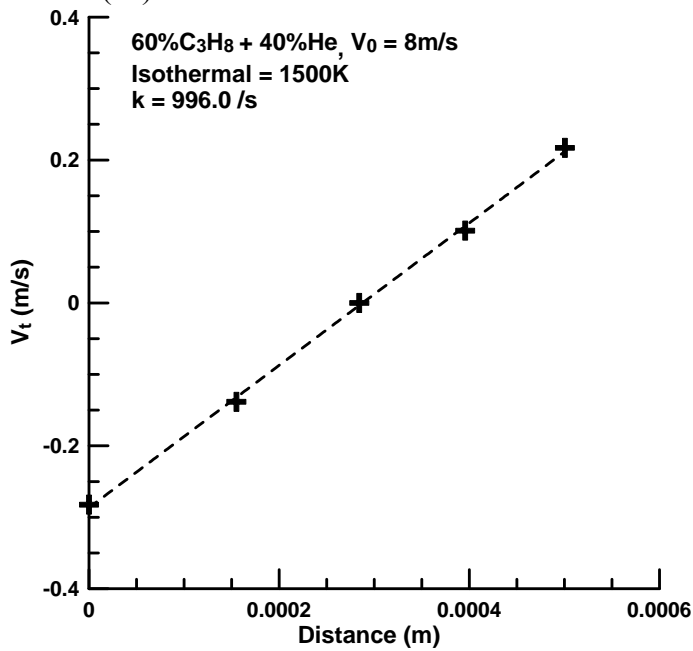
(d1) intersections of 1000 K isotherm and streamlines
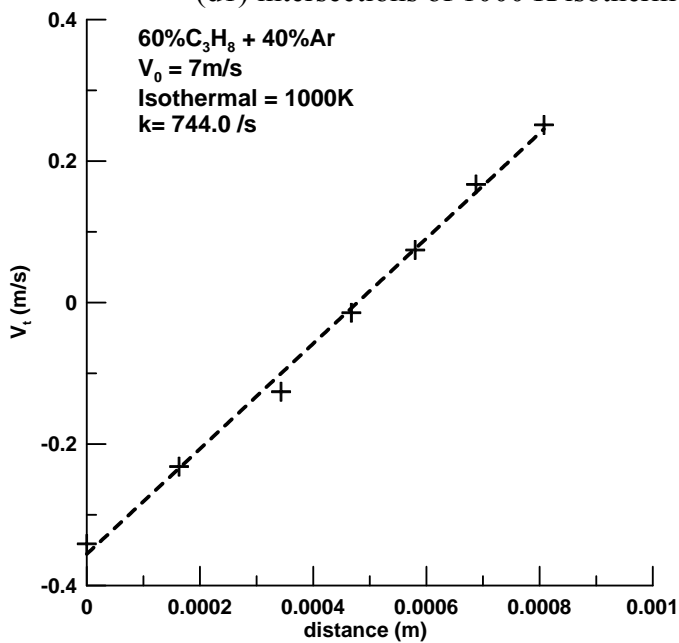
(d2) stretch rate fit along 1000 K isotherm
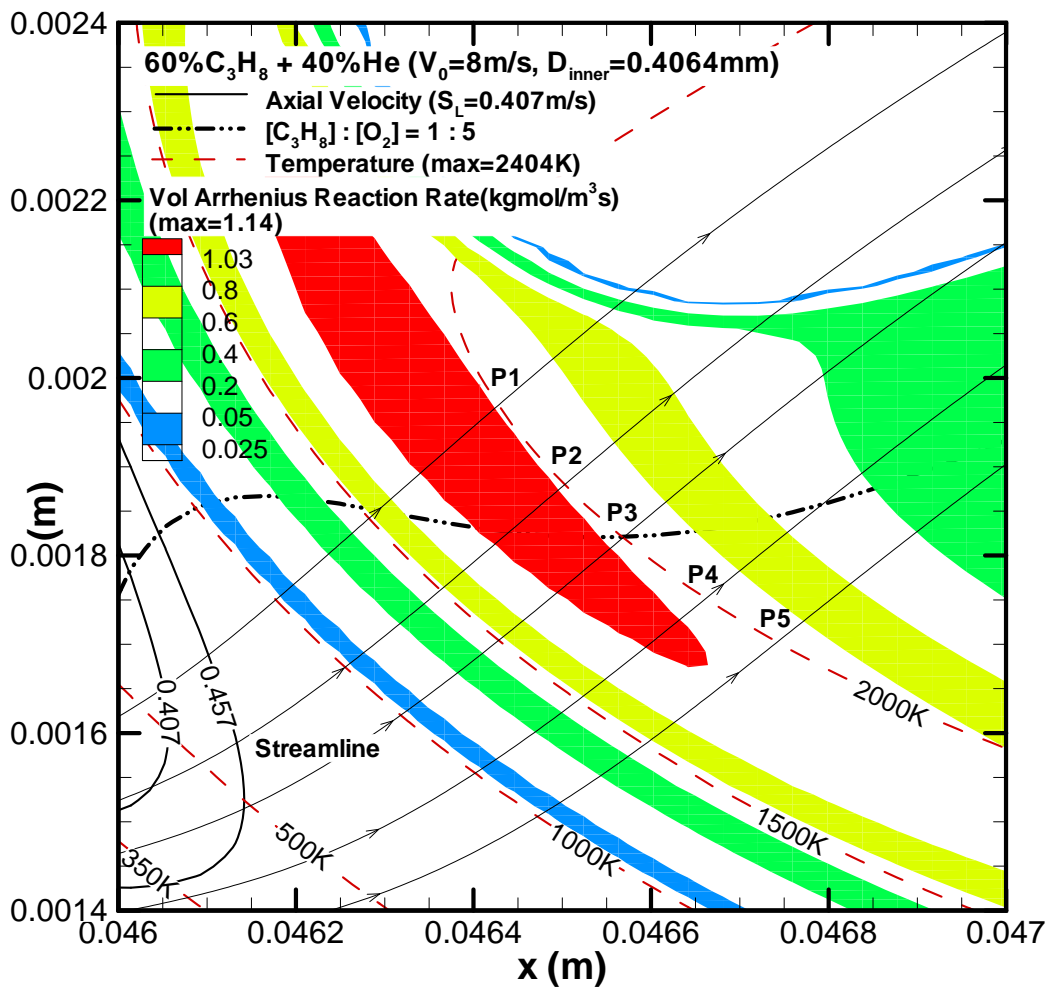
Figure A.6 (a - f) – (continued)

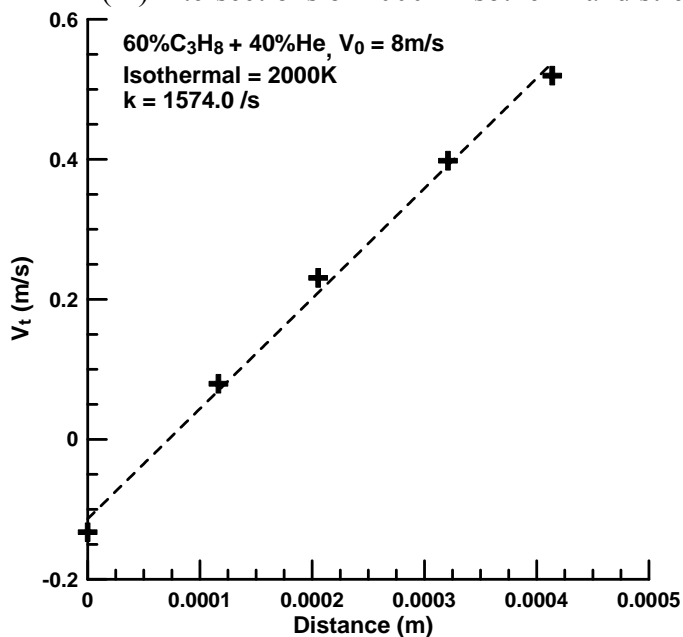(e1) intersections of 1500 K isotherm and streamlines
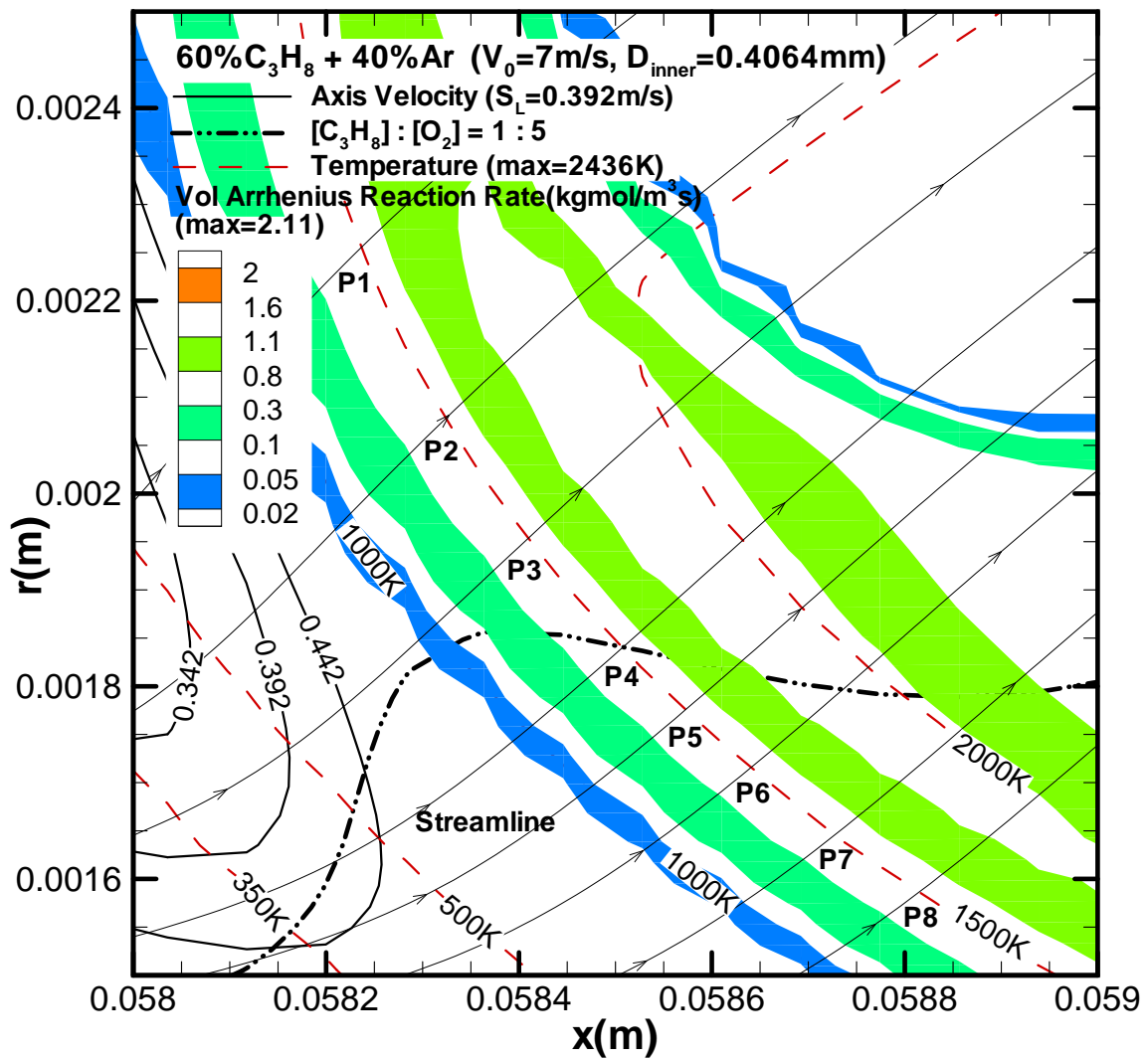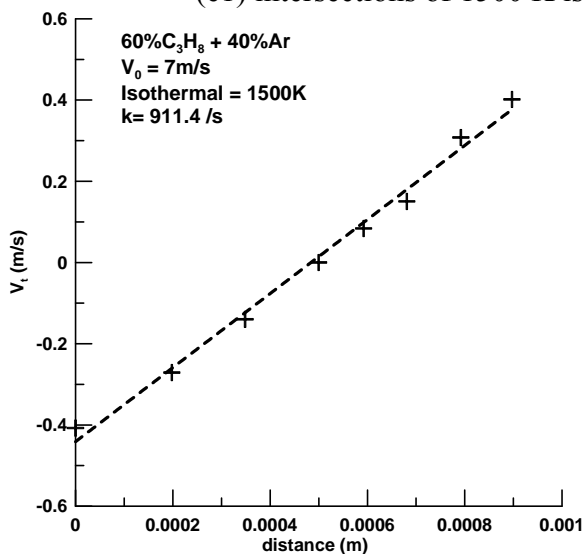
(e2) stretch rate fit along 1500 K isotherm

Figure A.6 (a - f) – (continued)

(f1) intersections of 2000 K isotherm and streamlines
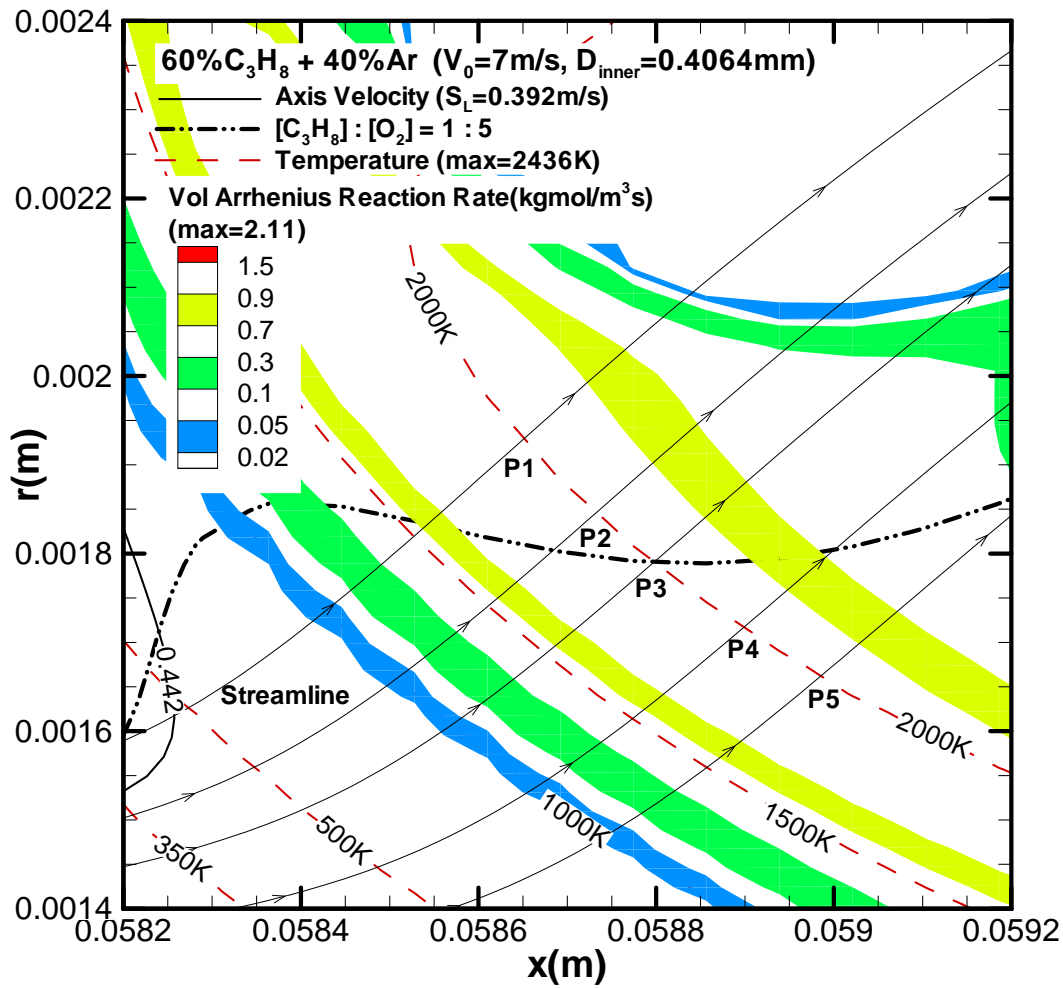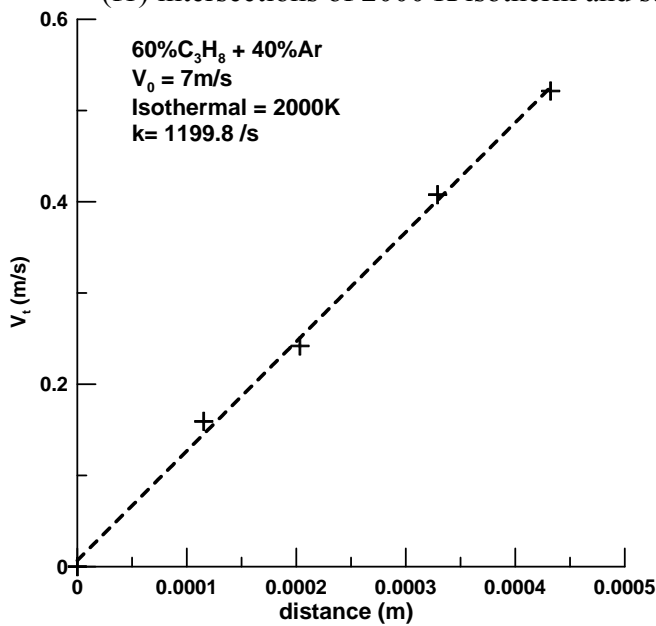
(f2) stretch rate fit along 2000 K isotherm
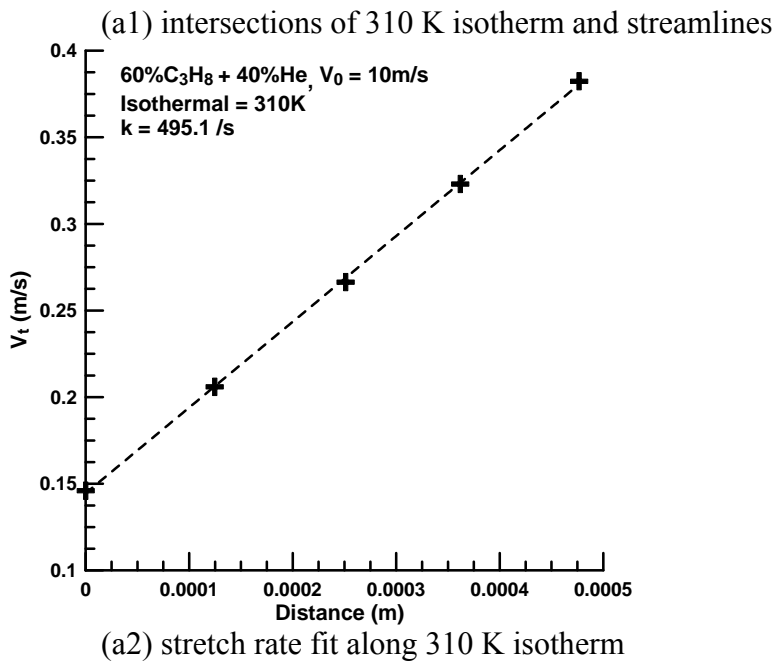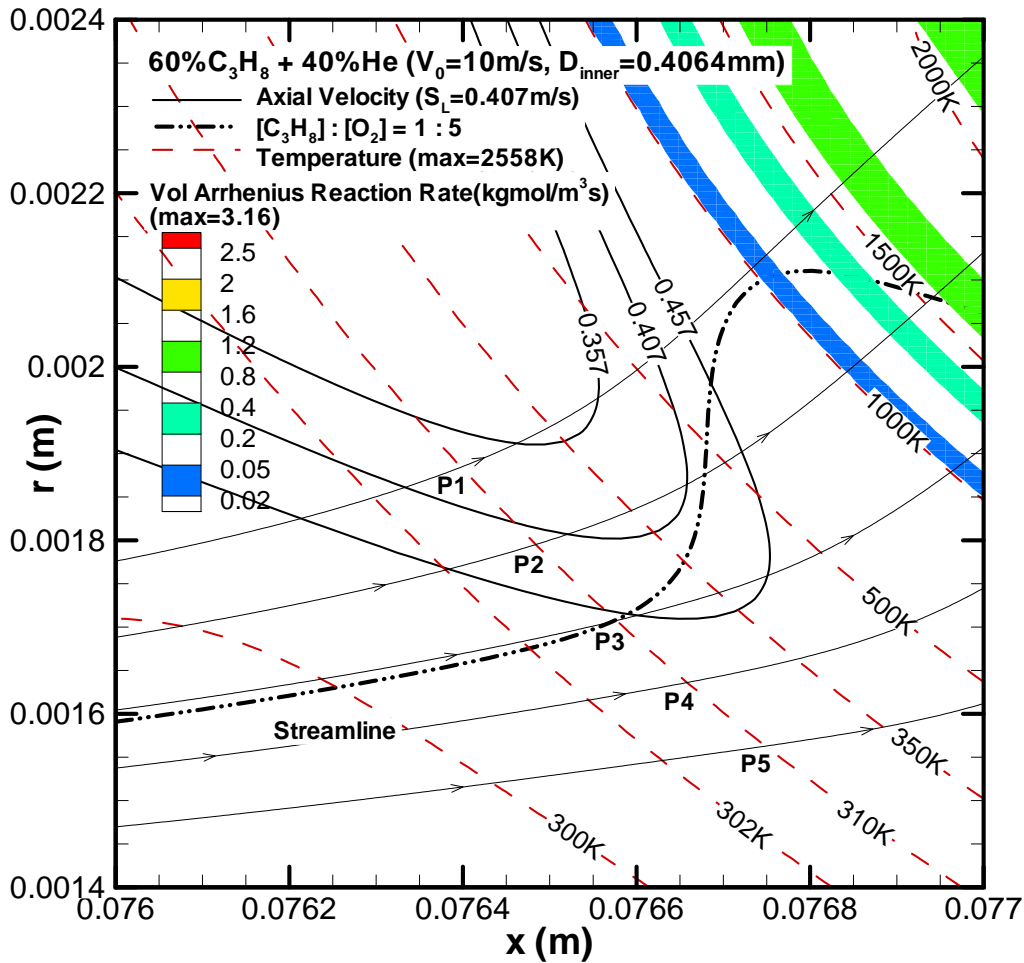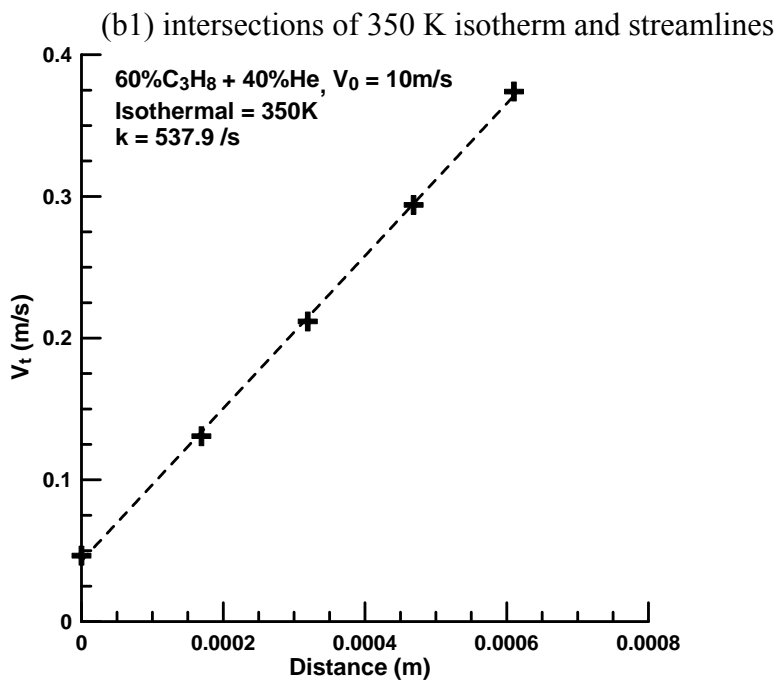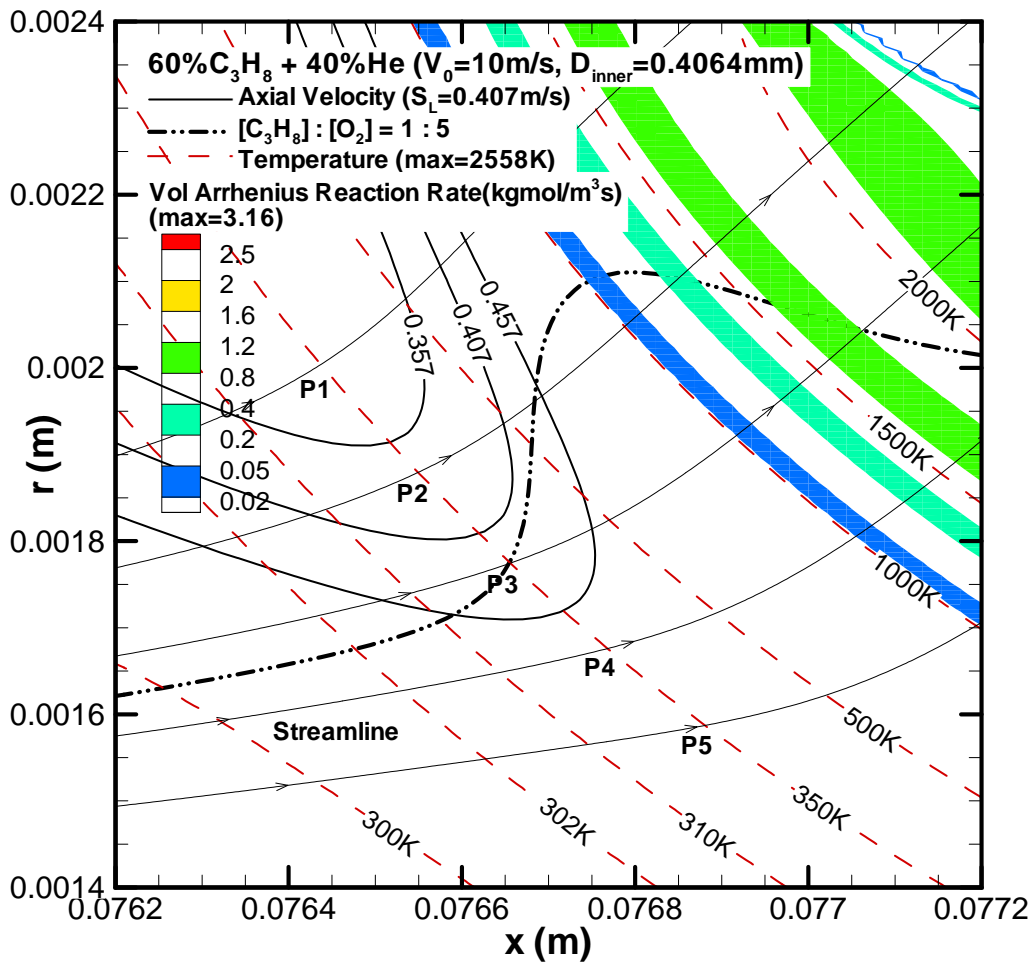
Figure A.6 (a - f) – (continued)

(a1) intersections of 302 K isotherm and streamlines
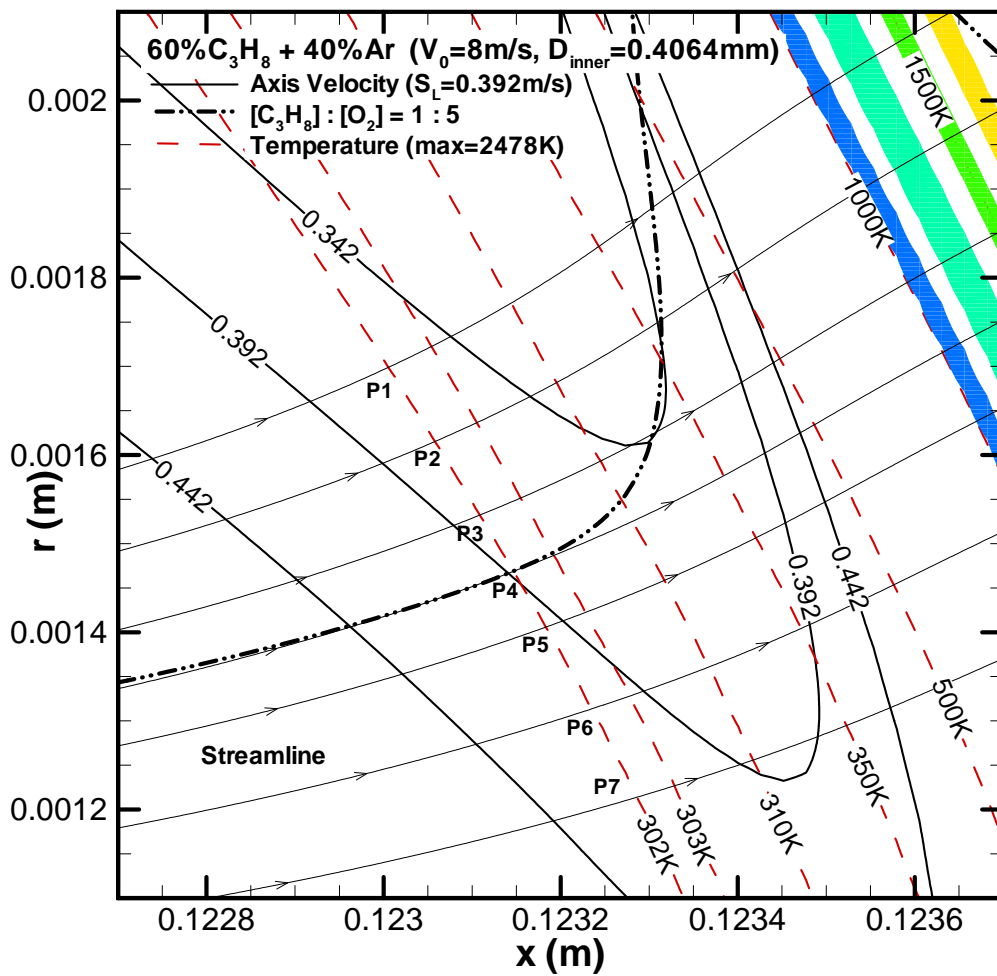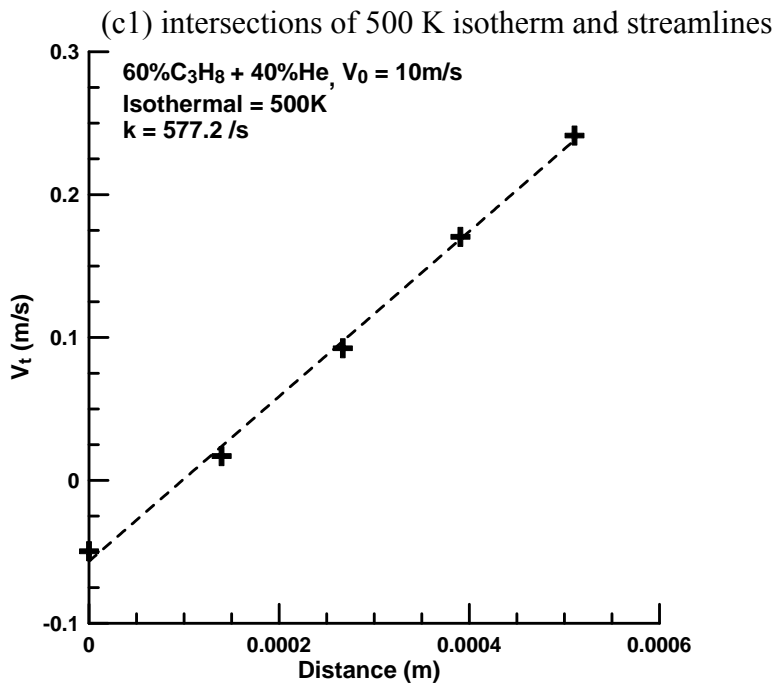

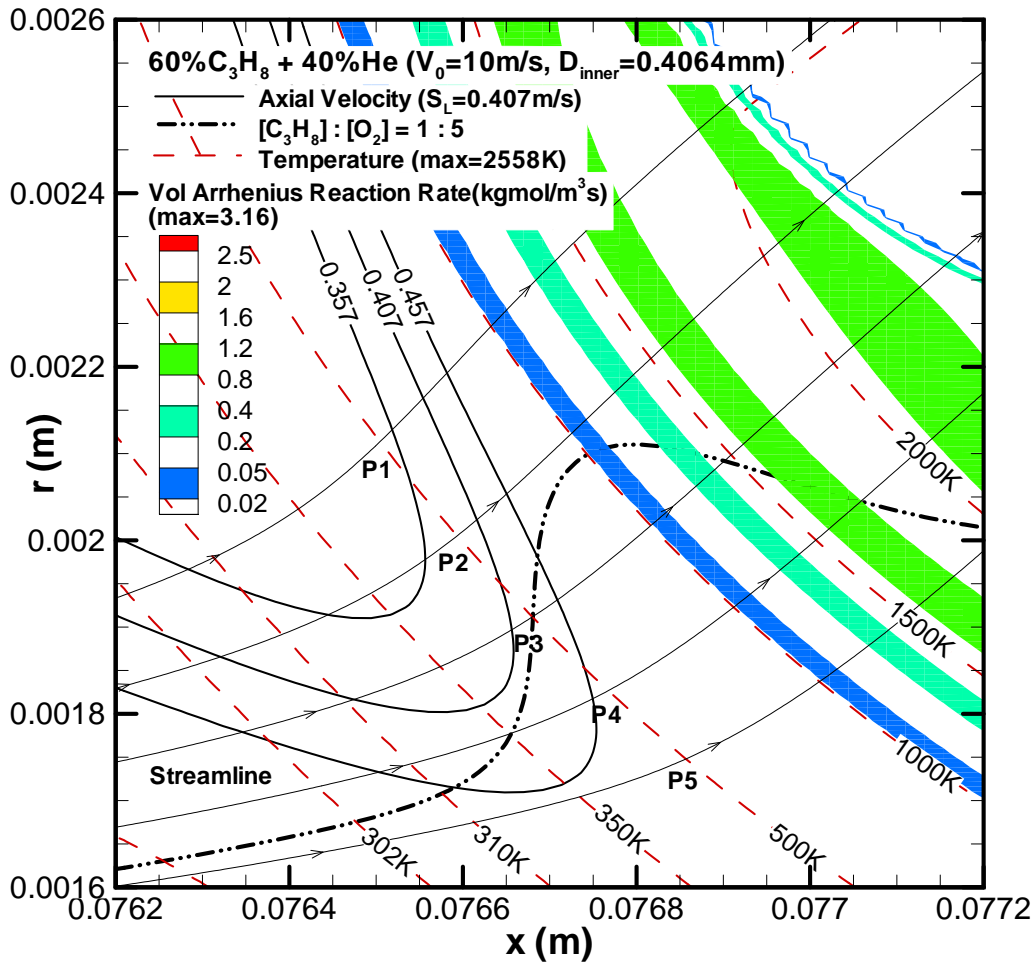(a2) stretch rate fit along 302 K isotherm

Figure A.7 (a - f) – Interpolation around the stoichiometric line and the stretch rate fit for a variety of isotherms (302K, 350K, 500K, 1000K, 1500K and 2000K) for 60% C_3H_8 with 40% Ar dilution at jet velocity of 8 m/s.
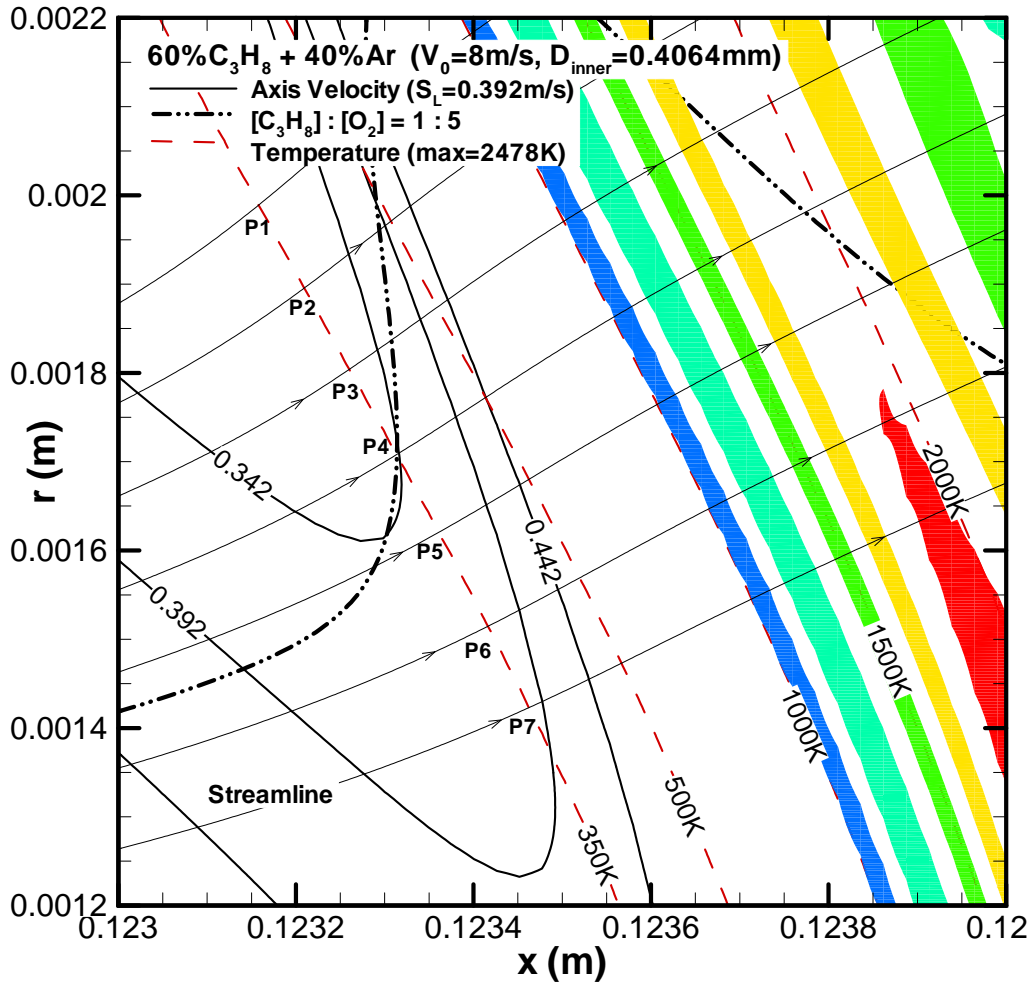
(b1) intersections of 350 K isotherm and streamlines

(b2) stretch rate fit along 350 K isotherm

Figure A.7 (a - f) – (continued)

(c1) intersections of 500 K isotherm and streamlines

(c2) stretch rate fit along 500 K isotherm

Figure A.7 (a - f) – (continued)

158

(d1) intersections of 1000 K isotherm and streamlines

(d2) stretch rate fit along 1000 K isotherm

Figure A.7 (a - f) – (continued)

(e1) intersections of 1500 K isotherm and streamlines

(e2) stretch rate fit along 1500 K isotherm

Figure A.7 (a - f) – (continued)

(f1) intersections of 2000 K isotherm and streamlines

(f2) stretch rate fit along 2000 K isotherm

Figure A.7 (a - f) – (continued)

(a1) intersections of 310 K isotherm and streamlines

(a2) stretch rate fit along 310 K isotherm

Figure A.8 (a - f) –Interpolation around the stoichiometric line and the stretch rate fit for a variety of isotherms (310K, 350K, 500K, 1000K, 1500K and 2000K) for 60% C_3H_8 with 40% He dilution at jet velocity of 6 m/s.
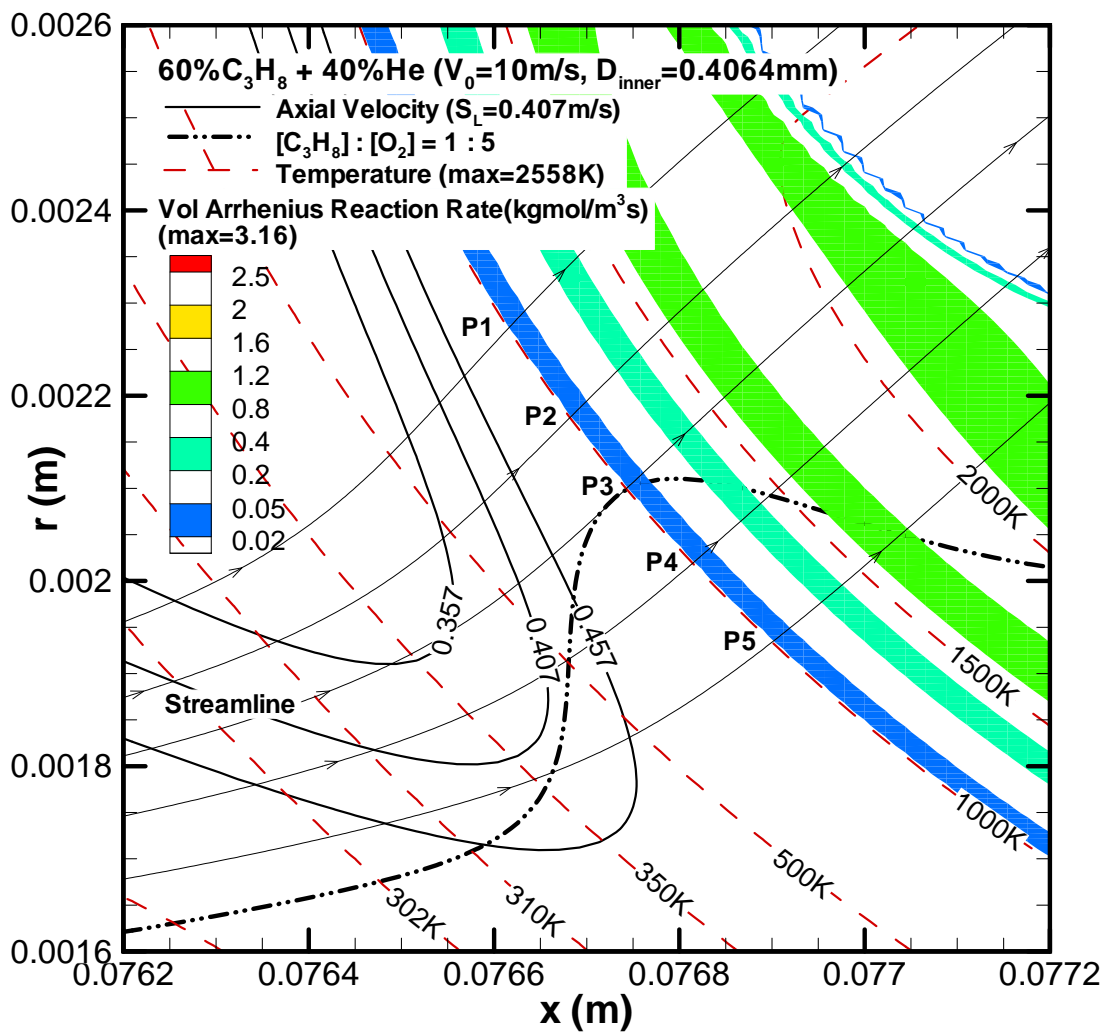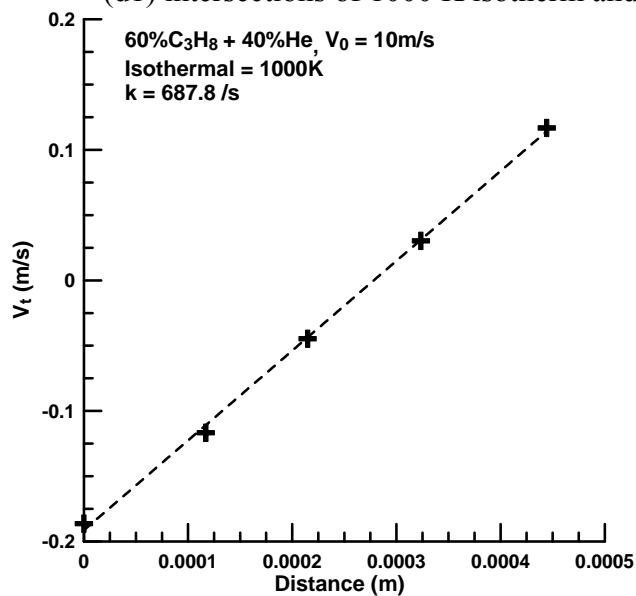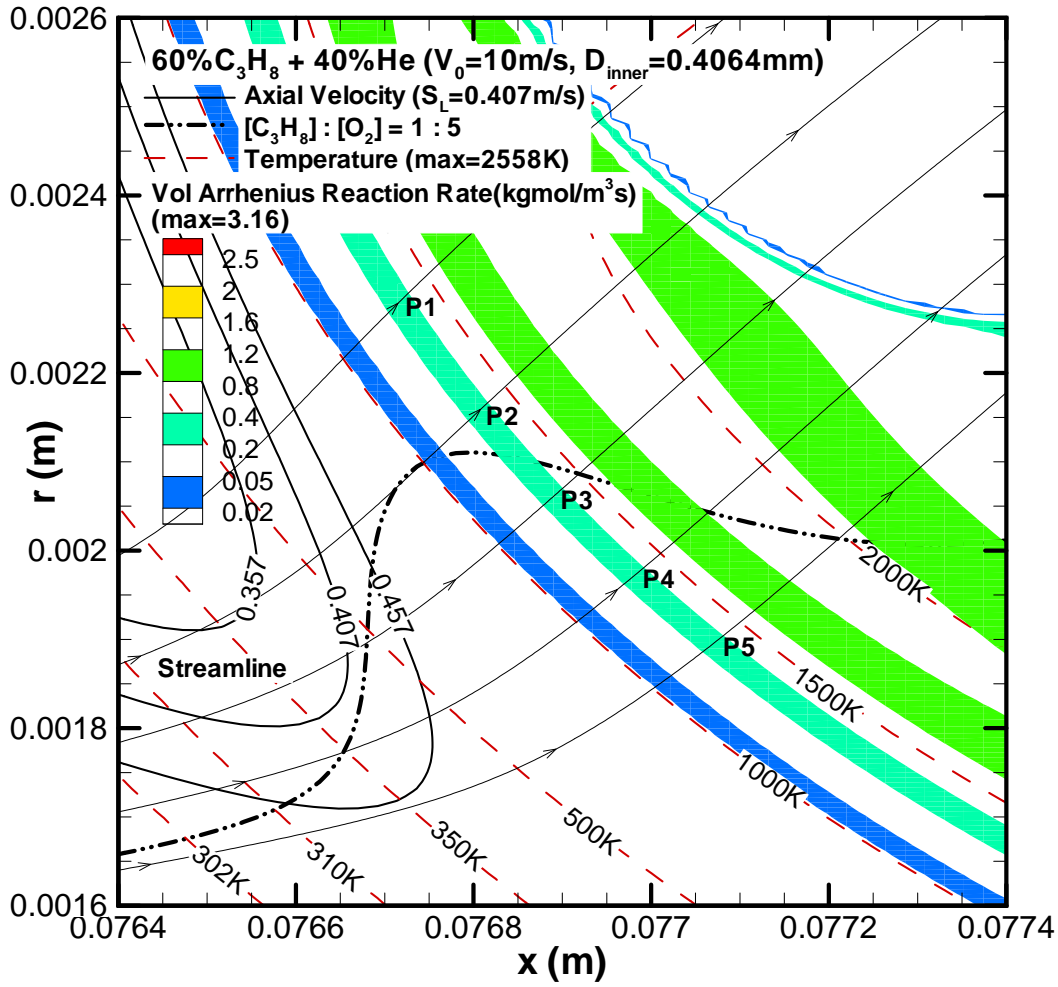
162

(b1) intersections of 350 K isotherm and streamlines

(b2) stretch rate fit along 350 K isotherm

Figure A.8 (a - f) – (continued)

(c1) intersections of 500 K isotherm and streamlines

(c2) stretch rate fit along 500 K isotherm

Figure A.8 (a - f) – (continued)

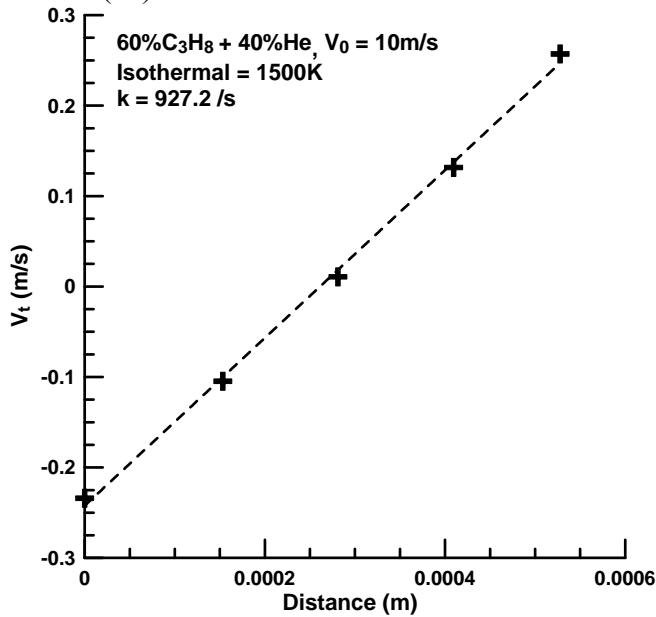(d1) intersections of 1000 K isotherm and streamlines

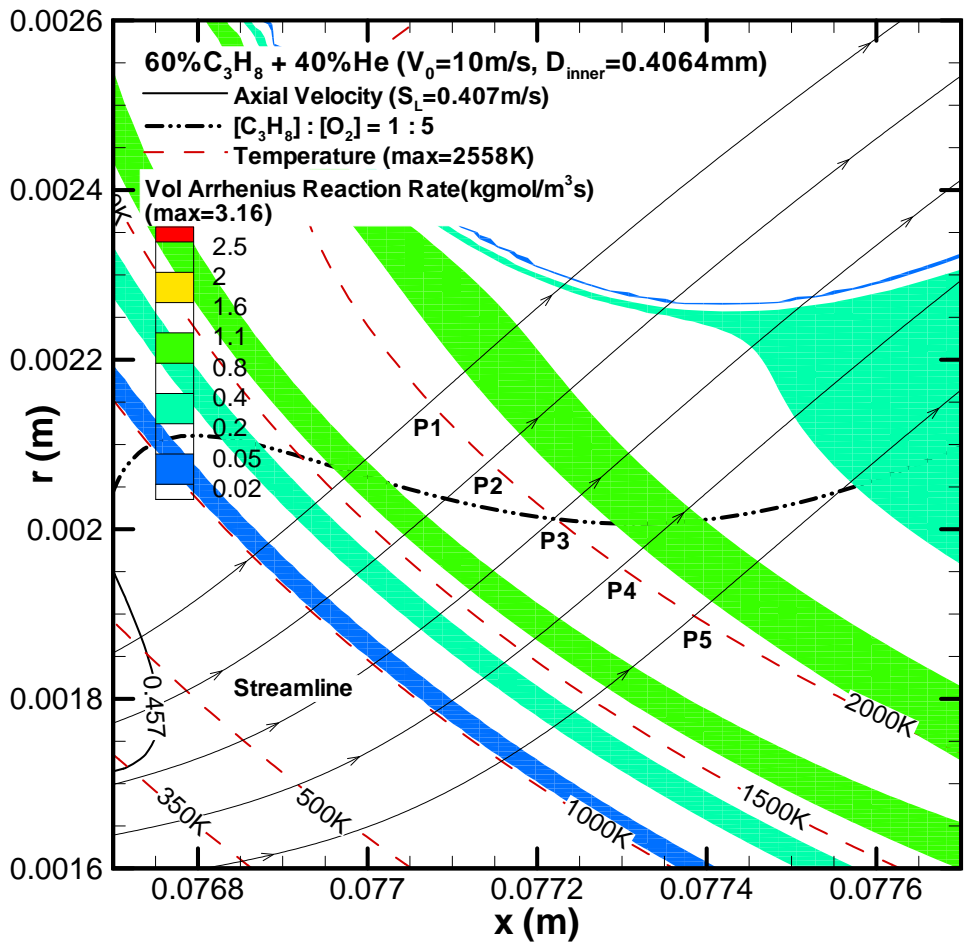(d2) stretch rate fit along 1000 K isotherm

Figure A.8 (a - f) – (continued)
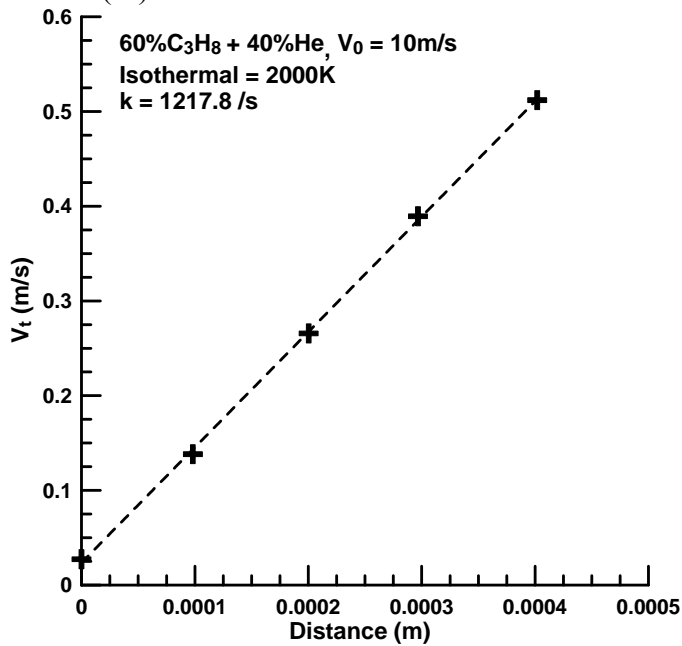
(e1) intersections of 1500 K isotherm and streamlines

(e2) stretch rate fit along 1500 K isotherm
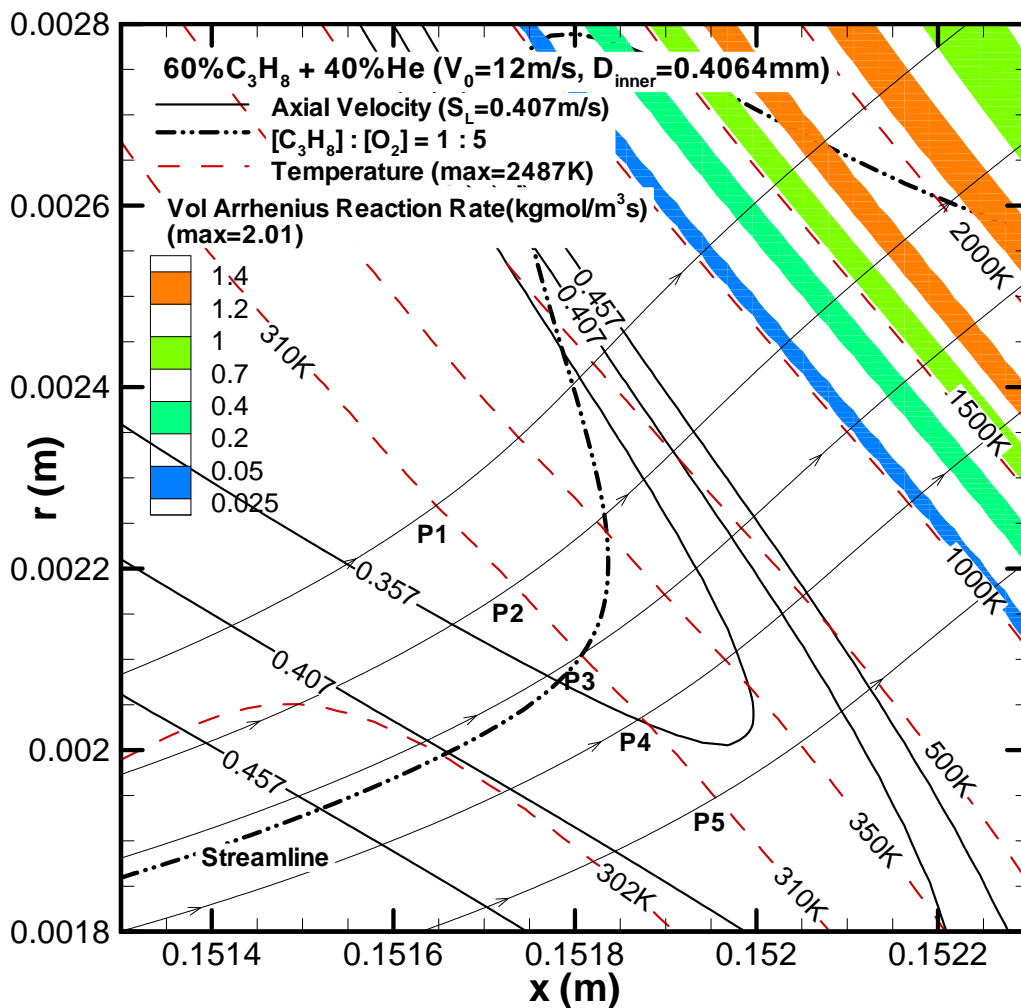
Figure A.8 (a - f) – (continued)

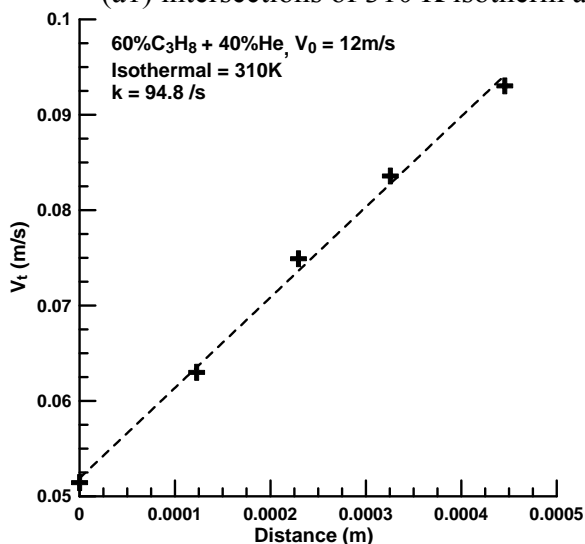(f1) intersections of 2000 K isotherm and streamlines

(f2) stretch rate fit along 2000 K isotherm

Figure A.8 (a - f) – (continued)

(a1) intersections of 310 K isotherm and streamlines

(a2) stretch rate fit along 310 K isotherm

Figure A.9 (a - f) – Interpolation around the stoichiometric line and the stretch rate fit for a variety of isotherms (310K, 350K, 500K, 1000K, 1500K and 2000K) for 60% C_3H_8 with 40% He dilution at jet velocity of 8 m/s.

(b1) intersections of 350 K isotherm and streamlines

(b2) stretch rate fit along 350 K isotherm

Figure A.9 (a - f) – (continued)

(c1) intersections of 500 K isotherm and streamlines

(c2) stretch rate fit along 500 K isotherm
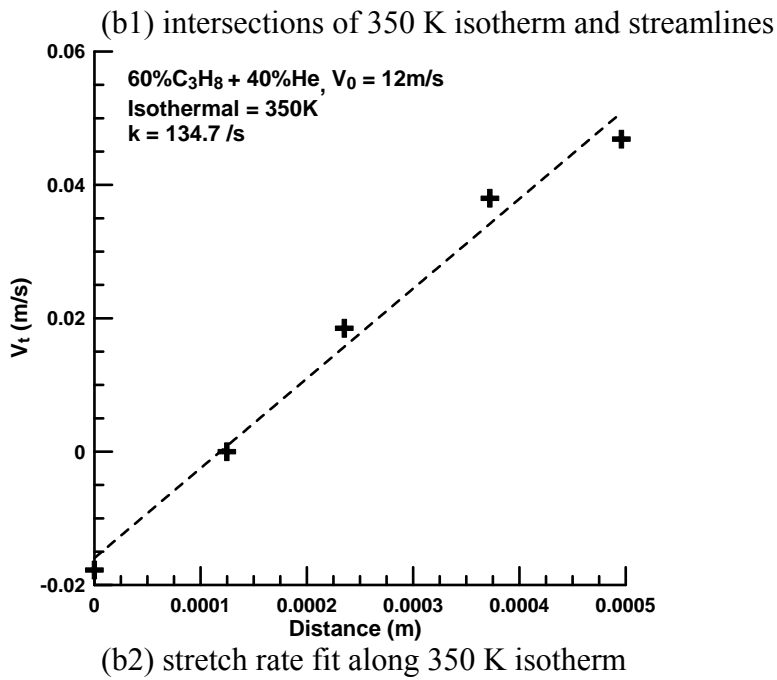
Figure A.9 (a - f) – (continued)

(d1) intersections of 1000 K isotherm and streamlines
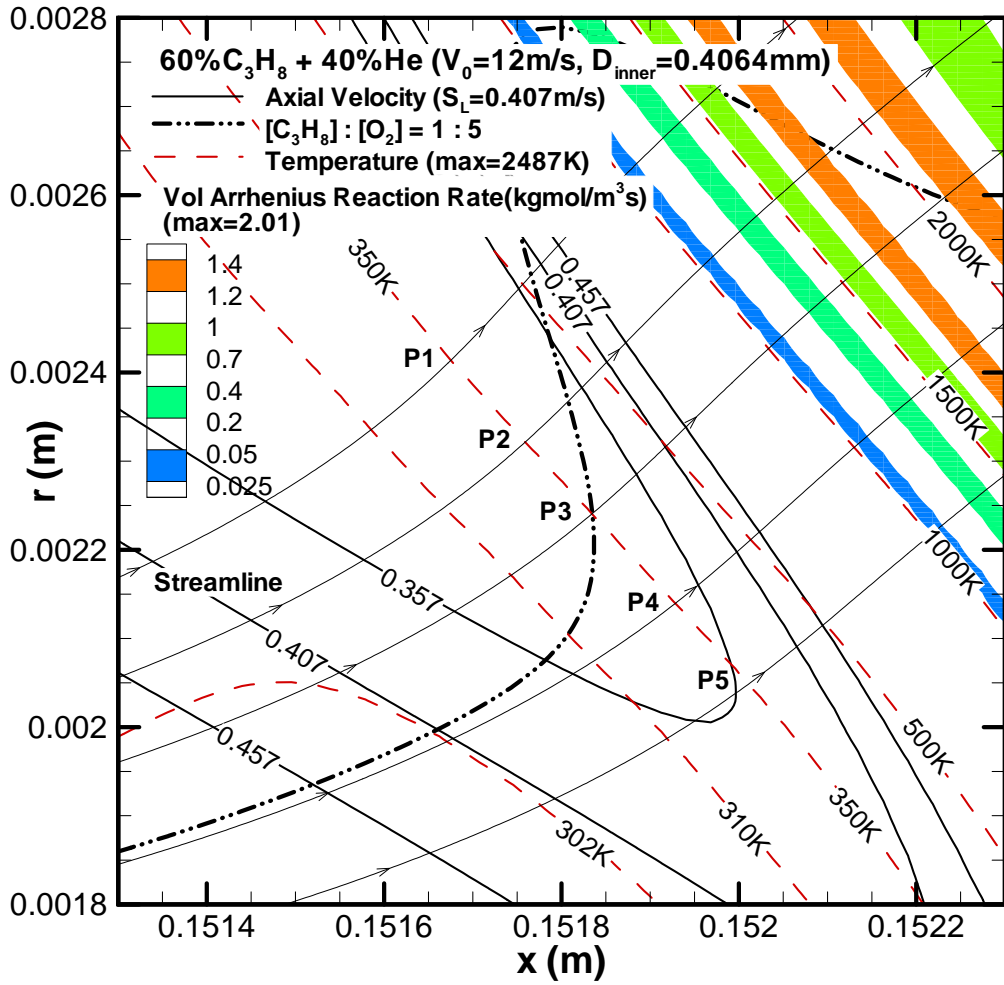

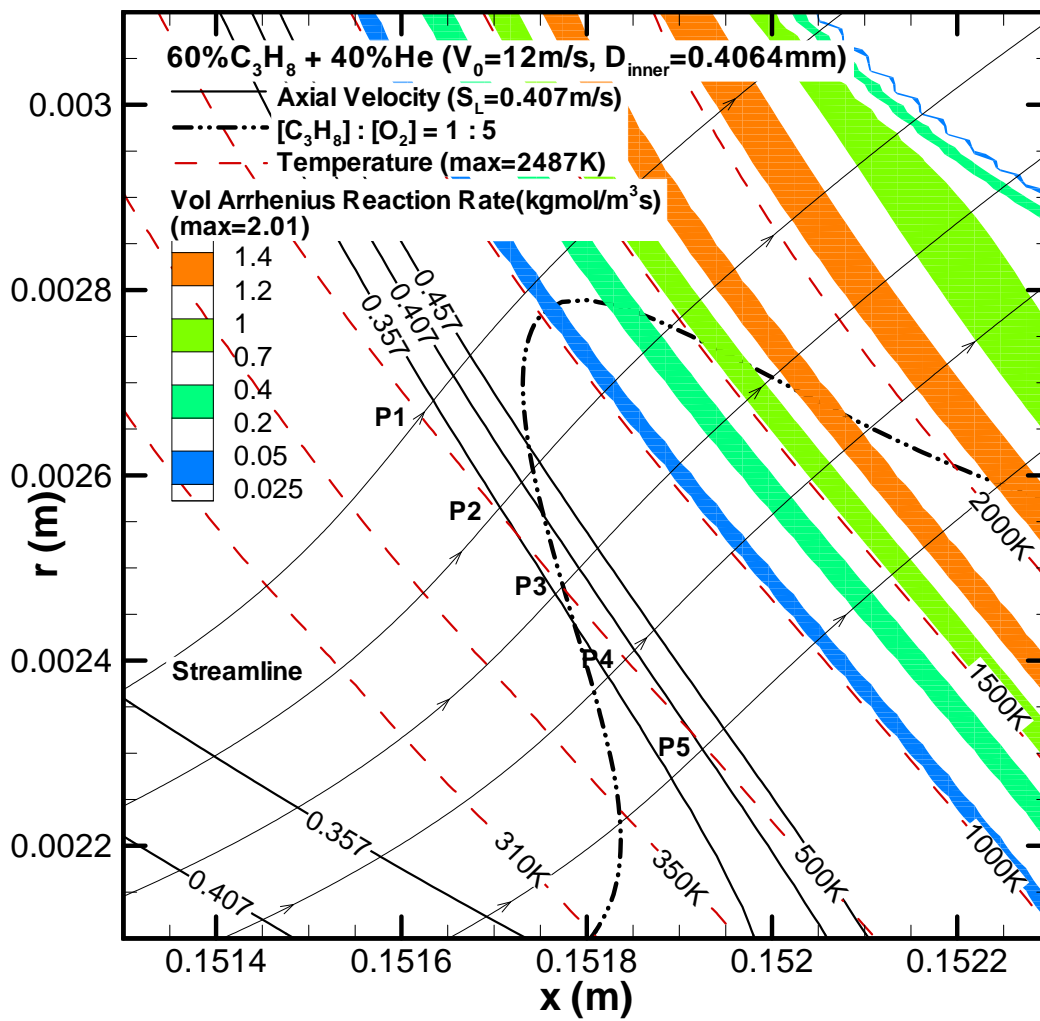(d2) stretch rate fit along 1000 K isotherm

Figure A.9 (a - f) – (continued)

(e1) intersections of 1500 K isotherm and streamlines

(e2) stretch rate fit along 1500 K isotherm

Figure A.9 (a - f) – (continued)

(f1) intersections of 2000 K isotherm and streamlines
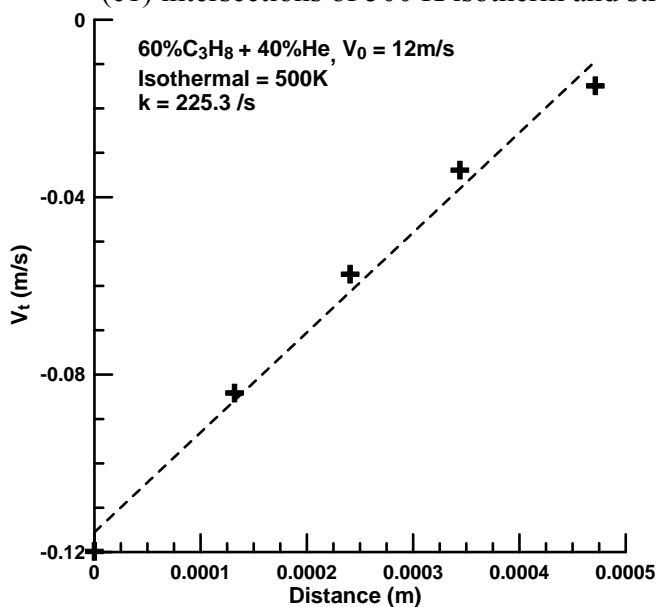

(f2) stretch rate fit along 2000 K isotherm

Figure A.9 (a - f) – (continued)

(a1) intersections of 310 K isotherm and streamlines

(a2) stretch rate fit along 310 K isotherm

Figure A.10 (a - f) – Interpolation around the stoichiometric line and the stretch rate fit for a variety of isotherms (310K, 350K, 500K, 1000K, 1500K and 2000K) for 60% C_3H_8 with 40% He dilution at jet velocity of 10 m/s.

(b1) intersections of 350 K isotherm and streamlines

(b2) stretch rate fit along 350 K isotherm
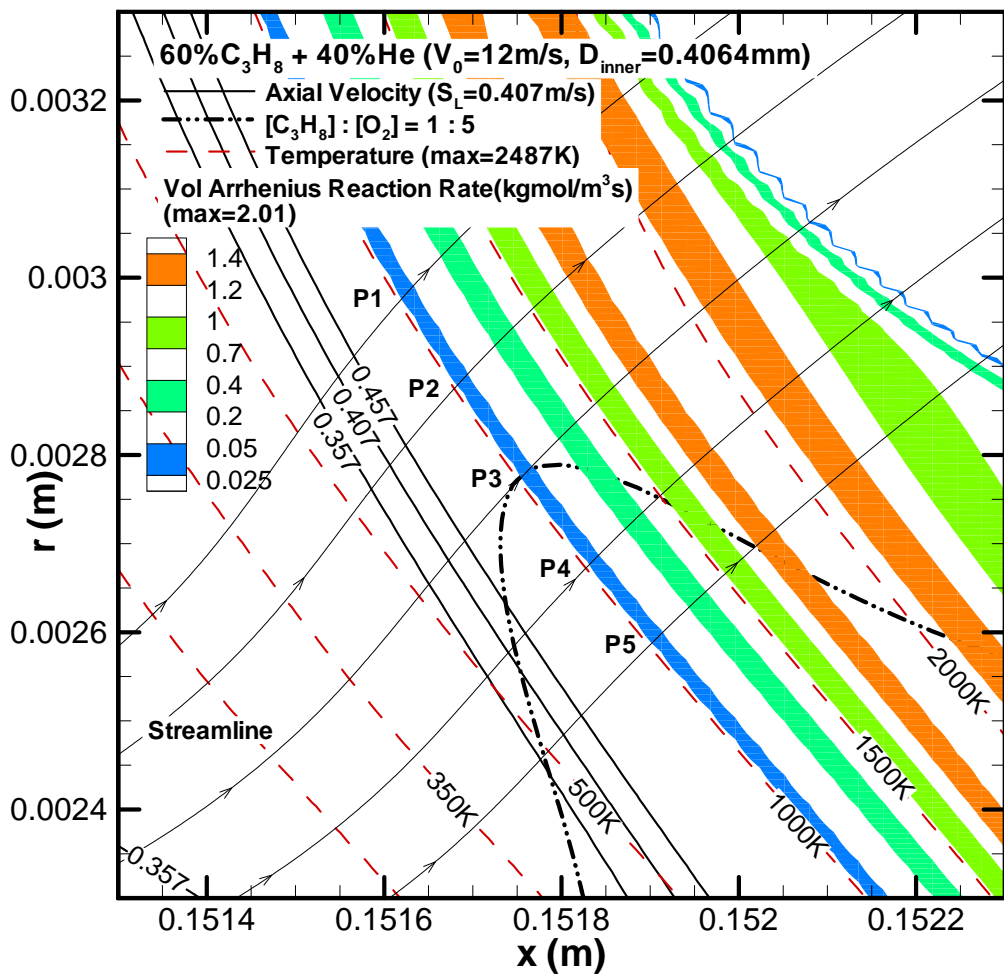
Figure A.10 (a - f) – (continued)

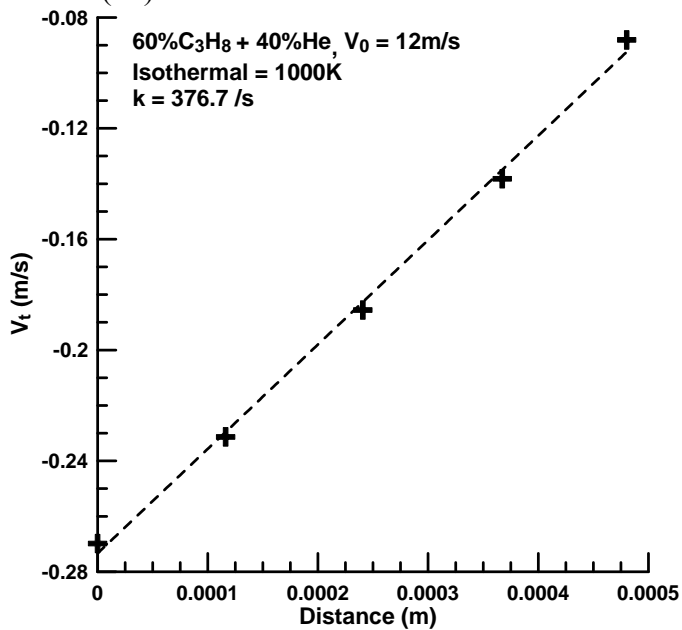(c1) intersections of 500 K isotherm and streamlines

(c2) stretch rate fit along 500 K isotherm
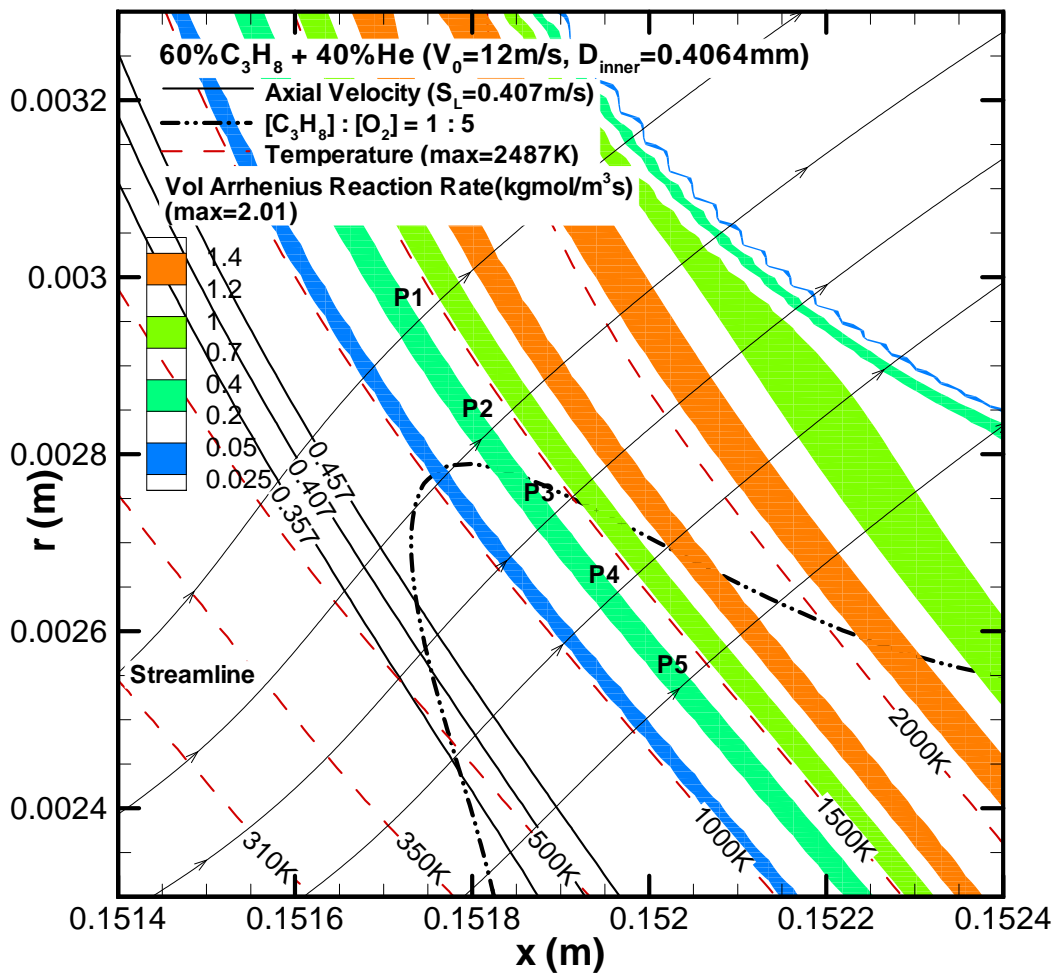
Figure A.10 (a - f) – (continued)

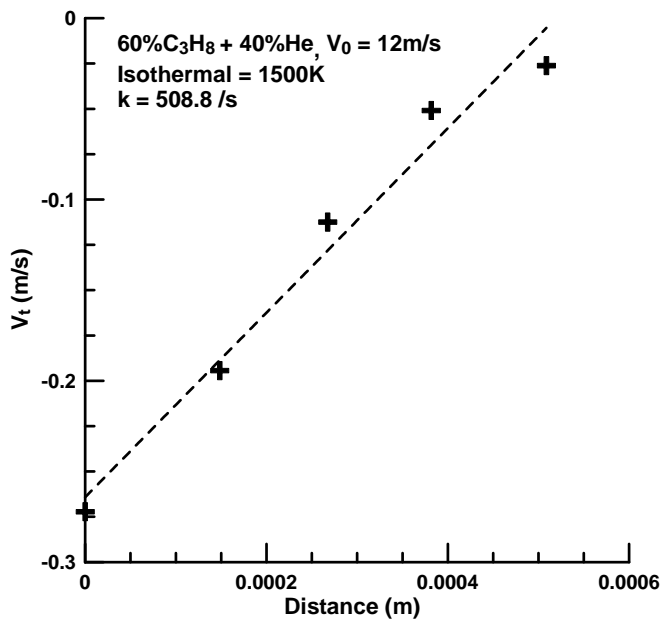(d1) intersections of 1000 K isotherm and streamlines

(d2) stretch rate fit along 1000 K isotherm
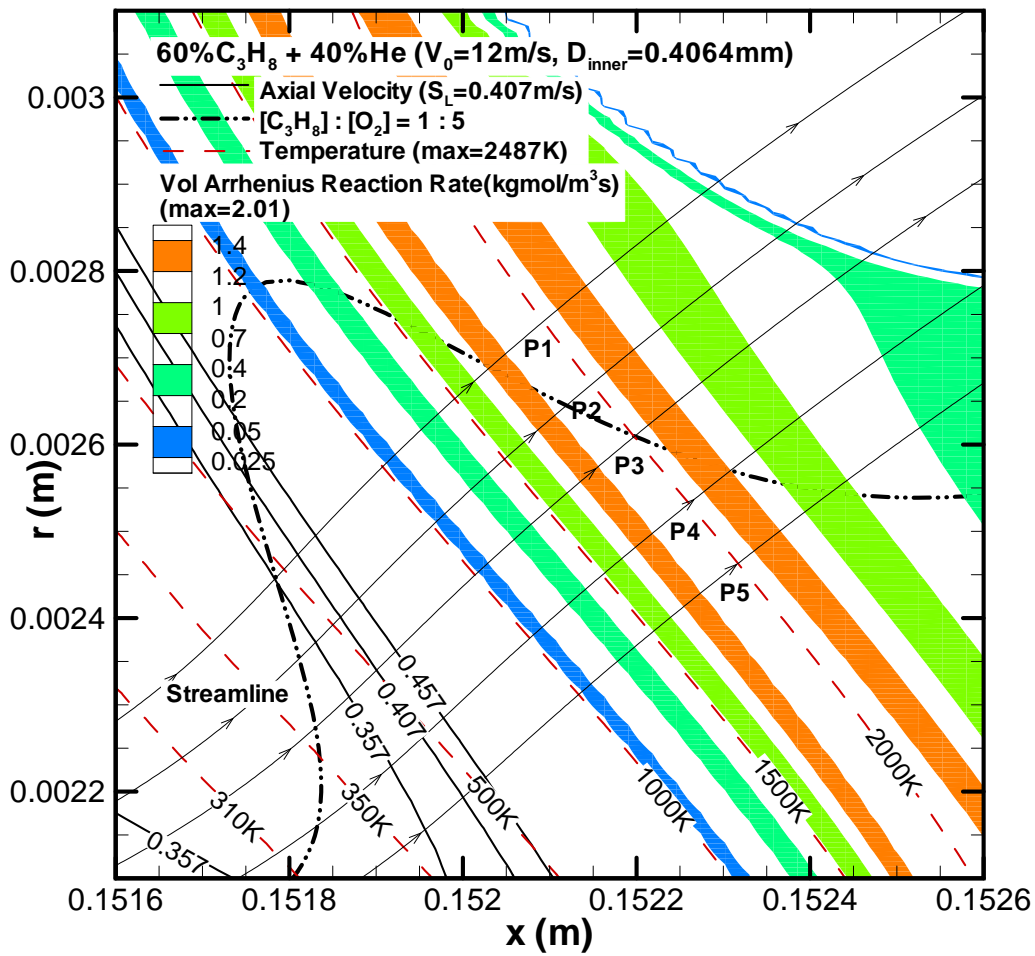
Figure A.10 (a - f) – (continued)

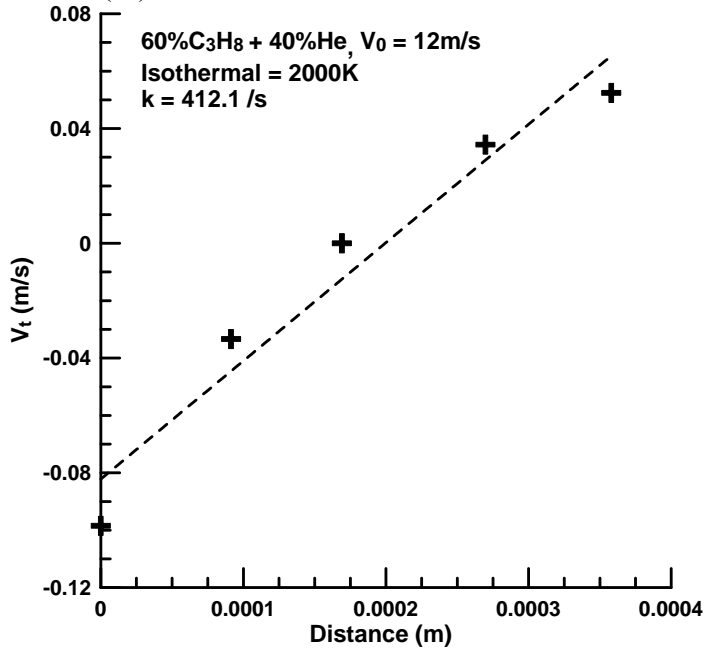(e1) intersections of 1500 K isotherm and streamlines

(e2) stretch rate fit along 1500 K isotherm

Figure A.10 (a - f) – (continued)

(f1) intersections of 2000 K isotherm and streamlines

(f2) stretch rate fit along 2000 K isotherm

Figure A.10 (a - f) – (continued)

(a1) intersections of 310 K isotherm and streamlines

(a2) stretch rate fit along 310 K isotherm

Figure A.11 (a - f) – Interpolation around the stoichiometric line and the stretch rate fit for a variety of isotherms (310K, 350K, 500K, 1000K, 1500K and 2000K) for 60% C_3H_8 with 40% He dilution at jet velocity of 12 m/s.

(b1) intersections of 350 K isotherm and streamlines

(b2) stretch rate fit along 350 K isotherm

Figure A.11 (a - f) – (continued)

(c1) intersections of 500 K isotherm and streamlines

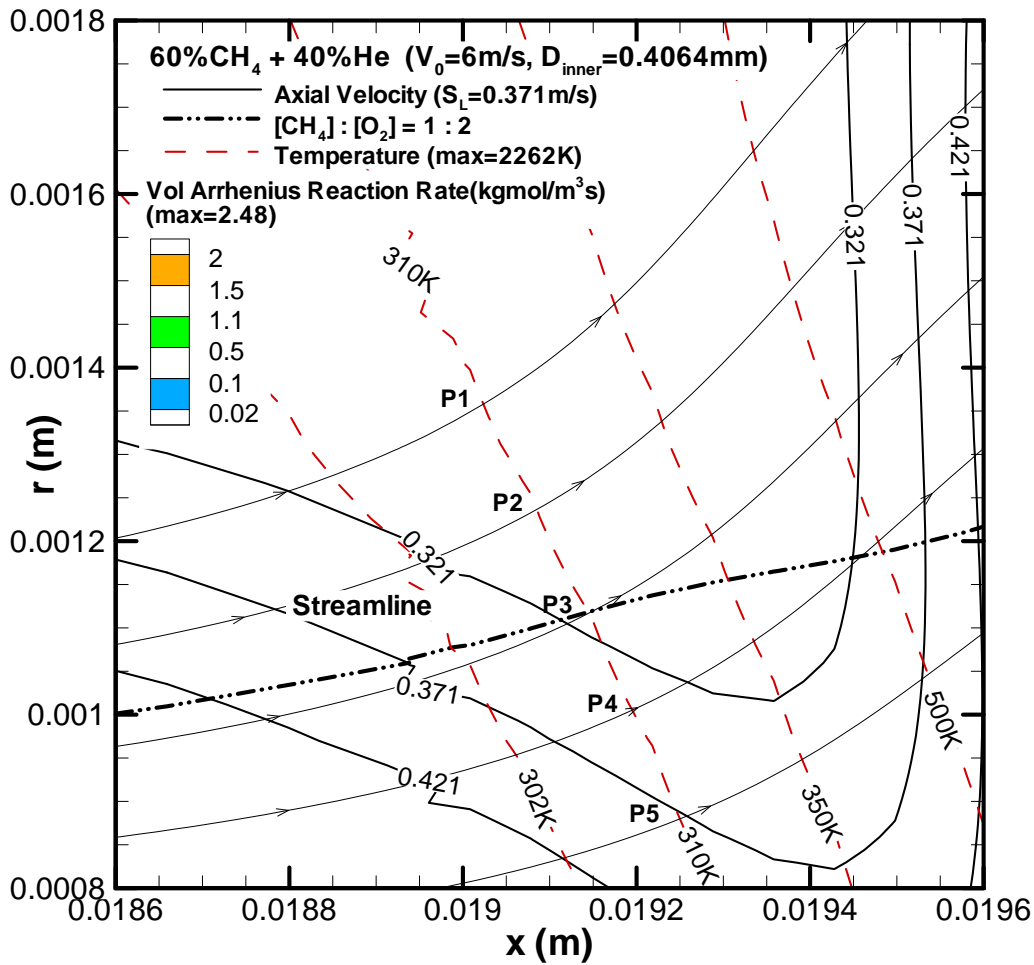(c2) stretch rate fit along 500 K isotherm

Figure A.11 (a - f) – (continued)
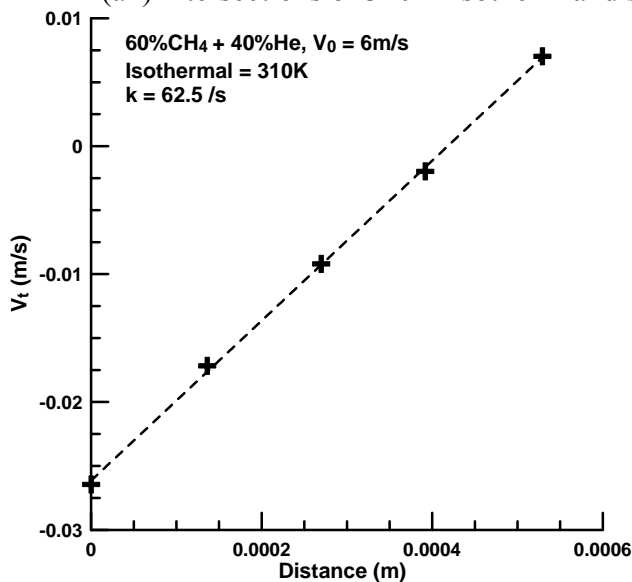
(d1) intersections of 1000 K isotherm and streamlines

(d2) stretch rate fit along 1000 K isotherm
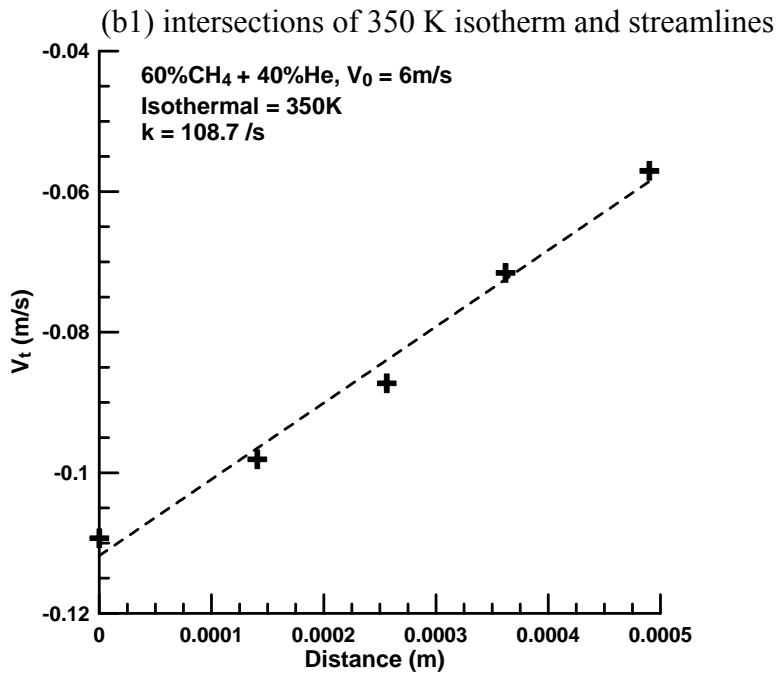
Figure A.11 (a - f) – (continued)

(e1) intersections of 1500 K isotherm and streamlines

(e2) stretch rate fit along 1500 K isotherm

Figure A.11 (a - f) – (continued)

(f1) intersections of 2000 K isotherm and streamlines

(f2) stretch rate fit along 2000 K isotherm

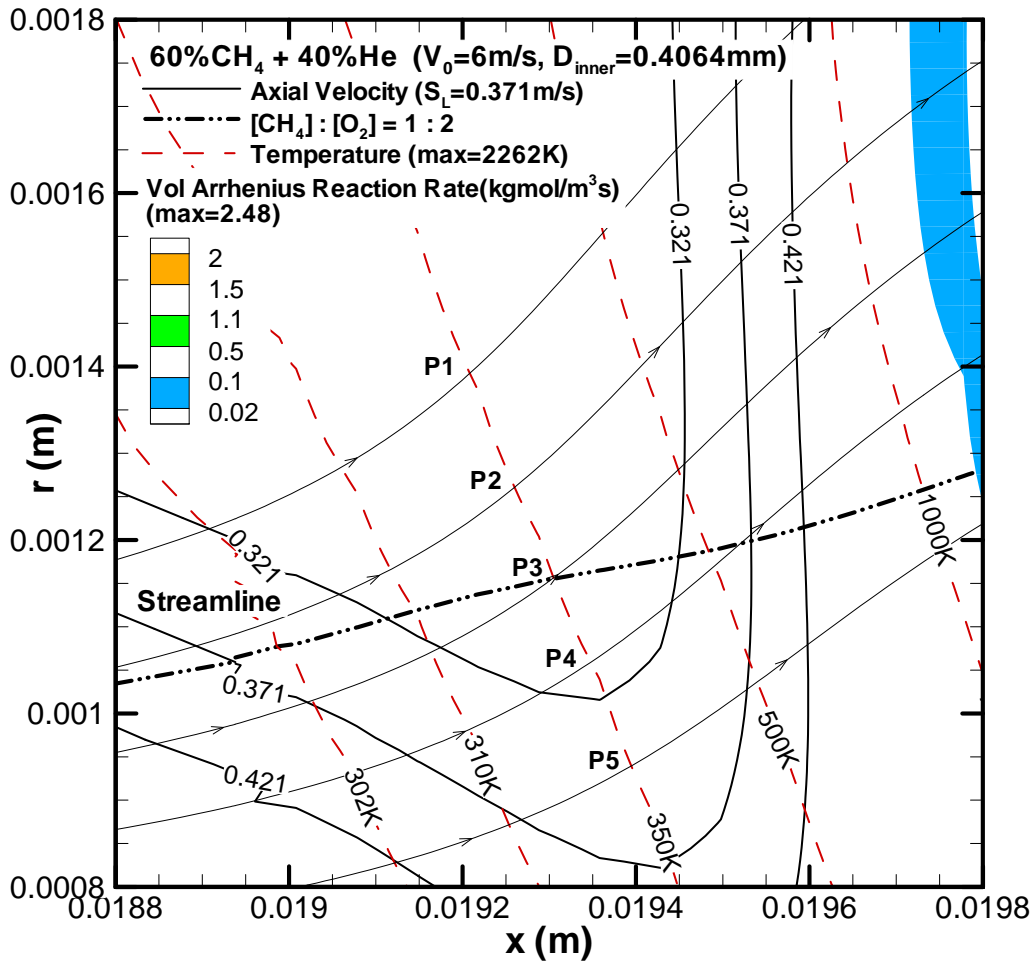Figure A.11 (a - f) – (continued)

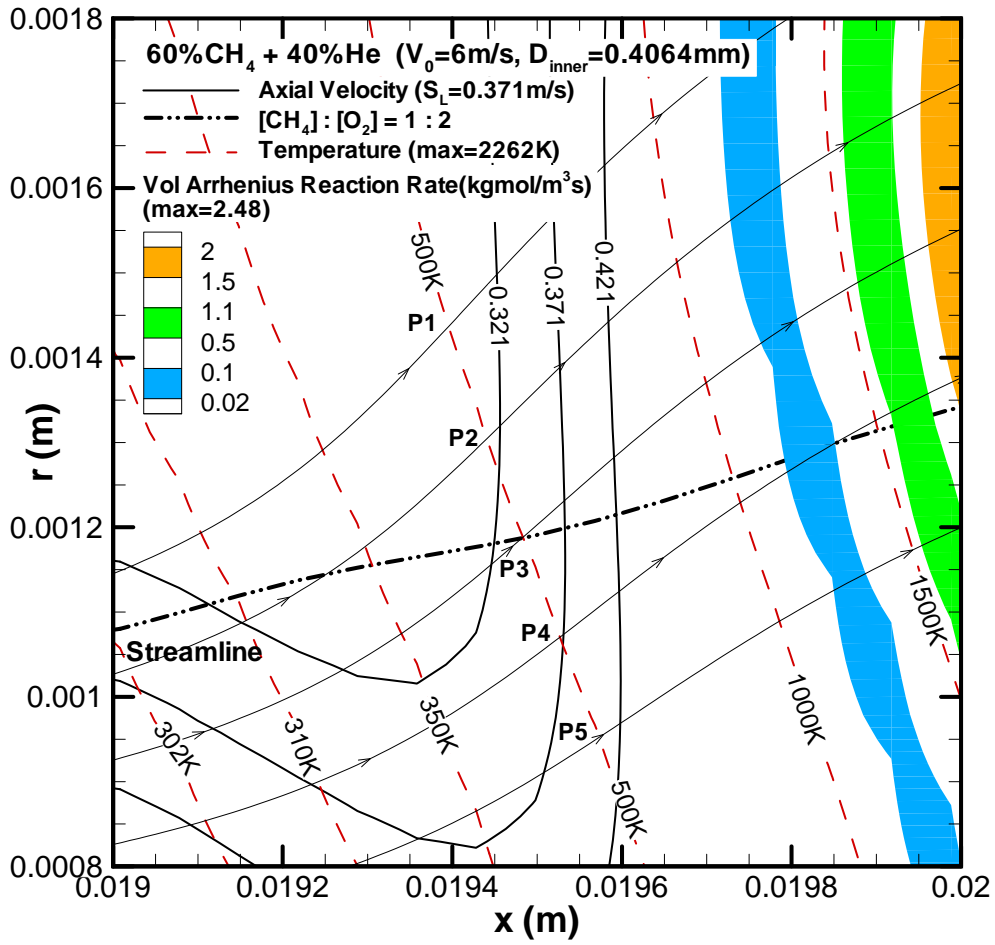(a1) intersections of 310 K isotherm and streamlines

(a2) stretch rate fit along 310 K isotherm

Figure A.12 (a - f) –Interpolation around the stoichiometric line and the stretch rate fit for a variety of isotherms (310K, 350K, 500K, 1000K, 1500K and 2000K) for 60% CH_4 with 40% He dilution at jet velocity of 6 m/s.

(b1) intersections of 350 K isotherm and streamlines
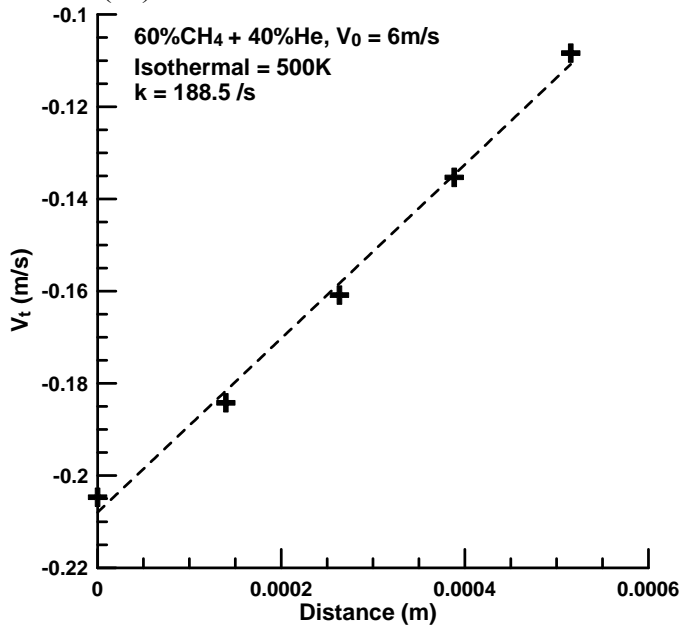

(b2) stretch rate fit along 350 K isotherm
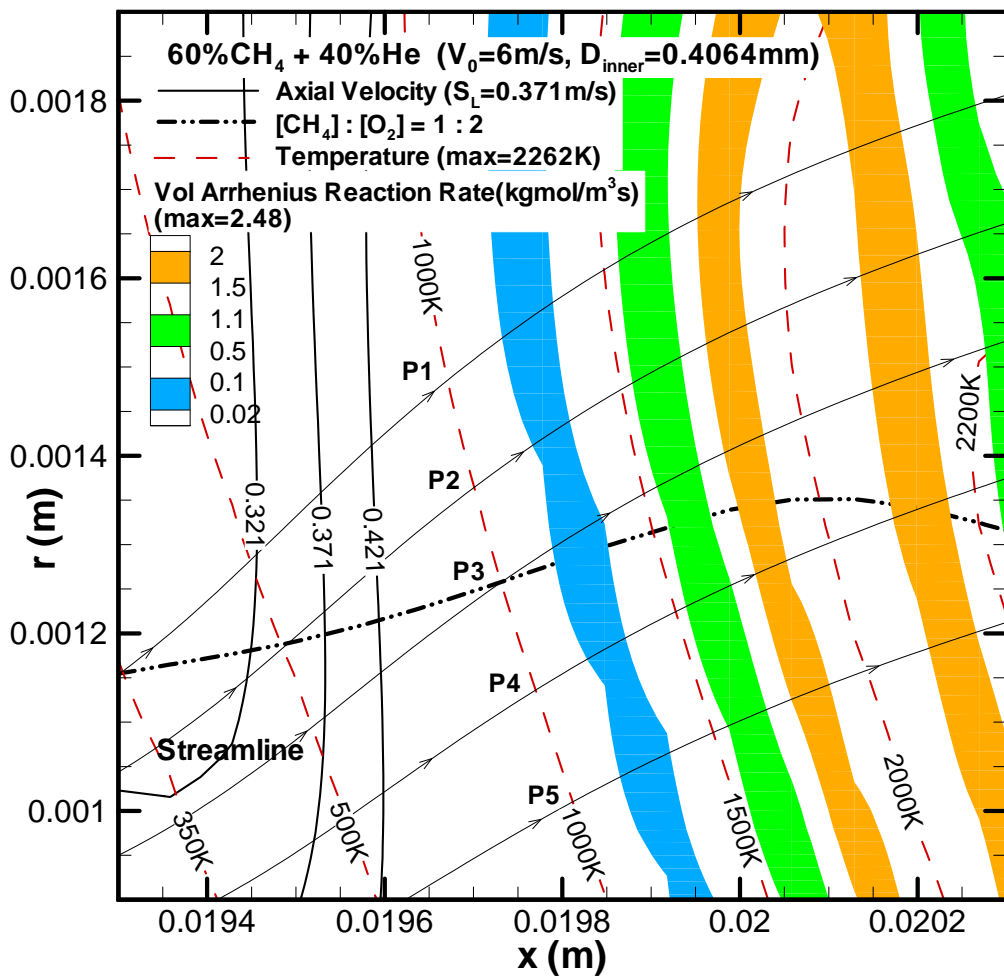
Figure A.12 (a - f) – (continued)

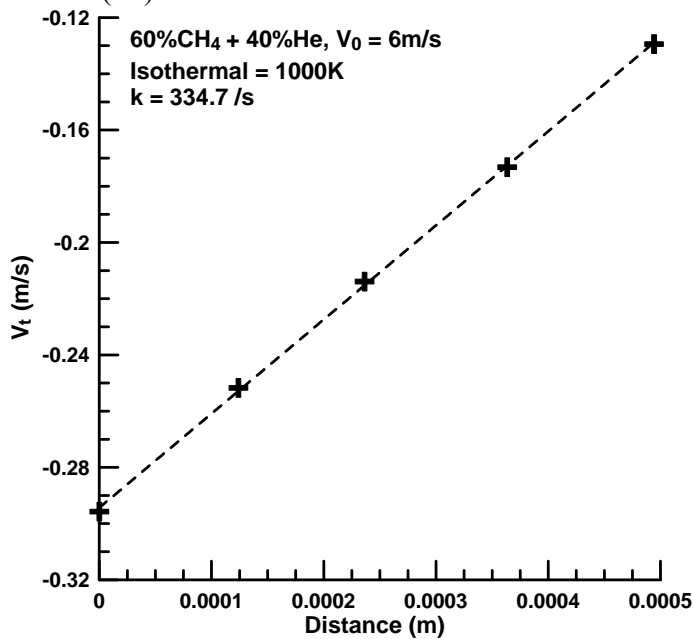(c1) intersections of 500 K isotherm and streamlines

(c2) stretch rate fit along 500 K isotherm
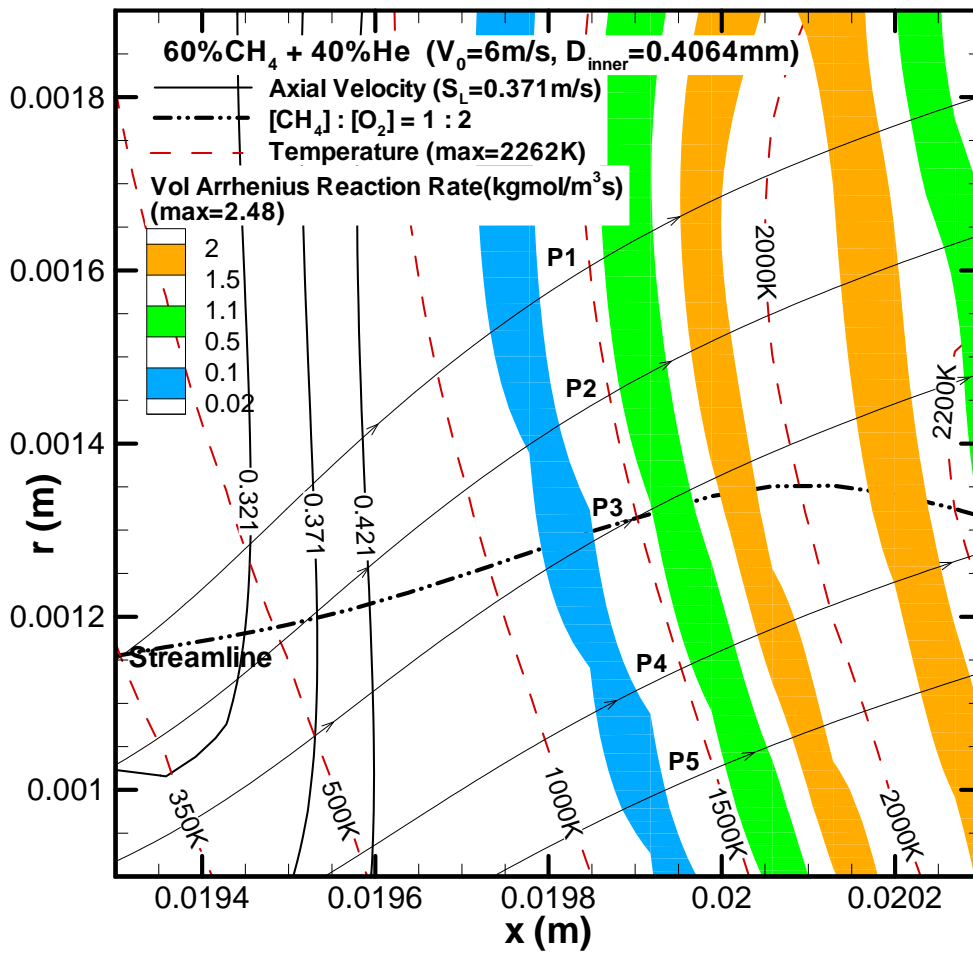
Figure A.12 (a - f) – (continued)

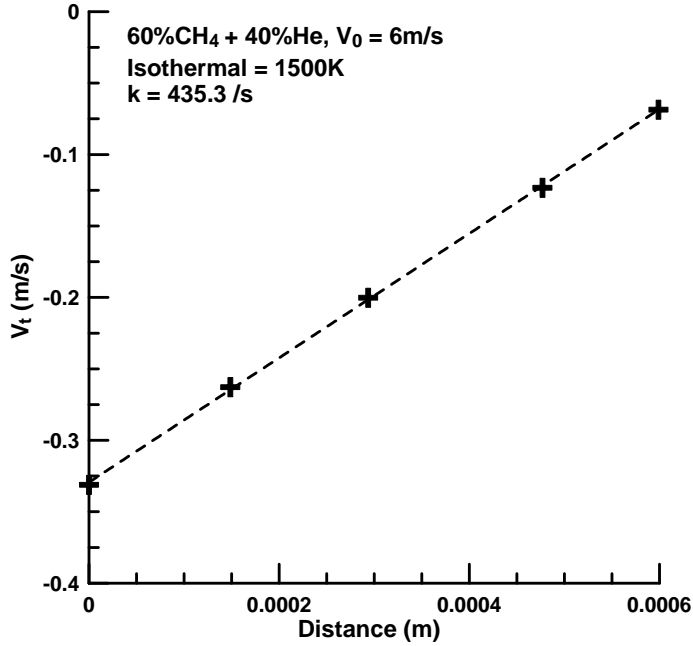(d1) intersections of 1000 K isotherm and streamlines

(d2) stretch rate fit along 1000 K isotherm

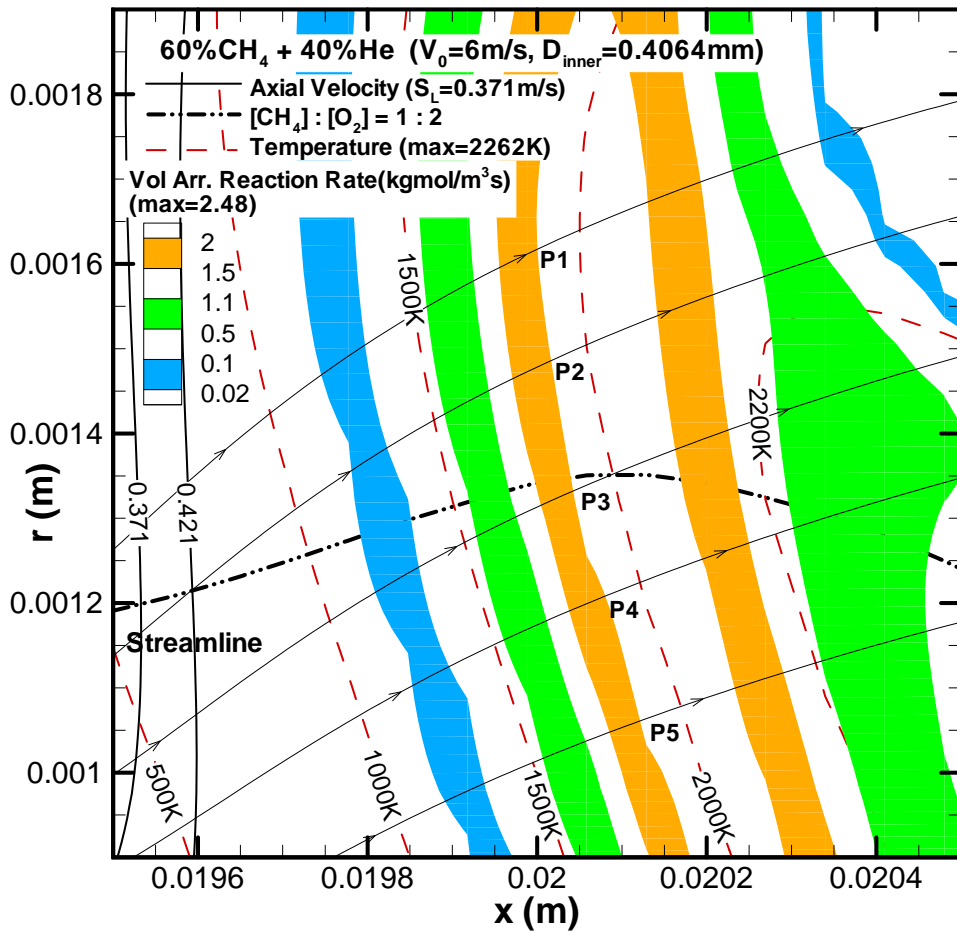Figure A.12 (a - f) – (continued)

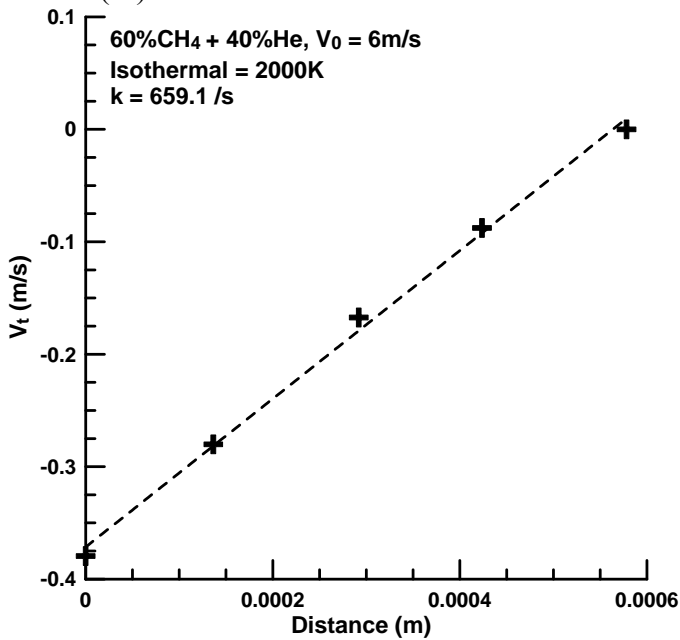(e1) intersections of 1500 K isotherm and streamlines

(e2) stretch rate fit along 1500 K isotherm

Figure A.12 (a - f) – (continued)

(f1) intersections of 2000 K isotherm and streamlines

(f2) stretch rate fit along 2000 K isotherm

Figure A.12 (a - f) – (continued)

LIST OF REFERENCES

[1] Chung, S. H. and Lee, B. J., *Combust. Flame* 86: 62-72 (1991).

[2] Savas, Ö., Gollahalli, S. R., J. *Fluid Mech.* 165: 297-318 (1986).

[3] Kuo, K. K., *Principles of Combustion*, Wiley, New York, 1986, 360-365.

[4] Lee, B. J., and Chung, S. H., *Combust. Flame* 109: 163-172 (1997).

[5] Ruetsch, G. R., Vervisch, L., and Liñán, A., *Phys. Fluids* 7 (6), 1447-1454 (1995).

[6] Ko, Y. S., and Chung, S. H., *Combust. Flame* 118: 151-163 (1999).

[7] Ghosal, S., Vervisch, L., *Combust. Flame* 123: 646-655 (2001).

[8] Boulanger, J., Vervisch, L., Reveillon, J., Ghosal, S., *Combust. Flame* 134: 355-368 (2003).

[9] R.-H. Chen, A. Kothawala, M. Chaos and L. P. Chew, *Combust. Flame* 141: 469-472 (2005).

[10] T. X. Phuoc and R.-H. Chen, *Optics Lasers Eng.*, 45 (2007) 834-842.

[11] Lee, B. J., and Chung, S. H., *Combust. Flame* 127: 2194-2204 (2001).

[12] F. Takahashi and V. Katta, *Proc. Combust. Inst.* 28 (2000) 2071-2078.

[13] F. Takahashi and V. Katta, *Proc. Combust. Inst.* 29 (2002) 2509-2518.

[14] F. Takahashi and V. Katta, *Proc. Combust. Inst.* 30 (2005) 383-390.

[15] Ko, Y. S., Chung, S. H., Kim, G. S., and Kim, S. W., *Combust. Flame* 123: 430-433 (2000).

[16] Won, S. H., Chung, S. H., Cha, M. S., and Lee, B. J., *Proc. Combust. Inst. 28*: 2093-2099 (2000).

[17] Law, C. K., in Reduced Kinetic Mechanisms for Application in Combustion Systems (N. Peters and B. Rogg, Eds.). Lecture Notes in Physics Series m15. Springer-Verlag, Berlin, 1993, pp. 15-26.

[18] Daou, J., and Liñán, A., "The Role of Unequal Diffusivities in Ignition and Extinction Fronts in Strained Mixing Layers", Combust. Theory Modeling 2, 1998, pp.449-477.

[19] Xue, Y., and Ju, Y., AIAA 2006-1166.

[20] G. K. Batchelor. *An Introduction to Fluid Dynamics*. Cambridge Univ. Press, Cambridge, England, 1967.

[21] Turns, Stephen R., An introduction to combustion: concepts and applications – 2nd ed. Page 227, 2000.

[22] H. J. Merk. The Macroscopic Equations for Simultaneous Heat and Mass Transfer in Isotropic, Continuous and Closed Systems. *Appl. Sci. Res.*, 8:73-99, 1959.

 [23] H. J. Curran, http://www.nuigalway.ie/chem/C3/mechanisms.htm

 [24] JomAas, G., Zheng, X.L., Zhu, D.L., Law, C. K., *Proc. Combust. Inst.* 30 (2005) 193-200.

[25] F. Halter et. al. Proc. Combust. Inst. 30 (2005) 201–208.

[26] Calcote, H. F., Gregory, C. A., Jr., Barnett, C. M., and Gilmer, R. B., Ind. Eng. Chem. 44, 2656 (1952).

[27] Turns, Stephen R., An introduction to combustion: concepts and applications. Page 236, 1996.

[28] Andrews, G. E., and Bradley, D., "The Burning Velocity of Methane-Air Mixtures," Combustion and Flame, 19: 275-288 (1972).

[29] S.H. Chung, C.K. Law, Combust. Flame 55 (1984) 123-125.

[30] Y. Otakeyama et al. Proceedings of the Combust. Institute 32 (2009) 1091-1097.